Simulation of multicomponent spray combustion in gas turbine engines

Varun Shastry

THÈSE

En vue de l'obtention du

DOCTORAT DE L'UNIVERSITÉ DE TOULOUSE

Délivré par :

Institut National Polytechnique de Toulouse (Toulouse INP)

Discipline ou spécialité :

Energétique et Transferts

Présentée et soutenue par :

M. VARUN SHASTRY

le mercredi 2 mars 2022

Titre :

Simulation of multicomponent spray combustion in gas turbine engines

---

Ecole doctorale :

Mécanique, Energétique, Génie civil, Procédés (MEGeP)

Unité de recherche :

Centre Européen de Recherche et Formation Avancées en Calcul Scientifique (CERFACS)

Directeur(s) de Thèse :

MME BÉNÉDICTE CUENOT

MME ELEONORE RIBER

Rapporteurs :

M. JIM KOK, UNIV. TWENTE ENSCHEDE PAYS-BAS

Membre(s) du jury :

M. BENOÎT FIORINA, CENTRALESUPELEC GIF SUR YVETTE, Président

M. LAURENT GICQUEL, CERFACS, Invité(e)

MME BÉNÉDICTE CUENOT, CERFACS, Membre

MME ELEONORE RIBER, CERFACS, Membre

M. NICOLAS BERTIER, ONERA, Membre

M. STEFANO PUGGELLI, GROUPE SAFRAN, Membre

Abstract

Liquid fuels are the dominant source of energy from combustion and will continue to be so until the maturity of emerging technologies. During this transition phase the use of Sustainable Aviation Fuels (SAF) as blends or in totality inside existing infrastructure is an attractive option. The operational aspects of these new fuels inside the combustion chambers are not known in detail. Further, gas turbine engines operate under high pressure ratios and lean conditions to achieve emission targets, making them susceptible to thermo-acoustic oscillations. Large Eddy Simulations (LES) have proven to be a successful tool in understanding fuel combustion processes. The focus of this thesis is on the modelling and simulation of complex multicomponent spray flame combustion in realistic systems.

First step deals with the multi-component evaporation of the liquid fuel. Realistic fuels have hundreds of components each with their vapourisation characteristics. The Abramzon-Siringnano evaporation in the AVBP solver is extended to handle this complex compositional aspect of realistic fuels. Comparison of the implemented model with experimental and numerical studies show a good agreement and ability to capture the preferential evaporation characteristics of multicomponent fuels.

Second, this multicomponent evaporation model is used in a canonical 1D laminar spray flame setup. A three-component jet fuel surrogate is coupled with Analytically Reduced Chemistry (ARC) to study the effects of droplet sizes, equivalence ratios and relative velocities on the spray flame structures. Correlations developed to estimate the spray flame speed agree with the numerical experiments indicating that the correct physical parameters have been chosen to describe multicomponent spray flame propagation.

Third part of the thesis deals with the simulations of swirled multicomponent spray flames in a large-scale LOTAR configuration. A three component description of conventional jet fuel and a sustainable aviation fuel spray is coupled with turbulent combustion models and complex chemistry description to perform 3D-LES. The fuels composition effects on the overall vapour distribution and its effects on the spray flame structure indicate the role of preferential evaporation on flame stabilisation and combustion regimes.

Finally, the forced response of the spray flame in the configuration is studied. The flame transfer function extracted using global chemistry agrees well with the experimental trends. Varying injection patterns to account for the effects of forcing on the droplet distribution shows a change in the flame response. The multicomponent spray flame response shows a strong role of composition and volatility of the fuel components.

Résumé

La plupart des combustibles utilisés pour la propulsion sont aujourd'hui sous forme liquide et vont le rester jusqu'à la maturité des nouvelles technologies énergétiques. Pendant cette phase de transition l'utilisation des Carburants Aéronautiques Renouvelables (SAF en anglais) mélangés aux carburants existants ou purs est une solution attractive. Le comportement de ces carburants dans les chambres de combustion dans des conditions opérationnelles n'est, à l'heure actuelle, pas complètement compris. Les turbines à gaz fonctionnent à haute pression et avec des mélanges pauvres en combustible d'atteindre leurs objectifs d'émission, ce qui les rend susceptibles de générer des oscillations thermo-acoustiques, ajoutant un autre niveau de complexité à leur étude. La Simulation aux Grandes Échelles (SGE) s'est montrée très utile pour modéliser et comprendre les mécanismes complexes et leurs interactions dans les flammes turbulentes. Cette thèse se concentre sur la modélisation et la simulation de flammes diphasiques de carburant complexe dans des systèmes réalistes.

Dans une première partie, l'évaporation multi-composants d'un carburant liquide est etudiee. Les carburants réalistes se composent en effect de centaines d'espèces chimiques ayant chacune des caractéristiques de vaporisation différentes. Le modèle d'évaporation d'Abramzon-Sirignano implémenté dans le solveur AVBP est étendu pour prendre en compte la composition multi-composants du combustible. Des comparaisons avec des précédentes études expérimentales et numériques montrent que la présente implémentation est en bon accord avec celles-ci et est capable de capturer l'évaporation préférentielle des carburants multi-composants.

Dans une deuxième étape, le modèle d'évaporation multi-composants est utilisé dans une flamme laminaire 1D diphasique canonique. Un carburant aéronautique représenté par un modèle à 3 composants couplé à une Chimie Analytiquement Réduite (Analytically Reduced Chemistry ou ARC en anglais) est utilisé afin d'étudier l'effet de la taille de goutte, de la richesse et de la vitesse relative sur la structure des flammes diphasiques. La cohérence des corrélations développées pour estimer la vitesse de flamme diphasique avec les expériences numériques indique que des paramètres physiques pertinents ont été choisis pour décrire la propagation de ces flammes.

Dans une troisième partie, des flammes diphasiques swirlées multi-composants sont simulées dans la configuration grande échelle LOTAR mesurée à l'ONERA Fauga. Une description multi-composants d'un spray de carburant aéronautique conventionnel et de carburant renouvelable couplée avec un modèle de combustion turbulente et une description complexe de la chimie sont utilisés pour réaliser et analyser les SGE. Les effets du carburant

sur la structure de flamme et les régimes de combustion sont discutés.

Enfin, la réponse acoustique forcée de la flamme diphasique dans cette configuration est étudiée. La fonction de transfert de flamme extraite de la simulation est en bon accord avec les tendances expérimentales. La variation du schéma d'injection pour simuler l'effet du forçage sur la distribution des gouttes montre un changement dans la réponse de la flamme. La réponse forcée de la flamme multi-composants diphasique montre l'impact de la description du carburant sur la réponse thermo-acoustique du système.

यथैधांसि समिद्धोऽग्निर्भस्मसात्कुरुतेऽर्जुन ।
ज्ञानाग्निः सर्वकर्माणि भस्मसात्कुरुते तथा ॥ ४.३७

yathaidhānsi samiddho 'gnir bhasma-sāt kurute 'rjuna
jñānāgniḥ sarva-karmāṇi bhasma-sāt kurute tathā

"As the blazing fire reduces fuel to ashes, O Arjuna, so does the fire of knowledge reduce all karma to ashes."

Bhagwad Gita, Chapter 4, Sloka 37

This small study on "fire" is dedicated to and a part of the lifelong quest for absolute knowledge. Deepest gratitude to the teachers in all forms I have found and hope to find on this journey.

Acknowledgments

I want to begin by thanking the reviewers Benoît Fiorina and Jim Kok who agreed to read the thesis and offer their comments. The critical analysis in the thesis report and the discussions during the defence were extremely stimulating and helped me look deeper into the work done. I would also like to thank Nicolas Bertier and Stefano Puggelli who agreed to be a part of the jury and for all the comments that followed about the practical applications of the thesis. Overall, a big thank you to all of the external members to make the culmination of this thesis really enjoyable and personally, a day to remember.

This work would have been incomplete if not for the support, patience and encouragement shown by my advisor Bénédicte Cuenot and co-advisor Eleonore Riber. Thank you for everything and I mean it from deep within. Thank you for being patient, giving me the space to try stuff and encouraging me during the writing phase in the crazy covid times where I truly felt stuck. I wonder how you both manage to remain calm, chill and patient, it's one skill I want to imbibe from all the years working together.

I had the chance of working closely with Laurent Gicquel and value the excellent ideas and inputs from his side right from the start until this final stage. Thank you, Thierry Poinsot for hiring me and giving the opportunity to explore this interesting research topic. The TAIAC meetings and the discussions will surely be missed from now on.

I cannot stress enough the support from the seniors, fellow colleagues and other staff in CERFACS who have been extremely approachable during the course of my PhD. Davide (still don't know if he's a senior, post-doc or PhD student) for all the constant follow-up and tips; Olivier for handling the merging integration of the code; Gabriel for patiently answering every stupid question and code related issue I went with and every other senior researcher who has been around for help. Thank you Quentin and Jonathan for all the collaboration and constantly answering my questions and helping with the chemistry stuff. Bastien who was there earlier and helped me with the paper and other things in the code. Must not forget to mention the crazy office for most part with Fabien and Charlelie for everything from AVBP, combustion to blue-dogs in India, Russian anthems; you both helped me immensely to settle down in. Finally most importantly the support from the secretaries (Michele, Marie, Chantal), CSG (Fred, Gerard and all of the others) have absolutely been crucial in finishing the thesis.

A lot of my time outside of CERFACS was spent with Ermanno and Dominik, but even then we never spoke about work. All the concerts, the dal-rice dinners in my house, random beers and exploring alternate realities are really memories to treasure. We still have Fusion finally in 2022 to look forward to

and a trip the Brazil I hope. Will remember the things we have done together in all states of conciousness.

Thank you to Willca, for all the time spent together and being around till almost the very end, good luck in the US. To the rest of them who started their PhD with me, Quentin (again), Thomas (now my post doc boss from safran), Simon (now in anime land), Julien (whose pamela I still debug today :P), I wish all of you the very best.

I was lucky to have a small Indian group in CERFACS, who made me feel close to home in this place far away. Shreejith, Abhijeet, Soumyo, Shubham, Pavan and Suman (meteo but still) you guys have been great just by being around, talking and making sure there is some home like entertainment always. The times spent eating good desi food, watching arsenal games, IPL, worldcup, random bollywood movies, board games, have truly helped take the mind away from the thesis, lonely times during the pandemic. Thank you all so much and I hope we can keep in touch always.

The Marie Curie project MAGISTER involved a lot of partners, and along with the other ANNULIGHT project there have been a lot of fun meetings, in different places. It's sad that we couldn't meet one last time after the amazing week in Munich back in 2019 September. Thank you Jim for the project, bridgette for all the other aspects, and the fellow ESRs for a great time and experience. Good luck and success to all of you.

The constant support and encouragement behind the scenes has always come from my parents and family in India. Thank you amma, papa for being available to talk, listening if you didn't understand anything sometimes, being patient/impatient with this step I took. I hope you are little proud of what I have done. Ajji, Tata, Vanaja chikki, Prassana uncle for always being around and helping me from the time I decided to pursue my masters. Pranav for all the timepass, I'm glad we had the trip to Bhutan, it certainly was the last week of real relaxation before what turned out to be 2+ years of just being in the same place. Hope we do more of it in life. Vidya aunty, suresh mama, shashank for always coming around during my India trip and spending time. Girish, beena, my akkas (tanaya and manya) for keep in touch even after all these years outside. Everyone else who followed the defence in the family, thank you so much for the support.

The last two years 2020 and 2021 was hard for everyone, the covid pandemic, the lockdowns, the uncertainty and with all this managing the final year and thesis writing got to me as well. Even with everyone around, in the end it was a lonely journey. Apart form all the people I have mentioned here, there surely was another source of motivation, strength I found though yoga, meditation and slowly learning to find comfort in things the way they are. Perhaps that is the biggest take away from the time of my thesis and I hope

it remains with me for the rest of my life.

I hope I haven't missed out on anyone, I am really sorry if I have. Once again thank you and my deepest gratitude to everyone.

Contents

Part I

Introduction

Chapter 1

Introduction

Contents

1.1 General Introduction

The efforts to mitigate humankind's ecological impact is going to be a defining story of our civilisation in the 21st century. The now very (in)famous club of Rome report titled "The limits to growth: A Report for the Club of Rome's Project on the Predicament of Mankind" [1] highlighted multiple possible scenarios of human civilisation using the dynamics of five interconnected systems viz. consumption of non-renewable resources, pollution, industrial production, food production and population. Of particular interest is the "standard run" case where the extrapolations were made based on continuing the then existing systems and policies. The authors back then forecasted serious environmental pressures stressing the system into an overshoot and collapse somewhere in the 21st century driven primarily by excess resource utilisation. Subsequent studies using updated data and models do suggest our trajectory is close the "standard run" (Figure 1.1) indicating the need to scale up the global efforts to ameliorate the situation of environmental destruction [2, 3].

The use of fossil fuels leading to an increase the greenhouse gases and a correlated rise in the global temperatures is a worrying sign. An increase of over 2°C compared considering pre-industrial temperature levels can cause catastrophic changes to the natural environment. First order effects include but aren't limited to:

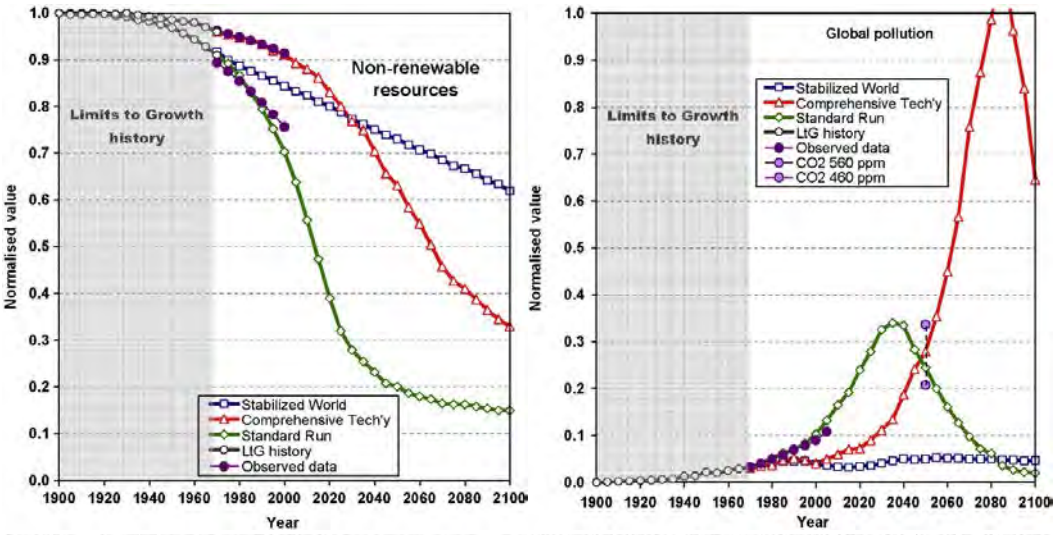

Fig. 9. Comparison of observed data (solid circles ●) for non-renewable resources remaining with the LtG model output for each scenario ("standard run" with open diamonds ◇, "comprehensive technology" with open triangles △, and "stabilized world" with open squares □). The calibrated model output over 1900–1970 is shown with open cirlces ○.

Fig. 10. Comparison of observed data (solid circles ●) for global persistent pollution with the LtG model output for each scenario ("standard run" with open diamonds ◇, "comprehensive technology" with open triangles △, and "stabilized world" with open squares □). The calibrated model output over 1900–1970 is shown with open cirlces ○. Separate points at 2050 show IPCC estimates of possible upper and lower CO_2 levels at 2050 (from A1F1 and B2 scenarios), corresponding to 560 and 460 ppm, respectively.

Figure 1.1: Comparison of "standard run" model with real data on resources and pollution taken from Turner [2].

— Frequent extremes in weather from heat waves, precipitation to drought. These are already being observed with progressively hotter summers in Europe and extreme monsoon conditions in the subcontinent [4, 5].
— Melting of polar ice caps leading to mean sea level rises, loss of small island. A bigger cause of concern is the large-scale displacement of coastal populations towards the hinterlands [6, 7].
— Destruction of animal ecosystems leading to extinction of several species due to acidification of oceans, loss of forest covers [8, 9].
— On the human side adverse effects on health and productivity cause by the impact on cultivable land due to degradation, poor air quality due to increased pollutants and clean water scarcity [10, 11].

At these cross roads we find ourselves, 196 countries under the United Nations Framework Convention on Climate Change (UNFCC) signed the Paris Agreement, a legally binding international treaty on climate change [1]. The target is to keep temperatures below 2°C and push towards 1.5°C of pre-industrial level temperatures [12]. The only method to achieve this ambitious target is to reduce emissions progressively over the next decades, shown in Figure 1.2 [2].

1. https://unfccc.int/sites/default/files/english_paris_agreement.pdf
2. https://climateactiontracker.org/global/temperatures/

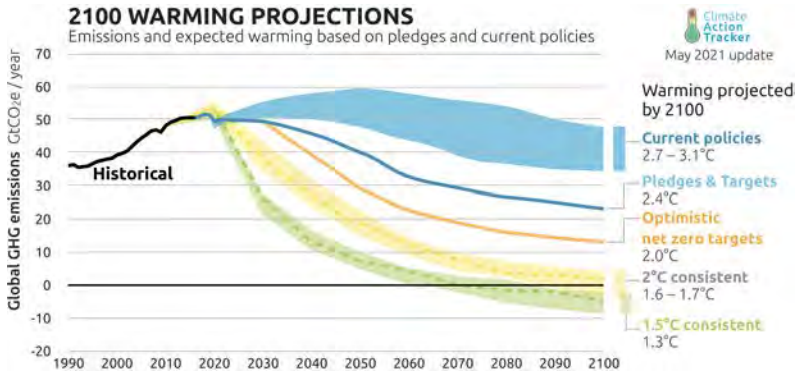

Figure 1.2: Emission targets based on policies and pledges.

1.2 Realities, global disruptions and disruptive technologies

Over 80% of the world energy demands are satisfied by fossil fuels (coal, oil, natural gas) with renewable forming only a small part of the matrix. The global energy demand is expected to rise from 275.4 mboe/d in 2020 to 352 mboe/d (million barrels of oil equivalent/day) by 2045 with the transport sector continuing to be one of the major consumers. Aviation industry in particular is expected to expand - due to rapid urbanisation and access to low cost air travel - increasing the demand for aviation fuel [3] [13, 14, 15]. The aviation regulatory bodies are aiming for a 75% reduction in CO_2 emissions per passenger per kilometre, 90% reduction NO_x levels by the year 2050 (compared to year 2000) and 50% reduction in perceived noise levels.

No discussion of events in the decade is complete without a mention of the disruptions caused by the Covid-19 pandemic on all sectors. The aviation industry has taken a heavy hit due to reduction in air travel and other financial constraints, ultimately derailing the track towards matching emissions regulations. With recoveries form the pandemic already on track, the opportunity presents itself to make the industry more sustainable in its operation with renewed technological push.

The disruptive technologies like electric, solar and hydrogen propulsion (more popular in the land based passenger transportation sector) are slowly finding their way into the aircraft engines as well. Traditional aircraft manufacturers like Saran, Boeing and Airbus are looking at ambitious projects in line with the land based counterparts. Electric planes services [4], hydro-

3. https://www.iea.org/data-and-statistics
4. https://www.airbus.com/innovation/zero-emission/electric-flight.html

gen powered planes [5] are in initial developmental stages. Electric propulsion raises issues about abundant green electricity source and storage systems for long distance journeys. Hydrogen propulsion is an attractive option but allied technologies of production, transport and safety raise many technical concerns. For a complete overhaul across the world, a timeline of a few decades are needed after complete maturity of these systems. The near future will continue to see the utilisation and improvement of existing gas turbine technologies.

In this transition process, Sustainable Aviation Fuel (SAF) is a strong contender in the reducing emissions from aviation gas turbines. These refer to renewable hydrocarbons produced from a range of sustainable raw materials whose properties match the standard aviation fuels. These can then be blended with traditional fossil fuels to be utilised directly earning them the name "drop-in" fuels. The sustainable aspect comes from the raw materials like excess wood, municipal waste and technologies that include concentrated solar power to split H_2O and CO_2. Such sustainably produced fuel sources show up to 80% reduction in emission over the total life cycle. Understanding the performance and developing models for SAF combustion in existing gas turbine engines is the first step towards such a successful transition.

1.3 Gas turbine engines

Gas turbine engines are internal combustion devices consisting of roughly three important sections: compressor, combustion chamber and turbine shown in Figure 1.3. It operates on the open Brayton cycle seen in Figure 1.4. A part of the inlet air diverted through the multiple compressor stages undergoes isentropic compression (1-2). The compressed air at high temperature is mixed with fuel and burnt at constant pressure (2-3). The hot combustion products then expand through multiple turbine stages reaching external pressure (3-4) before the cycle starts again. A part of the energy from the isentropic expansion of the hot gases is transferred to the kinetic energy of the shaft which drives the compressor and fan while the remaining exits through a nozzle along with the bypass air to produce the thrust.

One of the methods to increase the propulsive efficiency is to increase the ByPass Ratio (BPR). A high BPR decreases the fuel consumption for same thrust levels, with modern day BPR's being of the order of 10-11 for engines like CFM LEAP, P&W PW1000G. Another method is to increase the compression such that the Overall Pressure Ratio (OPR), defined as the ratio of air pressure at intake and exit of compressor stages. As evident from Figure 1.4

5. https://www.safran-group.com/news/decarbonizing-aviation-hydrogen-all-its-forms-2021-08-04

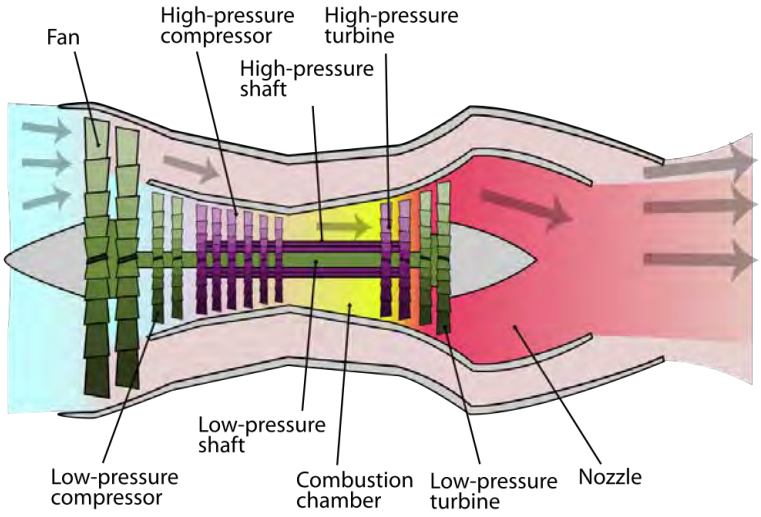

Figure 1.3: Schematic of a low bypass turbofan engine.

this increases the overall work produced. Apart from these methodologies, the efficiency of the system is a delicate optimisation considering other factors, but not limited to, material characteristics, turbine blade cooling, weight considerations and pollutant emissions.

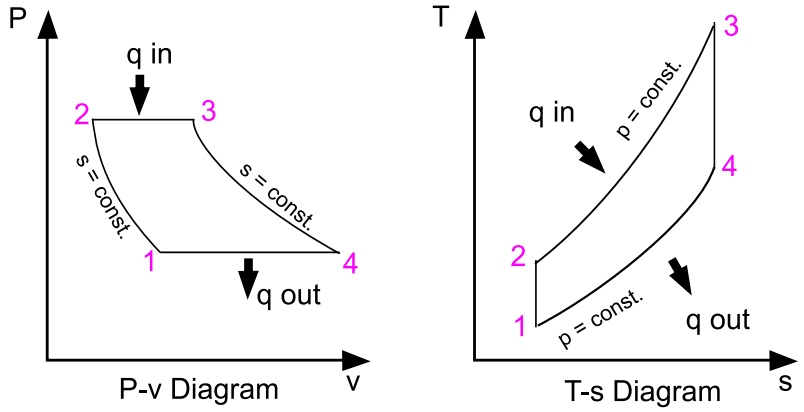

Figure 1.4: Brayton cycle P-V and T-S diagrams.

High pressure ratio while increasing efficiency also leads to high temperature promoting NO_x formation. This can be countered by reducing available oxygen but that leads to combustion on the richer side leading to formation of unburnt hydrocarbons and increased CO. The combustion chambers are designed to premix air and fuel before entering the reaction zone to ensure complete combustion and further dilution to reduce the temperature before exiting the combustion chamber. A non exhaustive list of combustion chamber technologies include Lean Direct Injection (LDI) [16, 17], Lean Premixed Pre-

vaporised (LPP) [18, 19], Rich-Quench-Lean combustors (RQL) [20, 21], Multi Point Injection (MPI) [22, 23] and others detailed in literature [24, 25, 26]. A common feature is the push towards leaner combustion which make them susceptible to thermoacoustic instabilities characterised by high amplitude pressure and heat release osculations leading to noise, flame extinction, structural damage and failure due to fatigue over time [27, 28].

1.4 Thermoacoutic Instabilities

The flame inside a combustion chamber of a gas turbine engine acts as an acoustic source and is itself affected by acoustics [29, 30]. Gases travelling through the reactive front expand leading to local pressure fluctuations propagating as acoustic waves. These interact with the boundaries and cause flow perturbation, again possibly leading to heat release fluctuations. When this feedback is constructive, as shown by a simple schematic in Figure 1.5, the natural acoustics, flow and combustion get strongly coupled and the system exhibits a thermoacoustic instability.

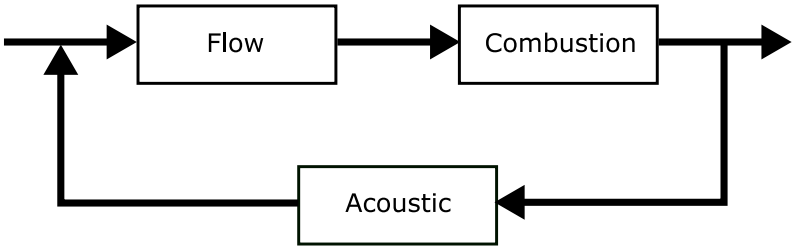

Figure 1.5: Thermoacoustic feedback loop.

The pressure fluctuations interact with the heat release in the following ways [31]:

- Variation of flame surface area: Pressure fluctuations are always associated with corresponding velocity fluctuations which lead to change of flame surface area and hence heat release
- Indirect variation of flame surface area: The interaction of vortices and the flame leads to strain rate variations which can lead again to heat release perturbation
- Variation of the chemical heat release: In practical cases where premixing of the fuel and air is done just before the combustion zone, the acoustic fluctuations can lead to mixture heterogeneities. When these reach the flame a variation of heat release is caused due to differences in the heat of combustion.

The Rayleigh criterion [32] relating the pressure and velocity fluctuations was first proposed as a condition to establish instabilities:

$$\int_{\Omega}\int_{0}^{\tau} p'q' d\Omega d\tau > 0, \tag{1.1}$$

where p' and q' are the pressure and volumetric heat release perturbations, Ω is the domain volume and τ the oscillation period. It states that pressure and heat release oscillations must be in phase for the instabilities to grow. Since these values are calculated over the entire domain, it is possible that local regions show varying behaviours of promoting and dampening the instabilities. The above criterion is only an essential condition and losses of acoustic energy through the boundaries should also be taken into account giving the modified criteria [33]:

$$\int_{\Omega}\int_{0}^{\tau} \frac{\gamma-1}{\gamma p_0} p'q' d\tau d\Omega > \int_{\Sigma}\int_{0}^{\tau} p'\mathbf{u}' d\tau d\Sigma, \tag{1.2}$$

where γ is the specific heat capacity of the gas, $\mathbf{u}'$ is the acoustic velocity and Σ the boundary surface of the combustor. According to the above modified equation, acoustic energy of a system grows only when the heat release and pressure oscillations are in phase and more than the losses though the system boundaries (right hand side term). In combustion applications where entropy fluctuations are also considered, the in-phase variations of temperature and heat release are needed for growth of the acoustic energy in the system [34].

Prediction of these instabilities is challenging but it is possible now at an early design stage. Two kinds of numerical methodologies exist. The first one includes relatively inexpensive tools that rely on analytical expressions or low-order models retaining only the acoustic characterisation and linearised flow equations which are detailed in literature [35, 36, 37, 38, 39, 40]. Such tools are adapted to stages when quick characterisation and numerous design modifications are being considered. The second approach relies on high fidelity simulations considering accurate chemistry and high-order numerical schemes yielding a complete description of the evolution and fluctuations of all flow variables across the entire domain [41].

Detailed computational fluid dynamic simulations of the complete system is capable of reproducing self-sustained instabilities. They mimic controlled experimental setups to obtain the exact frequency and growth of the instability. Such studies have been successfully conducted for both gas, and more recently, liquid fuelled combustors [42, 43, 44]. Reproducing the self-sustained instabilities require exact modelling of multiple effects and are generally on a single operating point. A complete information about all possible fundamental instability modes of the system are not obtained from such computations.

Another approach towards using simulations is to study the flame response to external forcing. The Flame Transfer Function (FTF) links the relation between incoming perturbations to the heat release fluctuations. In the frequency domain for a quantity a and heat release rate Q, it is written as:

$$FTF\left(\omega\right) = \frac{\hat{Q}/\bar{Q}}{\hat{a}/\bar{a}}, \tag{1.3}$$

where a generally is the velocity u or in some cases the equivalence ratio ϕ, with $(\hat{})$ representing the fluctuations and $(\bar{})$ the mean quantities. The simplest and most widely used approach to model the FTF is the $n-\tau$ model proposed by Crocco and Cheng [45]. The concept is that an acoustic disturbance from a reference location propagates and reaches the flame with a delay τ and produces a heat release response with a gain n. When calculated over a wide range of frequencies, the FTF can be expressed in the frequency domain as:

$$FTF\left(\omega\right) = n\left(\omega\right)\exp\left(i\omega\tau\left(\omega\right)\right). \tag{1.4}$$

A non-linear extension of the FTF approach is to study the gain and phase response of the flame over different amplitudes of inlet perturbations, leading to the Flame Describing Function (FDF) [46]. The general form of the FDF for varying velocity perturbations ($\hat{u}$) is:

$$FDF\left(\omega, |\hat{u}/\bar{u}|\right) = n\left(\omega, |\hat{u}/\bar{u}|\right)\exp\left(i\omega\tau\left(\omega, |\hat{u}/\bar{u}|\right)\right). \tag{1.5}$$

Computational techniques also utilise broadband excitation of the flame coupled with System Identification [47, 48] methods which offers the advantage of using a single run to extract the response over a wide range of frequencies unlike the earlier cited works which extract the flame response at a single frequency. Multiple studies have validated the use of CFD to determine the FTF/FDF of gaseous flames [49, 50, 51, 52]. On the contrary, the literature on two phase spray flames is very limited [53]. The aim of these FDF/FTF is to serve as an input to models that compute the acoustic behaviour of the system. Ultimately for complex systems, computational cost goes towards extracting the FTF/FDF compared to its applications in the low-order codes. For swirled spray flames, computationally extracting the transfer functions to determine various factors affecting the flame response is the best option available at present. Due to the inherent complexities of spray combustion, extracting FTFs also requires accurate modelling to correctly capture all instabilities.

1.5 Spray combustion

Liquid fuels have high energy density and are convenient to use in gas turbine combustors. They are injected into the combustion chamber using a high pressure atomizer. This brings in several multi-physics phenomena in addition to the already complex highly turbulent flow that exists. Vortices can modify the distribution of injected particles creating mixture inhomogeneities. Large droplets with higher inertia tend to be insensitive to the flow while smaller particles follow the streamlines [54, 55]. This impacts droplet evaporation which depends on droplet size. With such segregation, local zones of small fast vaporising droplets exist (Figure 1.6). In addition, turbulence and fuel vapour concentration can promote or impede evaporation and mixing. This results in a very stratified mixture entering the flame zone and altering the combustion characteristics [56].

Figure 1.6: Particles in homogeneous turbulence showing preferential concentration [54].

The role of turbulence in modifying flame surface area, flame speed, consumption and structures is well documented [33]. Since all the combustion reactions occur in the gaseous phase, the presence of a liquid phase leads to multiple possibilities depending on the evaporation time-scale, distance to the reaction zone and liquid volume fraction. Three regimes can be identified as shown in Figure 1.7:

— **Regime 1** In this case the droplets evaporate completely before the vapour-air mixture reaches the reaction zone. The resulting flame is purely a gaseous flame and uncorrelated to the liquid phase. This regime is the target of the LPP concept discussed earlier.

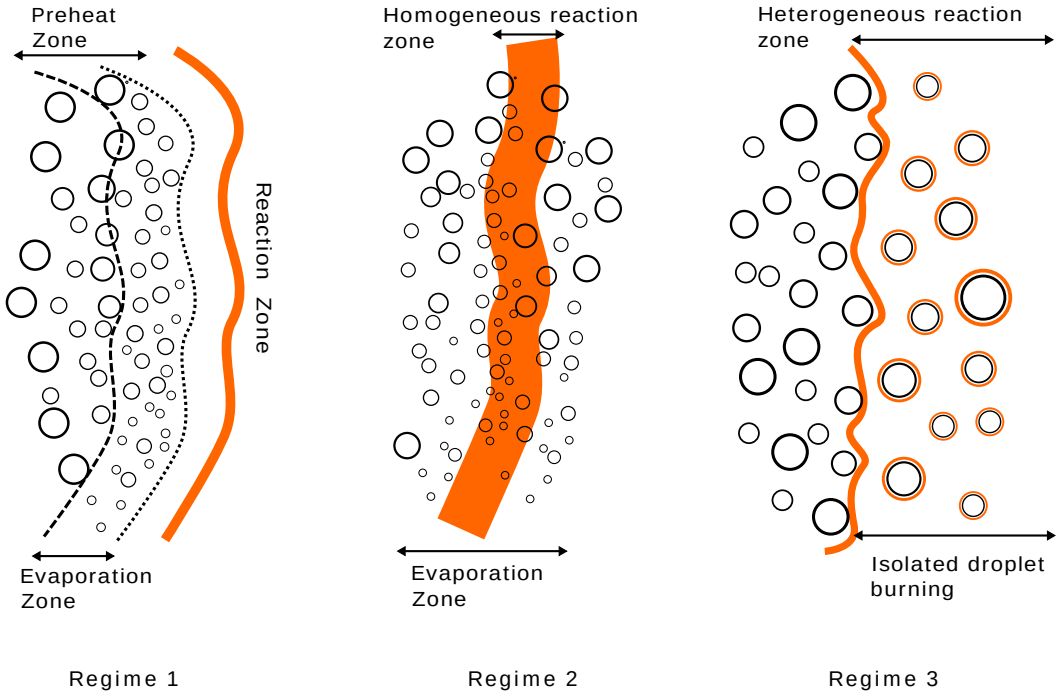

Figure 1.7: Different possibility of spray and reaction zone interaction, adapted from [57].

— **Regime 2** This case is observed when the pre-vapourising levels are not high as in the previous case and the liquid concentration is dense, a thick reaction zone is then observed. The droplets evaporate and provide fuel vapour inside the flame zone itself to sustain the gaseous reactions.

— **Regime 3** On the extreme end is the strong coupling of the spray and flame. The flame is located in between the spray. Possibilities exist of groups of droplets with a flame envelop, or of individual spray particles burning.

Chiu et al. [58], Chiu and Liu [59] studied the formation of a flame in a spherical domain filled with hot oxidiser and fuel droplets. They identified a group combustion number G defined as [56]:

$$G = \frac{3}{4} LeShN_d^{2/3} \frac{d_p}{\delta_{d_s}}, \tag{1.6}$$

where Le is the Lewis number, Sh is the sherwood number, N_d is the droplet number density, d_p is the diameter of the droplets and δ_{d_s} is the intra-droplet spacing.

Large values of G indicate long diffusion times for the vapour and lesser

penetration of thermal energy into the droplet cloud, whereas small values indicate increased thermal energy reaching the inner droplets present in the cloud. Iso-lines of G separate the various regimes shown in Figure 1.8. For $G \gg 1$ external sheath combustion takes place, where the heat doesn't penetrate and the core is in a non-evaporative state and a flame appears on the outside. On the other end of the spectrum for $G \ll 1$, single burning droplet mode is observed. In the intermediate values of $G \approx O(1)$ external and internal group combustion regimes are possible.

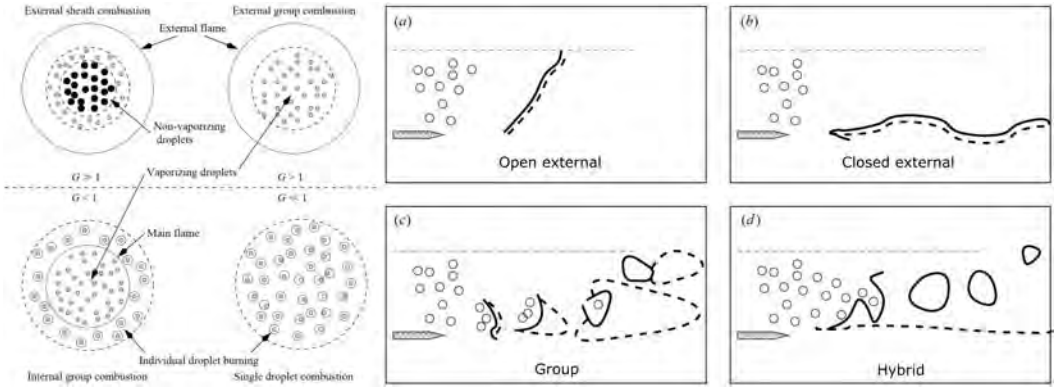

Figure 1.8: Combustion regimes from the analysis Chiu et al. [58] and DNS studies of Reveillon and Vervisch [60].

An extension of the spray flame regimes for weakly turbulent spray flames was done with the inclusion of equivalence ratio [60]. An external combustion mode was characterised by a continuous flame front with two further sub-regimes. Closed external combustion is a mostly premixed flame and open external combustion corresponds to two flame fronts stabilised on either side of the jet. Group combustion occurs when droplet clusters burn independently. Finally a hybrid mode exists which is a mixture of both the external and group combustion regimes. These modes are shown in Figure 1.8. Additionally, the propagation of a flame from one droplet to another is important and studies exist using a mono disperse train of droplets and two-phase counter-flow diffusion flames [61, 62].

The preferential concentration of spray particles due to turbulence leads to a varying mixture entering the flame zone as discussed earlier. The total equivalence ratio can then be expressed as a combination of the liquid and gaseous equivalence ratio, $\phi_{total} = \phi_{gas} + \phi_{liq}$. Due to evaporation these values are constantly varying which causes a change in the flame speed. A one dimensional approach has been extensively used in literature to study this aspect in a laminar spray flame [63, 64, 65, 66].

Initial experiments highlighted an inverse relation between the propagation

speed and droplet diameter as highlighted in the work of Ballal and Lefebvre [65]. Later experiments of Hayashi et al. [67] showed a trend contrary to the existing correlations and an optimum diameter was observed with maximum flame speed due equivalence ratio closer to 1. Analytical formulations for prediction of the laminar spray flame speed have been formulated using the sectional approach [68, 69, 70]. Computational studies [71, 72] indicate an effective equivalence ratio "seen" by the flame which Reveillon and Vervisch [60] compute in terms of the evaporation and chemical time scales as $D = \tau_{ev}/\tau_c$: depending on the droplet size the mixture reaching the flame can have an equivalence ratio between ϕ_{tot} and ϕ_{gas}. Measurements and analysis of laminar spray flame speed is necessary for accurate closure in most turbulent flame models [73].

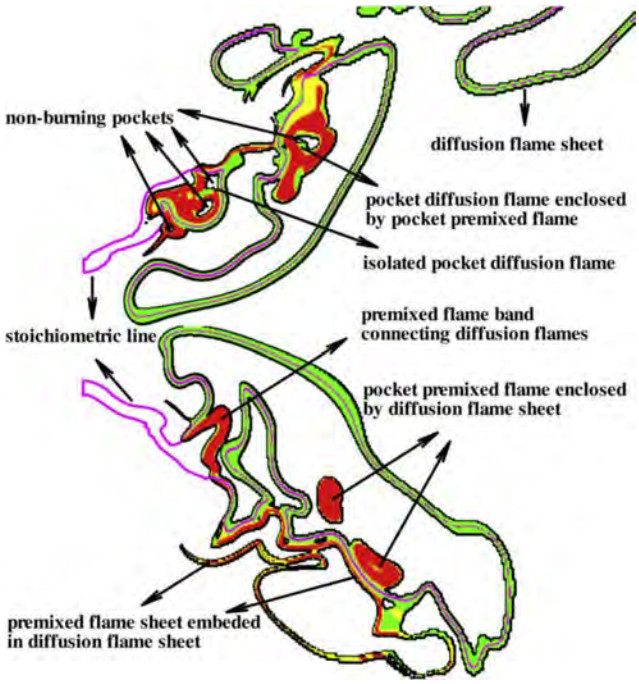

Figure 1.9: Instantaneous snapshot of a swirled spray flame (purple: stoichiometric mixture fraction iso-line; green:diffusion flames; red: premixed flames) [74].

The scale of complexity in realistic cases can be seen in Figure 1.9 [74] which demonstrates swirled turbulent spray flame. The flame is mainly premixed with pockets of diffusion flames. Group combustion pockets previously highlighted are also evident. To model these simultaneously existing regimes is a challenge especially with complex fuel blends which are currently introduced. Further chapter will revisit studies and methods used to compute spray flames.

1.6 Objectives and organisation of the thesis

The thesis was carried out as an Early Stage Researcher (ESR) in the framework of the innovative training network (ITN) MAGISTER [6]. The major goal of CERFACS in the project is to study the issue of thermoacoustic instability in spray flames. The development and application of AVBP to understand Sustainable Alternative Fuel (SAF) combustion and thermoacoustic instabilities in spray flames is the major theme of the thesis.

Part I is a recap of fundamentals of numerical combustions beginning with Chapter 1 discussing the major themes of the thesis. Chapter 2 discusses in brief the mathematical background for reactive flow simulations followed by the Lagrangian approach to spray modelling in Chapter 3.

In Part II we deal with the problem of Sustainable Aviation Fuel combustion. Chapter 4 introduces the details of reduced chemistry and surrogate representations of standard and alternative jet fuel. To handle the complex liquid phase composition, the standard single component evaporation models must be extended. A brief review of the existing methodologies, implementation and its validation is presented in Chapter 5. These evaporation and chemical models are integrated in a one-dimensional canonical configuration to study the laminar spray flame structures in Chapter 6.

The work is further extended with application to the LOTAR setup in Part III. The setup is introduced in Chapter 7 and the intial results with a simple global chemistry is discussed. The multicomponent swirled spray flames in the LOTAR configuration for standard and alternative jet fuels are studied in detail in Chapter 8. The last section of this part deals with the thermoacoustic applications. On the LOTAR configuration, an FTF is computationally extracted and compared with the experimental results with a discussion on the forced flame dynamics in Chapter 9. The first set of results for the forced multicomponent spray flame dynamics and fuel effects are shown in Chapter 10.

The concluding remarks are discussed in the final part of the thesis Part III. The major results and further developments for all the major topics are highlighted in Chapter 11.

6. https://www.magister-itn.eu/

Chapter 2

Mathematical methods for LES of turbulent reactive flows

Contents

2.1 General equations for reactive flow simulations

This chapter gives an overview and a recall of the basic concepts of turbulence, chemical kinetics and modelling approaches used for simulation of reacting and non reacting turbulent flows.

Reacting systems involve mixtures of several species interacting with one another. These must be tracked individually which makes it important to include chemical reactions and accurate transport properties in addition to the regular Naiver-Stokes equations used for non reacting simulations. For

detailed derivations and multiple forms of these multicomponent reactive flow equations, the reader is referred to the classical works of Williams [75], Kuo [76], Poinsot and Veynante [33], only the essential points are highlighted in this chapter.

2.1.1 Mixture

The normalised concentrations of a species k in the mixture can be represented using either mass fraction Y_k or mole fractions respective X_k. The are defined as the ratio of the mass (moles) of the particular species to the total mass (total number of moles) in the mixture. For a reactive mixture containing a total of N species, they can be calculated as:

$$Y_k = m_k/m, \qquad \sum_{k=1}^{N} Y_k = 1. \tag{2.1}$$

$$X_k = Y_k W/W_k, \qquad \sum_{k=1}^{N} X_k = 1. \tag{2.2}$$

The mole and mass fractions in the above equations are related by the mean molecular mass of the mixture W and the molecular mass of each species W_k, which follow the relation:

$$\frac{1}{W} = \sum_{k=1}^{N} \frac{Y_k}{W_k}. \tag{2.3}$$

To evaluate the chemical reaction rates, the molar concentration $[X_k]$ defined as the number of moles per unit volume is preferred given by:

$$[X_k] = \rho \frac{Y_k}{W_k} = \rho \frac{X_k}{W}, \tag{2.4}$$

where ρ is the density and is related to the thermodynamic variables pressure p and temperature T by the perfect gas relation:

$$p = \rho \frac{R}{W} T, \tag{2.5}$$

where $R = 8.314\,\mathrm{JK^{-1}mol^{-1}}$ is the universal gas constant.

The energy content can be represented using the total enthalpy h_k consisting of two parts. The sensible enthalpy h_{sk} is given by Eq. (2.6), and the enthalpy of formation $\Delta h^0_{f,k}$ is associated with the chemical energy needed to

produce the compound.

$$h_{sk} = \int_{T_0}^{T} C_{pk} dT, \tag{2.6}$$

where C_{pk} is the heat capacity at constant pressure of species k.

$$h_k = \underbrace{\int_{T_0}^{T} C_p^k dT}_{\text{sensible}} + \underbrace{\Delta h_{f,k}^0}_{\text{chemical}} . \tag{2.7}$$

In the above equations, the reference temperature T_0 is chosen as 298.15K where the h_{sk} is zero.

2.1.2 Transport properties

In a multispecies reactive mixture, the transport of mass and energy play a vital role. Non uniform temperatures and concentrations imply the need for accurate solutions to the interspecies transport equation, which is a problem in itself and adds to the computational cost. Often simplifications are used to get over this issue

In such cases, the Hirschfelder and Curtiss approximation to the full transport equation is utilised where the equivalent diffusion coefficient for each species D_k can be calculated using the binary diffusion coefficient $D_{jk} = D_{kj}$ as

$$D_k = \frac{1 - Y_k}{\sum_{j \neq k} (X_j / D_{jk})}. \tag{2.8}$$

The thermal conductivity (λ) and the heat capacity (C_p) can be used to calculate the heat diffusion D_{th} using:

$$D_{th} = \frac{\lambda}{\rho C_p}. \tag{2.9}$$

Three useful non dimensional quantities can be formulated which provide simplifications to the problem encountered. They are:

— The Lewis number of a species Le_k defined as the ratio of thermal to mass diffusion calculated in Eq. (2.10). For most practical purposes, the Le_k shows little variation and a constant Lewis number assumption is used.

$$Le_k = \frac{\lambda}{\rho C p D_k} = \frac{D_{th}}{D_k}. \tag{2.10}$$

— The momentum to heat diffusivity ratio is the Prandtl number Pr given

by:

$$\mathrm{Pr} = \frac{\nu}{\lambda/(\rho Cp)} = \frac{\mu Cp}{\lambda}. \tag{2.11}$$

— The schmidt number Sc_k is the ratio of the momentum and mass diffusivity given by:

$$Sc_k = \frac{\mu}{\rho D_k} = \mathrm{Pr}\, Le_k. \tag{2.12}$$

The viscosity of μ can be calculated using a power law formulation given by:

$$\mu = \mu_{ref} \left(\frac{T}{T_{ref}} \right)^a, \tag{2.13}$$

where T_{ref} and μ_{ref} are reference values of temperature and viscosity. The exponent a is obtained by curve fits over wide range of temperatures.

In practice, the constant individual Schmidt numbers Sc_k, the averaged molecular viscosity μ and mixture Prandtl numbers Pr are utilised to calculate the remaining transport properties.

2.1.3 Chemical kinetics

The various species in the reactive mixture undergo breakdown, combination and recombinations over several reaction steps. For this process to happen, the reactants must be present in the adequate quantities along with an energy source to initiate the chemical reaction. In reality, the path from reactants to products consists of several reactions and intermediary species. Consider the same system of N species reacting through M reactions, it can be represented as:

$$\sum_{k=1}^{N} \nu'_{kj} M_k \rightleftharpoons \sum_{k=1}^{N} \nu''_{kj} M_k \qquad \text{for } j = 1, M, \tag{2.14}$$

where M_k is a symbol of each species k, ν'_{kj} and ν''_{kj} are stoichiometric coefficients such that mass conservation is ensured as:

$$\sum_{k=1}^{N} \nu'_{kj} W_k = \sum_{k=1}^{N} \nu''_{kj} W_k \Rightarrow \nu_{kj} W_k = 0 \qquad \text{for } j = 1, M. \tag{2.15}$$

The production rate of a species $\dot{\omega}_k$ is the total of all production in each individual reaction $\dot{\omega}_{kj}$:

$$\dot{\omega}_k = \sum_{j=1}^{N} \dot{\omega}_{kj} = W_k \sum_{j=1}^{N} \nu_{kj} Q_j, \quad \text{with} \quad \frac{\dot{\omega}_{kj}}{W_k \nu_{kj}} = Q_j, \tag{2.16}$$

where Q_j the progress rate of each reaction is given by:

$$Q_j = K_{fj} \prod_{k=1}^{N} [X_k]^{\nu'_{kj}} - K_{rj} \prod_{k=1}^{N} [X_k]^{\nu''_{kj}} , \tag{2.17}$$

where K_{fj} and K_{rj} are the forward and reverse reaction rates of reactions which depend on the molar concentration of each of the components. For global reactions, exponents for the molar concentration used in Eq. (2.17) might be different to match the observed flame parameters over a wide range of equivalence ratios.

The reaction rates are calculated using an Arrhenius kind of expression given by:

$$K_{fj} = A_{fj} T^{\beta_j} \exp\left(-\frac{E_j}{RT}\right) = A_{fj} T^{\beta_j} \exp\left(-\frac{T_{aj}}{T}\right), \tag{2.18}$$

where A_{fj} is the pre-exponential constant, β_j is the temperature exponent and T_{aj} is the activation temperature.

The reverse reaction rates K_{rj} are related to the forward reaction rates K_{fj} by the equilibrium constant K_{eq}

$$K_{eq,j} = \frac{K_{fj}}{K_{rj}}, \tag{2.19}$$

$$K_{eq,j} = \left(\frac{p_0}{RT}\right)^{\sum_{k=1}^{N} \nu_{kj}} \exp\left(\frac{\Delta S_j^0}{R} - \frac{\Delta H_j^0}{RT}\right), \tag{2.20}$$

where $p_0 = 1\,\text{bar}$. ΔS_j^0 and ΔH_j^0 are the changes in the total entropy and enthalpy that happen when moving from products to reactants for each of the reaction j and are obtained from tabulations.

The central problem of combustion chemistry is identifying the correct set of species, reactions pathways and providing the constants required to obtain the correct reaction rates. In addition to this is the numerical issues of stiffness makes the chemistry aspect of combustion a challenge in itself.

2.1.4 Turbulent flows

Turbulence is characterised by stochastic flow phenomena over varying length, time scales. Such fluctuations of properties can be observed in small scale laboratory experiments all the way up to motion of gaseous planets (Jupiter's giant red spot) and stars.

While a standard well accepted definition of turbulence is not possible, turbulent flows are often characterised by the following features

— Randomness: Small fluctuations often grow and amplify making accurate predictions impossible.
— Vorticity: Vortical structures called eddies are present varying in size from the characteristic geometry length scale to smaller ones which are orders of magnitude apart
— Increased mixing: Increase mixing of mass, momentum and energy leading to so called turbulent diffusion
— Dissipation: The kinetic energy generated in the large vortical structures are often dissipated as heat in the smallest eddies due to viscous effects.

In his famous experiment Osborne Reynolds [77] identified the non-dimensional number, now named after him, which determines the transition from laminar to turbulent flow. The Reynolds number (Re) is the ratio of the momentum to the viscous forces determined by the velocity of the flow (U), length scale (D) and kinematic viscosity (ν).

$$Re = \frac{UD}{\nu}. \tag{2.21}$$

For Re = $\mathbf{O}\left(10^3\right)$ it has been observed that the flow transitions from laminar to turbulent. Large turbulent structures of the integral length scale l_T exist and the kinetic energy is transferred to the smaller structures until they are dissipated in the smallest Kolmogrov scales of size η_K [78]. For homogeneous isotropic turbulence the energy transfer happens trough a range of intermediate inertial range characterised by a constant dissipation rate ε. Further in this inertial range, the energy content is inversely proportional to the characteristic turbulent length scale, with an approximate slope of -5/3 [79]. This classical energy cascade process is illustrated in Figure 2.1.

In the smallest dissipating scales, the inertial and viscous forces balance each other out such that $Re_K = \mathbf{O}\left(1\right)$ and the energy is dissipated as heat. Using this universality of the dissipative scales, the length (η_K), time scales (τ_K) and velocity (u_K) of the Kolmogorov scale was approximated by as [80]

$$\begin{aligned} \eta_K &= \left(\nu^3/\varepsilon\right)^{1/4}. \\ \tau_K &= \left(\nu/\varepsilon\right)^{1/2}. \\ u_K &= \left(\nu\varepsilon\right)^{1/4}. \end{aligned} \tag{2.22}$$

An empirical relation between the integral length scales l_t and the dissipative length scales η_K is given by

$$\eta_K = l_T \left(Re\right)^{3/4}. \tag{2.23}$$

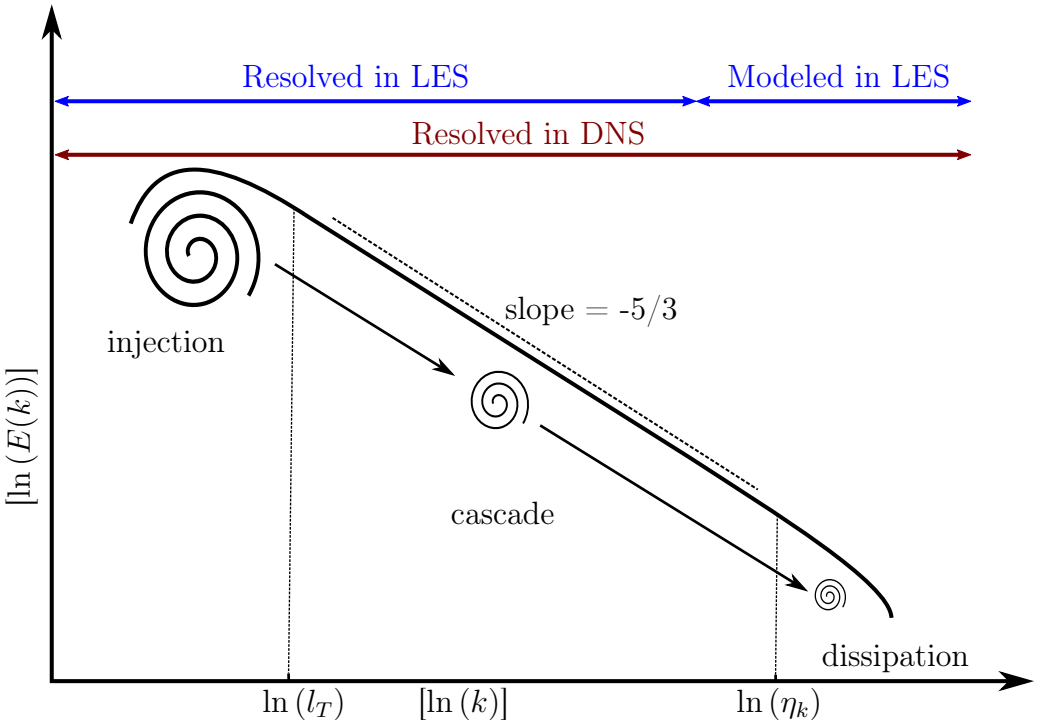

Figure 2.1: Sketch showing the turbulent energy spectrum (E) across different wave numbers (k) for homogenous isotropic turbulence.

Much of the discussion about turbulent flow simulations lie around the approaches to handle these smallest turbulent structures. On one extreme end is the RANS approach where all the scales are modelled and result in statistical mean flow quantities, which are too dissipative and do not represent the time varying quantities which are of interest. On the other extreme end are DNS approaches where all scales right down the smallest dissipative structures are resolved. Considering n points are needed to accurately capture these small turbulent structures, a quick look at Eq. (2.23) shows that this approach is out of range for practical cases at small cases and limited to small scale problems.

A smart practical approach lies in utilising aspects of both methods mentioned above wherein the eddies that can be captured by the utilised grid and filter sizes can be resolved accurately while the smaller scales are modelled. This approach is termed Large Eddy Simulation (LES). Again as shown in Figure 2.1, with an optimised mesh, LES approach can resolve the integral and inertial length scales while utilising models for the dissipation zones. For engineering problems especially, this provides the ability to capture time varying nature of the flow on scales of interest. In this work LES approach is used for the turbulent combustion simualtions.

2.1.5 Navier stokes equations for reacting mixture

The fundamental conservation equations are discussed in this section

Conservation of Mass and species

Since the process of combustion does not generate additional mass, the overall mass conversation equation holds:

$$\frac{\partial \rho}{\partial t} + \frac{\partial \rho u_i}{\partial x_i} = 0. \tag{2.24}$$

Each chemical species in the mixture must be tracked individually hence N transport equations are needed. At a particular point, the concentration depends on the convective, diffusive transport and the production rates of the species.

$$\frac{\partial \rho Y_k}{\partial t} + \frac{\partial}{\partial x_i}\left(\rho\left(u_i + V_{k,i}\right) Y_k\right) = \dot{\omega}_k \quad \text{for } k = 1, N. \tag{2.25}$$

In the above equation, $V_{k,i}$ is the diffusion velocity of the individual species. Using an equivalent diffusion coefficient, the Hirschfelder-Curtis approximation [81] is used along with a corrective velocity to ensure mass conservation yielding:

$$\frac{\partial \rho Y_k}{\partial t} + \frac{\partial}{\partial x_i}\rho\left(u_i + V_i^c\right) Y_k = \frac{\partial}{\partial x_i}\left(\rho D_k \frac{W_k}{W}\frac{\partial X_k}{\partial x_i}\right) + \dot{\omega}_k, \tag{2.26}$$

where the corrective velocity is obtained by the following expression:

$$V_i^c = \sum_{k=1}^{N}\left(D_k \frac{W_k}{W}\frac{\partial X_k}{\partial x_i}\right). \tag{2.27}$$

Conservation of momentum

$$\frac{\partial}{\partial t}\rho u_j + \frac{\partial}{\partial x_i}\rho u_i u_j = -\frac{\partial p}{\partial x_j} + \frac{\partial \tau_{ij}}{\partial x_i} + \rho \sum_{k=1}^{N} Y_k f_{k,j}, \tag{2.28}$$

where τ_{ij} is the viscous tensor defined as:

$$\tau_{ij} = -\frac{2}{3}\mu \frac{\partial u_k}{\partial x_k}\delta_{ij} + \mu\left(\frac{\partial u_i}{\partial x_j} + \frac{\partial u_j}{\partial x_i}\right). \tag{2.29}$$

Alternative, the viscous and pressure forces can be expressed together using the tensor $\sigma_{ij} = \tau_{ij} - p\delta_{ij}$. The volumetric force on the individual species is accounted for by $f_{k,j}$

Conservation of energy

$$\begin{aligned}\frac{\partial \rho E}{\partial t} + \frac{\partial}{\partial x_i}\left(\rho u E\right) = \dot{\omega}_T + \frac{\partial q_i}{\partial x_i} \\ + \frac{\partial}{\partial x_i}\left(\tau_{ij} u_i\right) + \dot{Q} \\ + \rho \sum_{k=1}^{N} Y_k f_{k,i}\left(u_i + V_{k,i}\right),\end{aligned} \tag{2.30}$$

where,

— $\dot{\omega}_T = -\sum_{k=1}^{N} \Delta h^0_{f,k} \dot{\omega}_k$ is the total heat released due to combustion

— $\dot{Q}$ is the additional energy due to a source like spark or radiative flux.

— $\rho \sum_{k=1}^{N} Y_k f_{k,i}\left(u_i + V_{k,i}\right)$ is the work done by the volume forces on each of the individual species

— $q_i = -\lambda \frac{\partial T}{\partial x_i} + \rho \sum_{k=1}^{N} h_k Y_k V_{k,i}$ is the total heat flux

  — $\lambda \frac{dT}{dx_i}$ is the heat diffusion consistent with Fourier's law

  — $\rho \sum_{k=1}^{N} h_k Y_k V_{k,i}$ is the diffusion of enthalpies due to species diffusion

These complex set of equations are closed using an equation of state mentioned earlier in Eq. (2.5).

2.2 LES approach

2.2.1 Filtered Navier stokes equations

The LES approach relies on the resolution of structures of the order of the mesh size and modelling of the smaller scales. Larger coherent structures are geometry dependent while the smaller dissipating scales have a more universal independent nature which can be modelled using the information of the larger resolved scales. These unresolved structures are referred to as the sub-grid scale (SGS) variables for which closure equations are required. The distinction between these scales is obtained by the filtering of the Navier-Stokes equations given earlier (Eq. (2.24), Eq. (2.26), Eq. (2.28) and Eq. (2.30)). A scalar f on convolution with a filter G_Δ with characteristic size Δ yields the filtered quantity $\bar{f}$:

$$\bar{f}\left(\mathbf{x}, t\right) = \int f\left(\mathbf{x}', t\right) G_\Delta\left(\mathbf{x} - \mathbf{x}'\right) d\mathbf{x}'. \tag{2.31}$$

For variable density flows, to avoid additional terms, a mass weighted Favre filtered is used such that the filtered quantity $\tilde{f}$ reads:

$$\widetilde{f} = \frac{\overline{\rho f}}{\overline{\rho}}. \tag{2.32}$$

The Favre filtering is done as:

$$\overline{\rho}\widetilde{f}\left(\mathbf{x},t\right) = \int \rho f\left(\mathbf{x}',t\right) G_{\Delta}\left(\mathbf{x}-\mathbf{x}'\right) d\mathbf{x}'. \tag{2.33}$$

The unfiltered part $f' = f - \widetilde{f}$ is the unresolved SGS which needs modelling. Applying this formalism to the reacting Navier-Stokes equations yield the filtered equations as follows:

Mass:

$$\frac{\partial\overline{\rho}}{\partial t} + \frac{\partial\overline{\rho}\widetilde{u_i}}{\partial x_i} = 0. \tag{2.34}$$

Species:

$$\frac{\partial\overline{\rho}\widetilde{Y_k}}{\partial t} + \frac{\partial\overline{\rho}\widetilde{u_i}\widetilde{Y_k}}{\partial x_i} = \frac{\partial}{\partial x_i}\left[\overline{\rho V_{k,i} Y_k} - \overline{\rho}\left(\widetilde{u_i Y_k} - \widetilde{u_i}\widetilde{Y_k}\right)\right] + \overline{\dot{\omega}}_k, \tag{2.35}$$

with the filtered diffusive flux approximated as:

$$\begin{aligned} -\overline{\rho V_{k,i} Y_k} = \overline{J}_{k,i} &= -\rho\left(\overline{D}_k \frac{W_k}{W}\frac{\partial\widetilde{X}_k}{\partial x_i} - \widetilde{Y}_k\widetilde{V}_i^c\right), \\ \widetilde{V}_i^c &\simeq \sum_{k=1}^{N} \overline{D}_k \frac{W_k}{W}\frac{\partial\widetilde{X}_k}{\partial x_i}, \\ \bar{D}_k &\simeq \frac{\bar{\mu}}{\bar{\rho} Sc_k}. \end{aligned} \tag{2.36}$$

Momentum:

$$\frac{\partial\overline{\rho}\widetilde{u_i}}{\partial t} + \frac{\partial}{\partial x_i}\left(\overline{\rho}\widetilde{u_i}\widetilde{u_j}\right) = -\frac{\partial\overline{p}}{\partial x_j} + \frac{\partial}{\partial x_i}\left[\overline{\tau}_{ij} - \overline{\rho}\left(\widetilde{u_i u_j} - \widetilde{u_i}\widetilde{u_j}\right)\right], \tag{2.37}$$

with the filtered viscous stress tensor $\overline{\tau}_{ij}$ approximated as:

$$\begin{aligned} \overline{\tau_{ij}} &\simeq \bar{\mu}\left(\frac{\partial\widetilde{u_i}}{\partial x_j} + \frac{\partial\widetilde{u_j}}{\partial x_i}\right) - \frac{2}{3}\bar{\mu}\left(\frac{\partial\widetilde{u_k}}{\partial x_k}\delta_{ij}\right), \\ \bar{\mu} &\simeq \mu(\tilde{T}). \end{aligned} \tag{2.38}$$

Energy

$$\begin{aligned}\frac{\partial \overline{\rho}\widetilde{E}}{\partial t}+\frac{\partial}{\partial x_i}\left(\overline{\rho}\widetilde{u_i}\widetilde{E}\right)=\frac{\partial \overline{u_i\sigma_{ij}}}{\partial x_j}+\frac{\partial}{\partial x_i}\left[\overline{\lambda\frac{\partial T}{\partial x_i}}-\overline{\rho\sum_{k=1}^{N}V_{k,i}Y_kh_{s,k}}\right]\\ -\frac{\partial}{\partial x_i}\left[\overline{\rho}\left(\widetilde{u_iE}-\widetilde{u_i}\widetilde{E}\right)\right]+\overline{\dot{\omega}}_T,\end{aligned} \tag{2.39}$$

with the filtered heat flux given by:

$$\begin{aligned}\overline{q}_i&=-\overline{\lambda\frac{\partial T}{\partial x_i}}+\overline{\rho\sum_{k=1}^{N}V_{k,i}Y_kh_{s,k}},\\ \overline{q}_i&\simeq-\overline{\lambda}\frac{\partial\widetilde{T}}{\partial x_i}+\sum_{k=1}^{N}\overline{J}_{k,i}\widetilde{h}_{s,k},\\ \overline{\lambda}&\simeq\frac{\overline{\mu}\overline{C_p}(\widetilde{T})}{Pr}.\end{aligned} \tag{2.40}$$

2.2.2 Modelling SGS terms

In the above equations the unresolved terms are modelled as:
Unresolved viscous stress tensor : $\overline{\tau}_{ij}^{sgs}=-\overline{\rho}\left(\widetilde{u_iu_j}-\widetilde{u}_i\widetilde{u}_j\right)$
A turbulent viscosity ν_t is introduced to obtain:

$$\overline{\tau}_{ij}^{sgs}=\bar{\rho}\nu_t\left(\frac{\partial\widetilde{u}_j}{\partial x_i}+\frac{\partial\widetilde{u}_i}{\partial x_j}\right)-\frac{2}{3}\bar{\rho}\nu_t\left(\frac{\partial\widetilde{u}_k}{\partial x_k}\delta_{ij}\right). \tag{2.41}$$

For combustion applications, two models WALE and Sigma are adopted to compute the turbulent viscosity ν_t.

— The WALE model

$$\nu_t=(C_w\Delta_x)^2\frac{\left(S_{ij}^dS_{ij}^d\right)^{3/2}}{\left(\widetilde{S}_{ij}\widetilde{S}_{ij}\right)^{5/2}+\left(S_{ij}^dS_{ij}^d\right)^{5/4}}, \tag{2.42}$$

with

$$S_{ij}^d=\frac{1}{2}\left[\left(\frac{\partial\widetilde{u}_i}{\partial x_j}\right)^2+\left(\frac{\partial\widetilde{u}_j}{\partial x_i}\right)^2\right]-\frac{1}{3}\left(\frac{\partial\widetilde{u}_k}{\partial x_k}\right)^2\delta_{ij}, \tag{2.43}$$

and

$$\widetilde{S}_{ij} = \frac{1}{2}\left(\frac{\partial \widetilde{u}_j}{\partial x_i} + \frac{\partial \widetilde{u}_i}{\partial x_j}\right). \tag{2.44}$$

$C_w = 0.4929$ is a model constant. This was developed for wall bounded flows to recover the correct scaling laws in the regions close to the walls.

— SIGMA model
Here the singular values of resolved velocity gradient tensor (σ_1, σ_2 and σ_3) are utilised to compute ν_t as:

$$\nu_t = (C_\sigma \Delta_x)^2 \frac{\sigma_3 (\sigma_1 - \sigma_2)(\sigma_2 - \sigma_3)}{\sigma_1^2}, \tag{2.45}$$

with $C_\sigma = 1.35$ being the model constant. For laminar flows where no subgrid scale activity is expected, this model vanishes and produces correct asymptotic behaviour close to the solid boundaries as with the WALE model. In this present work SIGMA model is utilised for all the reactive combustion cases.

Unresolved species fluxes : $\overline{J}_{ik}^{sgs} = -\overline{\rho}\left(\widetilde{u_i Y_k} - \widetilde{u}_i \widetilde{Y}_k\right)$

Turbulent Schmidt number Sc_t is introduced to obtain:

$$\begin{aligned}
\overline{J}_{ik}^{sgs} &= -\rho\left(\overline{D}_k^t \frac{W_k}{W}\frac{\partial \widetilde{X}_k}{\partial x_i} - \widetilde{Y}_k \widetilde{V}_i^{c,t}\right), \\
\widetilde{V}_i^{c,t} &\simeq \sum_{k=1}^{N} \overline{D}_k^t \frac{W_k}{W}\frac{\partial \widetilde{X}_k}{\partial x_i}, \\
\overline{D}_k^t &\simeq \frac{\mu_t}{\overline{\rho} Sc_k^t},
\end{aligned} \tag{2.46}$$

where Sc_k^t is the turbulent schmidt number for each species which is fixed to 0.6 in this work.

Unresolved energy fluxes : $\overline{q}_i^{sgs} = -\overline{\rho}\left(\widetilde{u_i E} - \widetilde{u}_i \widetilde{E}\right)$

Turbulent Prandtl number Pr_t is introduced to obtain:

$$\begin{aligned}
\overline{q}_i &\simeq -\lambda_t \frac{\partial \widetilde{T}}{\partial x_i} + \sum_{k=1}^{N} \overline{J}_{k,i}^{sgs} \widetilde{h}_{s,k}, \\
\lambda_t &\simeq \frac{\mu_t \overline{C_p}(\widetilde{T})}{Pr_t},
\end{aligned} \tag{2.47}$$

where the turbulent Prandtl number Pr_t again is fixed at 0.6 in the present work.

2.2.3 Thickened Flame LES (TFLES) model

Multiple approaches to turbulent combustion modelling exist in literature and codes. The G-equation model considers an infinitely thin flame corresponding to a particular iso-contour in the "G field". This is essentially a jump condition between the fresh and the burnt gasses propagated at the turbulent flame speed [82]. Tabulated methods use a reduced set of variables to address the turbulence chemistry interactions. A single progress variable evolving monotonically from the fresh to the burnt gases is related to a tabulation obtained from canonical one-dimensional flames [83, 84, 85].

In most LES simulations, though large scale structures can be resolved on the mesh, the reaction zones with high gradients are still too thin to be resolved on the mesh. Butler and O'rourke [86], O'Rourke and Bracco [87] initially prosed to artificially thicken the structure of the flame such that they can be handled on the LES mesh. The idea is to capture all the flame dynamics (ignition, flame/wall interactions etc.) while maintaining the correct propagation speed of the flame S_l. From premixed laminar flame theory [75, 33], the laminar flame speed S_L^0 and thickness δ_L^0 can be approximated using the thermal diffusivity D_{th} and the pre-exponential constant A for a single step reaction (corresponding to reaction rate $\dot{\omega}_F$). Using these relations, if D_{th} is scaled down by a factor F and A is scaled by the same factor - increasing the diffusion distance and slowing down the reaction rates - we essentially retain S_l^0 while increasing δ_l^0 as:

$$S_L^0 \propto \sqrt{D_{th}A} \xrightarrow{Thickening} \sqrt{FD_{th}\frac{A}{F}} = \sqrt{D_{th}A}. \tag{2.48}$$

$$\delta_L^0 \propto \sqrt{\frac{D_{th}}{A}} \xrightarrow{Thickening} \sqrt{FD_{th}\frac{F}{A}} = F\sqrt{\frac{D_{th}}{A}}. \tag{2.49}$$

With sufficiently large values of thickening factor F, the gradients and species profiles can be sufficiently resolved across the mesh, and as a general practice, F is used such that 5-6 mesh points lie inside the flame zone. For simple academic problems, a uniform thickening value of F can be applied across the domain, but a problem with this approach is altering the diffusivities in regions where no reactions occur. To overcome this issue, a flame sensor S is used to detect and apply a local thickening F only in necessary regions as:

$$F = 1 + (F_{max} - 1)S, \tag{2.50}$$

where F_{max} is the maximum thickening defined using the number of points n needed in the flame region, the local mesh size Δ_x and laminar flame thick-

ness δ_l^0 as:

$$F_{max} = \frac{\mathsf{n}\Delta_x}{\delta_L^0}. \tag{2.51}$$

This approach proposed by Legier et al. [88] is the Dynamically Thickened Flame LES (DTFLES)

For global chemistries (one-step, two-step), values of S are calculated using a modified reaction rate expression Ω given by:

$$\Omega = Y_F^{n_F} Y_O^{n_O} \exp\left(-\Gamma \frac{T_a}{T}\right), \tag{2.52}$$

where Γ extends thickening into the preheat zone (generally set to 0.5) and n is the exponents of fuel and oxidiser. Similarly from 1D canonical premixed flames, $\Omega_0 = max(\Omega_{1D})$ can be calculated. Finally the flame sensor reads:

$$S = \tanh\left(\beta' \frac{\Omega}{\Omega_0}\right), \tag{2.53}$$

with the parameter $\beta' \approx 50$ set to control the stiffness of the sensor S. When a two-step chemistry is utilised, generally the fuel oxidation reaction is used to evaluate Eq. (2.52). A generalization of the sensor S is needed when working with multistep chemistries as several reactions might be important in detecting a flamefront. Solutions proposed by Franzelli [89], Jaravel [90] evaluates the values of S using the reference reaction rate of the fuel $\dot{\omega}_F$. The calibrations for these sensors are done on the basis of simple canonical 1D cases.

For multicomponent spray flames, these approaches have to be modified to account for the locally varying conditions. Rochette et al. [91] developed a generic self-adapting flame sensor based solely on the geometric parameters, not requiring prior calibration. The flame front detection and thickening are separate processes.

In the fist step, the flame front detection takes into account the chemical activity, here heat release, making it independent of chemical kinetics modelling and reaction criteria. The double differential of this test function, the Hessian matrix $H(x) = \dfrac{\partial^2 f}{\partial x_i \, \partial x_j}$ is used to determine the local geometric evolution of the heat release. Geometrically, the flame font is characterised by a ridge line, which can be identified by the largest (absolute) negative eigen value of the $H(x)$ matrix as shown in Figure 2.2.

Once identified the next stage is to thicken the flame, which is a complex process because of the unstructured grid used in AVBP. The Lagrangian particle tracking algorithm is utilised to send computational particles in a di-

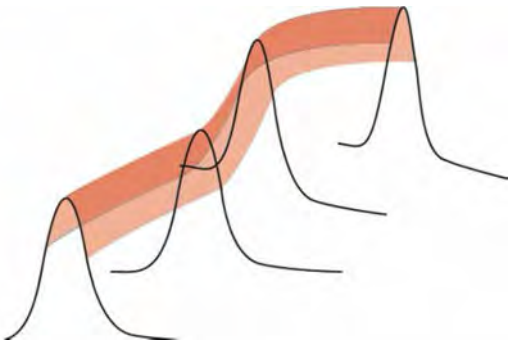

Figure 2.2: Test function f such that the concave region coincide with the flame front [91].

rection normal to the identified ride line until it reaches the limit of intended thickening. All the cells traversed by the tracking particles are thickened, with maximum near the identified ridge and decreasing away in the normal direction. This replaces the classical thickening approaches for fuels the complex multicomponent fuels.

Computationally the Generic sensor is more expensive because of-the-fly detection of the flame front and subsequent Lagrangian tracking to determine the thickened zone. Once the flame front is stabilised, assuming the globally stable flame, this operation is carried out once every 10 time steps. Successful applications to premixed gaseous flames and spray flames is detailed in Rochette [57]. The advantages it offers in terms of its generic nature and lesser parametrisation motivates its use for the simulations involving multicomponent fuels.

Another aspect of artificially thickening the flame front is the reduced Damköler number, Da. The non dimensional Da is the ratio of the turbulent to chemical timescales:

$$Da = \frac{\tau_t}{\tau_c} = \tau_t \frac{s_l^0}{\delta_l^0} \xrightarrow{Thickening} \tau_t \frac{s_l^0}{F\delta_l^0}. \tag{2.54}$$

Largely two situations of flame turbulence interactions are based on the Da:

- $Da \ll 1$: when the turbulent time scales are much faster compared to the chemical reaction time scales. The eddies have time to pass trough the reaction zone and effectively mix the inner flame structure.
- $Da \gg 1$: On the other end of the scale, when the chemical reactions are fast compared to the turbulent timescales, the inner structure of the flame is not impacted. A thin flamelet gets wrinkled by the vortices and changes the flame surface area.

As seen in Eq. (2.54), thickening the flame reduces Da, altering the flame wrinkling, hence the surface area leading to reduced fuel consumption rates. A comparison between the flame vortex interactions of unthickened and thickened approaches is shown in Figure 2.3.

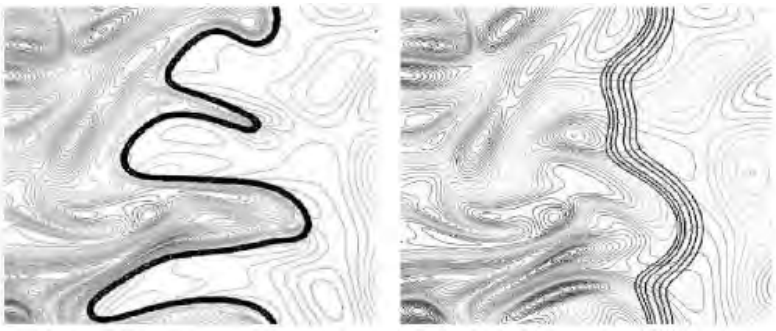

Figure 2.3: Effect of of thickening a turbulent flame. Left is the reference DNS and right is the thickened flame with F=5 showing reduced wrinkling [33].

An efficiency function $\mathcal{E}$ is introduced to handle this wrinkling effect resulting in the flame front of thickness $\mathcal{F}\delta_L^0$ propagating at a speed of $S_t = \mathcal{E}S_L$. The wrinkling ratio between the unthickened (DNS results) and the thickened flame gives the efficiency function $\mathcal{E}$ proposed by Colin et al. [92]:

$$\mathcal{E} = \frac{\Xi\left(\delta_L^0\right)}{\Xi\left(F\delta_L^0\right)}. \tag{2.55}$$

A power law expression was proposed by Charlette et al. [93] for the wrinkling factor taking into account inner and outer cutoff scales:

$$\Xi = \left(1 + \frac{\Delta}{\eta_c}\right)^{\beta}, \tag{2.56}$$

where the parameter β is set to 0.5 in the classical non-dynamic formulation. An extension of this to dynamically calculate the exponent as done by Charlette et al. [94] is used in the present work.

The Dynamic Thickened Flame Model relies on the sensor to identify the reaction zones such that thickening can be applied selectively. The theoretical robustness of these models have been demonstrated for the premixed combustion. The DTFLES approach has also been successfully used to simulate non-premixed combustion with good accuracy [88]. Poinsot and Veynante [33] demonstrate that real non-premixed flames actually are partially premixed which makes the DTFLES model practical for larger complex cases. To further apply the thickening selectively, the premixed and non-premixed

regimes can be identified by the Normalised Takeno Index [95, 96] calculated as:

$$TI = \frac{\boldsymbol{\nabla} Y_F . \boldsymbol{\nabla} Y_{Ox}}{|\boldsymbol{\nabla} Y_F| \, . \, |\boldsymbol{\nabla} Y_{Ox}|}, \tag{2.57}$$

where Y_F and Y_{Ox} are the mass fractions of the fuel and oxidiser respectively. Thickening is only applied to regions with $TI = +1$, signifying a premixed reaction zone. This approach is straightforward for global chemistries with a single fuel.

When using an ARC mechanism, the single fuel pyrolyses into several smaller components which are consumed through multiple pathways and calculation of the index using the main fuel component is not straightforward. This point was highlighted in the work by Felden et al. [97] who suggested the inclusion of all pyrolysis components to separate the premixed and non-premixed zones. For the simulation of the multicomponent flames in the present work, premixed reaction zones are considered and thickening is applied to the entire flame-front detected by the generic sensor.

2.3 Chemical Kinetics for LES simulations

An import piece in the simulations is correct estimation of species production and obtaining heats of reactions associated with the various species in the mixture. These are possible only when a chemical scheme is chosen such that it is adequate to describe all the features of interest in the configuration being studied. This topic is an active and independent field of research in itself right from deriving reactions pathways to optimisation and practical implementation. Only the basics and important aspects are highlighted here and detailed reviews, methods can be found abundantly in the other works of CERFACS [98, 99, 90].

2.3.1 Detailed chemistry

Detailed chemistries provide the benchmark and are the most comprehensive set of species and reaction description available for describing fuel oxidations. Often they run into hundreds of chemical species and thousands of reactions and are calibrated using extensive experiments. The computational cost of using these descriptions directly is immense for the following reasons:

— For each species the transport equation is needed to be solved across the entire domain and computation of the source terms $\dot{\omega}_k$ needs to be

performed
— Several species exist over a small length scale hence low resolutions of the physical domain would make it impractical for utilisation in large systems
— Some of the species exist for a short span which would need smaller timesteps to be utilised

In many cases, when accurate experimental data is unavailable such detailed chemistry description are extremely important. Canonical problems like 0D reactors, 1D flames are used along with such detailed chemistry descriptions to make accurate comparison with the lower order schemes.

2.3.2 Global Schemes

On the other extreme end are simpler chemistry descriptions using few species and 1-4 reaction steps called Globally Reduced Chemisty [100]. They are very effective and reproduce the major global parameters like laminar premixed flame speed or burnt gas temperature. The general form of such a chemical scheme for a hydrocarbon fuel is as follows:

$$\begin{aligned} F + sO_2 &\longrightarrow bCO + cH_2O, \\ CO + 0.5O_2 &\longleftrightarrow CO_2, \end{aligned} \tag{2.58}$$

where s, a, b are stoichiometric moles based on the number of carbon and hydrogen atoms in the fuel molecule. The Arrhenius expression for the reaction rate is in the form:

$$\dot{\omega}_1 = f_1(\phi)\, A_1 [F]^{n_1} [O_2]^{n_2} T^{\beta_1} \exp\left(-\frac{E_{a,1}}{RT}\right), \tag{2.59}$$

where A_1, β_1 and $E_{a,1}$ are adjustable parameters for obtaining the laminar flame speed, the reaction orders of fuel n_1 and oxidiser n_2 are used for pressure dependency. The Pre-Exponential Adjustment (PEA) coefficients in $f(\phi)$ are to obtain the correct behaviour in the rich mixture.

These schemes have been successfully utilised for flame simulations such as methane combustion [101] and for spray flames [102, 103]. Due to their simplicity and ease of used they valuable tools when chemistry details (auto ignition delays, stretch effects, ignition studies) are not important.

2.3.3 Tabulated Chemistry

These approaches take into account that after an initial time, the system can be described by a reduced set of variables [104, 105]. These maybe be a progress variables (Y_{CO_2} and Y_{CO} mass fractions), a level of mixing. This lower dimensional phase space is utilised though tabulation and the other quantities of interest are interpolated.

The Intrinsic Low-Dimensional Manifold (ILMD) has been extended independently to the Flame Propagation of ILDM (FPI) [106], Flamelet Progress Variable [107], Flamelet Generated Manifold (FGM) [108] and recently the Filtered Tabulated Chemistry for Large Eddy Simulation (F-TACLES) [85]. These methods create lookup tables form multiple simulation of one-dimensional canonical cases using detailed chemistry descriptions. Studies on complex geometries have been successfully performed with various turbulence combustion models using these approaches [109, 110].

The canonical cases (premixed, diffusion) used to generate the table may not be capable of reproducing all the flame structures observed in complex configurations with high flow-flame interactions and additional variables are required [111]. Including heat loss, preferential diffusion, dilution, pollutant formation and radiation requires modelling effects and is generally not trivial [112]. Especially in liquid fuelled systems local mixture inhomogeneity due to phase change are difficult to account for in such tabulations [113]. Practical costs associated with the present day massively parallel codes also need to be accounted for and methods of creating tables on the fly is also an option available for such constraints [114].

2.3.4 Analytically Reduced Chemistries (ARC)

The goal of ARC is to retain the thermochemical description of a system through multiple species and reactions contrary to modified/tabulated reactions mentioned earlier, but on a scale that can be readily used in LES codes. The ultimate goal is to retain anywhere between 10-30 transported species, and associated reactions essential to the problem at hand. A reduced chemistry needed to study pollutant formation needs additional information than the one that might be used to just study flames at a particular operating point. Various methods achieving this said goal of identifying superfluous components from the detailed chemistry are by definition analytical in nature and hence the terminology ARC. A step wise systematic approach integrating multiple techniques have been implemented in the code ARCANE [1] [115]. Few methods used in the reduction are discussed below.

1. https://chemistry.cerfacs.fr/en/arcane/

Skeletal Mechanisms - Graph based methods

Starting from the detailed chemistry mechanisms, the first step is to identify species and reaction pathways extraneous to the problem at hand and eliminate them. Several methods have been highlighted in literature and one of the intuitive and initial methods was the sensitivity analysis of the entire system to the concentration or production rates of the species [116]. More generalised theories are graph based methods where the species can be considered as nodes connected by paths represented by various reactions. Among these methods, the Path Flux Analysis (PFA) [117] considers the budget of atomic fluxes from one vertex to another through the various routes and the one with largest fluxes are retained.

An generalisation of the PFA methods was the Direct Relation Graph (DRG) [118] which considered the contribution of species A in either the production/consumption of B. Is r_{AB} is a measure of the contribution of species B to the production of A, B is discarded if r_{AB} is less than a threshold value of ε.

$$r_{AB} = \frac{\sum_{j=1,M} \nu_{j,A} Q_j \delta_{j,B}}{\sum_{j=1,M} \nu_{j,A} Q_j}, \tag{2.60}$$

where $\delta_{j,B}$ accounts for the contribution of only if B is present in reaction j. This definition can be extended to include relationships between global quantities of like heat release, temperature and species of interest. In addition to the direct relations between the considered points, there may be indirect paths linking two species in the mechanism and newer definition of path dependent r with error propagation is considered [119]:

$$\begin{aligned} r_{AB,p} &= \Pi_{i=1,n-1} r_{S_i S_{i+1}}, \\ R_{AB,p} &= \max r_{AB,p}, \end{aligned} \tag{2.61}$$

where S_i are the species found on the way from A to B in the path p.

As an example shown in Figure 2.4, though r_{AD} is the weakest link, but $r_{AC} = r_{AB} * r_{BC}$ can be used to remove the species C. For the reductions using this DRGEP, a target is essential which can be Heat release and some important species. This reduced set of mechanism obtained using this method of reduction is called a skeletal mechanism.

Quasi-Steady State Assumption

After the initial reduction many radicals remain in the skeletal mechanism which restricts timescales when used in CFD solvers.

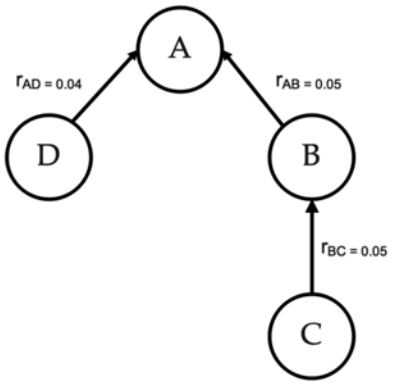

Figure 2.4: A sample graph showing the relation between 4 species taken from Pepiot-Desjardins and Pitsch [119].

The skeletal mechanism still contains many species and radicals causing stiffness issues making it impractical for direct application in CFD solvers. The limiting flow times steps are of the order 10^{-8} and stiff species are a few orders of magnitude lower than the flow time step. Quasi-Steady State Assumption (QSSA) is a technique of identifying species which have a very fast destruction time scale such that they are consumed almost instantaneously. They remain in low concentrations throughout and thus can be accounted for using an algebraic expression [120]. Essentially for a such a QSS species, we have:

$$\dot{\omega}_k \approx 0. \tag{2.62}$$

The first advantage offered is the reduction number of differential equations needed to solve for the chemical concentrations as these QSS species need not be transported. A second advantage is the reduction of the stiffness of the chemical systems as QSS species are by definition the shortest life-time species. The selection of which species can be modelled as a QSS is done based on the Level of Importance (LOI) [121] criterion which takes into account the sensitivity of the species S_K, the timescales τ_k and the concentrations c_k. Since the sensitivities are not straightforward calculations, the DRGEP coefficients r_k is utilised in ARCANE.

$$LOI_k = r_k c_k \tau_k. \tag{2.63}$$

Chemical Lumping of Species

Another method of reducing the size of a mechanism is by artificially lumping multiple species together and generating a new pseudo component. This

approach requires 1) determine the species which will be lumped; 2) the contribution of each chosen species into the lumped component; 3) estimate the thermo-physical parameters of the final lumped component so that other reduction targets are maintained.

One approach is to lump multiple isomers which have similar chemical and physical structures as a single species which need detailed knowledge of chemistry. Alternate mathematically based approaches have also been utilised [122]. In practice a robust methodology does not exist and some degree of error is expected. ARCANE follows the methodology proposed by Pepiot-Desjardins and Pitsch [119] where isomers are lumped using statistical information obtained from the detailed mechanism; species with exact thermodynamic and transport data are lumped or finally thermodynamically equivalent species are selected for lumping. The canonical cases run with detailed mechanism are used to assess the individual contribution.

Exponential Integration for ARC

Post the reduction process, though mechanism size is significantly reduced, a few stiff species still exist. In an explicit time integration, the chemical timestep is calculated as:

$$\Delta t_{chem} = \min\left(\frac{\rho Y_k}{\dot{\omega}_k}\right) \qquad \text{for each species } k \text{ in the mechanism.} \tag{2.64}$$

This Δt_{chem} when compared to the Courant–Friedrichs–Lewy (CFL) timestep of a realistic LES setup is at least an order of magnitude lesser and would lead to negative mass fractions during explicit time integration. To avoid this and to progress the simulations at a rate closer to the CFL timestep, an explicit time integration is utilised [123]. The production rate of a species is recast in terms of its concentration c_k as:

$$\dot{\omega}_k = \underbrace{A_k c_k}_{\text{production}} + \underbrace{B_k}_{\text{consumption}} , \tag{2.65}$$

where the coefficients A_k and B_k depend on local conditions and species other k. Integrating the above expression the concentrations at iteration n and $n+1$ over time step Δt is given by:

$$c_k^{n+1} = \left(c_k^n + \frac{B_k^n}{A_k^n}\right)\exp(A_k^n \Delta t) - \frac{B_k^n}{A_k^n}, \tag{2.66}$$

using which:

$$\dot{\omega}_k = \frac{c_k^{n+1} - c_k^n}{\Delta t}. \tag{2.67}$$

This ensures positive concentrations of the various species. An additional atomic balance is required which is enforced as a corrective step. This methods has been utilised in configurations with methane-oxygen combustion by Blanchard et al. [123] and methane-hydrogen combustion by Cazeres [98]. In the present work, it has been utilised for simulations of the multicomponent spray flames.

Chapter 3

Equation for LES of spray flames

Contents

3.1 Introduction

The previous chapter introduced the basic equations for LES of multi species reactive flows. When a liquid phase is introduced in the form of a spray, additional equations are needed to track its evolution. Modelling of the dilute spray sees two state-of-the art approaches. First is the mesoscopic Eulerian-Eulerian approach which assumes the liquid phase to be a continuum [124]. The methodology involves solving for the instantaneous mean quantities conditioned by the carrier phase. To this mean, an uncorrelated part is added representing the random motions leading to reorganisation and redistribution of particles. For LES applications, this set of equations is additionally filtered and the approach has been successfully used for spray computations [125, 126, 127].

The second methodology for dilute sprays is the Eulerian-Lagrangian approach where the individual spray particles can be tracked over the domain. The interaction and the influence of the carrier phase is through coupling that happens due to the exchange of mass, momentum and energy. Subgrid scale modelling is minimal and since no ensemble averaging is applied, it makes this approach suitable for handling polydisperse sprays and interactions with solid boundaries. Further sections deal with the equations, coupling and modelling involved in this approach.

3.2 Spray modelling

In this approach the spray particles are assumed to be discrete spheres dispersed in the Eluerian gas phase. The droplet sizes are of the order or smaller than the Kolmogorov length scales. The point particle assumption enables tracking the position, velocity and temperature due to its interaction with the surrounding gases. The approaches of Basset [128], Boussinesq [129], Oseen [130] commonly termed BBO equations give the equations of motion of a small spherical droplet in unsteady flow. For combustion applications, due to the high density difference between the two phase ($\rho_l \gg \rho_g$) many unsteady terms (added mass, Basset history effects) are neglected and mainly the drag forces become important. Collisions and coalescence of droplets in dense regions are neglected [131]. The fundamental equations tracking read:

$$\frac{dx_{p,i}}{dt} = u_{p,i}, \tag{3.1}$$

$$\frac{dm_p}{dt} = \dot{m}_p, \tag{3.2}$$

$$\frac{dm_p u_{p,i}}{dt} = F^{ext}_{p,i}, \tag{3.3}$$

$$\frac{dm_p h_{s,p}}{dt} = \dot{\Phi}_p, \tag{3.4}$$

where x_p, m_p are the position and mass of the droplet p, u_p its velocity and h_{sp} its sensible enthalpy. $F^{ext}_{p,i}$ is the total external force acting on the particle and Φ_p is the thermal energy exchange between the particle and the gas.

3.3 Coupling with the gas phase

The Lagrangian point sources are distributed to the nearest Eluerian nodes to account for the coupling between the phases. This accounting is done by considering individual particle positions and then distributing the source terms of the spray equations to the surrounding nodes using appropriate weightage. For a particle p present in a cell with N vertices, the projection weights for each of the vertex k represented as ψ_{n,v_k} is given by (Figure 3.1) :

$$\psi_{n,v_k} = \frac{1/d_k}{\sum_{N_v}^{k=1} 1/d_k}. \tag{3.5}$$

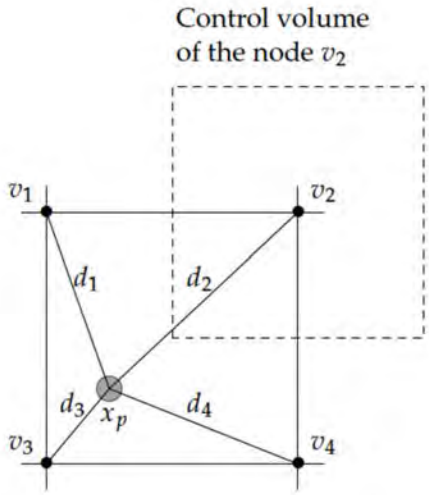

Figure 3.1: Source term projection from particle position to nearest nodes [57].

For N_p particles the source term for mass, momentum, species and energy coupling is given by:

$$S_{mass} = \frac{1}{\Delta V} \sum_{n=1}^{N_p} \psi_n \left(x_{p,n}\right) \dot{m}_{p,n}. \tag{3.6}$$

$$S_{momentum,i} = \frac{1}{\Delta V} \sum_{n=1}^{N_p} \psi_n \left(x_{p,n}\right) \left(-m_{p,n} F^{ext}_{p,n,j} + \dot{m}_{p,n} u_{p,n,j}\right). \tag{3.7}$$

$$S_{Energy} = \frac{1}{\Delta V} \sum_{n=1}^{N_p} \psi_n \left(x_{p,n}\right) \left(-m_{p,n} F^{ext}_{p,n,j} u_{p,n} + \frac{1}{2} \dot{m}_{p,n} \left\|u_{p,n}\right\|^2 - \Phi_{n,p}\right). \tag{3.8}$$

3.4 Models for isolated droplets

In the Lagrangian methodology spray evolution is a result of multiple isolated droplets that are tracked. Models are needed to obtain the forces on the droplets which control its motion and vapourisation which affect the formation of the combustible mixture.

3.4.1 Droplet dynamics

The steady state drag force is the drag force acting on the particle on account of the relative velocity between the particle and the fluid. The steady state drag force F_D can be calculated using

$$F_D = \frac{1}{2}\rho_g C_D A \left\| u_g - u_p \right\| \left(u_g - u_p \right), \tag{3.9}$$

where ρ_g is the gas density, u_p and u_g are the particle and gas velocity at particle position respectively. A is the projected surface area in the direction of the relative velocity vector. The term C_D represents the drag coefficient which needs to be modelled. C_D is a complex function of flow parameters like Reynolds number, turbulence levels, orientation of the particle etc. For a sphere the variation of C_D as a function of flow Reynolds number is shown in Figure 3.2.

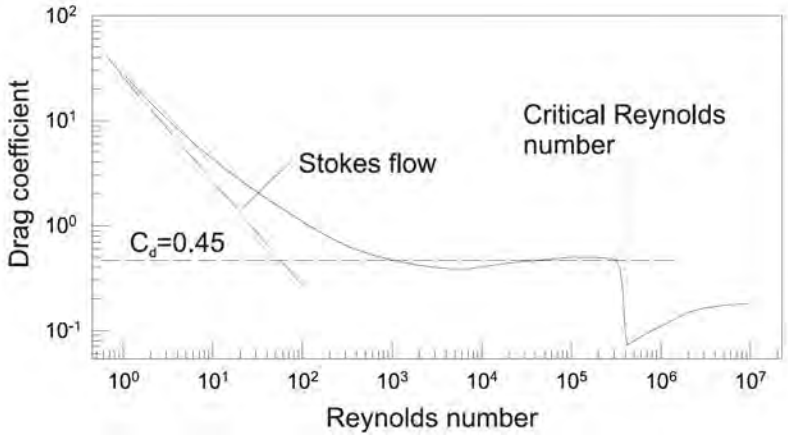

Figure 3.2: Drag coefficient of a sphere at different flow Reynolds numbers [131].

Correlations developed from experimental data are generally used to determine C_D, applicable to a large range of particle numbers encountered in practical situations. The correlations of Schiller and Nauman [132] are used in the computations performed for this work and they read as follows:

$$\begin{aligned} C_D &= \frac{24}{Re_p}\left[1 + 0.15 Re_p^{0.687}\right], \\ Re_p &= \frac{\rho_g d_p \left\| u_g - u_p \right\|}{\mu_g}. \end{aligned} \tag{3.10}$$

The other source of forces on the droplet is due to the pressure gradients

and shear stresses present in the undisturbed flow. This force F_{ud} is written as:

$$F_{ud} = F_{p,i} + F_{\tau,i} = V_d \left(-\frac{\partial p}{\partial x_i} + \frac{\partial \tau_{ij}}{\partial x_j} \right), \tag{3.11}$$

where V_d is the droplet volume. The first term is the force due to the pressure gradients which in the direction of gravity is buoyant "Archimede" force. Because of the large density differences between the two phases, these are neglected.

Additionally two time scales, the characteristic particle relaxation time (τ_p) and the flow time scale (τ_g), and their ratio, the Stokes number of the particle (S_t) can be used to understand particle trajectories. They are given by:

$$\begin{aligned} \tau_p &= \frac{\rho_l d_p^2}{18\mu_g \left(1 + 0.15 Re_p^{0.687}\right)}, \\ \tau_g &= \frac{\mathbf{l}_g}{\mathbf{u}_g}, \\ S_t &= \frac{\tau_p}{\tau_g}. \end{aligned} \tag{3.12}$$

where $\mathbf{l}_g$ and $\mathbf{u}_g$ are representative space and time scales of the gaseous phase. A large value of S_t indicates ballistic trajectories while those droplets with small S_t can be assumed to follow the bulk gaseous flow as tracers.

The final equation for droplet velocity can be written with contribution of the bulk forces g_i and steady state drag as:

$$\frac{du_{p,i}}{dt} = \frac{1}{\tau_p} \left(u_{g,i} - u_{p,i} \right) + g_i. \tag{3.13}$$

3.4.2 Droplet Evaporation

The models developed for an evaporating droplet in a quiescent environment is extended to moving droplets and utilized for studying vaporization of spray droplets. A simple model for a spherically symmetric coordinate system is introduced and the extension to modelling evaporation of multicomponent fuel droplets is presented.

In a hot environment the physical process of droplet single evaporation can be described as follows Figure 3.3

1. Heat conduction from the hot surrounding gas into the fuel droplet
2. One part of thermal energy goes into heating up the droplet and the

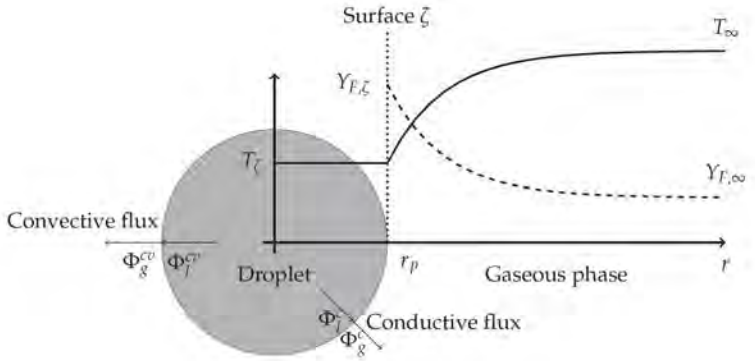

Figure 3.3: Isolated spherical evaporating droplet [57].

rest is utilized to overcome the latent heat of vaporization of the liquid at the interface

3. This ensures sufficient buildup of fuel vapour at droplet surface interface between the two phases
4. Diffusion and convection of this fuel vapour into the gas ensures the formation of a combustible mixture.

A number of practical assumptions are made for mathematical modelling of the evaporation, they are:

1. Radiative heat transfer is neglected because it is small compared to the convective heat transfer.
2. Averaged flow fields around the droplet are considered and averaged transfer coefficients are considered around the fuel droplet.
3. A well-mixed droplet is considered without gradients in concentration, temperature and critical properties.
4. The surrounding gas is assumed to be insoluble in the liquid droplet.

The mass flux $\dot{m}''$ across the droplet surface of radius r and the evaporation rate $\dot{m}$ be expressed as:

$$\dot{m}\left(r\right) = 4\pi r^2 \dot{m}'' \tag{3.14}$$

This mass flow rate in a quiescent environment depends on the mass diffusion rates and the concentration gradients of the fuel vapour:

$$\dot{m}'' = Y_F \dot{m}'' - \rho \mathcal{D}_f \frac{\mathrm{d}Y_F}{\mathrm{d}r}. \tag{3.15}$$

Combining the above equations, the evaporation rate can be expressed as:

$$\dot{m} = -4\pi r^2 \frac{\rho \mathcal{D}_f}{1 - Y_F} \frac{\mathrm{d}Y_F}{\mathrm{d}r}. \tag{3.16}$$

Integrating the above equation between from the droplet surface to far field conditions ($Y_F = Y_{surf},\ r = r$ and $Y_F = Y_\infty,\ r = \infty$)

$$\dot{m} = -4\pi r \rho \mathcal{D}_F \ln \left[\frac{(1 - Y_{F,\infty})}{(1 - Y_{F,surf})} \right]. \tag{3.17}$$

A more common representation of the above is in terms of the Spalding mass transfer number (B_M) and the Sherwood number (Sh)

$$\begin{aligned} B_M &= \frac{Y_{F,surf} - Y_{F,\infty}}{1 - Y_{F,surf}}. \\ \frac{\mathrm{d}m_p}{\mathrm{d}t} &= \dot{m} = -\pi d_p \mathsf{Sh} \rho_g \mathcal{D}_F \ln\left(1 + B_M\right). \end{aligned} \tag{3.18}$$

The fraction of fuel vapour at the droplet surface is calculated by the vapour pressure (P_{vap}) of the liquid fuel at the average droplet temperature (T_p). Vapour pressure of the liquid fuel inturn is obtained using the Clausius-Clayperyon relation. A known point on the saturation curve ($P0$ and $T0$) needs to be plugged in the relation:

$$Y_{F,s} = \frac{P_{vap}\left(T_p\right)}{P} \frac{MW_f}{MW_{mix}}. \tag{3.19a}$$

$$P_{vap}\left(T_p\right) = P_0 \exp\left[\frac{h_{fg}}{R T_0} \left(1 - \frac{T_0}{T_p} \right) \right]. \tag{3.19b}$$

In order to completely characterize the evaporation process of the fuel, the evolution of the droplet temperature needs to be characterized by balance of the energy flux across the surface of the evaporating liquid. This balance gives:

$$\frac{\mathrm{d}T_p}{\mathrm{d}t} = \frac{1}{m_p C_{p,l}} \left(-\mathbf{\Phi}_g^c + \dot{m}_p L_v\left(T_P\right) \right) \tag{3.20}$$

In the above equation, T_p is the droplet temperature and L_v the latent heat of vaporization of the liquid. Φ_g is the head conducted into the liquid droplet due to the temperature difference between the hot gases and the cold liquid which contributes to the phase change and sensible enthalphy increase. Assuming a constant thermal conductivity the heat conducted into the droplet

from the gas is

$$\mathbf{\Phi}_g^c = \pi d_p \mathsf{Nu} \rho_g \left(T_p - T_\infty\right) \frac{\ln\left(B_T + 1\right)}{B_T}. \tag{3.21}$$

B_T, the thermal Spalding number estimated using B_M as:

$$B_T = \left(1 + B_M\right)^\beta - 1 \quad \text{with} \quad \beta = \frac{\mathsf{Sh}\ \mathsf{Pr}}{\mathsf{Nu}\ \mathsf{Sc}}. \tag{3.22}$$

Nusselt number (Nu) is the ratio of convective and conductive heat transfer coefficients. The Schmidt Number (Sc) and Prandtl Number (Pr) are non dimensional numbers which are the ratios of momentum diffusivity to the mass and thermal diffusivity respectively.

The evaporation model discussed so far does not consider relative flow that exists between the droplets and the gas, which is generally the case. This relative velocity causes increase of evaporation and heating rates of the droplets. Further the internal circulation inside the liquid causes quick mixing and a homogenized droplet temperature.

To account for this, Abramzon and Sirignano [133] proposed a correction to the Nusselt and Sherwood numbers used in the equations described above. Two correction factors F_M and F_T are proposed using the B_M and B_T described above:

$$F_x = \left(1 + B_x\right)^{0.7} \frac{\ln\left(1 + B_x\right)}{B_x} \qquad \text{where } x = M, T. \tag{3.23}$$

Using this the corrected Nusselt and Sherwood number are calculated as:

$$\begin{aligned} \mathsf{Sh}^* &= 2 + \frac{\mathsf{Sh} - 2}{F_M}. \\ \mathsf{Nu}^* &= 2 + \frac{\mathsf{Nu} - 2}{F_T}. \end{aligned} \tag{3.24}$$

In the above expression, Nu and Sh are calculated using the Ranz and Marshall correlations [134] using the Reynolds number. For a stationary droplet in a quiescent environment, one obtains back $\mathsf{Nu},\ \mathsf{Sh}\ =\ 2$.

$$\begin{aligned} \mathsf{Sh} &= 2 + 0.55 Re_p^{1/2} \mathsf{Sc}_F^{1/3}. \\ \mathsf{Nu} &= 2 + 0.55 Re_p^{1/2} \mathsf{Pr}_F^{1/3}. \end{aligned} \tag{3.25}$$

The transport properties of the gas around the droplet used in the above correlations are calculated using the 1/3rd rule.

Part II

Sustainable Alternative Fuel Combustion

Chapter 4

Sustainable Aviation Fuel Combustion

Contents

4.1 Introduction

Strict testing procedures and standards exist for fuels used in aircrafts. This is to ensure smooth and seamless operation across multiple points. Some of the properties for a standard JetA-1 fuel as per the ASTM D1655 specifications are given in Table 4.1.

Property	Value Range
Density at 15°C	775.0-840.0 $^{kg}/_{m^3}$
Flash point	min 38° C
Freezing point	max -47° C
Aromatics content	max 25% by volume
Sulphur content	max 0.30% by mass
Heat of combustion	42.8 $^{MJ}/_{kg}$

Table 4.1: Some typical properties of standard JetA-1 fuel as per the ASTM D1655 standards.

Apart from the heat release which is of primary interest in this work, a newly proposed Sustainable Alaternative Fuel (SAF) needs to satisfy other aspects such a being self lubricating in pumping systems, acting as a coolant and

satisfying long term storage requirements. The JETSCREEN project [1] was aimed at a holistic procedure to develop multiple tools to analyse potential new aviation fuels [135]. In the context of combustion studies the first stage was to extract a composition definition and validate it using canonical cases. This chapter discusses details of the ARC for a standard three-component multicomponent representation of Jet-A1 and a sustainable alcohol to jet alternative termed At-J.

4.2 Complex fuel composition

Due to the distillation process and extraction of components form crude oil over specific temperature range, a multitude of components contribute to the commercial jet fuels. While the exact composition varies according to source, they consist of the following major group of hydrocarbon families.

— **Alkanes**

These are simplest hydrocarbons with a formula of C_nH_{2n+2} with all carbon atoms having saturated bonds. From $n = 5$ until $n = 16$, these are liquid components and are often used as a representative of fuels in experiments. Another aspect of these alkanes is the varying possibilities of chemical structures that exist. When all the carbons are in a straight chain, these are referred to as **n-alkanes** as shown in Figure 4.1

(a) n-octane **(b)** n-dodecane

Figure 4.1: Structure of straight chain alkanes.

(a) iso-octane **(b)** iso-dodecane

Figure 4.2: Structure of branched chain alkanes.

As the size of alkanes increases, the number of possible arrangements begins to rise. For an alkane having $n = 12$, the number of possible isomers is 355. These set of saturated alkanes are referred to as branched

1. https://cordis.europa.eu/project/id/723525

or **iso-alkanes** shown for the same components in Figure 4.2. Though the chemical formulae and physical properties are very similar for both cases, branching increases the reactivity of the iso-alkanes.

— **cyclolkanes**
Cycloalkanes also termed naphthenes are another category of saturated hydrocarbons in which ring a structure exists. The cycloalkanes can be represented with a formula of C_nH_{2n+r-1} where r is the number of saturated rings present. Due to this limitations, a minimum of 3 carbon atoms are needed to form a ring. However in liquid fuels the components of interest are cyclohexanes and their derivatives which have a main ring of 6 carbon atoms as seen in Figure 4.3.

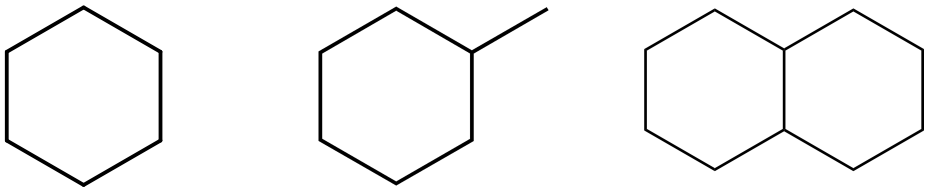

(a) cyclohexane **(b)** methyl-cyclohexane **(c)** decalin

Figure 4.3: Structure cycloalkanes.

Apart from the common cyclohexane and its alkyl-derivatives, two fused cyclohexane rings are also possible (decalin). The properties of cycloalkanes are very close to the alkanes because they have a very similar H/C ratio, however the presence of the ring structure reduces its reactivity compared to n-, iso- alkanes.

— **Aromatics**
These compounds are made up of the benzene ring and its derivatives as shown in Figure 4.4. The benzene rings consists of 6 carbon atoms bonded to a hydrogen atom each with a non-localised set of shared electrons. Benzene, and it derivatives with alkyl groups leads to multiple isomers. As an example with 2 methyl groups, three possibilities otho-, para-, meta- xylene exist. Like cycloalknes, multiple benzene rings can be fused, naphthalene being an example of two fused benzene rings. Aromatics because of the relatively stable nature of the benzene ring structure are less reactive, and have a higher sooting propensity compared to the alkanes and naphtenes.

A complete map of the standard reference JetA-1 composition is shown in Figure 4.5, taken from the internal reports of the JETSCREEN project [136]. The four important groups discussed earlier are present with split of 19.2% n-alaknes, 30.7% iso-alkanes, 32.9% cycloalkanes, 15.5% mono-aromatics and

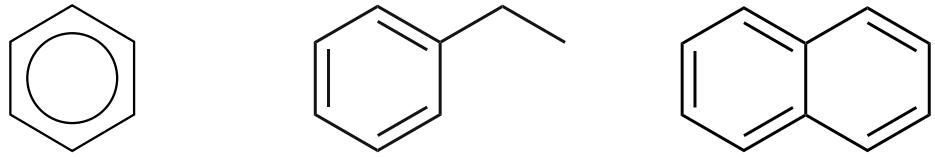

(a) benzene **(b)** ethyl-benzene **(c)** decalin

Figure 4.4: Structure of aromatics.

1.7% di-aromatics. Across all these hydrocarbon families, the carbon number varies from 7 to 18 (di-aromatics has not been shown in Figure 4.5). A complex mixture such as this needs simplification for its use in CFD codes. From the composition Hajiw-Riberaud and Alves-Fortunato [136] suggest a 1,2,3,4-tetramethylcyclohexane as a realistic representation of mean molecular formula for JetA-1. However, such a component is not an ideal representation of either vapourisation or reaction mechanics of JetA-1.

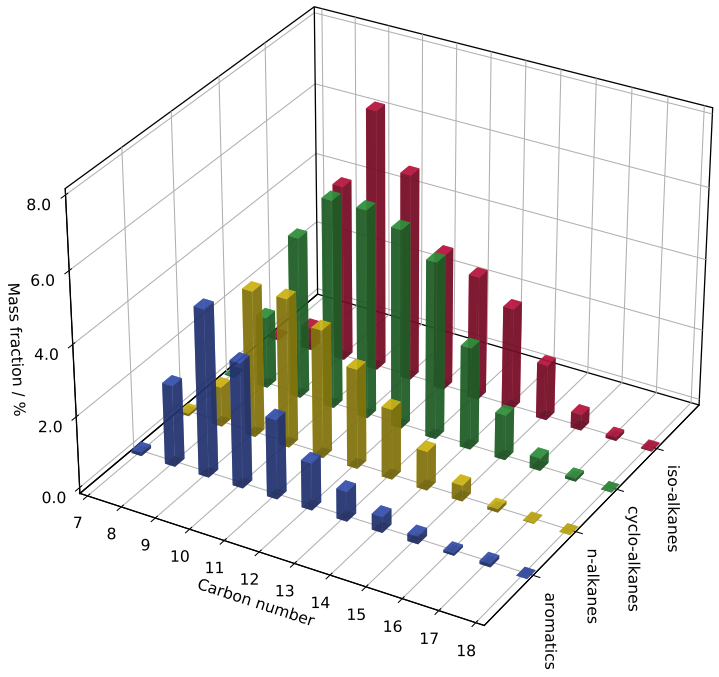

Figure 4.5: Composition of JetA-1 from GCxGC measurements [136].

Single component representations of JetA-1 are mainly done using n-decane or n-dodecane because of their close physical properties [137, 90]. Looking at Figure 4.5 it is evident that an n-alkane representation misses out on the two most dominant hydrocarbon groups namely iso-alkanes and

cyclo-alkanes, but provides the intermediate in terms of reactivity compared to the two. Adding to an n-alkane, components from other two mentioned hydrocarbon groups results in representation with an approximate formula $C_{10}H_{20}$ [138, 102] and has been successfully employed in multiple studies.

These single component representation are used for studies with a singular focus of matching physical properties, ignition timings, flame speeds, heat release, emissions etc, they fail to capture the two phase effects of preferential evaporation. In the following sections, a three component surrogate is introduced for the standard JetA-1 fuel and Alcohol To Jet Synthesized Paraffinic Kerosene (ATJ-SPK) called At-J.

4.2.1 Surrogate representation of complex fuels

The concept of surrogates implies selecting a mixture of up to 10 simple compounds which can be used for modelling with a focus to match a set of real fuel target properties. While this can be done manually and requires expert knowledge, semi analytical tools are available. The CRECK modelling group [2] has developed tools to optimize the fuel presentation based on a list of real fuel properties (Derived Cetane Number(DCN), average molecular weight, threshold sooting index, density, distillation curve and liquid viscosity). This optimisation is run on a "palette" of components shown in Figure 4.6 for which the detailed chemical kinetics have been individually validated.

4.2.2 Three component mixture for JetA-1

A three component mixture consisting of n-dodecane, methyl-cyclohexane and xylene [3] is considered as a representation of JetA-1 Humer et al. [140] [4]. This composition has been utilised in the works of Narayanaswamy and Pepiot [141], Narayanaswamy et al. [142] for the development and optimisation of a component library framework. In terms of molar composition, 60% n-dodecane is a representative of the alkanes, 20% methyl-cyclohexane is included to account for cycloalkanes representation. Aromatics which are important to reproduce the soot formation propensity is represented by a lumped xylene species for the remaining 20%. Details comparing the properties of reference and surrogate JetA-1 fuel is given in Table 4.2 and a good match between the properties is obtained.

2. http://creckmodeling.chem.polimi.it/
3. o-, p-, m- xylene is lumped into a single species
4. Surrogate C in the original work

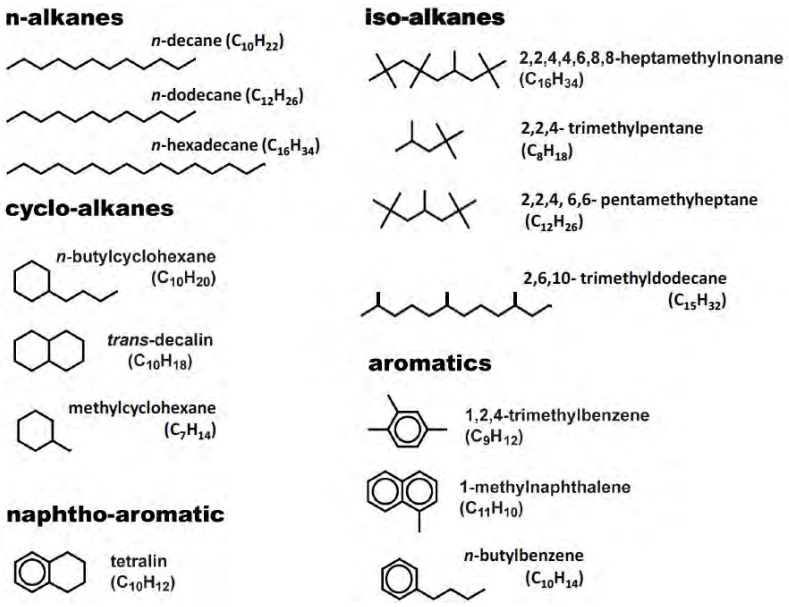

Figure 4.6: Palette of candidates selected for surrogate formulation, taken from [139].

Fuel	Density	H/C ratio	ΔH_c
Reference JetA-1	790 $^{kg}/_{m^3}$	1.95	46.929 $^{MJ}/_{kg}$
2S KERO[102]	781 $^{kg}/_{m^3}$	2.0	46.883 $^{MJ}/_{kg}$
3 component representation	775 $^{kg}/_{m^3}$	2.0	45 $^{MJ}/_{kg}$

Table 4.2: Comparison between the standard reference JetA-1 and chosen multicomponent representation.

4.2.3 Three component mixture for At-J

The AtJ-SPK is the pathway where isobutanol, ethanol and methanol can be converted into usable fuel. Using the isobutanol the blending limits are 30% as of 2016 while for the ethanol pathway, a blending limit of 50% has been set as of 2018. Since the production process is controlled, the composition is composed of only iso-alkanes as reported by Hajiw-Riberaud and Alves-Fortunato [136]. In terms of molar composition, this corresponds to 8% iso-octane, 84% iso-dodecane and 8% iso-hexadecane (iso-centane) and experimentally the combustion properties have been validated against standard jet fuel [143, 136]. Details comparing the properties of reference and At-J fuel is given in Table 4.3 and a good match between the properties is obtained.

Fuel	Density	H/C ratio	ΔH_c
Reference JetA-1	790 $^{kg}/_{m^3}$	1.95	45 $^{MJ}/_{kg}$
3 component representation	775 $^{kg}/_{m^3}$	2	45 $^{MJ}/_{kg}$

Table 4.3: Comparison between the standard reference AtJ-SPK and chosen multicomponent representation.

4.3 Chemistry for SAF combustion

The CRECK_1909_TOT_HT mechanism has been used for as reference the reduction of the two multicomponent fuels considered. Since the primary interest is the applications in a realistic burner conditions, the following cases were used for the chemistry reduction:

— Laminar one-dimensional flames with an inlet temperature of 400 K, pressure 1 bar and equivalence ratios of $\phi_{gas} = 0.6,\ 1.0,\ 1.4$ to cover both lean and rich mixtures.

— Autoignition studies using zero-dimensional reactors at 1000 K, 1500 K with a mixture of $\phi_{gas} = 1$ and 1 bar pressure.

The threshold for the error has been set at 15% for the autoignition time delay, 5% for the laminar flame speed and 1% for the final gas temperature. The targets for reduction were the mass fractions of the three fuel components, as well as CO, CO_2 and heat release rate. The reductions have been done using the ARCANE code [115] and the ARCs have been utilised in the work of [98] to study one-dimensional spray flames.

	n-dodecane	methyl-cyclohexane	xylene
X	0.6	0.2	0.2
Y	0.578	0.198	0.224
	Transported Species	QSS species	Reactions
ARC	36	16	543

Table 4.4: Details of the ARC for multicomponent JetA-1.

The final statistics of the reduced mechanism are shown in Table 4.4 and Table 4.5. The JetA-1 reduction is constrained by the presence of components from different hydrocarbon groups and hence results in a heavy mechanism. On the other hand for At-J, because of the component distribution from a single family, the ARC scheme is significantly smaller.

The comparisons shown for the autoignition delay times and laminar flame speed in Figure 4.7 and Figure 4.8 indicate a good match with the detailed

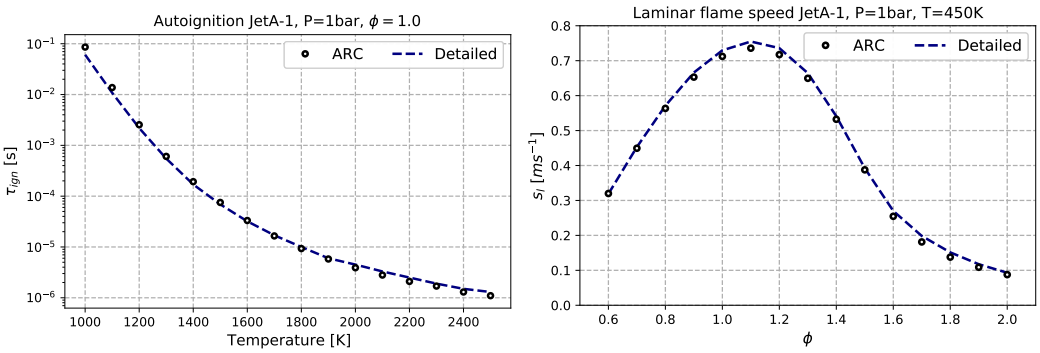

(a) Autoignition delay **(b)** Laminar flame speed

Figure 4.7: Comparison between the detailed and ARC for JetA-1 fuel.

	iso-octane	iso-dodecane	iso-hexadecane
X	0.08	0.84	0.08
Y	0.054	0.840	0.106
	Transported Species	QSS species	Reactions
ARC	31	24	394

Table 4.5: Details of the ARC for multicomponent At-J.

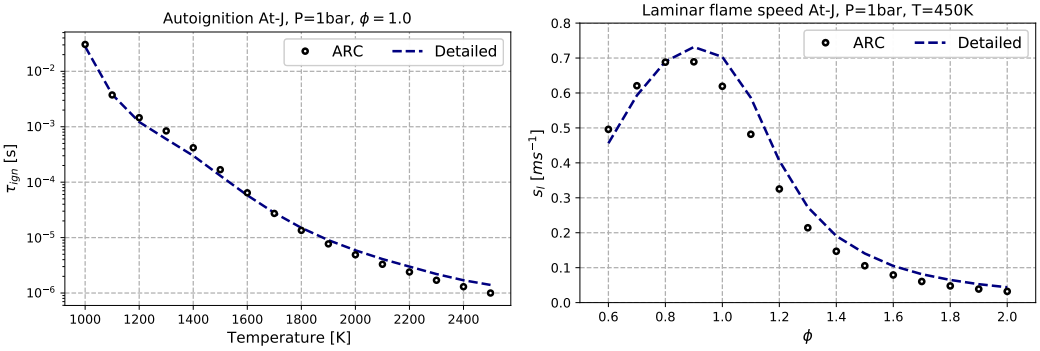

(a) Autoignition delay **(b)** Laminar flame speed

Figure 4.8: Comparison between the detailed and ARC for At-J.

mechanism. These reductions are done with a specific starting composition, however the presence of liquid fuel and preferential evaporation (will be shown later in Chapter 6) can cause multiple compositions across the domain. The reduced chemistry should be capable of handling this aspect and additional discussion is presented in Chapter 8.

Chapter 5

Multicomponent evaporation models

Contents

There is long standing and consistent interest in the understanding of multicomponent fuel evaporation. This chapter deals with a brief review of the multicomponent evaporation models presented in literature. The discrete multicomponent model implemented in the code AVBP will be validated against a set of reference cases.

5.1 Literature review

The modelling approach in literature can be broadly divided into two categories, first in which individual components are considered called the discrete multicomponent model and second in which a distribution is fit to match the composition termed as the continuous multicomponent model. These representations for a sample fuel are as shown in Figure 5.1.

5.1.1 Discrete Multicomponent evaporation model

The basic models discussed earlier (Subsection 3.4.2) hold in case of liquid with a complex composition. In a discrete multicomponent approach, each individual component of the liquid phase is tracked over the droplet lifetime. This is a straightforward popular implementation and most of the early studies on multicomponent fuels were limited to this approach.

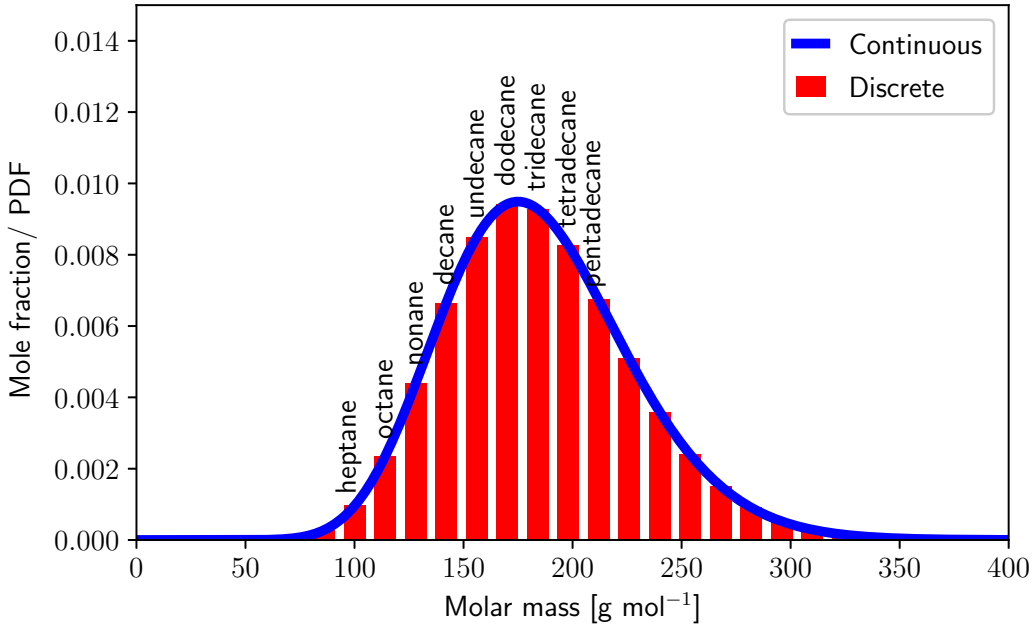

Figure 5.1: Different modelling strategies for multicomponent evaporation.

An additional complexity introduced by the liquid composition is the mass transport phenomenon occurring inside the droplet. The mass fractions of the individual liquid components $Y_{l,i}(r,t)$ inside the droplet is given by:

$$\frac{\partial Y_{l,i}}{\partial t} = D_{l,i}\left(\frac{\partial^2 Y_{l,i}}{\partial r^2} + \frac{2}{r}\frac{\partial Y_{l,i}}{\partial r}\right). \tag{5.1}$$

In Eq. (5.1) a binary diffusion coefficient $D_{l,i}$ of a single component inside the liquid droplet is often replaced by D_l assuming equal mass diffusivity for all components inside the liquid. It is solved subject to the following boundary conditions:

— An initial uniform concentration ($Y_{l,i0}$) inside the liquid phase is assumed leading to

$$Y_{l,i}(r,0) = Y_{l,i0}. \tag{5.2}$$

— At the centre of the droplet,

$$\left.\frac{\partial Y_{l,i}}{\partial r}\right|_{r=0} = 0. \tag{5.3}$$

— The volatile component evaporate from the liquid surface and diffuse away into the surrounding gas producing the concentration gradients and driving intra droplet diffusion. The conditions at interface (droplet

surface) needed to solve Eq. (5.1) is given by

$$\left.\frac{\partial Y_{l,i}}{\partial r}\right|_{surf} = \frac{\rho D}{\rho_l D_l}\frac{\ln\left(1+B_M\right)}{R_d}\left(Y_{l,i\ surf} - \varepsilon^i\right). \tag{5.4}$$

The new term introduced in Eq. (5.4) ε^i is the mass fraction of the individual components in the vapourisation flux. Three possible cases arise:

- The diffusion limit models - In these cases Eq. (5.1) is solved by additional discretisation inside the liquid droplets
- Infinite mass diffusivity/well mixed models - The internal composition is assumed to be spatially homogeneous but temporally varying. Any change gradients created by the evaporation form the surface is quickly compensated.
- Frozen limit models - the evaporation proceeds rapidly and the vapour flux composition is always same as the initial liquid compositions.

Finite difference solution to the unsteady diffusions inside the droplet were reported by Landis and Mills [144]. Binary mixtures of pentane, hexane, heptane with octane were respectively considered. At low vapourisation rates, the infinite diffusion model predicted agreeable trends compared to the detailed diffusion controlled model. At higher temperature resulting in large vapourisation rates, the vapour flux was same as the initial liquid composition.

Law [145] extended the Ideal Mixture model and proposed a Shell model. Based on the volatilities, components of the liquid were distributed in shells with the most volatile being in the outer most such shell. Simpler formulation of single component vapourisation was then applied to each of these regions obtaining good match with the multicomponent formulation assuming an Ideal Mixture (infinite conductivity/ diffusivity model).

Further work by Law and co-workers involved solutions to the heat and mass diffusion processes inside the fuel droplet [146] to understand the mechanism. An initial transient regime involves the vapourisation of volatile components from the outer surface. This sets up a concentration gradient and leads to a mass diffusion controlled quasi steady intermediate regime, where the diffusion form the inner core is balanced by the surface regression. Towards the very end when the droplet size is comparable to the diffusion length scale, a volatility controlled regime, characteristic of the rapid mixing models was shown to exist [147]. A d^2 law for multicomponent droplets was proposed based on this intermediate steady state to obtain the important parameters of evaporation as a function of droplet temperatures [148].

In practical spray applications, where droplets are injected with high velocities the conditions inside are not completely governed by liquid diffusion alone. The relative velocities cause internal circulations enhancing mass trans-

port, and the in reality, conditions lie between the limiting cases of diffusion controlled and well mixed regimes. To address these points Law et al. [149], Lara-Urbaneja and Sirignano [150], Tong and Sirignano [151] extended the vortex model to account for internal droplet circulation. Their analysis included two boundary layers across the interface of gas and liquid. Even at very large Reynolds numbers it was shown that the mass fractions are uniform across the streamlines but non negligible gradients still exist in the normal directions.

Though internal recirculation reduces timescales, the transient behaviour prevailed and the often assumed rapid mixing limit was not reachable. For spray simulations in gas turbine conditions Aggarwal et al. [152], Aggarwal [153] suggested the use of a diffusion limit model due to its easier implementation and close results to the vortex models especially in case of multicomponent fuels. In further works the same authors [154] reported similar evaporation timescales for both the well mixed and diffusion limit models. Gauthier et al. [155] showed that the rapid mixing model was able to capture the role of preferential vaporisation of volatile components in the study of cold start characteristics of kerosense.

This discrepancy between the diffusion limit and rapid mixing was addressed very early in the review on evaporation of liquid fuels by Law [146]. On examination of the then available experimental results [156, 157, 158] (contrary to observations of computational studies highlighted in the earlier paragraphs), it was found that even moderate internal droplet circulation generated due to external conditions results in a batch distillation behaviour with the vapour flux dominated by the volatile components present in the fuel.

Later experiments also showed similar conclusions regarding the mixing inside the droplet. Rainbow refractometry to study droplet temperatures and concentration did not show the concentration gradients predicted by the diffusion limit model. For the binary and ternary mixtures of hydrocarbons, a very good agreement with the observed data was reached with the rapid mixing model [159]. In a study of acoustically levitated droplets by Brenn et al. [160], the comparison with experimental data for a 5 component (methanol, ethanol, 1-butanol, n-heptane, n-decane) mixture was well captured by the rapid mixing assumption. It can be argued that the strong effects of internal circulation due to the experimental setup are reproduced in realistic conditions with high injection velocities.

In newer studies, Rauch et al. [161] conducted experiments using monodisperse freely falling droplets and concluded the that the rapid mixing model reproduced the trends of vapourisation rate accurately and showed little difference form the diffusion limit model. Chen et al. [162, 163] made a comparison of the rapid mixing, diffusion limit and frozen evaporation models

for kerosene alcohol blends, again highlighting that the rapid mixing inside a droplet is valid upto pressures of 3 bar. In this thesis the Discrete Multicomponent (DMC) model with an infinite thermal, mass diffusivity inside the liquid droplet is implemented.

5.1.2 Continuous Multicomponent approach

The number of fuel components present tend to be hundreds, distributed across multiple hydrocarbon families and carbon numbers. Tracking each of them individually as done in the discrete multicomponent approach can tedious and computationally inefficient for large spray cases. Detailed analysis of the fuel composition using experimental techniques reveal that the individual components of each chemical group can be represented by a distribution function (Figure 5.1).

A continuous distribution of composition, generally in terms of the molar mass of the components is assumed. Important moments (mean, variance) are tracked by developing equations for both the liquid and gaseous phases. The elegant approach termed the continuous multicomponent model (CMC) is especially useful as multiple species can be tracked using very few variables improving the computational cost. Early efforts were focussed at developing conservation laws, redefining transportation parameters and understanding phase equilibria [164, 165, 166, 167, 168, 169] of multicomponent mixtures encountered in the petroleum and polymer industries.

Tamim and Hallett [170] were the first to extend this concept to evaporating droplets. Using a Gamma distribution function over the molar mass (I), the composition is given as:

$$f(I) = \frac{(I-\gamma)^{\alpha-1}}{\beta^{\alpha}\Gamma(\alpha)} \exp\left[-\left(\frac{I-\gamma}{\beta}\right)\right], \tag{5.5}$$

where $I = \gamma$ is the origin, α and β control the distribution shape and $\Gamma(\alpha)$ is the Gamma function. Evolution of the mean (θ) and the variance (σ) are tracked over the droplet lifetime, given in terms of the distribution parameters as:

$$\theta = \alpha\beta + \gamma \quad \text{and} \quad \sigma^2 = \alpha\beta^2. \tag{5.6}$$

Spherically symmetric fully transient equations were solved by considering a mixture of n-alkanes to represent gasoline and diesel, similar to the one shown in Figure 5.1. The preferential evaporation behaviour was recovered by studying the evolution of θ whose values increase as the evaporation progresses, indicating the shift towards heavier less volatile components.

The above work was extended for use in practical spray applications by incorporating the work of Tamim and Hallett [170] in a quasi steady state model evaporation model. Spray simulations showed the presence of high molar mass components in the outer edges which play a role in spray ignition [171]. Considering internal droplet diffusion [148] in the continuous multicomponent case again led to again led to similar evaporation timescales and trends [172].

Most of the CMC models use a single Γ-PDF with the assumption that shape of the distribution is retained over the phase transformation process. Harstad et al. [173] showed the evolution starting from a single Γ-PDF proceeds to double Γ-PDF (combination of 2 Γ-PDF's, having two peaks). Comparison with a DMC model of 32 paraffin species showed good agreement in the overall evaporation profiles and the ability to capture condensation at the droplet surface, eventually leading to two peaks in the distribution. This occurs when the spray is introduced in an environment with pre-existing vapour in small quantities, as is the case in many applications. This double Γ-PDF was used to model evaporation of Jet fuels over a wide range of pressures and study nucleation in a complex multicomponent vapour [174, 175].

The CMC model has found applications in DNS of droplet laden simulations performed by Le Clercq and Bellan [176, 177, 178]. Evaporation of such liquid mixtures was shown to result in a high level of mixture heterogeneity. Initially, low molar mass components evaporated in the particle laden steam, the species with intermediate volatilities in the mixing layers where the droplets were entrained and the heavier components in regions with high droplet density. Such segregation was predicted to have important role in practical combustion systems in terms of reaction regimes and zones. Selle and Bellan [179, 180, 181, 182] further produced detailed DNS datasets with a similar approach to provide insights into LES modelling of multicomponent particle laden flows.

Though the representation of multiple components using Γ-PDF's was computationally efficient, each distribution was restricted to a single family of compounds (mainly n-heptanes). Yang et al. [183, 184] introduced the Discrete Continuous Multicomponent model which uses multiple hydrocarbon families each represented by a distribution function. Gasoline was composed of n-alkanes, iso-alkanes, naphthalenes, aromatics, olefins, each with its own set of properties. In a similar approach after detailed analysis of the GCxMS data of Jet-A1 fuel, Le Clercq et al. [185] introduced a formulation with 3 hydrocarbons groups n-alaknes, cyclo-alkanes and mono-aromatics. These composition representations are given in Figure 5.2 and by considering multiple distributions a complete representation is possible in the CMC approach.

Recently, Hinrichs et al. [186] addressed three important issues in the cur-

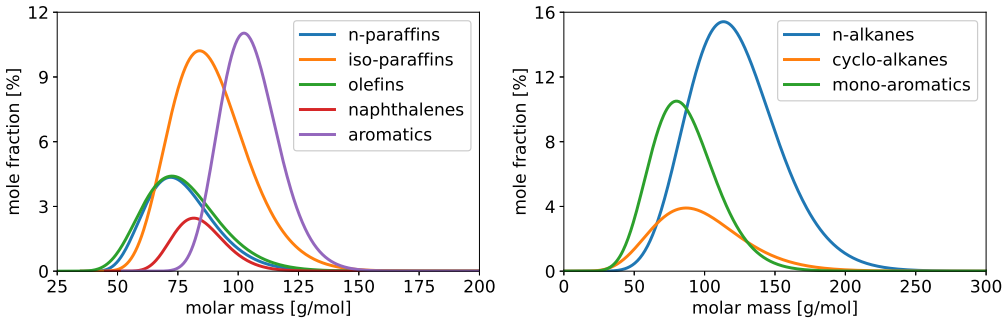

(a) Compositon of Gasoline [183] **(b)** Composition of JetA-1 [185]

Figure 5.2: Continuous multicomponent fuel representation.

rent approach using realistic diesel fuel data. First, an accurate composition analysis was provided from which four groups namely n-alkanes, mono-naphthenics, mono-aromatics and naphthenic mono aromatics were identified as the dominant groups. Detailed estimates of fuel properties for both liquid and gaseous phases were developed from existing correlations and fitted over a wide range of molar masses from 50 $^{g}/_{mol}$ to 450 $^{g}/_{mol}$. Finally, these were implemented in a quasi steady evaporation model and compared with experimental data of acoustically levitated droplets over a wide range of conditions. The need to use accurate estimations of composition and properties when using the continuous multicomponent approach was highlighted.

The approach of using multiple distribution for accurate fuel representation has recently found significant applications in modelling evaporation characteristics of biofuel blends. A CMC representation of the major petroleum fuel (gasoline, diesel, JetA, Kerosene) along with a discrete component representation of the biofuel is considered. Additional constrains regarding activity coefficients, real gas properties are needed along with the hybrid evaporation model to capture the phase change. With newer fuel considerations this approach is gaining increasing interest [187, 188, 189, 190].

The multiple Γ-PDF approach with accurate property calculations is advantageous for tracking muticomponent spray evolution. However its use in reactive simulations is not straightforward. Recent work by Eckel et al. [191] uses a continuous approach for the multicomponent liquid phase. These distributions collapse to a single representative component for computing the gas phase reactions as given in Table 5.1. This combined approach was applied to a laboratory scale burner and reproduced the experimental results accurately.

Liquid Phase (CMC representation)	Reactive Gas Phase (Representative component)
n-alkanes	n-dodecane
iso-alkanes	iso-octane
cyclo-alkanes	cyclo-hexane
mono-aromatics	toluene

Table 5.1: Coupling between CMC distributions and discrete multicomponent gas phase reaction mechanism [191].

5.2 Model implementation in AVBP

The DMC model is built on top of the existing Abramzon Sirignano (AS) evaporation model [192]. The equations for change of droplet mass and temperature are recalled here:

$$\frac{\mathrm{d}m_p}{\mathrm{d}t} = \dot{m} = -\pi d_p \frac{\mathsf{Sh}^*}{\mathsf{Sc}} \mu \ln\left(1 + B_M\right). \tag{5.7}$$

$$\frac{\mathrm{d}T_p}{\mathrm{d}t} = \frac{1}{m_p C_{p,l}} \left(\pi d_p \mu C_{p,ref} \frac{\mathsf{Nu}^*}{\mathsf{Pr}} \left(T_\infty - T_p\right) \frac{\ln\left(B_T + 1\right)}{B_T} + \dot{m}_p L_v\left(T_P\right) \right). \tag{5.8}$$

The Spalding heat and mass transfer numbers used in Eq. (5.7) and Eq. (5.8) respectively given by:

$$B_M = \frac{Y_{F,surf} - Y_{F,\infty}}{1 - Y_{F,surf}}. \tag{5.9}$$

$$B_T = (1 + B_M)^{\phi} - 1 \quad \text{with} \quad \phi = \frac{C_{p,F}}{C_{p,ref}} \frac{Sh^*}{Nu^*} \frac{Pr}{Sc}. \tag{5.10}$$

To extend these equations to the multicomponent mixture, the fractional evaporation rate ε of each component i is calculated. A global B_M is obtained by extending Eq. (5.9), using the individual component mass fractions (Y^i) at the surface ($surf$) and far field (∞) locations. This global B_M is then used to find the mass fraction of individual components ε_i in the evaporation flux $\dot{m}_p$. It is possible to encounter a scenario where a particular component has completely evaporated, hence only the components still existing in the liquid phase are considered in Eq. (5.11).

$$B_M = \frac{\sum_{i=1}^{k} Y^i_{F,surf} - \sum_{i=1}^{k} Y^i_{F,\infty}}{1 - \sum_{i=1}^{k} Y^i_{F,surf}} = \frac{Y^i_{F,surf} - Y^i_{F,\infty}}{\varepsilon^i - Y^i_{F,surf}}. \tag{5.11}$$

The Clausius-Clayperyon relation Eq. (3.19) in conjunction with Eq. (5.12) is used to obtain the composition at the droplet surface (X^i_{surf}) using the liquid mole fractions (X^i_{liq}) and the vapour pressure (P^i_{vap}) of the different components. Calculating the surface mass fractions Y^i_{surf} to be used in Eq. (5.11) is then straightforward.

$$X^i_{surf} P_{gas} = X^i_{liq} P^i_{vap}. \tag{5.12}$$

The composition of the vapour flux then becomes

$$\dot{m}^i_p = \varepsilon^i \dot{m}_p \quad \text{with} \sum_{i=1}^{k} \varepsilon^i = 1. \tag{5.13}$$

Most of the transport properties used in the calculations depend reference state surrounding the droplet. The reference state has multiple fuel components which vary in composition as the droplet evaporates. Initially, vapour surrounding the droplets has a large quantity of highly volatile components but during later stages of evaporation only the heavier ones are present. This needs calculations of the physical and chemical properties on the fly. A simple mole/mass fraction based averaging is utilised as shown in Eq. (5.14) for liquid density ρ_L and specific heat $C_{p,L}$:

$$\bar{\rho}_L = \sum_{i=1}^{k} X^i \rho^i_L. \qquad \bar{C}_{p,L} = \sum_{i=1}^{k} Y^i C^i_{p,L}. \tag{5.14}$$

The evaporation rates are very sensitive to the non dimensional numbers which in-turn depend on the three fundamental parameters viscosity μ, thermal conductivity k and mass diffusivity D of the reference state. Correlations from literature have been used [193, 194] to update the reference state properties. These are especially useful because to handle the reacting cases where droplets cross zones with high temperature gradients. Every time a new species and blend is to be simulated, some physical properties like latent heat or vaporisation, saturation pressure are required. These are claculated using the methods given in Reid et al. [195] and are adapted into the solver.

5.3 Validation cases

The discrete multicomponent model implemented in AVBP has been validated against experimental and numerical data available in literature on single droplet evaporation. The experimental techniques used are mainly based on the using a large fibre to suspend the droplets in a quiescent environment,

freely falling or acoustically levitated droplets. The experimental techniques come with unavoidable uncertainties like heat loss through the fibre for suspended single droplets [196, 197], inability capture large droplet diameters, uncertainties in initial sizes for falling cases [198, 199] and acoustic streaming effects for levitated conditions [200, 201]. These can result in deviations from models discussed earlier for practical spray applications.

Here the chosen cases are of two-component [202, 203], three-component [159] and seven-component [204] mixtures. Cases for JetA-1 and alternative jet fuel are discussed in a future chapter.

Bi-component mixtures

Mixtures of n-heptane and n-decane were suspended using a quartz fibre of 0.2 mm at ambient conditions of 293 K in the experiments of Birouk [202]. Two mixtures were considered, Mixture 1 having 70% n-heptane and 30% n-decane by volume; and Mixture 2 having 30% n-heptane and 70% n-decane by volume. The comparison with experimental measurements are shown in Figure 5.3 and reveal a distillation curve which is captured well numerically. The latter half of the vapourisation is similar to that of a single component. In the beginning, a steep decrease in temperature is associated with rapid evaporation (Part 1, Figure 5.3a). This transient is associated with difference in the ambient conditions and the liquid droplet. The heat transfer through the fibre can enhance evaporation, explaining the steeper drop of the experimentally observed normalised diameter (ND). In the latter part (Part 2, Figure 5.3a) where the temperatures and composition are stabilised, the evaporation rates are accurately captured as evident by the matching slopes of the curves. Ebrahimian Shiadeh [203] recommended a slightly altered composition (65% n-heptane and 35% n-decane by volume) for this experimental dataset - the change of composition attributed the initial evaporation of n-heptane owing to its volatility - which reproduced the experimental and computational results on this configuration accurately. Similarly for Mixture 2, a similar trend is observed albeit with slower evaporation rate due to presence larger quantities of n-decane in the liquid Figure 5.3b.

Tri-component mixtures

Wilms [159] conducted extensive experimental studies on evaporation of freely falling and levitated multicomponent droplets. Comparisons of the DMC model with the experimental results for the ternary mixtures are presented here. Experiments were conducted at 300K and due the uncertainties in initial droplet diameter, $d_{p_0} = 100\,\mu$m was considered for the simulations.

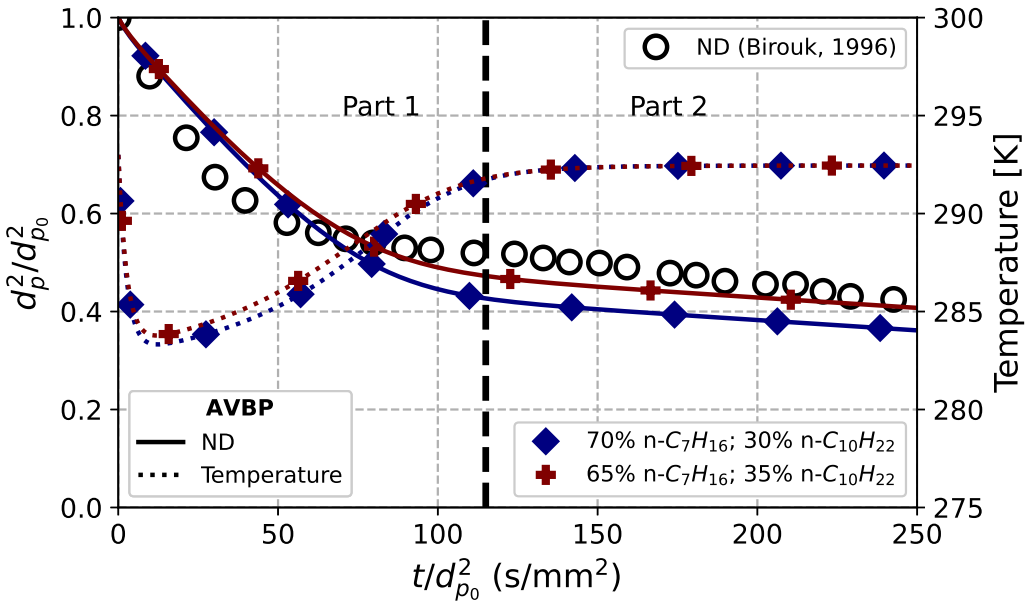

(a) Mixture 1

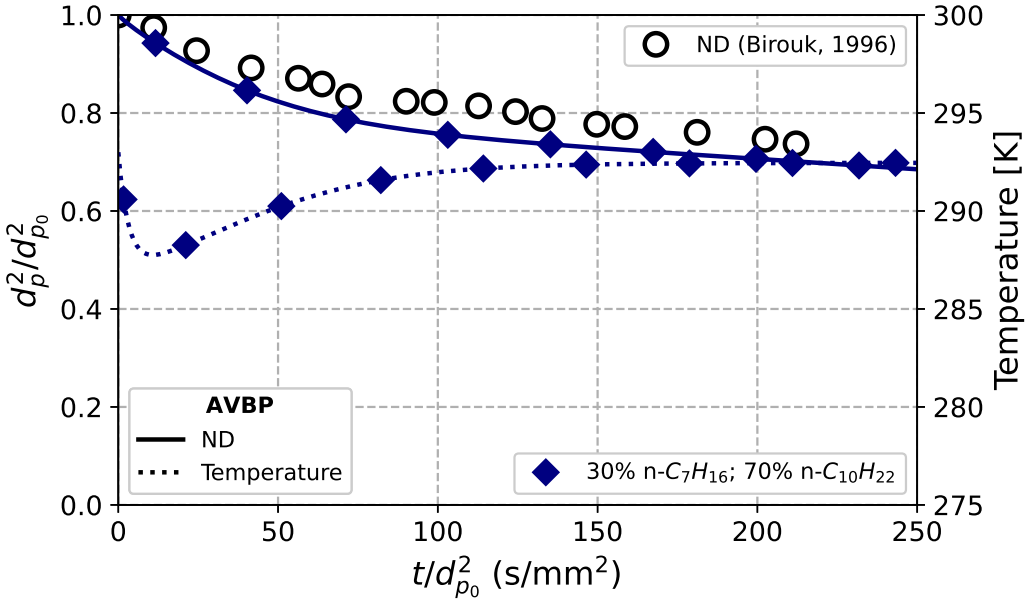

(b) Mixture 2

Figure 5.3: Bi component droplet evaporation [202].

As in the previous case, two mixtures have been chosen, in particular the two cases where the experimental data was calibrated and collated for both measurement techniques. Mixture 1 consists of n-octane, n-decane, n-dodecane and Mixture 2 is composed of n-octane, n-dodecane, n-hexadecane with equal

volumetric contribution of 1/3 from each component.

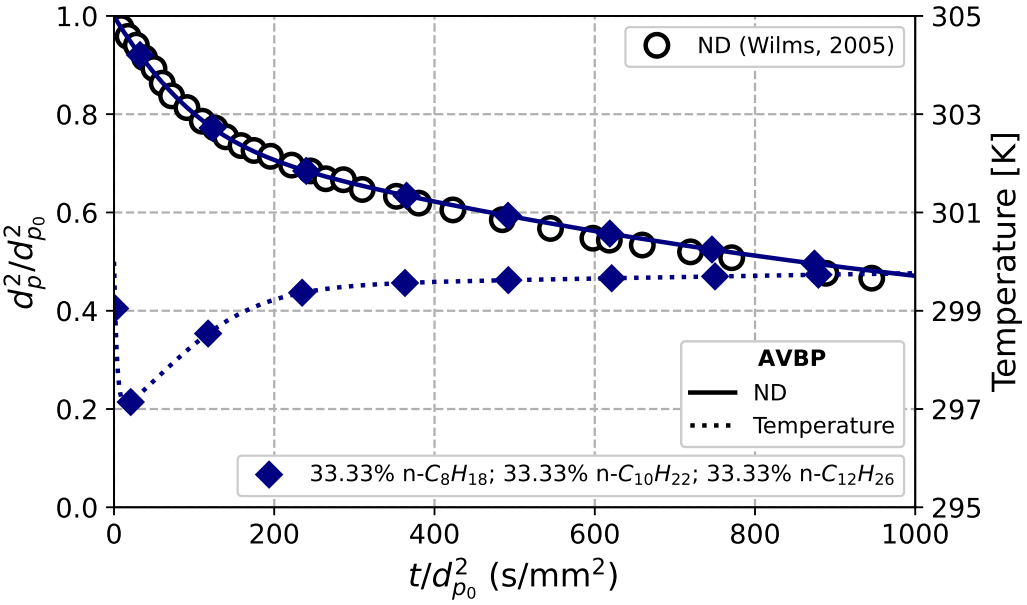

(a) Mixture 1

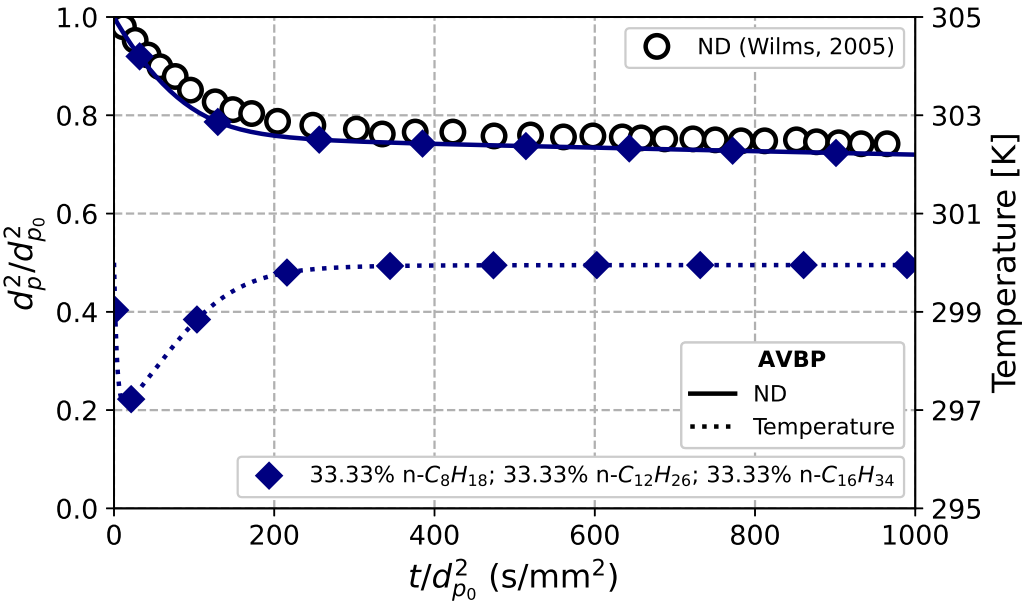

(b) Mixture 2

Figure 5.4: Tri component droplet evaporation [159].

The comparisons shown in Figure 5.4 with the evaporation model shows an excellent match with the experimental data for both cases. Mixture 1 (Figure 5.4a) has a larger evaporation rate where the surface area reduces to

50% of the starting values while for the heavier Mixture 2 (Figure 5.4b) it reaches 75% of its initial surface area over recorded time. The mixtures considered contain components over a wide range of volatiles whose interactions and effects are well reproduced by the implemented DMC model. Temperature evolution is similar to the earlier cases where an initial drop in liquid temperature is associated with larger evaporation of the volatile components post which a steady state condition is reached. In both the experimental techniques used for recoding the evaporation data, internal recirculation is induced due the relative velocity between the liquid and gas. The well mixed infinite mass diffusion assumed in the evaporation model captures the droplet size evolution accurately supporting the earlier observation where even moderate internal circulation resulted in distillation behaviours [146]. Such conditions are common in realistic applications where liquid injection, atomisation and droplet formation induce a degree of internal recirculation.

Complex multicomponent mixture

The internal composition of the multicomponent droplet are difficult to track using experimental techniques. A seven component gasoline droplet evaporating under normal conditions is considered to test the ability to capture the temporal evolution of the internal droplet composition. The gasoline mixture assumed to made of straight and branched chain hydrocarbons over a wide volatility range, having a mean molar mass of 108 $^{g}/_{mol}$ is given in Table 5.2. A 100 μm droplet at 313 K in a quiescent gas of 500 K is simulated and compared with results reported by Ra and Reitz [204].

Component	Mole Fraction (X)	Mass fraction (Y)
iC_5H_{12}	0.25	0.17
iC_6H_{14}	0.09	0.07
iC_7H_{16}	0.11	0.10
iC_8H_{18}	0.22	0.23
C_9H_{20}	0.16	0.19
$C_{10}H_{22}$	0.10	0.13
$C_{12}H_{26}$	0.07	0.11

Table 5.2: 7 component composition of diesel fuel [204].

The evolution of Normalised Diameter (ND) and droplet temperature are compared in Figure 5.5a show the ability to capture the overall droplet lifetime and trends of temperature accurately. The present model with the film assumption reduces the heat transfer into the droplet, while authors of the referenced work used a standard Spalding evaporation model with internal

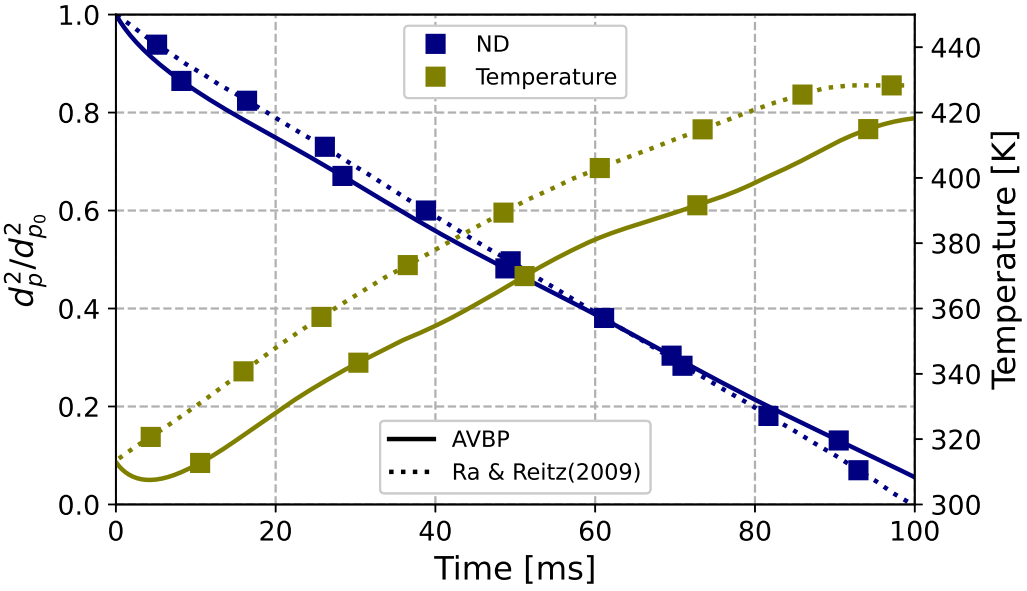

(a) Evolution of normalised diameter and droplet temperature

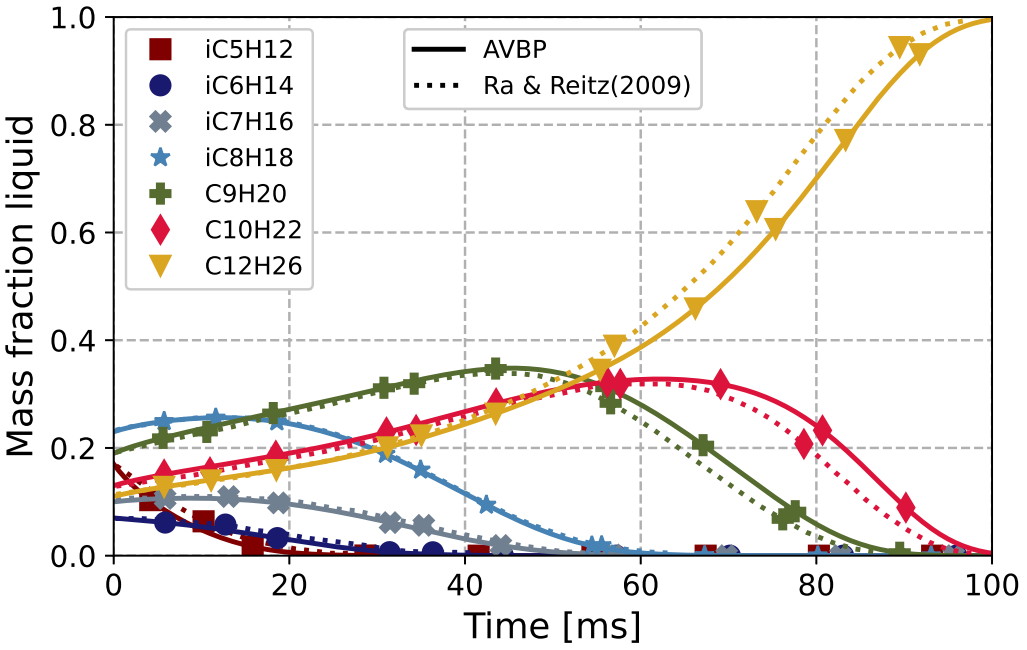

(b) Internal droplet composition

Figure 5.5: Multicomponent gasoline evaporation [204].

droplet heat diffusion. This difference in the modelling can be attributed to the deviation in liquid temperatures and hence the slight difference in evolution of droplet sizes.

Since each of the seven components have varying vapour pressures and contribute differently to the vaporisation flux, the internal liquid composition is continuously changing. Due the infinite mass diffusivity limit used here, we obtain the internal droplet composition to be spatially uniform but temporally varying. An excellent match with reported data is obtained as shown in Figure 5.5b. The volatile iC_5H_{12}, iC_6H_{14} evaporate immediately before 25% of the droplet lifetime followed by the moderately heavy components. Towards the end of the evaporation process, the liquid phase is composed only of the heavier components. An inversion of Figure 5.5b gives the composition of the vapour flux form the droplet surface (not shown). Accurate capture of such continuously changing composition is essential to understand the effect of realistic fuel vapourisation on spray flame characterstics.

5.4 Conclusions

A 0D multicomponent evaporation model has been implemented successfully in AVBP by extending the existing Abramzon-Siringnano model. The discrete multicomponent approach was chosen which takes into account individual components present in the liquid and provides an easy integration with combustion chemistry. The implemented multicomponent model was validated against a range of bi-, tri- and multicomponent mixtures and the predictions match th experimental recording well. This indicates that the preferential evaporation rates are reproduced using the discrete multicomponent approach and an infinite thermal conductivity, diffusivity assumptions are valid for practical cases.

Chapter 6

Numerical simulation on multicomponent spray flame propagation

This is a self contained chapter and an exact reproduction of: Shastry, V., Cazeres, Q., Rochette, B., Riber, E., Cuenot, B. (2021). Numerical study of multicomponent spray flame propagation. Proceedings of the Combustion Institute, 38(2), 3201-3211 https://doi.org/10.1016/j.proci.2020.07.090

Abbreviations used to represent the fuel components slightly differ from the ones used in Subsection 4.2.2. They are properly introduced and limited to this chapter alone.

Contents

6.1 Abstract

A computational study of one dimensional multicomponent laminar Jet-A/air spray flames is presented. The objective is to understand the effect of various spray parameters (diameter, droplet velocity, liquid loading) on the spray flame structure and propagation. Simulation of the Eulerian gas phase

is coupled with a Lagrangian tracking of the dispersed liquid phase. Jet-A surrogate of n-dodecane, methyl-cyclohexane and xylene is considered. A discrete multicomponent model for spray vapourisation is used along with an analytically reduced chemistry for computing the gas phase reactions. Both overall lean and rich cases are examined and compared with existing literature for single component spray flames. The preferential evaporation effect, unique to multicomponent fuels causes a variation of fuel vapour composition on both sides of the flamefront and this has a direct impact on the spray flame structure and propagation speed. In the rich cases, multiple flame structures exist due to the staged release of vapours across the reactive zone. Spray flame speed correlations proposed for single component fuels are extended to the multicomponent case, for both zero and high relative velocity between the liquid and the gas. The correlations are able to accurately predict the effective equivalence ratio at which the flame burns and hence the laminar spray flame speeds of multicomponent fuels for all cases studied in this work.

6.2 Introduction

Spray formation and combustion have been extensively studied due to the wide ranging applications in propulsion and power generation[205]. The various mechanisms involved, occurring at different length and time scales lead to a very complex combustion process with multiple flame structures and combustion regimes [206]. Large Eddy Simulations (LES) coupled with detailed chemistry descriptions have been recently performed to get an insight into these highly coupled systems. However a single component representation of the liquid fuel has been mostly utilised [207, 208, 209].

Real fuels used in these combustion systems contain a large number of components belonging to a range of hydrocarbon families. Differences in their volatilities cause a spatio-temporal variation of the reactive gas phase mixture as the spray evolves. Additionally, preferential evaporation significantly affects the mixture reactivity specially when vaporisation and autoignition timescales are comparable and in the presence of turbulent structures [210, 211]. To address these, a detailed study of multicomponent spray flame structure and propagation is thus necessary in understanding turbulent combustion of fuel blends and developing corresponding models in addition to the existing LES studies [212].

To the authors knowledge, little literature exists on multicomponent laminar spray flames and the parameters influencing it. The one dimensional laminar premixed spray flame configuration using a single component fuel has been studied to understand the main propagation mechanisms. For lean and

stoichiometric mixtures, Ballal and Lefebvre [65] experimentally showed that compared to a gaseous premixed laminar flame at the same overall equivalence ratio, increasing droplet diameter reduces the laminar spray flame speed. This is due to the vapourisation of smaller droplets before reaching the flamefront, which increases the equivalence ratio seen by the flame. For rich mixtures, Hayashi et al. [67] observed an enhanced flame speed over a specific range of droplet diameters. Here the partial evaporation causes the mixture to burn at stoichiometric conditions enhancing the flame speed. Based on detailed chemistry simulations, Neophytou and Mastorakos [213] marginally correlated the laminar spray flame speed trends with an effective equivalence ratio ϕ_{eff} seen by the flame. All of these studies were performed for zero relative velocity between the liquid and the gas phases. However recently, Rochette et al. [214] performed one dimensional n-heptane laminar spray flame simulations using a two-step chemistry and showed that the relative velocity between the liquid phase and the carrier gas phase also has significant impact on ϕ_{eff} and hence the propagation speed. They also derived correlations for the estimation of ϕ_{eff} and the laminar spray flame speed as a function of the spray parameters.

This work aims to analyse the effect of a multicomponent fuel on spray flames, including evaporation and chemistry effects. It is the first attempt to include both Analytically Reduced Chemistry (ARC) and multicomponent evaporation in one dimensional numerical simulations to understand the effect of various spray parameters (diameter, liquid loading, relative velocity and equivalence ratio) on the structure and propagation of a multicomponent spray flame.

6.3 Numerical setup

Computations are performed using the CFD code AVBP with a Lagrangian point particle formulation to represent the spray. Source terms for transfer of mass, momentum and energy from the liquid to gaseous phase are distributed to the closest nodes in the Eulerian gas phase in a two-way coupling approach (http://cerfacs.fr/avbp7x/).

6.3.1 Chemical Mechanism

In this work, the surrogate for Jet-A proposed by Narayanaswamy et al. [142] is reduced. The three components of the surrogate are n-dodecane (NDC), methyl-cyclohexane (MCH) and a xylene (XYL) species that represents the three possible isomers (ortho-, para- and meta-xylene). The mole fractions of each component in the fuel are $X_{NDC} = 0.451$,

$X_{MCH} = 0.268$ and $X_{XYL} = 0.281$. The detailed mechanism with 230 species and 4868 reversible reactions of [215] has been reduced with the reduction code ARCANE (https://chemistry.cerfacs.fr/en/arcane/) based on YARC [216]. The resulting mechanism, **JetA_3Comp_45_686_16_QC**, comprising of 45 transported species, 16 Quasi-Steady State species and 686 irreversible reactions is provided in the supplementary material. The **JetA_3Comp_45_686_16_QC** scheme for the surrogate is in very good agreement with the detailed mechanism for premixed flames on the whole equivalence ratio range at 400 K and 1 bar as shown in Figure 6.1.

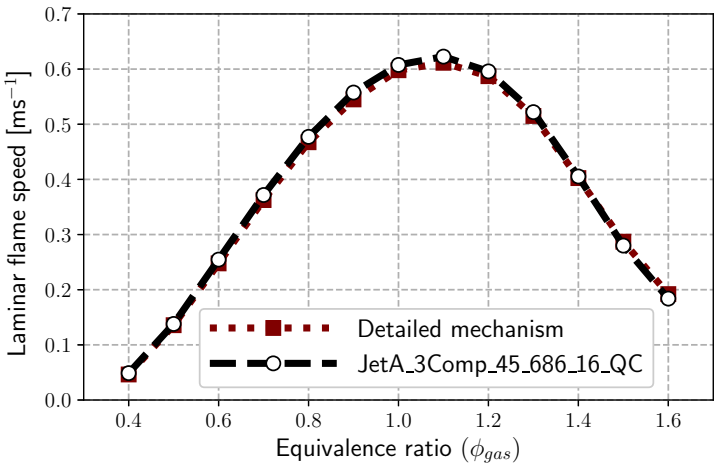

Figure 6.1: Laminar flame speed for gaseous mixture of Jet-A surrogate/Air at 400 K and 1 bar.

6.3.2 Droplet Evaporation Model

The droplet evaporation is modelled using a quasi steady state assumption. It was shown in [217] that including the liquid phase diffusion did not lead to significant difference of the evaporation rate in comparison with infinite liquid diffusivity (as used here). Time scales for droplet heating (τ_{heat}) and mass diffusion inside the liquid (τ_{diff}) for a droplet of radius R are:

$$\tau_{heat} = \mathbf{O}\left(\frac{R^2}{\alpha_{liq}}\right) \quad ; \quad \tau_{diff} = \mathbf{O}\left(\frac{R^2}{D_{liq}}\right) \tag{6.1}$$

where α_{liq} and D_{liq} are the thermal and mass diffusivity in the liquid phase. For small droplets of diameter less than 100μm, $\tau_{heat}, \tau_{diff} \ll \tau_{ev}$ (evaporation timescale). Detailed description of the evaporation model can be found in earlier studies [214, 207]. The multicomponent extension is discussed

here. The Spalding mass transfer number B_M and the fraction of vapour ε^i for an individual component i are calculated as [205]:

$$B_M = \frac{\sum_{i=1}^{k} Y^i_{surf} - \sum_{i=1}^{k} Y^i_{\infty}}{1 - \sum_{i=1}^{k} Y^i_{surf}} = \frac{Y^i_{surf} - Y^i_{\infty}}{\varepsilon^i - Y^i_{surf}} \tag{6.2}$$

where Y^i is the mass fraction of the individual component i and the subscripts $surf$ and ∞ denote the droplet surface and far-field locations respectively. Only the components present in the liquid phase are considered in Eq. (6.2).

Vapour liquid equilibrium Eq. (6.3) is used to obtain the mole fractions of the fuel components at the droplet surface ($X_{i,surf}$) using the liquid mole fractions ($X_{i,liq}$) and the vapour pressure ($P_{sat,i}(T)$) of the different components. Calculating the surface mass fractions Y^i_{surf} to be used in Eq. (6.2) is then straightforward.

$$X_{i,surf} P_{gas} = X_{i,liq} P_{sat,i} \tag{6.3}$$

Using the above equations, the evaporation rate m^i_p of an individual component can be calculated using the total evaporation rate of the droplet $\dot{m}_p$ and the fraction of vapour ε_i as:

$$\dot{m}^i_p = \varepsilon^i \dot{m}_p \quad \text{with} \sum_{i=1}^{k} \varepsilon^i = 1 \tag{6.4}$$

The evaporation model is validated against experiments in Figure 6.2 showing the evolution of Normalised Diameter (ND) and temperature for a single evaporating droplet. After an initial heating phase, the droplet surface area reduces linearly following the D^2, agreeing well with the experimental data of [218]. The highly volatile MCH dominates the composition initially. As MCH and XYL completely evaporate, the liquid and vapour composition in the latter part is composed of only NDC.

6.3.3 Configuration

The one-dimensional domain shown in Figure 6.3 is $0.02m$ long and is discretised using 500 equally spaced elements. To avoid the influence of droplet residence time and to better control of the liquid and gaseous fluxes into the reaction zone, fuel droplets are injected just in front of the flame. Interaction of the fuel droplets and the premixed flame causes a change in flame speed and position. The inlet velocity (u_g) must be adjusted to a new value of the two-phase laminar flame speed $S_{L_{TP}}$ to stabilize the flame.

The simulated cases are summarised in Table 6.1 . Cases A and B represent overall lean and rich cases. Case C is overall lean and only liquid fuel is

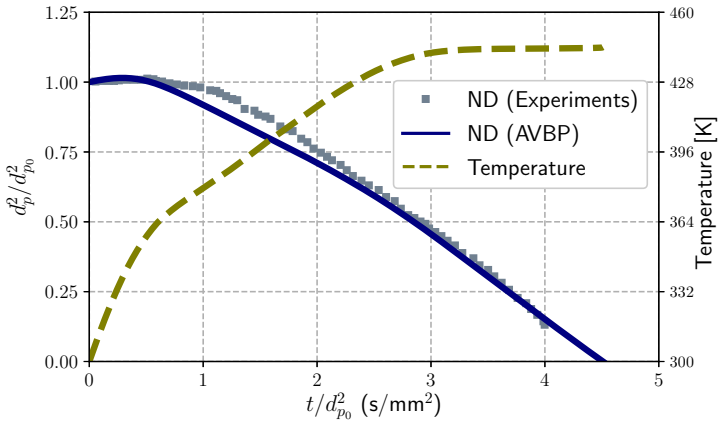

(a) Evolution of ND and temperature

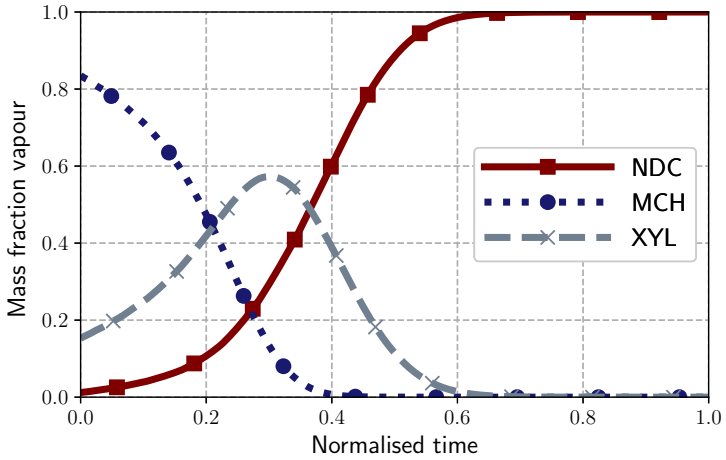

(b) Composition of the evaporating flux

Figure 6.2: Single Jet-A droplet evaporation. d_{p_0} =1000 μm at 300 K in a quiescent air at 773 K.

provided to the flame. These cover a wide range of typical burning regimes observed in real combustors where preferential concentration may lead to a variety of both local liquid loadings and gaseous equivalence ratios with varying relative velocities between the two phases. Total equivalence ratio describes the overall fuel (gaseous and liquid)-to-oxidizer ratio, hence is represented as the sum of gaseous and liquid equivalence ratios ($\phi_{\text{tot}} = \phi_{\text{gas}} + \phi_{\text{liq}}$).

Inlet gas temperature is 400K and droplets are injected at 300K. The flame speeds and structures are computed over a range of droplet diameters ranging from $d_{p_0} = 5\mu m$ to $80\mu m$. For a given droplet diameter, the number of injected droplets is adjusted to fulfil the targeted equivalence ratio. Under saturated conditions and in flame regions it is possible to encounter isolated

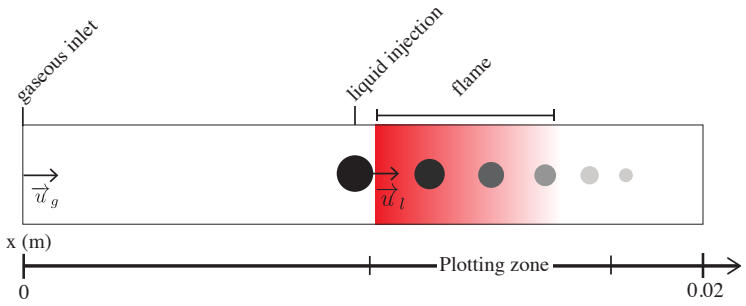

Figure 6.3: Computational configuration [214].

droplet combustion. The diameter of flame (d_f) around a droplet of size (d_p) can be calculated as $d_f \approx 12d_p$ [205]. Droplets are injected such that the inter-droplet distance $S < d_f$ and the isolated burning regime is not activated. The relative velocity between the phases is taken into account by introducing a velocity ratio $u^* = u_{liq}/u_{gas}$ [214].

Case name	ϕ_{tot}	$\phi_{gas,liq}$	u^*	d_{p_0} (μm)
A	0.9	$\phi_{gas} = 0.8$ $\phi_{liq} = 0.1$	1, 30	5-80
B	1.3	$\phi_{gas} = 0.8$ $\phi_{liq} = 0.5$	1, 30	5-80
C	0.9	$\phi_{gas} = 0.0$ $\phi_{liq} = 0.9$	1, 30	5-80

Table 6.1: Conditions of simulated cases.

6.4 Results

6.4.1 Multicomponent spray flame structure

Flame structures for the cases in Table 6.1 are compared for $d_{p_0} = 20\mu m$, $u^* = 1$ and 30. The heat release (HR) profiles are plotted with the evaporation source terms (Γ_F) and the volumetric consumption ($-\dot{\omega}_F$) speed of the components. Droplets injected just before the flamefront begin to release vapour in the reacting zone and the evaporation zone extends beyond the main flame region.

In Figure 6.4 for Case A and $u^* = 1$ MCH is shown to evaporate completely in the main flame region followed by XYL and finally NDC. The preferential evaporation of MCH and its complete consumption within the main premixed flame zone shown in Figure 6.4b causes a slight increase in ϕ_{eff} compared to ϕ_{gas}. As the droplets move through the main flamefront gradually they contain

only XYL and NDC, and finally only NDC, whose evaporation rate reaches a maximum in the post-flame high temperature region. Due to the lower volatility and longer evaporation distance of NDC, a secondary consumption zone with very low but non-zero reaction rates exists as seen in Figure 6.4c.

Increasing the droplet velocity so that $u^* = 30$ shifts the evaporation zone behind the main flamefront as shown in Figure 6.5. The dominant flame structure is that of the premixed gaseous flame at $\phi_{gas} = 0.8$ and the contribution of the liquid phase towards ϕ_{eff} is negligible. An extended secondary combustion zone behind the main reaction zone exists where the evaporating droplets react with the excess oxygen. This zone for NDC is shown in Figure 6.5b, and similar ones for MCH and XYL are observed (not shown).

In Case A two limiting regimes may be encountered. The first corresponds to droplets small or slow enough to evaporate completely in the main reaction zone leading to $\phi_{eff} = \phi_{tot}$ while in the second limit large or fast droplets contribute very little to the flame propagation and $\phi_{eff} = \phi_{gas}$. As the flame is overall lean, this leads to the spray flame speed limits for Case A to lie between $S_{L_{\phi_{gas}}} \leq S_{L_{TP}} \leq S_{L_{\phi_{tot}}}$.

The spatial profiles of HR, Γ_F and $-\dot{\omega}_F$ for Case B are shown in Figure 6.6 and Figure 6.7. The evaporation trends are very similar to Case A, however due to the high liquid loading the amount of vapour released is significantly higher. For the condition $u^* = 1$ the evaporation and consumption profiles of MCH (not shown) are similar to that observed in Figure 6.4b. NDC shows a strong and prominent secondary reaction zone behind the main premixed flamefront where the remaining oxidiser is consumed in long droplet burning regime highlighted in Figure 6.6b. As in Case A, this secondary reaction zone does not affect the propagation speed but contributes towards the overall heat release.

For $u^* = 30$, a distinct secondary reaction zone away from the premixed flamefront is observed for NDC. Since the main premixed flame is lean with $\phi_{\text{gas}} = 0.8$, the remaining oxidiser is consumed as the evaporation progresses. Multiple reaction pathways are possible for the consumption of fuel components due to the ARC mechanism used. Some vapour released in this region also undergoes pyrolysis producing new smaller fuel species which diffuse back to burn with oxygen. This complex diffusion flame structure is illustrated with two components formed by NDC pyrolysis (H_2, C_2H_2) having a slope of opposite sign compared to the oxygen (O_2) profile, shown in Figure 6.7b. Burnt gas composition contains the standard combustion products CO_2, H_2O, CO together with smaller components.

As in Case A, the upper and lower limits of ϕ_{eff} for Case B are ϕ_{tot} (fast evaporation) and ϕ_{gas} (slow evaporation). However, with $\phi_{tot} = 1.3$ it is possible to find conditions for which $\phi_{eff} \approx 1.0$ leading to $S_{L_{TP}} > S_{L_{\phi_{tot}}}$.

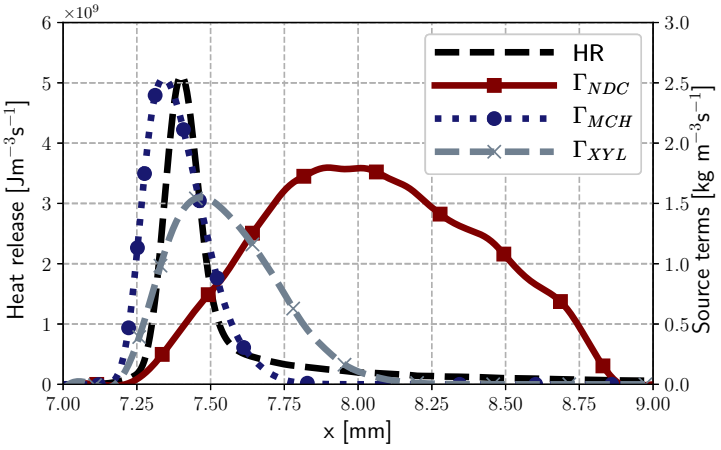

(a) Heat release and evaporation source terms

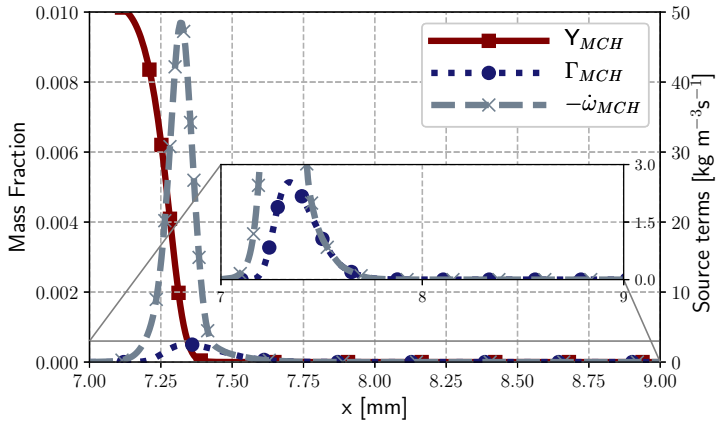

(b) Mass fractions and consumption rates of MCH

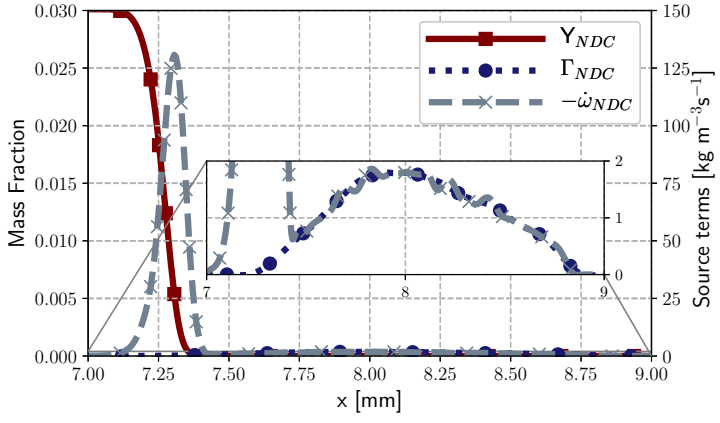

(c) Mass fractions and consumption rates of NDC

Figure 6.4: Profiles of heat release, mass fractions, evaporation and consumption rates for Case A, $d_{p0} = 20\mu m$ and $u^* = 1$.

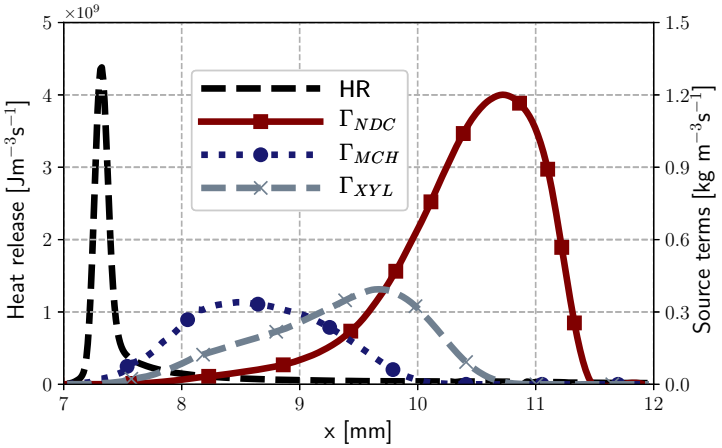

(a) Heat release and evaporation source terms

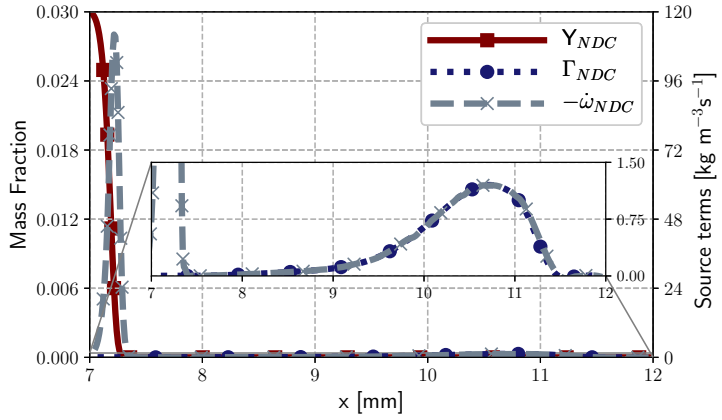

(b) Mass fractions and consumption rates of NDC

Figure 6.5: Profiles of heat release, mass fractions, evaporation and consumption rates for Case A, $d_{p_0} = 20\mu m$ and $u^* = 30$.

Results for Case C where all the fuel is in the liquid phase are shown in Figure 6.8 and Figure 6.9. For $u^* = 1$, the faster evaporation of MCH initiates the flame. Significant amounts of XYL and NDC also vaporise before the location of peak heat release. Energy from the reactions provides the latent heat of evaporation needed to sustain the flame. This causes significantly lower heat release rates and flame speeds compared to a purely gaseous flame or spray flame with lower liquid loading as Case A. For higher droplet velocities $u^* = 30$, the reaction zone develops later after significant amount of liquid fuel has vaporised. For the purely liquid controlled Case C, the HR zone extends across the entire evaporation zone of the droplets with $-\dot{\omega}_F$ and Γ_F superimposed in this region.

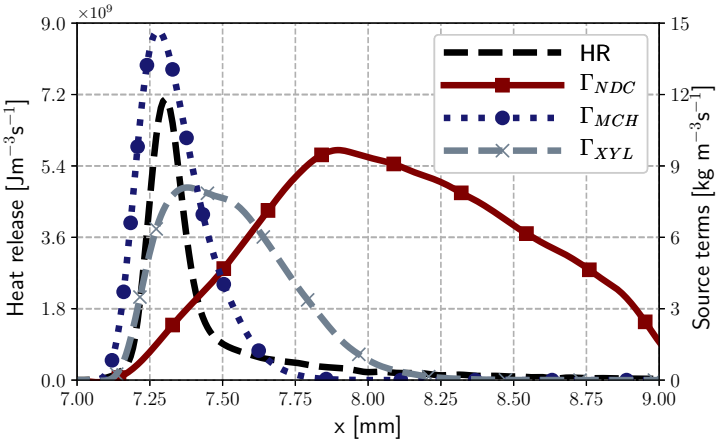

(a) Heat release and evaporation source terms

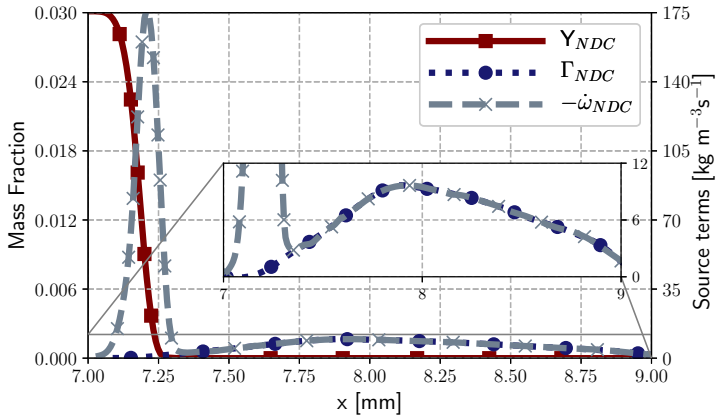

(b) Mass fractions and consumption rates of NDC

Figure 6.6: Profiles of heat release, mass fractions, evaporation and consumption rates for Case B, $d_{p_0} = 20\mu m$ and $u^* = 1$.

6.4.2 Laminar two-phase flame speeds for multicomponent droplets

The laminar two-phase flame speed is controlled by ϕ_{eff} which is a function of the gaseous equivalence ratio and the evaporation of liquid inside the flamefront of thickness δ_L^0. The distance over which the droplets evaporate, compared against δ_L^0 can be used to estimate the contribution of evaporation to ϕ_{eff}. Previously laminar flame speed correlations have been developed and validated for a single component n-heptane case [214]. To extend these correlations to the present case, it is necessary to consider the varying evaporation rates (Figure 6.2) and contributions of the liquid fuel components.

The different evaporation time scales (τ_{ev}^i), of the liquid components are

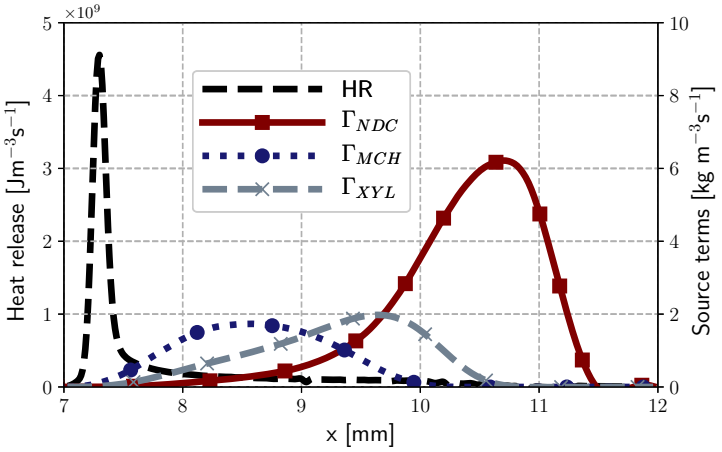

(a) Heat release and evaporation source terms

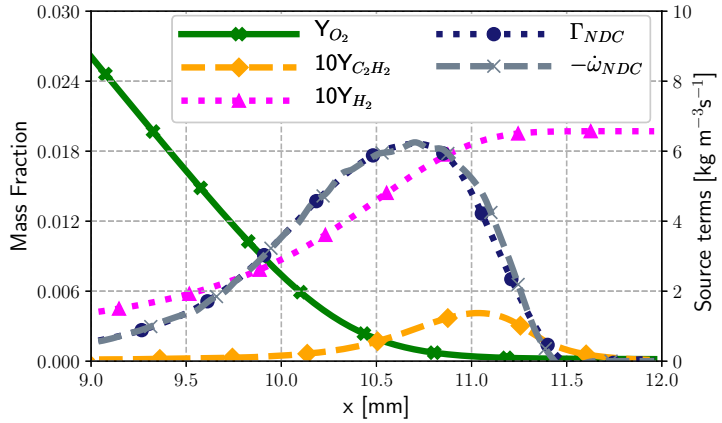

(b) Diffusion flame structure for NDC

Figure 6.7: Profiles of heat release, mass fractions, evaporation and consumption rates for Case B, $d_{p_0} = 20\mu m$ and $u^* = 30$.

calculated using the fraction of each component ε_i averaged over the lifetime of i in the liquid state. In Eq. (6.5) the Spalding mass transfer number B_M is calculated at the mean of liquid injection and wet bulb temperatures, $(T_{inj} + T_{wb})/2$ (using the T_{wb} of NDC in this case because it is the last remaining component) for a droplet evaporating in flame conditions.

$$\tau_{ev}^{i} = \frac{\rho_{liq} d_{p_0}^2}{12 \rho_{gas} D_F \varepsilon_i \ln(1+B_M)} \underbrace{\left[1 + \frac{k Sc^{1/3} Re_p^{1/2}}{2 \frac{(1+B_M)^{0.7} \ln(1+B_M)}{B_M}}\right]^{-1}}_{\text{accounts for droplet velocity}} \tag{6.5}$$

where d_{p_0}, ρ_{liq} and ρ_{gas} are the initial droplet diameter, liquid and gas

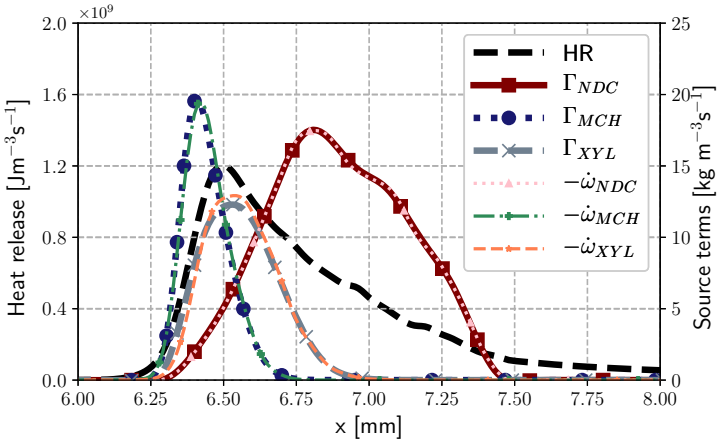

Figure 6.8: Profiles of heat release, evaporation and consumption rates for Case C, $d_{p_0} = 20\mu m$ and $u^* = 1$.

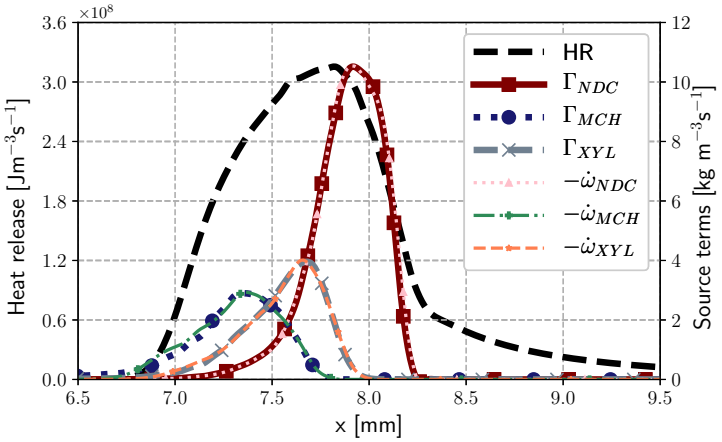

Figure 6.9: Profiles of heat release, evaporation and consumption rates for Case C, $d_{p_0} = 20\mu m$ and $u^* = 30$.

density respectively. D_F is the diffusion coefficient of the fuel vapour, Sc is the Schmidt number of the surrounding gas and Re_p is the Reynolds number of the droplet. k is a factor whose value is taken as 0.6. [205].

For droplets with high relative velocity, it is important to take into account drag force acting on them. Using the droplet relaxation time $\tau_p = \rho_{liq} d_{p0}^2 / 18\mu_{gas}$ (μ_{gas} is the dynamic viscosity of the surrounding gas) and the flame time $\tau_f = \delta_{S_L}^0 / S_L^0$, a flame Stokes number is identified as $St_f = \tau_p / \tau_f$. A droplet injected with a velocity u_{p_0} reaches after crossing the flame thickness the velocity u_p:

$$u_p = u_{gas} \left(1 - e^{-1/St_f}\right) + u_{p_0} e^{-1/St_f} \tag{6.6}$$

The evaporation length for each component i is then given by $\delta^i_{ev} = u_p \tau^i_{ev}$. Following Rochette et al. [214] and using the above expressions, ϕ_{eff} is

$$\phi_{eff} = \sum_i \left(\frac{\delta^0_L}{max\left(\delta^0_L, \delta^i_{ev}\right)} \right)^{\frac{2}{3}} \left(\frac{s_i}{s_{Jet\text{-}A}} \right) \phi_{liq} + \phi_{gas} \tag{6.7}$$

In Eq. (6.7), s is the stoichiometric ratio. For a hydrocarbon fuel C_xH_y, $s = x + y/4$. The term $s_i/s_{Jet\text{-}A}$ accounts for the varying contribution of each component present in the liquid fuel to ϕ_{eff}. For small droplets which evaporate fast, Eq. (6.7) yields $\phi_{eff} = \phi_{tot}$. For larger droplets having non-negligible evaporation times, Eq. (6.7) gives $\phi_{gas} < \phi_{eff} < \phi_{tot}$. Similarly, volatile components with $\delta^i_{ev} \leq \delta^0_L$ contribute completely to ϕ_{eff} whereas less volatile components with large evaporation thickness only partially contribute to the flame.

For flames controlled by evaporation (Case C), the flame speed correlations from Rochette et al. [214] considering the smallest evaporation timescale of MCH (τ^{MCH}_{ev}) is used.

$$S_{L_{TP}} = \frac{\delta_{S_{L_{\phi gas}}}}{\tau^{MCH}_{ev}} \tag{6.8}$$

The correlations are compared with the simulation results for all cases in Table 6.1 and overall a good agreement with the trends are observed. Comparison for Case A is shown in Figure 6.10 . The laminar flame speed is less than $S_{L_{\phi_{tot}}} = 0.56\,\mathrm{m}s^{-1}$ for all droplet sizes. For large droplets the contribution of evaporation to ϕ_{eff} is negligible. Increasing the droplet velocity reduces the residence time in the reactive zone, reducing further the liquid phase contribution leading to $\phi_{eff} = \phi_{gas}$ and $S_{L_{TP}} = S_{L_{\phi gas}} = 0.48\,\mathrm{m}s^{-1}$.

For Case B (Figure 6.11), an optimum diameter exists at which the two phase flame burns close to stoichiometry. For $u^* = 1$ it is found at $20\,\mu$m and for $u^* = 30$ at $10\,\mu$m. Due to the varying volatilities of the multicomponent fuel, such an optimum diameter exists even when the droplets move very quickly across the flame.

For the evaporation controlled flames of Case C (Figure 6.13), correlation follows the trend but with some deviation from the simulation results. It is observed in Figure 6.13 that a flame can be sustained for gaseous equivalence ratios lower than the flammability limit if droplets have low or zero relative velocities. As was observed in Figure 6.8 and Figure 6.9, significant amounts of liquid components evaporate before a stable flame can be sustained. This leads to multiple reaction pathways involving all components, hence τ^{MCH}_{ev} cannot be used alone for the estimation of the flame speed. A detailed comparison between the evaporation and chemical timescales is needed to obtain a better

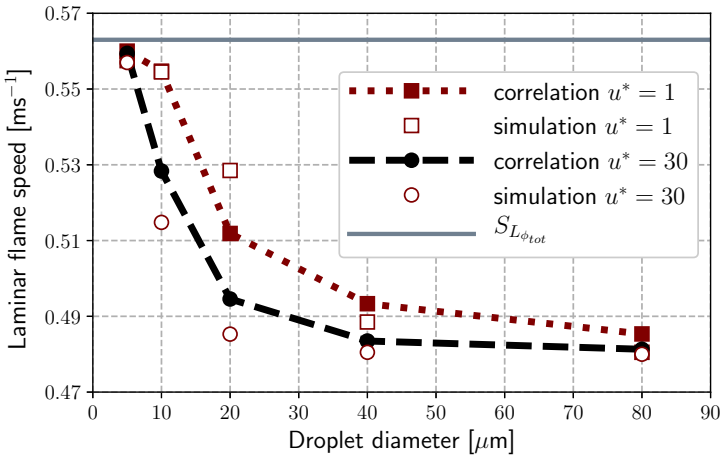

Figure 6.10: Two-phase flame speed of Jet-A vs initial droplet diameter. Comparison between simulations and correlations (Eq. (6.7)) for Case A.

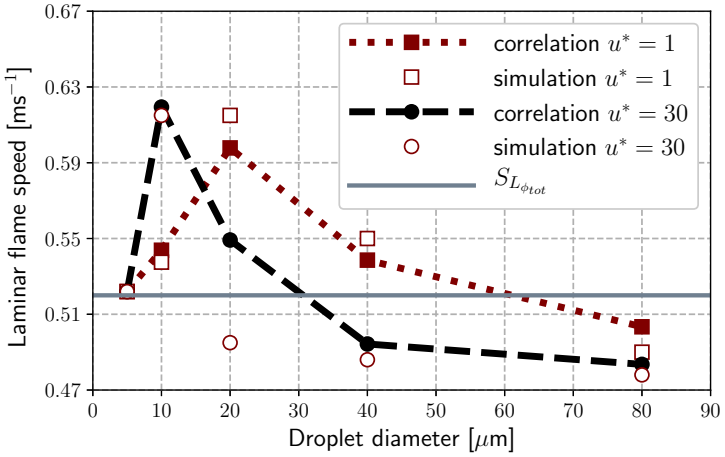

Figure 6.11: Two-phase flame speed of Jet-A vs initial droplet diameter. Comparison between simulations and correlations (Eq. (6.7)) for Case B.

agreement with the simulated data for Case C.

6.5 Conclusions

Multicomponent one-dimensional spray flame simulations were performed for a Jet-A surrogate composed of n-dodecane (NDC), methyl-cyclohexane (MCH) and xylene (XYL). Flame structure and spray flame speed have been examined for a wide range of equivalence ratios, droplet diameters and droplet velocities. Due to the varying volatilities of these components, a staged evaporation behaviour was observed as the droplets move through the reactive

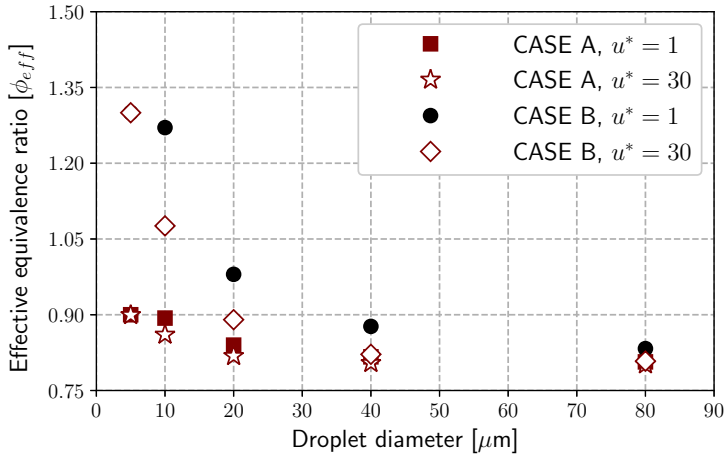

Figure 6.12: Effective equivalence ration calculated by Eq. (6.7).

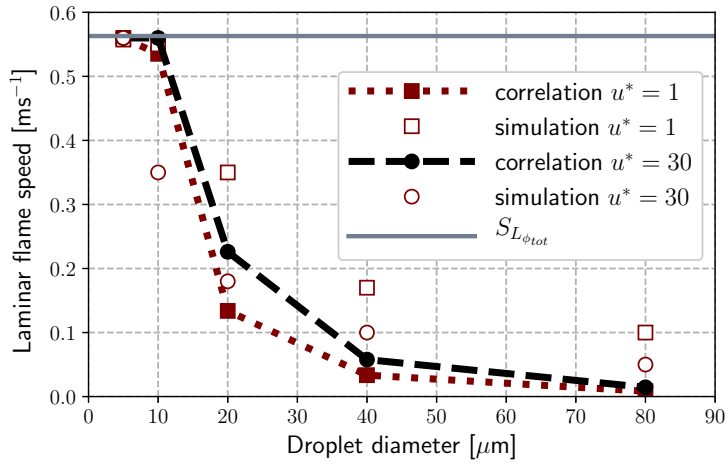

Figure 6.13: Two-phase flame speed of Jet-A vs initial droplet diameter. Comparison between simulations and correlations (Eq. (6.8)) for Case C.

flamefront. MCH being the most volatile component enhances the effective equivalence ratio and this effect is more pronounced for low relative velocities. NDC being the least volatile component leads to an extended secondary reaction zone following the primary flame zone. For rich cases with high relative velocity, a separated secondary diffusion flame of NDC can even be observed. For purely liquid fuels the heat release zone extends over the entire evaporation zone. Correlations were proposed to estimate laminar spray flame speeds considering the varying vapour fluxes and contributions of the different liquid components as well as the drag effect. These correlations are in very good agreement with numerical results, except for purely liquid flames which demand an accurate comparison of the various evaporation and chemical

timescales and will be the focus of future work. Overall the various mechanisms controlling the laminar spray flame speed for multicomponent droplets have been identified and may be used in turbulent combustion modelling of multicomponent sprays.

Part III

Applications to the realistic gas turbine combustion chamber - LOTAR configuration

Chapter 7

LOTAR - setup and results on global chemistry

Contents

7.1 Introduction

At present, the state-of-the-art gas turbine combustors use complex liquid injection systems and combustion strategies for efficient energy conversion. This is done by the introduction of the liquid phase as a fine spray of droplets into a swirling airflow leading to breakup, evaporation, mixing and ultimately combustion. Simultaneous occurrence of mechanisms over multiple length and time scales which include gaseous and droplet combustion are widely reported in the existing literature [56]. Of these, the droplet evaporation and reaction times were identified as being particularly important by Ma and Roekaerts [219]. It was further demonstrated that varying the initial conditions (droplet diameter, inlet air temperature) but maintaining identical time-scales resulted in flame structures that are reproducible on realistic configurations [219, 220]. Other studies show the introduction of droplets in swirling gaseous flow as is the case in real gas turbine engines leads to the coexistence of premixed and non-premixed combustion regions and highlight the need to also model the often-neglected single droplet combustion mechanisms [74, 103].

Large Eddy Simulations (LES) with an Eulerian description of the gas phase and a Lagrangian discrete particle representation of the spray is a standard approach in the research community for such problems. Most of these two-phase simulations are however usually performed on lab scale burners

with smaller power ratings which do not represent the operating points of a realistic gas turbine combustor.

The aim of this study is hence to analyse the results of the LES of a realistic large-scale swirling spray combustor. To do so, the "Liquid fueled Onera Thermo-Acoustic Rig" (LOTAR) test bench chosen due to its proximity in complexity to an industrial case [221]. This chapter introduces first the LOTAR test rig and the numerical setup used to compute it. The computations are then validated against available experimental results. For this preliminary step, a global chemical scheme is utilised to look at the initial flame structures and regimes.

7.2 Experimental Setup

The LOTAR setup installed on the ONERA LACOM testbench is designed to study the thermoacoustic instabilities arising in spray combustion systems. The system can be operated with inlet air mass flow rates of 1 $^{kg}/_{s}$ upto 50 bars pressure. The inlet air can also be heated to a temperature of 900 K using the 1 MW heating unit. The inlet flow rate measurements obtained with sonic valves show variations of ±3.5%. Liquid fuel is delivered to the injection system using two lines from a pressurised tank and monitored using a Coriolis flow meter with an uncertainty of ±0.15%. The operating Global Equivalence Ratio (GER) calculated using the mean fuel and air flowrates have a measurement uncertainty of ±3.5% [221, 222, 223].

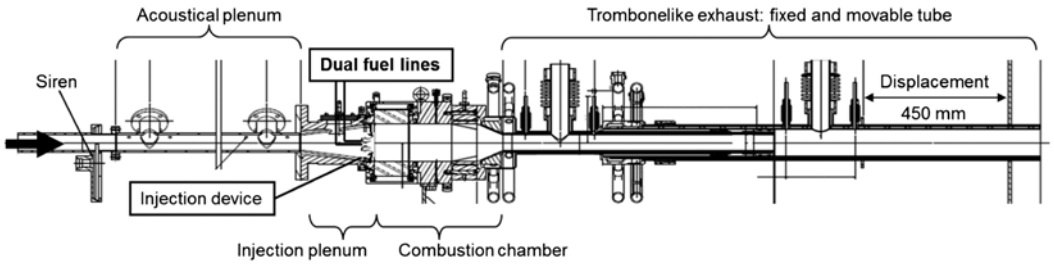

Figure 7.1: Cross section of the experimental LOTAR setup [221].

A cross section of the complete setup is shown in Figure 7.1 for which the direction operation is from left to right. On the inlet side at the left is a siren which is used to pulse the incoming heated gases at various amplitudes and frequencies. The combustion chamber shown in Figure 7.2 consists of a plenum to mount the injection system and a water cooled combustion chamber with quartz windows for optical access. Optical diagnostics is possible near the exit plane of the injector system which separates the plenum and the chamber.

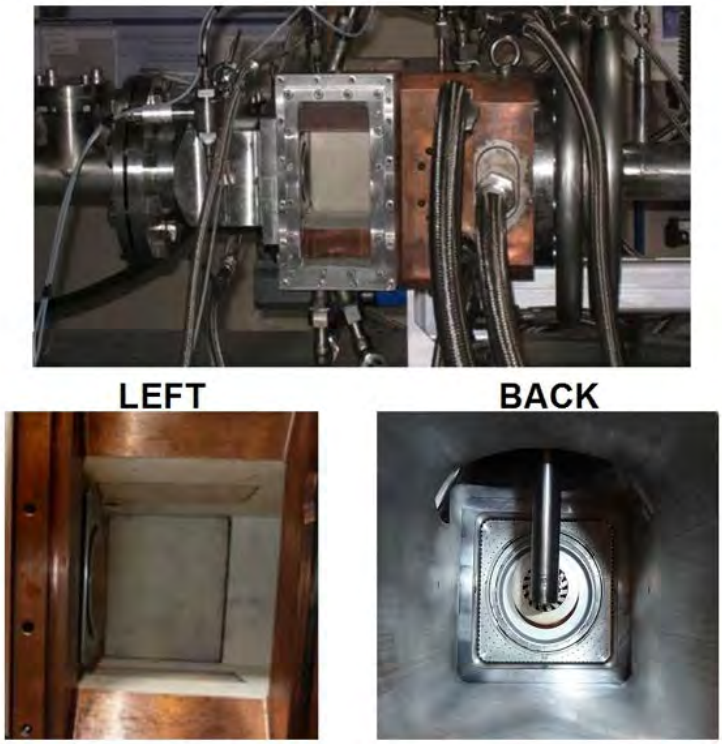

Figure 7.2: Complete computational domain for LES (top); combustion chamber and injection plenum (bottom).

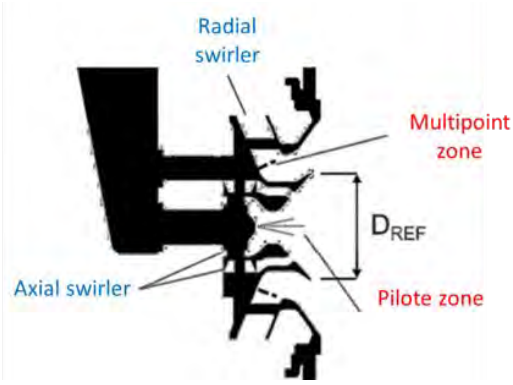

Figure 7.3: Fuel injection system.

The complex injection system, Figure 7.3 consists of two counter rotating axial swirlers to break up the central pilot jet of liquid fuel. This is surrounded by a radial swirler through which the bulk of injected air passes. Multipoint injectors (24 holes) are also present in the periphery of the radial swirler. A perforated plate integrated into the system diverts a portion of the incoming airflow to cool the back plate of the combustor and also creates a cooling film

on the combustion chamber walls. The Fuel Split Parameter (FSP), defined as the ratio between pilot to the total inlet liquid mass flow rate specifies the fuel injection pattern between the two possible delivery methods that are: the pilot and multipoint.

The combustion chamber exit has a long fixed tube along with a movable coaxial tube. A motorised mechanism allows the movement of the inner tube thereby altering the Inner Exhaust Length (IEL), defined as the distance between the exit planes of the injector and exhaust tube. Varying the IEL allows control of the natural acoustic frequencies of the system. It is to be noted that the exhaust tube is also water cooled and is equipped for acoustic characterisation, similar to that of the inlet tube.

Stability of the system depends on GER, FSP and IEL as shown in Figure 7.4 for a constant air mass flow rate of 100 g/s at 450 K operated with kerosene at 1 bar. The dashed lines represent iso-contours of a constant mass flow rate through the pilot injector. Stable operating points are observed for all conditions when GER is less than 0.6 and the system has higher chances of unstable operation when the GER increases. It was observed during the experimental campaign that the non-negligible partial heat losses induced the need for a minimum power rating to sustain the instabilities that are triggered in the system at higher GER [224].

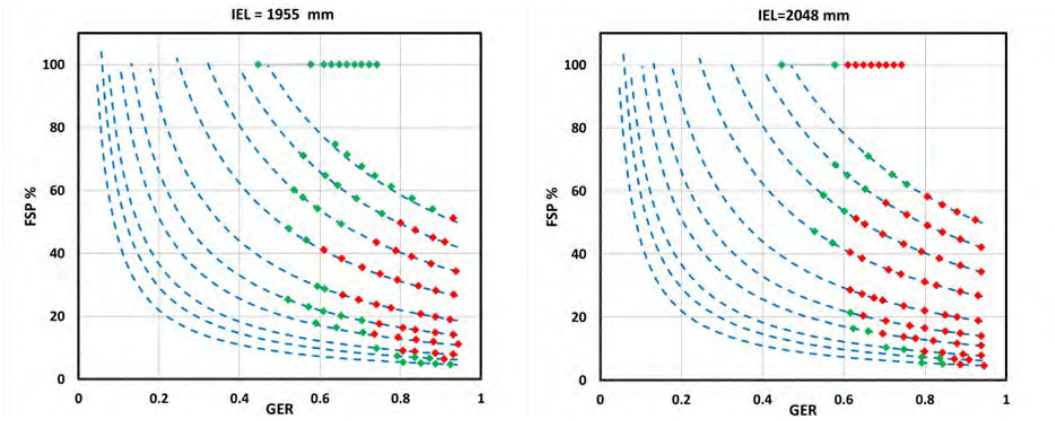

(a) IEL=1955 mm **(b)** IEL=2048 mm

Figure 7.4: Stability map for LOTAR with kerosene fuel operated at over range of GER, FSP and IEL [224, 222]. Green are stable, red are unstable operation points.

The targeted operating conditions for reactive LES simulations are cases with FSP=100%; that is all the fuel is injected using only the pilot injector. For a IEL of 1955 mm, these coincide with stable operating conditions which were then forced over a range of frequencies and amplitudes. The flow rate

Case	$\dot{m}_{air}$	$\dot{m}_{liq}$	T_{air}	T_{liq}
Coldflow	100 g/s	-	298 K	-
Reactive	100 g/s	4.55 g/s	450 K	298 K

Table 7.1: Experimental conditions, atmospheric pressure for all cases.

of liquid fuel is fixed at 4.55 g/s and 298K, while the incoming air mass flow rate is 100 g/s and 450K. For kerosene with an average chemical composition of $C_{10}H_{20}$, this corresponds to an operating GER of 0.67. The non reactive tests were performed for 100 g/s and 298K. These conditions are summarised in Table 7.1. The corresponding parameters for the LOTAR configuration are highlighted in Table 7.2 confirming that the rig operates on par with an actual industrial configuration for which similar details available in Moin and Apte [225].

Parameter	Value
Reynolds number	$\mathbf{O}\,(10^6)$
Density ratio	$\mathbf{O}\,(10^6)$
Stokes number	$3-13$
Thermal power	200 kW

Table 7.2: Major parameters of the LOTAR configuration.

7.3 Numerical Setup

The computational domain chosen covers the plenum and the chamber as described earlier (Figure 7.2) for a total length of 515 mm. The corresponding internal volume was then discretised with tetrahedral elements. Major features with a mid section of the computational mesh and orientation of the inlet and outlet planes are shown in Figure 7.5.

The meshing strategy included starting with a relatively coarse baseline mesh of 18 million elements and subsequent improvement using the strategy proposed by Daviller et al. [226]. The time averaged viscous dissipation fields - with high values corresponding to the regions of high loss of turbulent kinetic energy - are used for refining the initial mesh. A normalised metric of this field is used to identify specific regions that need refining. The mesh used for the LES is composed of 32 million tetrahedrons with a refined swirler region shown in Figure 7.6. The smallest mesh size of about 0.2 mm is used in the injector region.

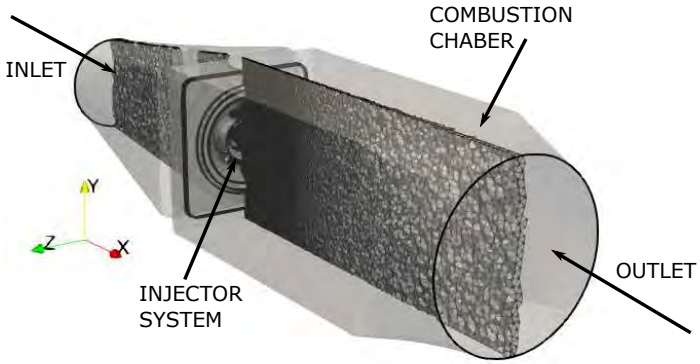

Figure 7.5: Computational domain.

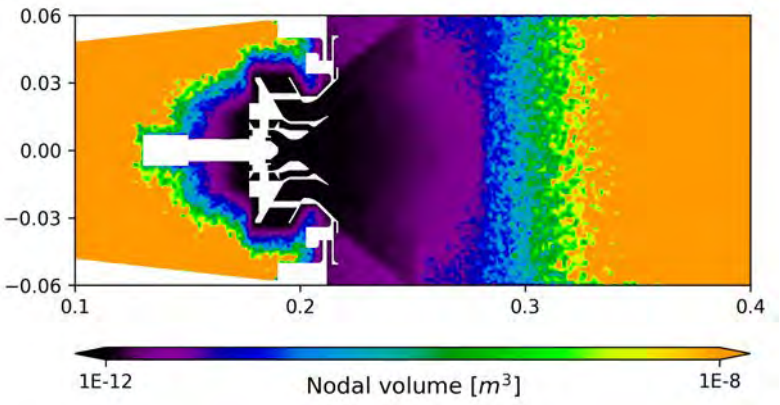

Figure 7.6: Nodal volumes representing relative mesh sizes in the computational domain.

Simulations have been performed using the 3-D fully compressible reactive solver AVBP (http://cerfacs.fr/avbp7x/). The second-order accurate Lax-Wendroff convective scheme [227] is used with an explicit Runge-Kutta time stepping. The subgrid-scale closure for turbulence is addressed using the SIGMA model [228]. Finally, for modelling the reactive flow, the Dynamic Thickened Flame LES [92] turbulent combustion model is employed together with the classical sensor [93, 94] (global chemistry) to thicken the flame front on 5 mesh points.

In the experiments, cooling holes in the separation plate between the plenum and the chamber divert a portion of the incoming air towards the quartz walls and lip of the injector where the flame stabilises. Diameters of these holes are of the order 0.1 mm which is not practical to resolve for the

present simulations. These surfaces have thus been replaced with a perforated plate model [229, 230, 231] through which 10% (calculated based on the approximate fraction of normal area through which flow goes) of the incoming mass flow rate is diverted from the plenum and injected into the chamber base.

Note also that the presence of cooled chamber walls necessitates the use of heat loss conditions at these walls. For reacting simulations, the injection and the swirler systems, burner base plate and quartz wall boundary conditions were specified through the use of a temperature and heat resistance. A thermal conductivity of $\lambda_{steel} = 25\,\mathrm{Wm^{-1}K^{-1}}$ and $\lambda_{quartz} = 1.5\,\mathrm{Wm^{-1}K^{-1}}$ is considered. The thickness obtained from the CAD data is utilised to calculate the heat resistances of these respective surfaces. The experimental data for the flow rate of cooling water ($6.8\,\mathrm{m^3h^{-1}}$) and temperature change (1 K) indicates a heat transfer of approximately $-75000.0\,\mathrm{Jm^{-2}s{-}1}$ (negative to signify heat out of the domain), which is then imposed as a constant heat flux through the rest of chamber walls as marked in Figure 7.7.

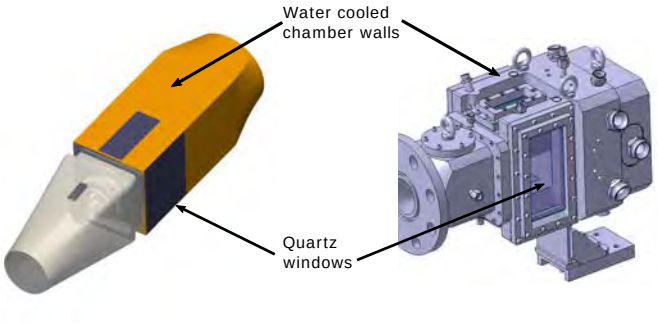

Figure 7.7: Patches where thermal boundary conditions are applied in the simulation setup.

The global chemical scheme used is the two-step 2S_KERO_BFER mechanism [102]. The first step is the oxidation reaction followed by a fast $CO - CO_2$ equilibrium reaction which reads:

$$\begin{aligned} C_{10}H_{20} + 10O_2 &\longrightarrow 10CO + 10H_2O, \\ CO + 0.5O_2 &\longleftrightarrow CO_2, \end{aligned} \tag{7.1}$$

and for which the reaction rates are given by Arrhenius equations of the form:

$$\dot{\omega}_1 = A_1 \left(\frac{\rho Y_{C_{10}H_{20}}}{W_{C_{10}H_{20}}}\right)^{0.55} \left(\frac{\rho Y_{O_2}}{W_{O_2}}\right)^{0.9} \exp\left(\frac{-E_{a,1}}{RT}\right) f_1(\phi),$$
$$\dot{\omega}_2 = A_2 \left[\left(\frac{\rho Y_{CO}}{W_{CO}}\right)^{1.0} \left(\frac{\rho Y_{O_2}}{W_{O_2}}\right)^{0.5} - \frac{1}{K_2}\left(\frac{\rho Y_{CO_2}}{W_{CO_2}}\right)^{1.0}\right] \exp\left(\frac{-E_{a,2}}{RT}\right) f_2(\phi). \tag{7.2}$$

The constants used in the above equations are given in Table 7.3. The Pre-Exponential Adjustment (PEA) functions $f_1(\phi)$ and $f_2(\phi)$ are used to recover the correct flame speeds in rich mixtures and is applied to both equations [102]. The function $f_1(\phi)$ is used in the oxidation reaction for the correct prediction of the laminar flame speed and is function of the local equivalence ratio, while $f_2(\phi)$ is used for the adjustment of the $CO - CO_2$ equilibrium to obtain the sudden change from rich to lean conditions. Franzelli et al. [102] fitted these global schemes over a wide range pressures (1-12 bars) and temperatures (300-700 K). A comparison between the skeletal mechanism with 91 species and 64 reactions of LUCHE et al. [232] and the 2S_KERO_BFER is shown in Figure 7.8. The laminar flame speeds are calculated over the entire range of equivalence ratios using cantera and excellent agreement is observed for the conditions of interest in the present configuration.

	A_j [cgs]	A_j [cgs]
Reaction 1	8×10^{11}	4.15×10^4
Reaction 2	4.5×10^{10}	2.0×10^4

Table 7.3: Pre-exponential factors (A) and activation energies E_a used in Eq. (7.2) for 2S_KERO_BFER scheme.

Concerning the liquid injection profile, it is chosen considering a fuel split ratio of 100%, i.e., all the fuel is injected through the pilot injector. The hollow cone spray is modelled using the semi-empirical FIM-UR model [233] and a Rosin-Rammler droplet diameter distribution having a Sauter Mean Diameter (SMD) of 30 μm and a shape parameter q=1.7 are prescribed.

7.4 Results

The simulation setup was validated with the non-reacting experimental data as summarised in Table 7.1. An averaged coldflow (averaged over 4 flow through times of the domain $\approx$ 75 ms) aerodynamic field is shown in the mid

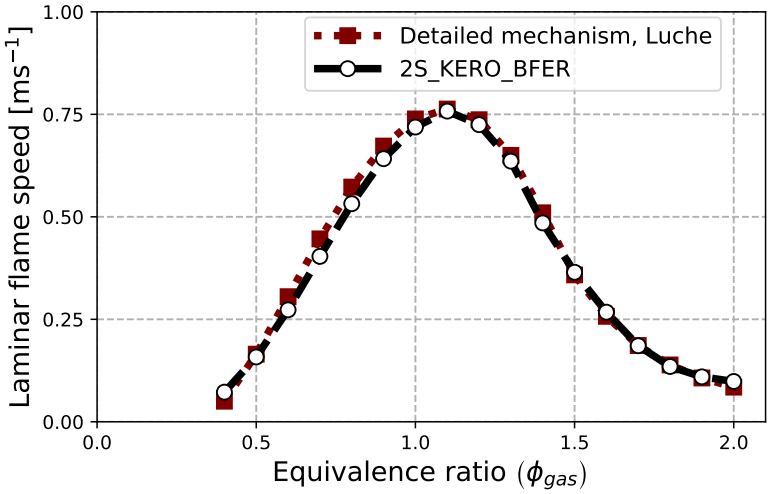

Figure 7.8: Comparison between the detailed Luche mechanism [232] and 2S_KERO_BFER [102] at 450 K and 1 atm.

plane (y-axis, Figure 7.5) of the combustor in Figure 7.9. The recirculation zones, identified by an iso-contour of axial velocity, $u_x = 0$, reveals the classical swirled flow features. A large Central Recirculation Zone (CRZ) extends from the exit of the inner most swirler until half of the chamber length (x $\approx$ 0.4 m). Two much smaller Outer Recirculation Zones (ORZ) are present between the incoming streams from the radial swirlers and the chamber walls. These ORZ's also interact with the cooling film introduced from the base of the chamber.

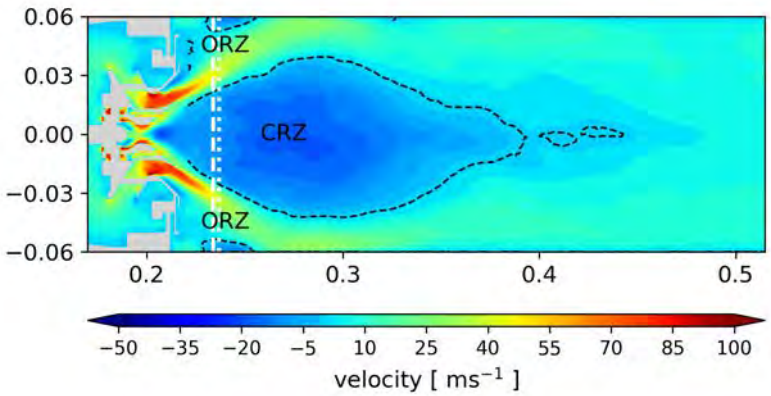

Figure 7.9: Averaged axial velocity in the mid plane highlighting the major flow features for the non-reacting case (dashed black lines: iso contours of $u_x = 00$; vertical white lines are the experimental measurement planes: dashed $x = 22$ mm, dotted $x = 25$ mm).

Experimental measurements were obtained for two axial visualisation

planes at a distance of 22 mm and 25 mm from the backplane of the chamber (Figure 7.9). A comparison between the axial, radial and transverse gas velocities obtained at these planes are shown in Figure 7.10. Note that the asymmetry in the flow profile caused by the large liquid injection system present in the plenum is well captured numerically. On the lower branch, the axial jet velocity reaches 50 ms^{-1} compared to 30 ms^{-1} which is also observable in Figure 7.9 indicating a large deviation of the incoming airflow because of the liquid injection structure. The transverse velocity field indicating the feature of jet opening inside the combustion chamber is also adequately captured. Overall, the numerical setup reproduces the split of inlet air mass flow rate over the three swirlers and cooling holes correctly.

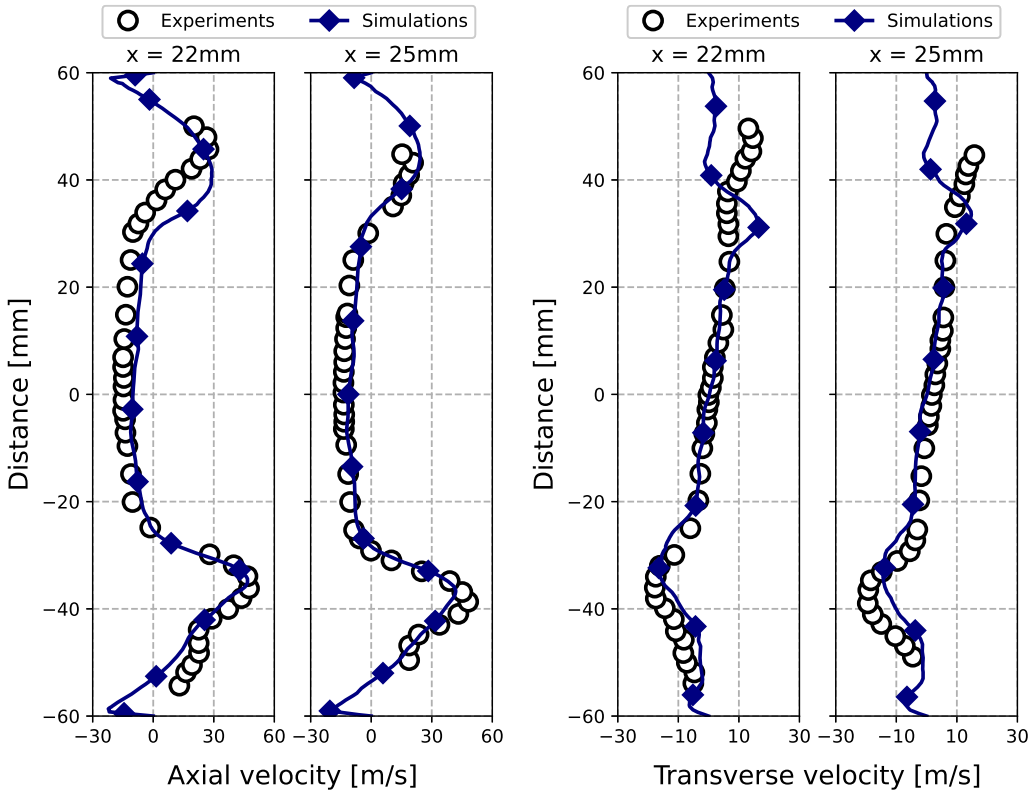

(a) Axial velocities. **(b)** Transverse velocities.

Figure 7.10: Coldflow velocity profiles at planes $x = 22$ mm and $x = 25$ mm.

The swirler can be characterised using the swirl number (S_w), defined as the ratio of tangential (G_θ) to axial momentum flux (G_x) calculated using the cylindrical coordinates as [234, 235]:

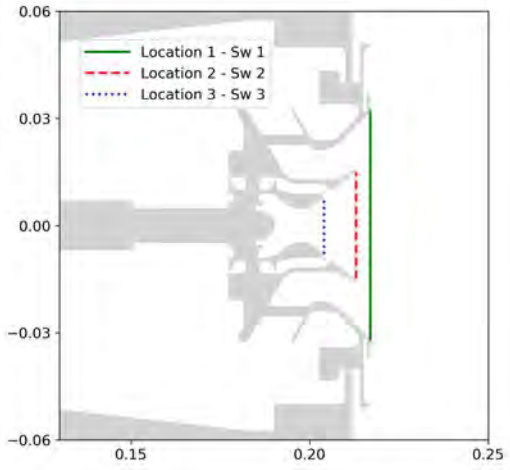

Figure 7.12: Exit plane of individual siwrlers used for calculation of the swirl numbers given in Table 7.4.

	S_w (cold)	S_w (reacting)	$\dot{m}$ [%]
Sw 1	0.4(+)	0.35(+)	86%
Sw 2	0.4(−)	0.34(−)	7%
Sw 3	0.4(+)	0.42(+)	5%

Table 7.4: Swirl numbers and mass flow split through the 3 individual swirler stages at locations given in Figure 7.12.

$$S_w = \frac{G_\theta}{RG_x} = \frac{\int_0^R \rho u_x u_\theta 2\pi r^2 dr}{R\int_0^R \rho {u_x}^2 2\pi r dr}, \tag{7.3}$$

where u_x and u_θ are the axial and tangential velocities across a section of radius R. For the present case, Eq. (7.3) is computed at the exit plane of individual stages marked in Figure 7.12 of the injector system and tabulated in Table 7.4 along with mass flow rates through each unit. The (+) and (-) signs indicate the opposing directions of rotation added by each individual stage as per design. Finally at Location 1, air enters the combustion camber with a value of $S_w = 0.4$. The mass flow rate split across the three stages shows that majority of the flow passes through the radial swirler. Only 13% of the flow is diverted through the coaxial stages present in the vicinity of the liquid injection system. This split remains the same for the reacting case, although variations in the swirl number of the inner coaxial swirlers are observed due to the density variations caused by the reacting front across the planes considered.

Figure 7.13 shows an averaged axial velocity in the mid plane for the reacting cases along with the contours of $u_x = 0$. Again a classical swirling flow with the CRZ penetrating inside the injector and ORZ is observed. An iso-contour of the Heat Release (HR) $= 1 \times 10^8\,\mathrm{Jm^{-3}s^{-1}}$ is superimposed to represent the turbulent flame brush, which is coloured by the local gas phase temperature. For this visualisation, the flame exhibits a classical V shape whose root is anchored inside the injector by the CRZ. The lower part of the reactive zone at 450 K indicates that the combustion reactions take place with

the fresh incoming air and evaporated fuel. The high temperatures, $> 1500\,\mathrm{K}$, in the upper regions correspond to the recirculation zone, where reactions are driven by the hot gases and excess of fuel vapour.

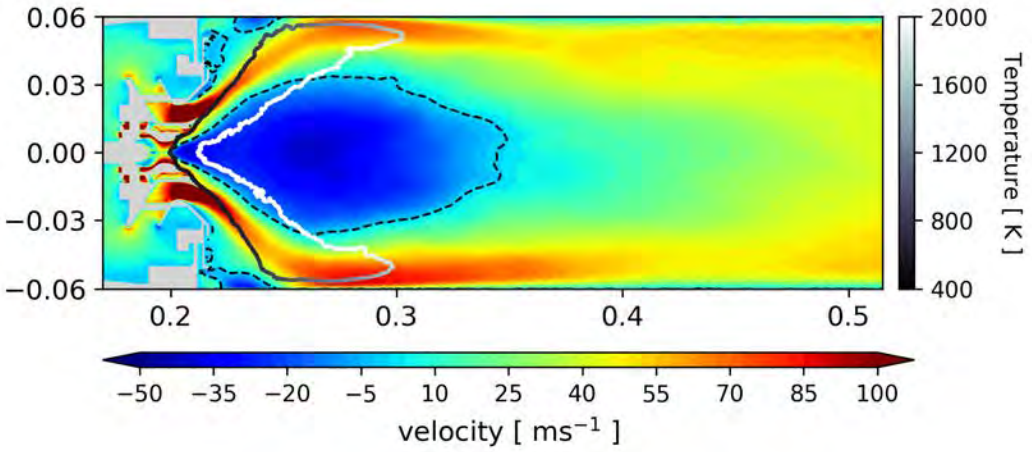

Figure 7.13: Major flow features observed in the reactive case (dashed lines: iso contours of 0 axial velocity, solid line: iso contour of heat release$= 1 \times 10^8\,\mathrm{Jm^{-3}s^{-1}}$ coloured by gas temperature).

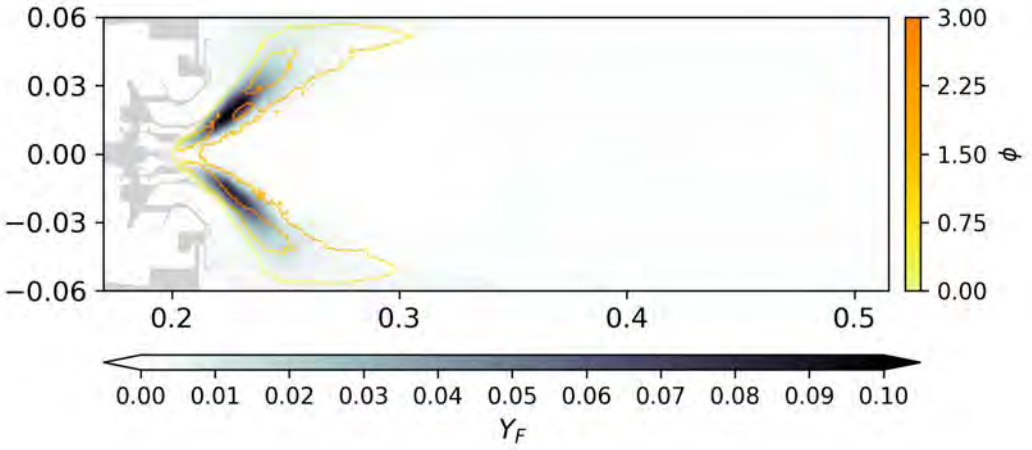

Figure 7.14: Averaged mass faction of fuel in the domain (solid lines: iso contour of heat release$= 1 \times 10^8\,\mathrm{Jm^{-3}s^{-1}}$(inner) and $5 \times 10^8\,\mathrm{Jm^{-3}s^{-1}}$ (outer) coloured by ϕ_{gas}).

Looking at the mean fuel concentration in Figure 7.14, a region of high fuel accumulation is evident near the exit of the injection system in the combustion chamber. Around this region the outer and inner contour lines of HR$=1 \times 10^8\,\mathrm{Jm^{-3}s^{-1}}$ and HR$=5 \times 10^8\,\mathrm{Jm^{-3}s^{-1}}$ respectively are added and

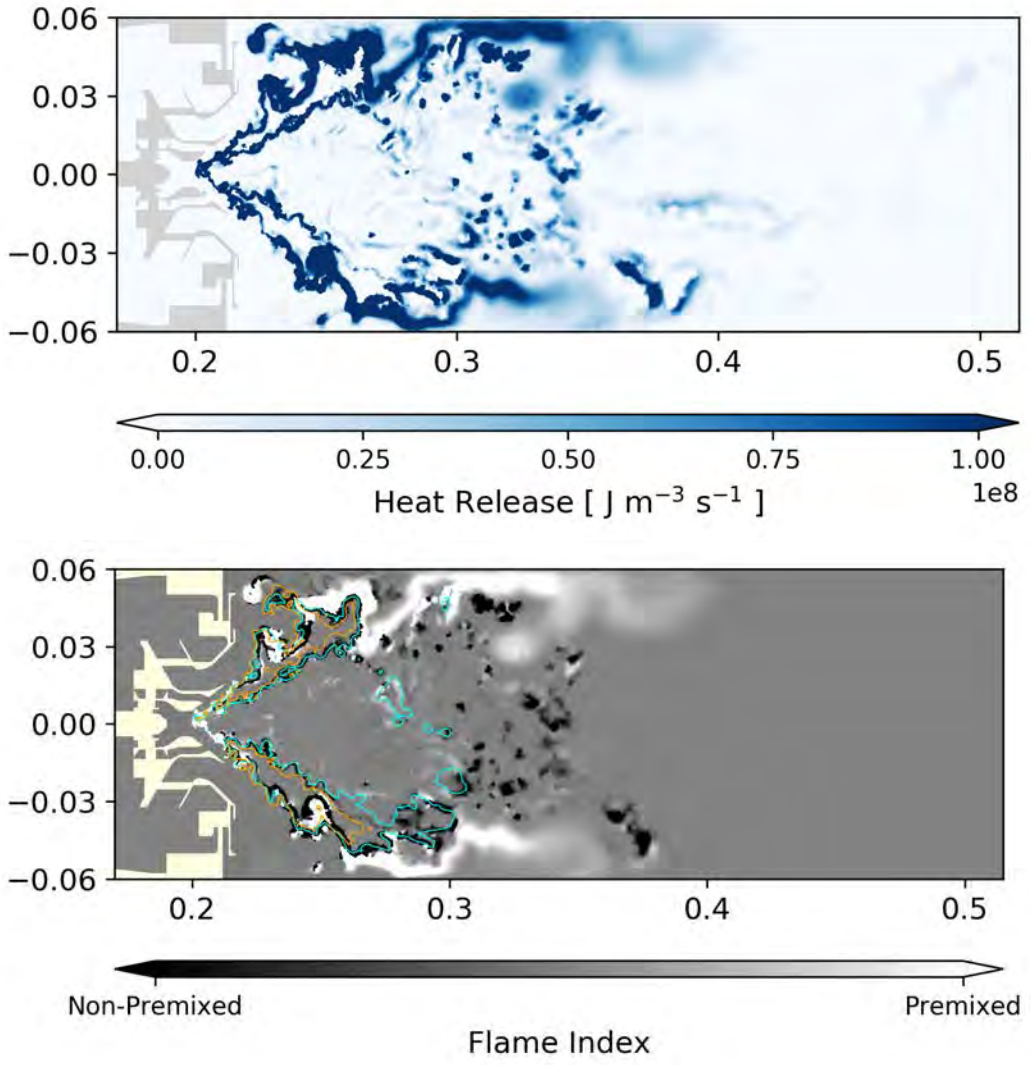

Figure 7.15: Instantaneous field of heat release (top) and Flame index (bottom) indicating combustion regimes (cyan line: iso contour of $\phi_{gas} = 1$; orange line: iso contour $Y_F = 0.02$).

coloured by the local ϕ_{gas}. Upon injection, evaporation produces sufficient vapour leading to an initial lean premixed zone where reactions occur at 450 K. Droplets that cross this first reacting front are then exposed to regions with high relative velocities and temperatures (CRZ) which accelerate the vapourisation process leading to the rich zone of vapour. This resulting region burns above stoichiometric conditions when encountering the oxygen depleted air brought back by the CRZ. The temperature of this inner flame branch is thus higher than the outer one as observed previously.

To investigate the nature of the combustion regimes, an instantaneous

Flame Index (FI) is calculated using the normalised Takeno Index (Eq. (2.57)) and conditioned by the heat release rate ($> \ 1 \times 10^8\,\mathrm{Jm^{-3}s^{-1}}$). Opposing gradients leading to FI = -1 are an indication of non-premixed flames while premixed zones correspond to FI = 1. The majority of the reactions take place in the premixed mode which is standard for lean operation of combustors. Just attached to the main premixed flame in the lower branch however a non premixed zone can be observed. Large fuel droplets which cross and evaporate after the initial premixed zone region create this front. Note also that in the regions where high fuel vapour accumulation takes place and stoichiometric conditions exist a purely diffusion zone is observed (overlapping cyan, orange lines). This zone does not however have classical features i.e. no unity mass fractions present on both sides of the reaction zone. Finally, a large premixed flame front close to the chamber walls is evident further downstream, due to the mixing upstream between the accumulated fuel vapour as a result of the fast evaporation of droplets that have impacted the wall and the incoming fresh gases.

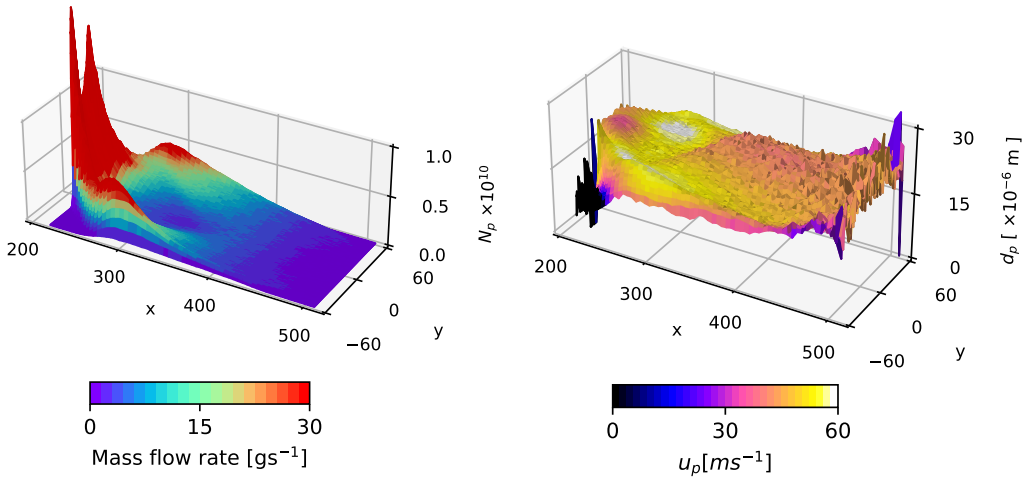

(a) Number of particles (N_p).

(b) Particle diameters (d_p.)

Figure 7.16: Particle statistics for the steady state case.

Basic statistics of the liquid phase can be extracted using particle solution fields sampled at a rate of 2 kHz on the basis of which tracking the number of particles that cross specific analysis planes present in the combustion chamber is possible. In Figure 7.16, the large number of particles at the entrance of the combustion chamber indicates that the narrow spray expands from the injection system when crossing across Location 1 (Figure 7.12). Two regions of high particle concentrations are also found along the chamber walls at an approximate axial distance of $x = 300\,\mathrm{mm}$. This accumulation of particles

is also associated with larger high velocity droplets impacting the walls as clearly seen in Figure 7.16b.

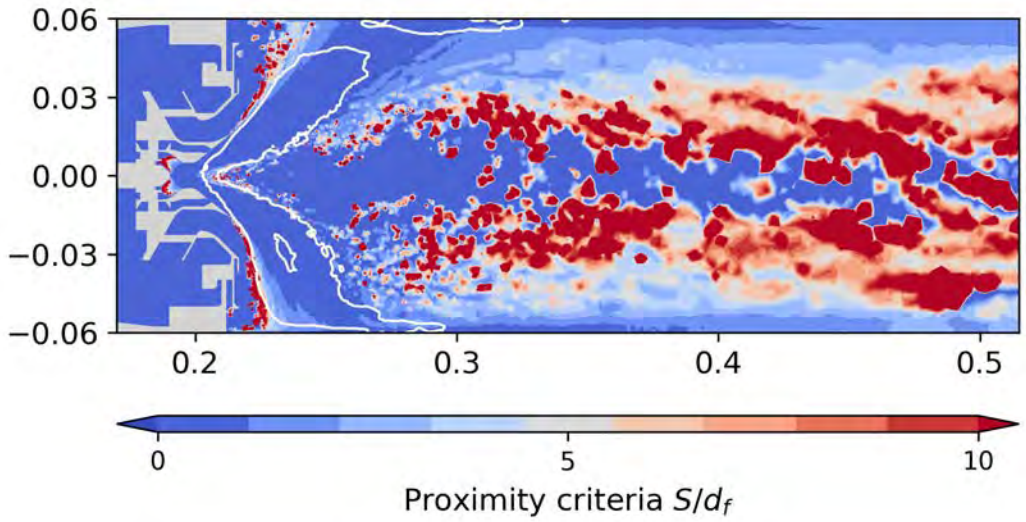

Figure 7.17: Proximity criteria to identify possible regions of isolated droplet combustion. White iso-contours are the turbulent flame brush corresponding to a HRR $= 1 \times 10^8\,\mathrm{Jm^{-3}s^{-1}}$.

Post the main flame zone at an axial position of $x = 400\,\mathrm{mm}$, large droplets are seen to still exist in the domain. This number of remaining droplets is however 2 orders of magnitude lower than the number injected and entering the domain, indicating a small amount of liquid fuel exits the domain. Using the liquid volume fraction α_l and the droplet diameter d_p, the inter droplet distance S can be approximated by [131]:

$$S = d_p \left(\frac{\pi}{6\alpha_l} \right)^{\frac{1}{3}}. \tag{7.4}$$

For a isolated burning liquid fuel droplet, the diameter of the reactive zone surrounding d_f is given by [236]:

$$d_f = d_p \left[1 - \frac{\ln\left(1 - Y_F^{surf}\right)}{\ln\left(1 + \nu Y_O^{\infty}\right)} \right]. \tag{7.5}$$

In regions where $d_f > S$, the single droplet combustion is not achievable. However, in regions where $S/d_f > 1$ there is a possibility for isolated droplet combustion. In this regime the flame surrounding an individual fuel particle is sustained by the evaporated fuel diffusing towards the reactive zone while

the excess oxygen from the burnt gases come from the opposite direction. The proximity criteria S/d_f for the LOTAR configuration is plotted in Figure 7.17. Results indicate a possibility of single droplet combustion the in downstream regions post the main flame zone. It is to be noted however that in these simulations a model specifically dedicated to the single droplet combustion (as developed by Paulhiac [237]) has not been utilised, but the necessity of such modelling for accurate large scale combustion is here highlighted [103].

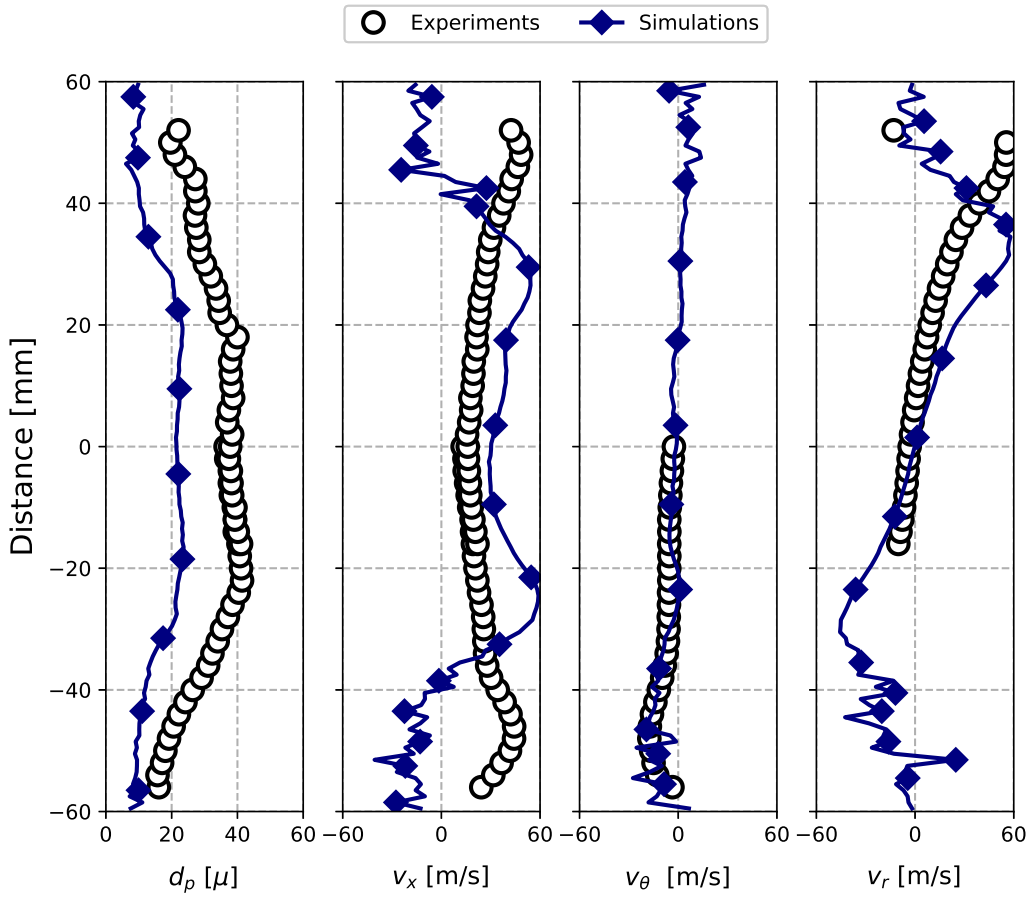

Figure 7.18: Experimental liquid phase statistics.

Finally, a post priori comparison is made of the droplet statistics obtained experimentally and from the simulations in Figure 7.18. Data was made available for an operating condition with $\dot{m}_{liq} = 3.08\,\mathrm{g/s}$ through the pilot injector only, which is different to the ones targeted in this work (in terms of the liquid mass flow rate only). The aim of this comparison is hence to verify overall global trends of the liquid phase statistics.

In the experimental data since a lower mass flow rate passes through the same atomizer larger droplet sizes are expected due to a reduced relative

velocity of the injected liquid and the surrounding gases. This difference between the diameters is evident with the largest droplet size variation upto 20 μm seen in Figure 7.18. This difference in diameters should also lead to a varying spread of the spray as it enters the chamber. Larger droplets of the experiments follow a ballistic trajectory while the injected PDF in the simulations with smaller droplets quickly relax to the gas velocity resulting in a narrower opening angle. This phenomenon also observable in Figure 7.18, where the maximum axial velocities are of the same order, but the simulation show a much narrower spray opening closer to the gas axial velocities shown earlier in Figure 7.10.

Further, since the experimental liquid phase data was carried out in reactive conditions, the difference in overall operating points along with the other uncertainties require further review of the droplet statistics. This comparison only serves as a satisfactory reasoning to validate the liquid phase models with data that was made available deep into the simulation campaign. Regardless it is to be noted that since only the pilot injector is used in both cases, the overall characteristics of the flame in terms of positioning, shape, structure and combustion regimes should hold irrespective of the slight variations in liquid injection parameters.

7.5 Conclusions

The LOTAR experimental setup has been chosen as a test case due to its proximity with a realistic gas turbine combustion camber. The simulation strategy consisted of discretising the plenum and chamber with tetrahedral elements and using appropriate boundary conditions to handle the heat transfer at the walls. The setup initially has been validated against experimental data gathered across two planes which show an asymmetry introduced by the liquid fuel inlet in the plenum. The liquid phase models compared with a slightly different set of experimental data reveal the expected differences arising due to droplet sizes differences. Reactive simulations done using a global two step chemistry shows the flame stabilised by the recirculation zone, a classical result for such swirled flames. The combustion is mostly premixed, however non-premised regions exist due to accumulation of fuel vapour above the injection system. Further downstream, the possibility for isolated droplet combustion regimes was established by comparing the inter-droplet distance and the diameter of a flame around a single droplet. The present approach show the ability to capture such features in a complex configuration while also highlighting the need for specialised models needed to handle such regimes.

Chapter 8

LOTAR - multicomponent spray flames

The results discussed in this chapter have been submitted to the 39th International Symposium on Combustion and is currently under review.

Contents

8.1 Introduction

Multicomponent spray flame simulations have until now been limited to small laboratory scale burners [191]. As a step forward, the LES of the previously introduced LOTAR setup is performed using a Lagrangian DMC model for the liquid phase coupled to an ARC scheme to handle the gas phase reactions. Furthermore, two complex fuel descriptions are addressed: first being one the standard jet fuel surrogate (Jet-A1) and second an alternative jet fuel (At-J) introduced in Chapter 4. The feasibility of using LES for such complex cases is demonstrated and insights on the flame structures obtained using the multicomponent model are highlighted in the chapter.

8.2 Setup - validity of the chemistry, evaporation models and composition

The setup in terms of mesh, boundary conditions and injection parameters remain the same as described in Chapter 7. Once a stabilised flame with the two step chemistry is obtained, an instantaneous gas and particle solution is chosen to transition to the multicomponent simulations. Gas phase interpolation is done using multiple canonical one-dimensional laminar flame solutions. For the spray, temperature of the particles is used to interpolate the composition using reference single droplet evaporation cases. The generic flame sensor and chemistry integration introduced earlier are used and the flame is thickened over five mesh points. The entire flame front detected is thickened assuming a premixed combustion regime.

8.2.1 Applicability of ARC schemes

The preferential evaporation can cause a variation of composition throughout the domain. The ARC needs to handle the multiple possibilities that arise apart from the reference composition used for the reduction. Ternary plots of the flame speeds (s_l^0) at $\phi_{gas} = 1.0$ and $T = 450\,\mathrm{K}$ is shown for a complete composition matrix in Figure 8.1. For JetA-1 regions with larger concentration of NC12H26 show higher flame speeds, while the less reactive XYLENE rich regions have the lower propagation speeds. In case of At-J, minimal variation of the laminar flame speed across the composition matrix is observed.

Similar to the laminar flame speed, the auto ignition delay time (τ_{ign}) are shown in Figure 8.2 across possible compositions. For both fuels, the variation of τ_{ign} shows similar trends to the ones observed for laminar flame speeds. The validity over a wide composition ensures it can be used with confidence in realistic simulations where such compositional differences exist throughout the domain due to preferential evaporation.

8.2.2 Validation of the liquid composition

The liquid composition of JetA-1 and At-J have been compared against experimental data from Stöhr et al. [199]. The experiments were done using freely-falling droplets in a hot gaseous environment produced using a methane-air flame. The time evolution of the droplet diameter and the vapour fluxes for both fuels are compared in Figure 8.3 and Figure 8.4. Both cases show good agreement with the experimental data. The expansion of the droplet resulting form the initial heating is not captured in the model because of the constant density assumption, after which the evaporation rates are accurately

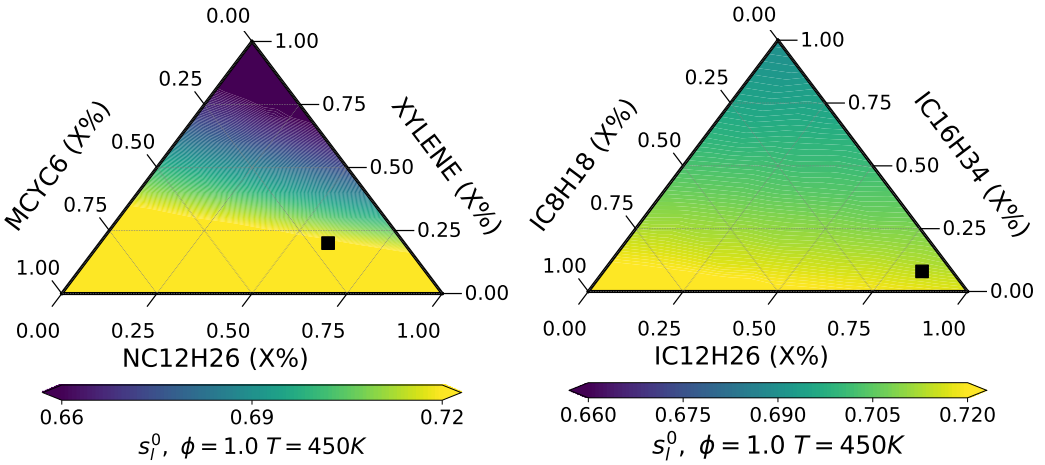

(a) JetA-1. **(b)** At-J.

Figure 8.1: Variation of the laminar flame speed (s_l^0) for a complete composition matrix at stoichiometry. Black square is the liquid composition.

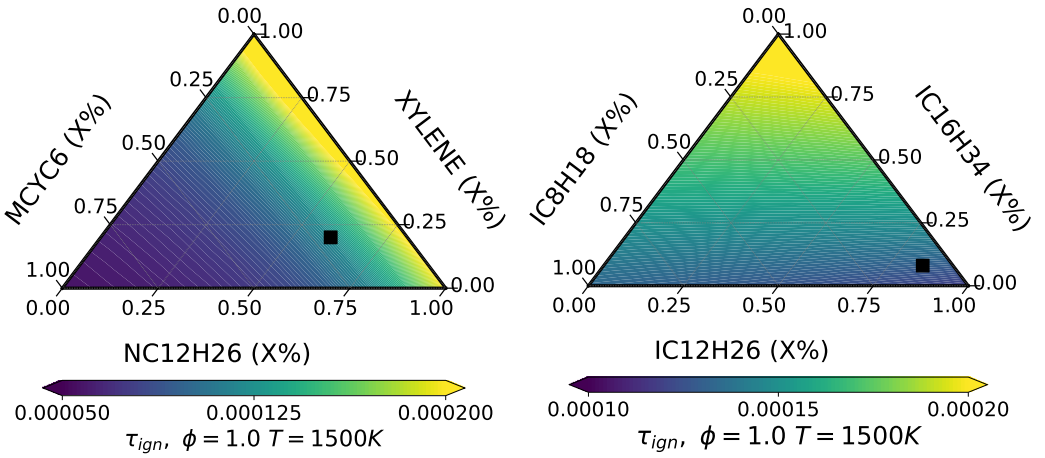

(a) JetA-1. **(b)** At-J.

Figure 8.2: Variation of the ignition delay time (τ_{ign}) for a complete composition matrix at stoichiometry. Black square is the liquid composition.

reproduced. Though JetA-1 is lighter in comparison to At-J, a negative correlation of the mean liquid molar mass and the evaporation rate is observed in Figure 8.3, with At-J evaporating faster than JetA-1.

In addition to the different evaporation rates, the evolution of the vapour flux composition also show completely different behaviours. This is due to the varying concentrations of liquid species present in each fuel. Since At-J has a single dominant species IC12H26 (X = 84 %), its effect on the vapour composition is clearly reflected, with contribution from the volatile IC8H18

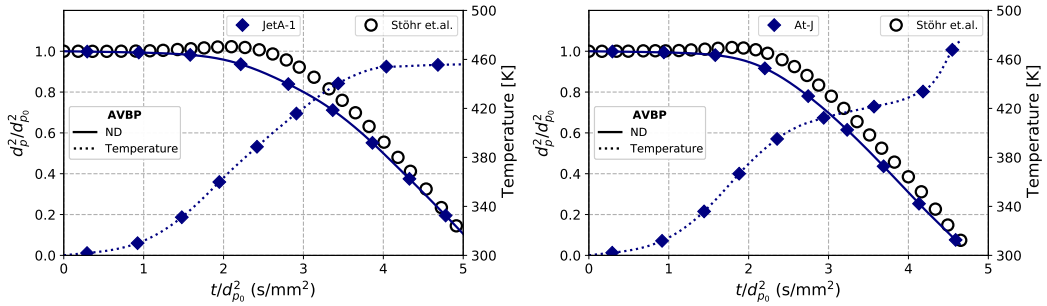

Figure 8.3: Time evolution of the normalized diameter: comparison of JetA-1 (left) and At-J (right).

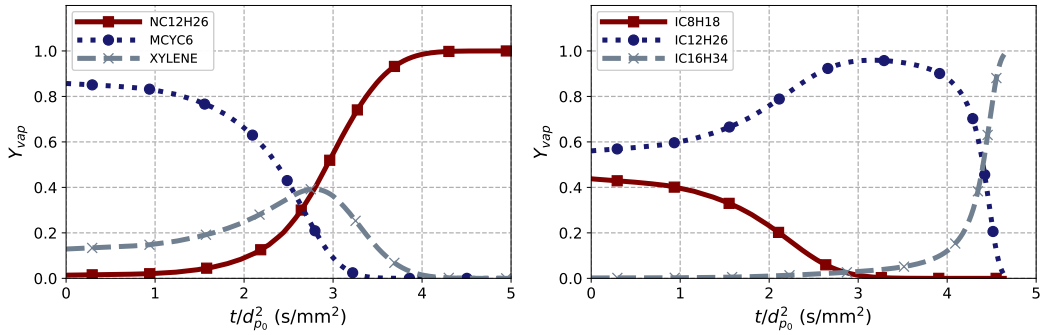

Figure 8.4: Time evolution of vapour composition for JetA-1 (left) and At-J (right).

only present in the initial stages (Figure 8.4, right) and negligible contribution from the heavy IC16H34 until close to the end. In the vapour flux composition of JetA-1 (Figure 8.4, left) two stages can be identified: the first quarter of the droplet lifetime where the volatile MCYC6 dominates and the final half consisting only of NC12H26.

8.3 Global evaporation, heat release trends

The differences in composition have a significant effect on the overall evaporation zones of the two fuels in the LOTAR configuration, leading to different flame structures and regimes. In Figure 8.5 and Figure 8.6 , the evaporation fluxes in the mid-plane averaged over 6 ms is shown for both the multicomponent fuels. Additionally, averaged evaporation rates along the length of the chamber showing contributions of individual fuel components are also plotted.

JetA-1 having a longer vapourisation timescale evaporates with a peak observed in the region around $x = 0.22\,\mathrm{m} - 0.24\,\mathrm{m}$ and a weaker zone beyond in the burnt gases. NC12H26 being the heaviest component which remains in the

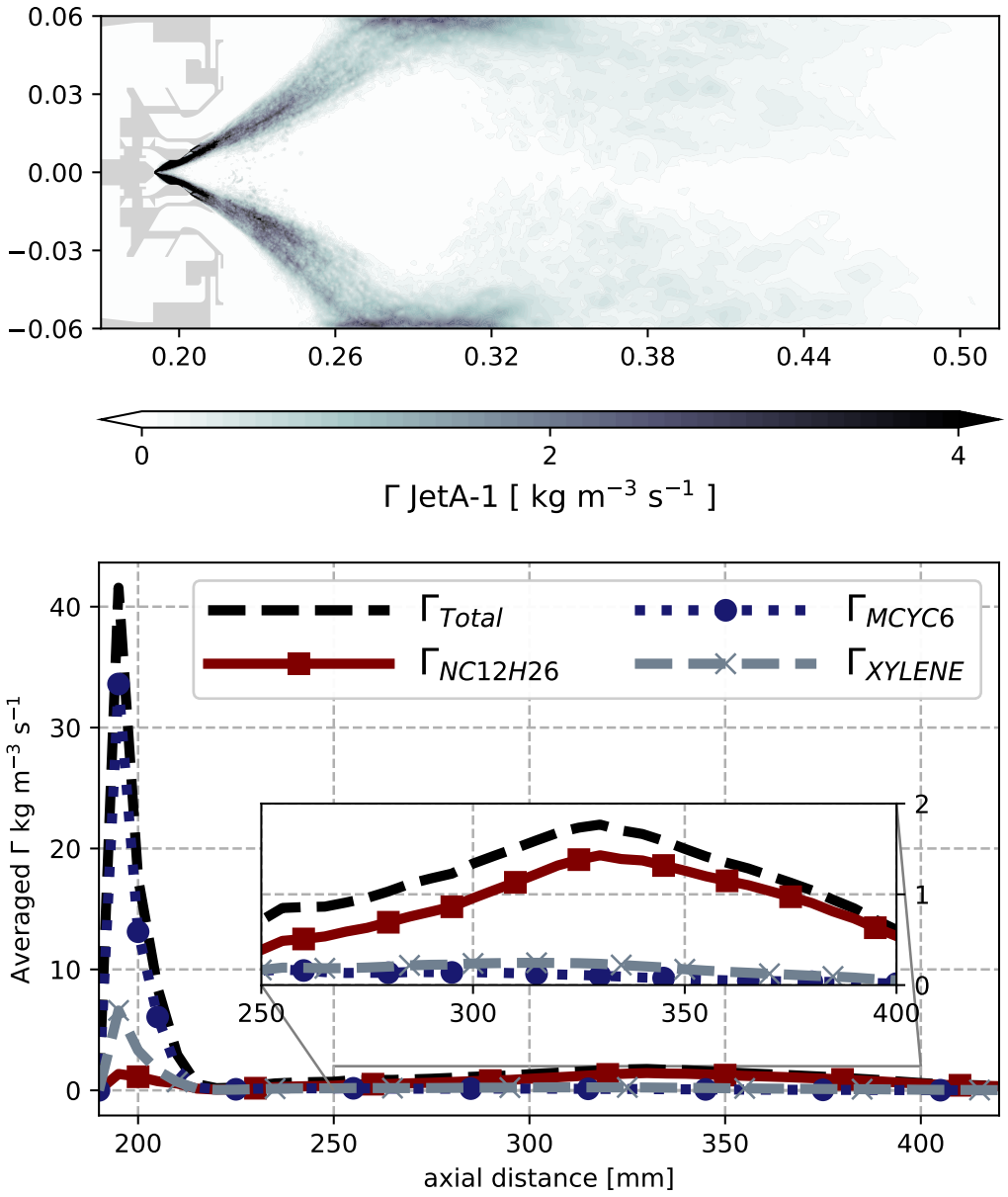

Figure 8.5: Time averaged evaporation rate of JetA-1 in the mid-plane.

liquid fuel contributes completely to the total evaporation in this downstream region. At-J with a shorter vapourisation time scale completely evaporates over a shorter distance with negligible evaporation rate beyond $x = 0.24\,\mathrm{m}$. The dominant species iC12H26 closely follows the complete evaporation trends across the chamber. Large droplets do not reach the downstream observed in the previous case of JetA-1.

In comparison to single droplet profiles, evaporation in complex turbulent

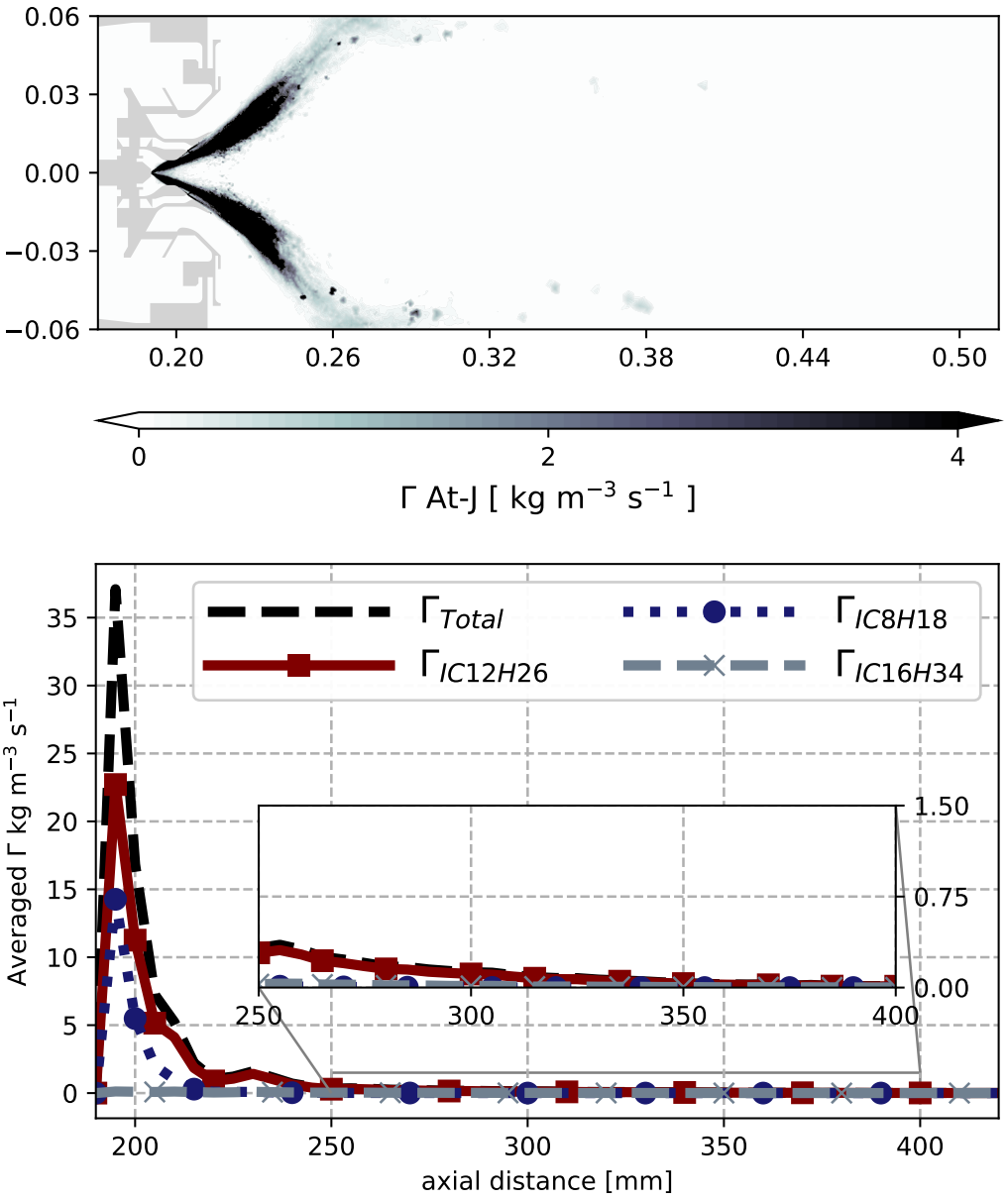

Figure 8.6: Time averaged evaporation rate of At-J in the mid-plane.

environments is impacted by other factors such as:

1. saturation of fuel vapors inhibiting further evaporation
2. distribution of droplet diameters leading to large range of evaporation time scales
3. temperature gradient which may accelerate evaporation rates
4. the use of TP-TFLES which alters the evaporation rates according to

the local thickening applied to the reactive regions detected by the sensor

The time-averaged heat release rate fields for JetA-1 and At-J are shown in Figure 8.7 and Figure 8.8 respectively. The swirl induced on the incoming flow results in the formation of a large Central Recirculation Zone (CRZ) containing hot combustion products. This CRZ serves the dual purpose of both stabilizing the flame and promoting quick evaporation and mixing of the injected liquid fuel to sustain the flame. The CRZ is marked by the black dashed lines corresponding to $u_x = 0$ on both figures (on averaged profiles only). The flame base for both cases lies inside the injector bowl at $x = 0.2\,\mathrm{m}$ along the marked CRZ highlighting this stabilizing mechanism.

Also plotted are the cross sectional averaged consumption rates of the individual liquid fuel components along the domain. Both fuels show two regions with heat release rate peaks. The first peak occurring between $x = 0.200\,\mathrm{m}$ and $x = 0.225\,\mathrm{m}$ is due the reactions occurring in the injector bowl where the flame stabilisation and initialisation occurs. For JetA-1 this peak corresponds with a large peak in the consumption of MCYC6. For At-J the initial increase in heat release is associated with the evaporation of IC12H26, the dominant fuel component.

Further downstream the heat release patterns for the fuels show a considerable change. As seen previously a significant evaporation of JetA-1 continues further in the domain. The evaporation, consumption and heat release follow each other indicating a distributed combustion of the heavier NC12H26. For At-J, the secondary heat release peak follows the consumption of IC12H26, and indicates a complete combustion of fuel before the exit.

8.4 Flame structures for JetA-1

Instantaneous snapshots of heat release visualised in Figure 8.9 clearly mark separate features where fuel is consumed. **Region I**, extending from the flame base in the injector bowl into the chamber is a continuous reactive zone, where the evaporated components mix with the incoming air and are consumed. A part of this continuous reaction zone is dominated by MCYC6 in the injector and NC12H26 in the combustion chamber.

A visual representation is shown by plotting the evaporation and consumption of MCYC6 in Figure 8.10. High vapourisation rates inside the injector (Figure 8.5) correspond mainly to the preferential release of MCYC6 vapour. The weaker evaporation zone of MCYC6 observed inside the chamber is due to the larger droplets and enhanced evaporation in the unsaturated regions further downstream. This MCYC6 vapour mixes with the fresh incoming

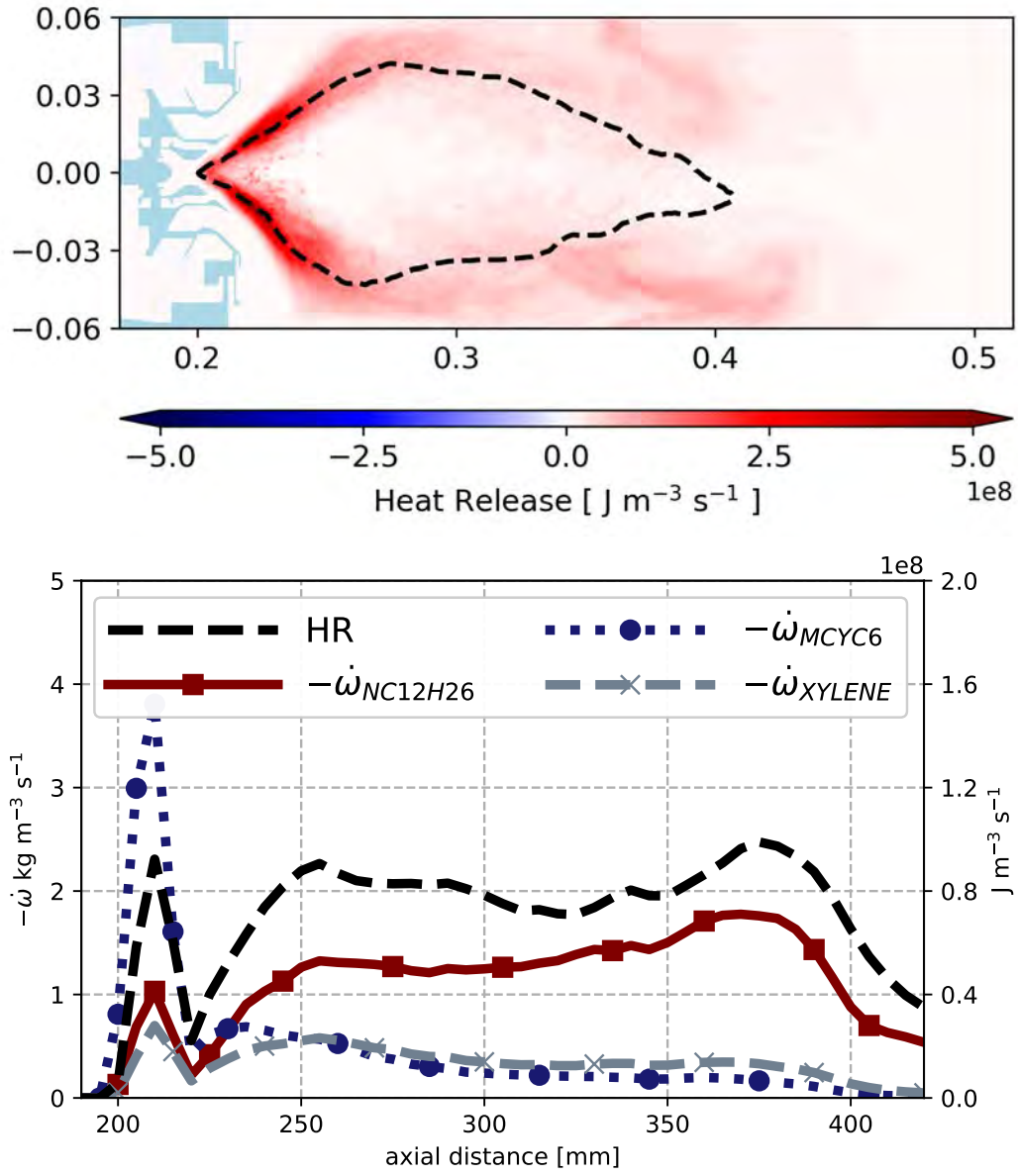

Figure 8.7: Time averaged heat release rate field in the mid-plane (top) and cross sectional averaged consumption rates along the domain for JetA-1.

gases and its consumption region (Figure 8.10, right) overlaps with the high heat release rate region observed in Figure 8.7, indicating the role of volatile components in flame stabilization. NC12H26 vapour are released in the latter stages of the droplet lifetime as seen in Figure 8.11. This leads to an extended consumption zone extending through the domain.

A wide turbulent flame brush with two regions of fuel combustion can be observed, delineated approximately by the recirculation zone. The inner zone

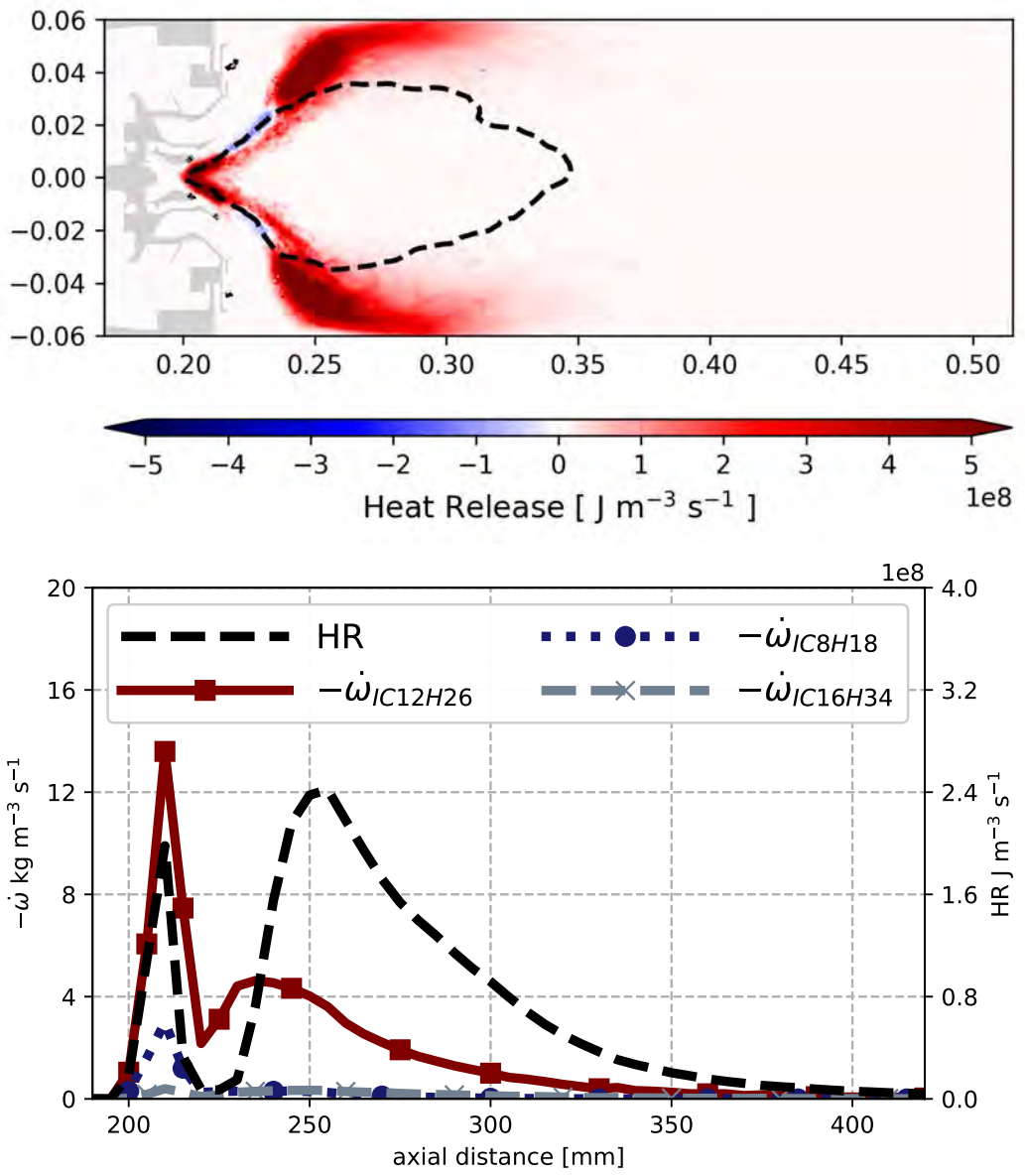

Figure 8.8: Time averaged heat release rate field in the mid-plane (top) and cross sectional averaged consumption rates along the domain for At-J.

is marked as **Region II**. Large droplets with ballistic trajectories cross this reactive **Region I** and enter the CRZ. These are visualised as scatter plots of the droplet axial velocities and the gas velocities projected at the particle locations in Figure 8.12. The droplets that cross the **Region I** and enter the recirculation zone are associated with regions of negative axial gas velocity and high temperature as marked by the blue dashed ellipse. The high relative velocity and high temperature promotes rapid evaporation of these droplets.

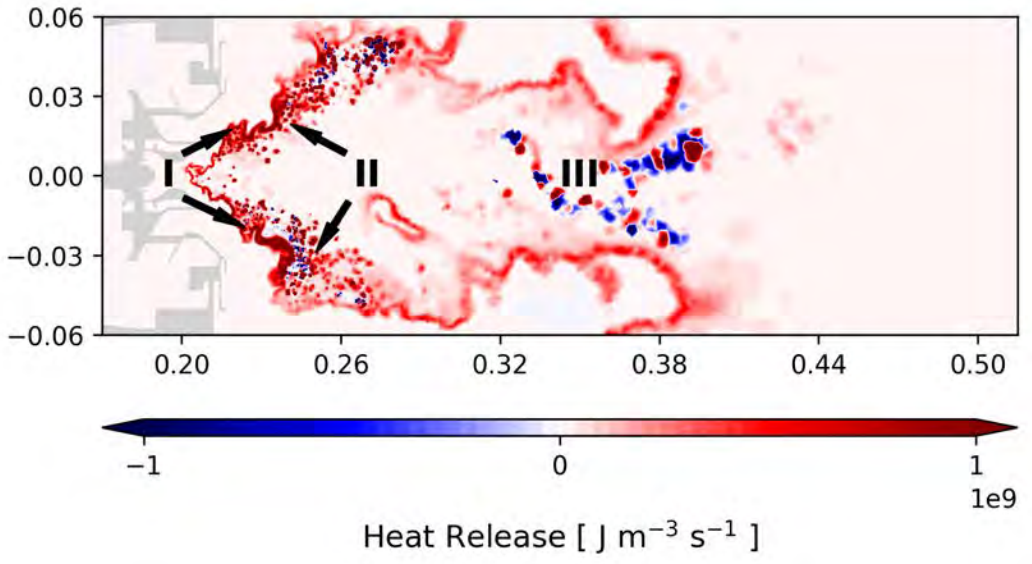

Figure 8.9: Instantaneous heat release rate field in the mid-plane for JetA-1.

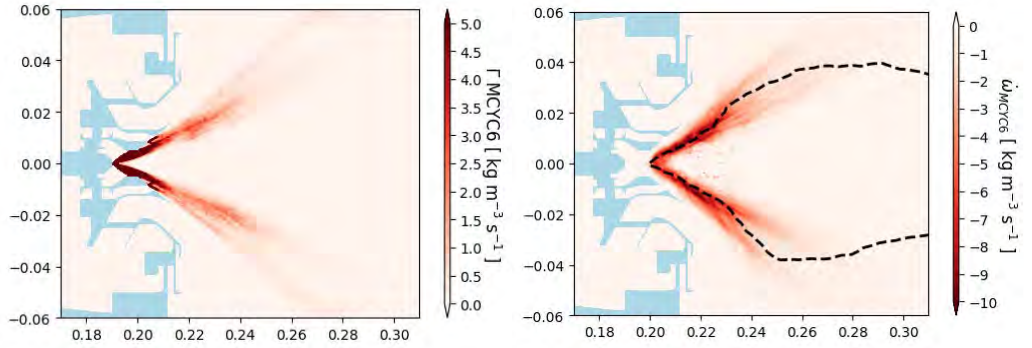

Figure 8.10: Time averaged evaporation and consumption zones of MCYC6, the most volatile component of JetA-1 indicating flame stabilization mechanisms.

This quick phase change leads to rapid consumption and heat release which appear as the discrete spots in **Region II**.

Further downstream, a large impact of the spray and chamber walls is seen around the region $x = 0.3\,\mathrm{m}$. At this point, the smaller droplets in the final stages of evaporation containing mainly NC12H26 and larger ballistic droplets with more than one component find themselves in a mixture of fresh and burnt gases. This manifests as a complex reaction zone with an extension of **Region I** and the possibility for droplets to burn individually or as clusters. This complex downstream region is marked as **Region III** and is well captured by the present approach. Such behaviour was already observed in [103]. Since

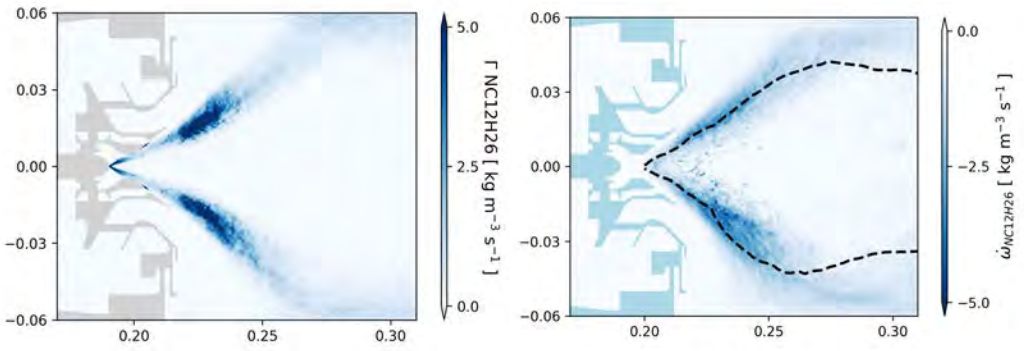

Figure 8.11: Time averaged evaporation and consumption zones of NC12H26, the dominant component of JetA-1 indicating flame stabilization mechanisms.

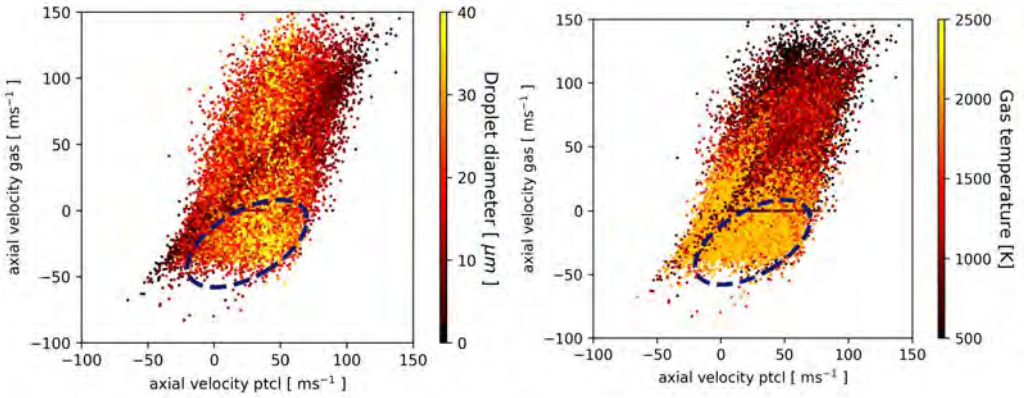

Figure 8.12: Scatter plot of droplet and gas axial velocities at droplet positions coloured by droplet diamter (left) and gas temperature at droplet position (right).

the evaporation zone is extending towards the combustor exit and the vapour flux is mainly consisting of the large NC12H26, it leads to the possibility of incomplete combustion.

The various regimes of combustion can be identified using the Takeno Index. The presence of three main fuel components and various smaller fuel molecules due to pyrolysis necessitates an altered definition of Eq. (2.57) [97]. For multicomponent cases, Takeno is reconstructed using the three individual fuel components and used for post priori analysis as:

$$\begin{aligned} Y_F &= Y_{NC12H26} + Y_{MCYC6} + Y_{XYLENE}. \\ Y_{Ox} &= Y_{O2} + Y_O. \end{aligned} \tag{8.1}$$

The flame structure in terms of the ZT space coloured by the new definition

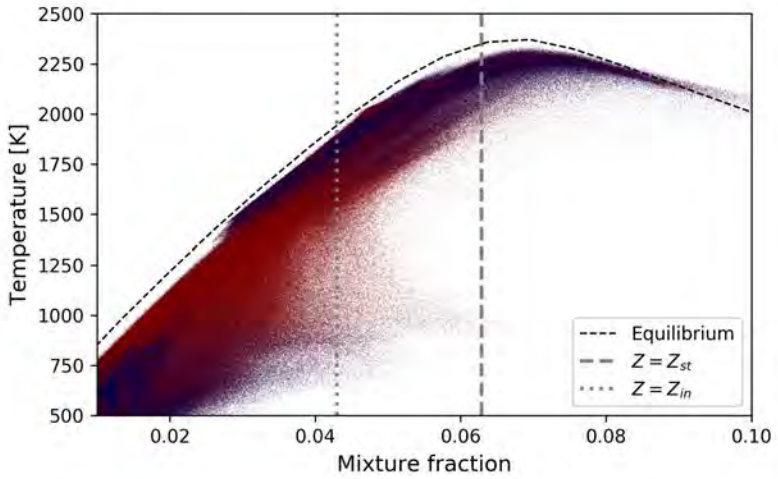

Figure 8.13: Scatter plot for JetA-1 flame in the mixture fraction, temperature. Blue and red points indicate a Takeno(Eq. (8.1), Eq. (2.57)) of -1 and +1 respectively.

of Takeno is plotted in Figure 8.13. The infinitely fast chemistry limit obtained by CANTERA equilibrium calculations is shown by the black dashed curve. The boundary of all scattered points lie very close but below this adiabatic limit indicating the effects of heat losses and evaporation. The significant scattering of the points indicate complex reaction regimes existing due to flow, vapourisation and dilution. The dominance of premixed points in the temperature range of 1000 K-1500 K correspond to the main flame **Region I**.

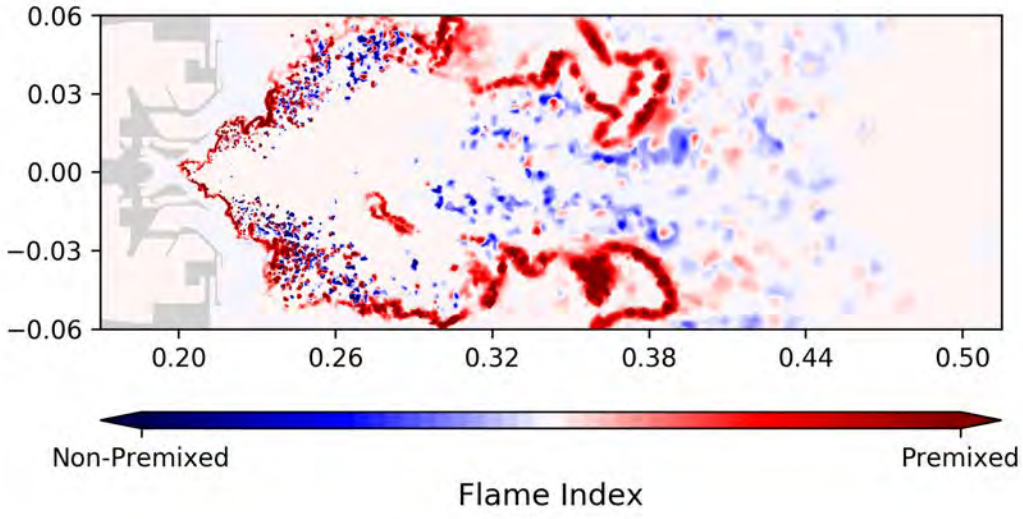

Figure 8.14: Flame Index for JetA-1.

Another characterisation to see individual flame regimes it to use the consumption of NC12H26 as the reference. This make sense because it is the dominant component in the liquid fuel and its presence throughout the reactive zone from point of injection to the downstream regions was seen previously. The Flame index constructed using $\dot{\omega}_{NC12H26}$ and the Takeno is plotted in Figure 8.14. The **Region I** is seen as a premixed region, where the highly turbulent flow from the radial swirlers enhance the mixing resulting in a wrinkled flame.

In **Region II** and **Region III**, where droplet clusters are more probable to burn as individual particles or small localised clusters, non premixed combustion modes are more prominent. Such behaviours was also observed in the multicomponent simulations by Eckel et al. [191] using a similar fuel composition. However, in their work, this localised combustion regime was not observed in the CRZ as here but closer to the chamber walls with high temperature gases.

8.5 Flame structures for At-J

An instantaneous snapshot of the heat release identifying three distinct zones is shown in Figure 8.15. **Region I** is the flame base inside the injector bowl, where the premixed combustion of the volatile species with the incoming air initiates the flame. This is similar to one observed for JetA-1 (Figure 8.10, bottom), however along with IC8H18 (most volatile), the dominant IC12H26 plays a role in flame stabilization (consumption rates not shown).

A Takeno index is calculated with the three fuel components using Eq. (8.2). The Flame Index considering the majority component IC12H26 is shown in Figure 8.16 for an instantaneous solution along the mid plane of the combustor. The entire reaction zone can be characterised as a continuous premixed flame. Individual droplet combustion regions appearing as "spots" are insignificant compared to JetA-1, observed mainly in downstream regions where the occasional large droplet exists after with the chamber walls. The quick evaporation rate reduces the number of ballistic droplets that cross over into the recirculation zones.

$$\begin{aligned} Y_F &= Y_{IC12H26} + Y_{IC8H18} + Y_{IC16H34}. \\ Y_{Ox} &= Y_{O2} + Y_O. \end{aligned} \tag{8.2}$$

The evaporation zone ends by the point the spray reaches $x = 0.24\,\mathrm{m}$ and results in a pool fuel vapour just above the injector exit. This zone having discernible negative heat release is marked **Region II** and can be observed in both the instantaneous (Figure 8.8, top) and time-averaged fields

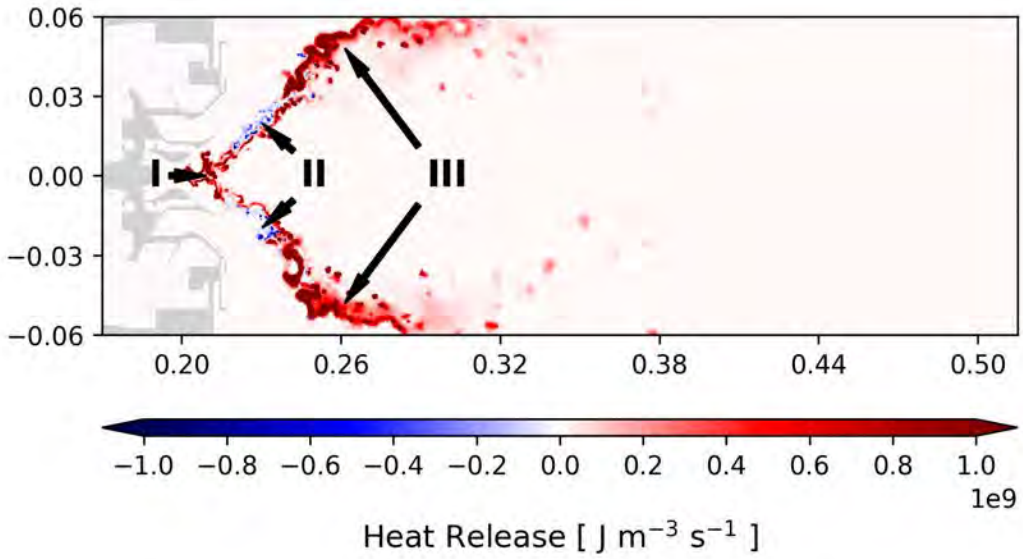

Figure 8.15: Instantaneous heat release rate field in the mid-plane for At-J.

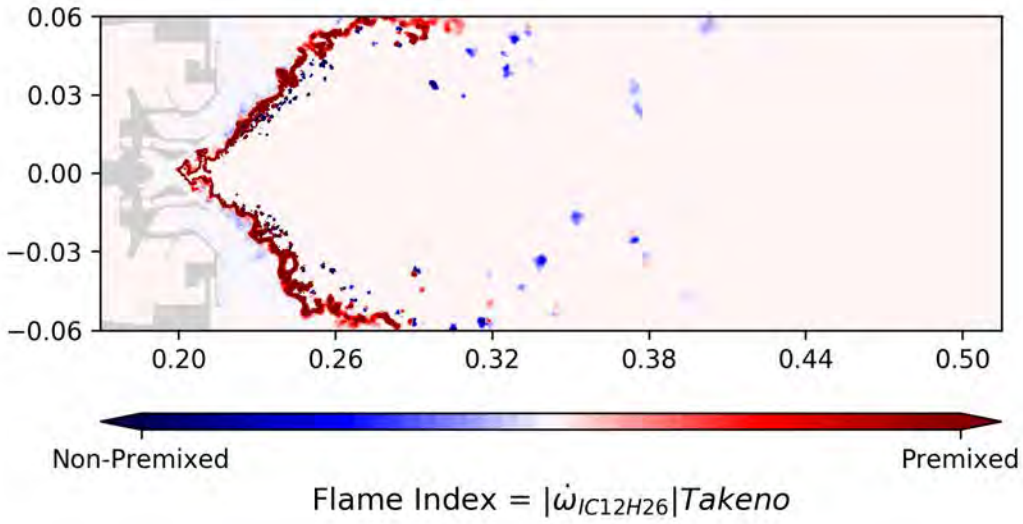

Figure 8.16: Flame Index for At-J.

(Figure 8.15). This is due to a combination of fast evaporation due to the high relative velocities and the hot gases in the CRZ. This pool of vapour comes in contact with the hot recirculation gases and undergoes dissociation into smaller components.

Two such component as a result of the pyrolysis C_2H_2 and CH_4 are shown in Figure 8.17. In this region, some of these components react with rich recirculation zone as seen by a thin heat release region towards the recirculation

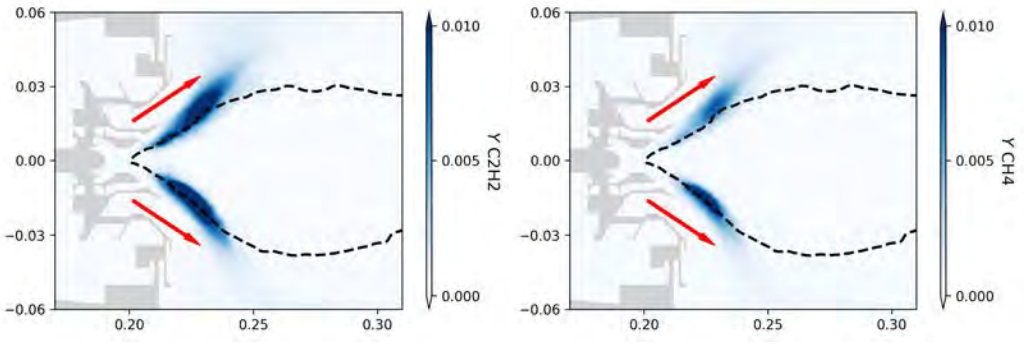

(a) Mass fraction of C_2H_2 **(b)** Mass fraction of CH_4

Figure 8.17: Time averaged mass fractions of the pyrolysed components.

zone. Also a non-premixed reaction zone is seen in Figure 8.16, towards the exit of the swirlers, which however is very insignificant.

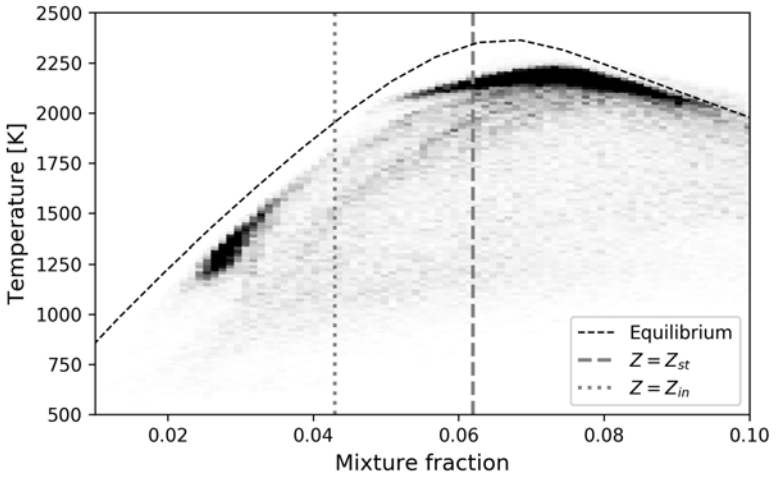

Figure 8.18: Scatter plot in the temperature- mixture fraction space for Region II of the At-J flame.

A probability map of **Region II** is shown in Figure 8.18 with the dark regions indicating higher probabilities. Dashed line are stoichiometric conditions and dotted line represents the global inlet conditions. It is very clear that increasing fuel concentration due to quick evaporation followed by its dissociation increases the local equivalence ratio leading to a rich reactive zone.

The incoming fresh gases from the radial swirlers under turbulent conditions promote quick mixing and ignition of the smaller pyrolysis components. This mixture ignites further downstream in **Region III** causing the sudden increase in the thickness and intensity of the heat release rate zone (Figure 8.8,

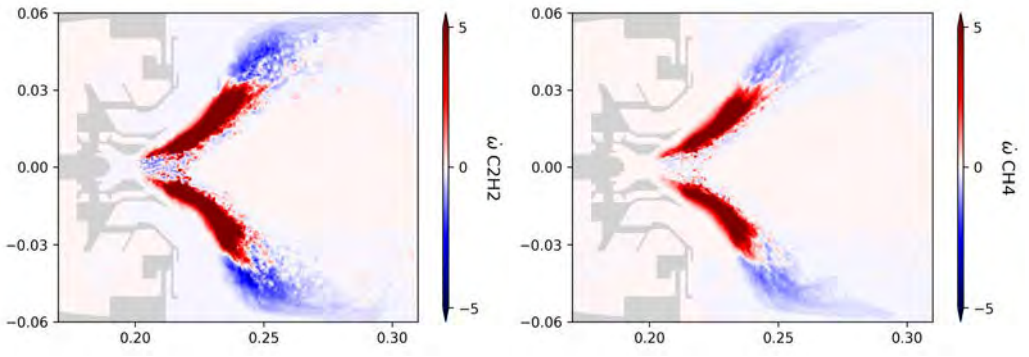

(a) Mass fraction of C_2H_2 **(b)** Mass fraction of CH_4

Figure 8.19: Time averaged reaction rates of the pyrolysed components.

bottom). The consumption rates of the same components C2H2 and CH4 can be seen Figure 8.19. The regions of productions (red) and consumption (blue) correspond with **Region II** and **Region III** respectively. Since little fuel evaporation is observed in this region, it corresponds to a premixed prevaporized combustion regime and is not directly affected by the liquid phase. The PDF scatter plot for this part shown in Figure 8.20 also indicate reactions on the leaner side.

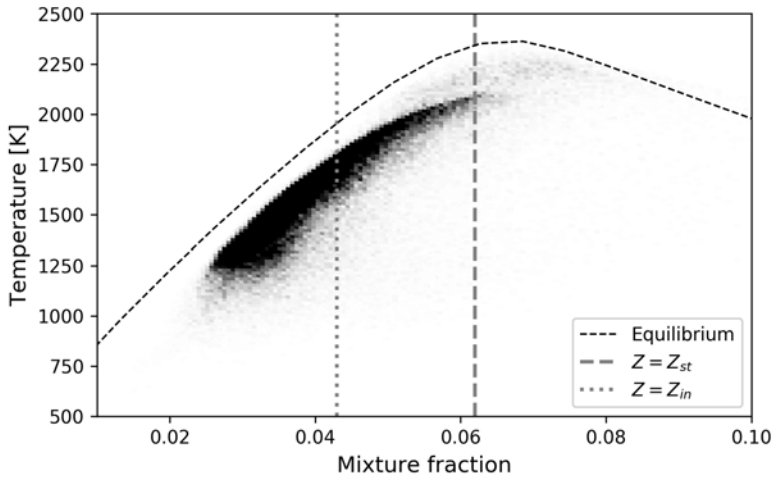

Figure 8.20: Scatter plot in the temperature- mixture fraction space for Region III of the At-J flame.

8.6 Conclusions

The large-scale realistic configuration LOTAR operated at ONERA was chosen as a simulation test case to understand the mechanism and structures of turbulent multicomponent spray flame combustion. Two fuels were chosen: first a multi-component representation of JetA-1 and secondly an alternative jet fuel At-J both of which were modelled using a discrete multi-component approach. The fuel compositions, evaporation models and chemistries introduced earlier were validated for a large range of possibilities encountered in such a configuration. The feasibility of coupling the multi-component spray evaporation model with ARC in large scale configuration has been established.

These differences in the two fuels lead to an extended evaporation zone for JetA-1 inside the combustor and a significantly shorter evaporation zone for At-J. The volatile components for both fuels evaporate immediately after injection and help in stabilising the flame by initiating the reactions.

The JetA-1 flame showed structures consisting of **Region I**, a main flame front and the existence of discrete spots of heat release due to quick evaporation and consumption in **Region II**. A more complex **Region III** consisted of mixture multiple reaction zones with varying levels of premixing and single droplet combustion. The evaporation region of JetA-1 extends towards the rich downstream of the chamber leading to possibility of unburnt hydrocarbons exiting the domain.

In case of At-J, three flame regions were observed. In **Region II**, the evaporated fuel breaks down into smaller components indicated by a negative heat release. The pyrolysis products mix with the incoming air from the radial swirlers leading to a sudden and intense heat release in **Region III**. This downstream region which accounts for the maximum heat release due to the lean premixed reactions is independent of the liquid phase.

Chapter 9

Forced simulations of LOTAR - global chemistry

Contents

9.1 Introduction

The majority of combustion instability research produced focuses on experiments and simulations of systems powered by gaseous fuels. Spray flame instabilities are known to be different due to the dispersed liquid phase. A detailed study on the self sustained oscillations of a kerosene spray flame in a laboratory swirl burner was first reported by de la Cruz García et al. [238]. Two operating points with the same global equivalence ratio $\phi = 0.75$ but different air/fuel mass flow rates exhibited two distinct instability modes. These were mainly observed due to the spray penetration and vapourisation effects. In other studies, for the same instability mode, the presence of liquid droplets resulted in larger oscillation amplitudes as compared to a gaseous/pre-vapourised premixed flame [239].

LES of spray flame instabilities is a recent and evolving research topic. Kitano et al. [240], Pillai et al. [241] used a classical backward facing step configuration known to show instabilities due to a vortex shedding at the dump plane to understand the effects of the liquid phase. However, instead of premixing, liquid fuel was injected just before the step. Through numerical experiments over a range of initial droplet sizes, it was shown that an optimal diameter exists and changes the amplitude of the recorded pressure oscillations due to the changes in the evaporation timescale. In a joint experimental-simulation effort

by the same group, a first of its kind brute force LES employing an Euler-Lagrange approach was able to capture the instability mode . The multiple uncertainties of the spray flame modelling, liquid atomisation, fuel injection affecting the flame dynamics were however highlighted in this work of [44].

It is also recognised that a thermoacoustic instability of spray systems can affect the spray itself. Typically, simulations of the SICCA configuration have been used to analyse the effects of the liquid phase on the limit cycle observed in the experiments [242, 243, 244]. The simulations mainly highlighted the effects of direct spray wall interactions (considering slip, film formation [242]) as well as indirect effects such as the varying injection angle [243]. In the former case, a liquid film model impacted the time between injection and droplets reaching the chamber, which subsequently locked in with the self sustained mode of the system. Varying the injection angles in the latter case, affected the amount of droplets forming the liquid film *vs.* ones reaching the chamber directly, leading to different effects on the thermoacoustic coupling.

While brute force LES is a route to understand combustion instabilities, another use of LES is to extract the Flame Transfer Functions/Flame Describing Functions (FTF/FDF). These FTF's/FDF's plugged into Helmholtz solvers [245] or reduced order network models [38] can then be used for more comprehensive stability analyses of large systems. However, determining FTF's over a wide frequency range for complex systems like swirled spray burners for which no analytical formulations exist, is a computationally demanding task. In fact, very little experimental FTF's of spray swirled burners exist to model liquid injection. The goal of this chapter is then to revisit the simulations from Chapter 7 in forced conditions and compare the LES response with available experimental data.

9.2 Acousting forcing of the LOTAR configuration

As described earlier in Chapter 7 (Figure 7.1), the setup is equipped with a siren that is capable of introducing acoustic perturbations at different frequencies and amplitudes. To do so, the incoming jet is periodically interrupted by a sprocket wheel, and the frequency of pulsation is determined by the velocity of this wheel. The excitation amplitude is adjusted by varying the amount of flow blocked, which is achieved by changing the distance between the axis of rotation and the inlet nozzle. To damp the high turbulent fluctuation levels and achieve acoustic propagation with plane waves, the pulsed flow passes through a 1 m long tube of 50 mm diameter. The facility is furthermore equipped with microphone taps for acoustic characterisation, before reaching

the combustion chamber [221, 222, 223]. The forced response was measured for a narrow frequency range of 170 Hz - 212 Hz. Multiple forcing amplitudes ranging from 1.5 ms^{-1} - 45 ms^{-1} were then used to determine the experimental Flame Describing Functions.

To force the flame numerically to compare with the experiments, multiple points have to be taken into account. Boundary conditions are first needed to maintain the mean imposed mass flow rate of 100 gs^{-1} and not cause it to drift, as well as to ensure that spurious reflections from the inlet/outlet boundaries are avoided. This is done by using low relaxation coefficients and non reflecting characteristic boundaries [246, 247]. Theoretically, the acoustic velocity u' and pressure perturbations p' can be induced by upstream or downstream forcing [248] to obtain equivalent results. However, this equivalence is not necessarily true for larger and complex configurations. As recently seen, for the same levels of velocity perturbations at reference locations, the heat release response and hence the flame transfer functions significantly vary, with the upstream forcing yielding lower values [249].

A downstream excitation from the pressure outlet is utilised in the present work with an excitation amplitude of $\hat{p}/P_{out} = 0.06$, or a corresponding amplitude of $\hat{u}/\bar{u}_{in} = 30\%$. After the initial transients, the system exhibits a stabilised response to the imposed harmonic fluctuations and at least 10 full periods are simulated for each forcing frequency. For further post processing and analysis, this initial transient is excluded. The typical initial transient and the established harmonic response for a frequency of 200 Hz can be seen in Figure 9.1.

To calculate the flame response, input velocity signals are averaged over 9 probes placed on the inlet surface of the computational domain. The averaging ensures removal of incoherent turbulence effects and retention of only acoustic perturbations.

Prior to averaging, the fourier coefficients of the recorded signals at all probes are studied as marked in Figure 9.2 along with their mean value (red circle and line) along with the recorded mean heat release rate (black square). The outlier probes which have a large deviation (not in the case shown) and scatter from the mean values are discarded from the calculations of the FTFs. Finally, the spectral content of the mean velocity and heat release signals are used as shown in the same figure for which the response of the applied frequency (200 Hz) is obtained.

With these mean velocity and heat release signals, gain n_{FTF} and phase

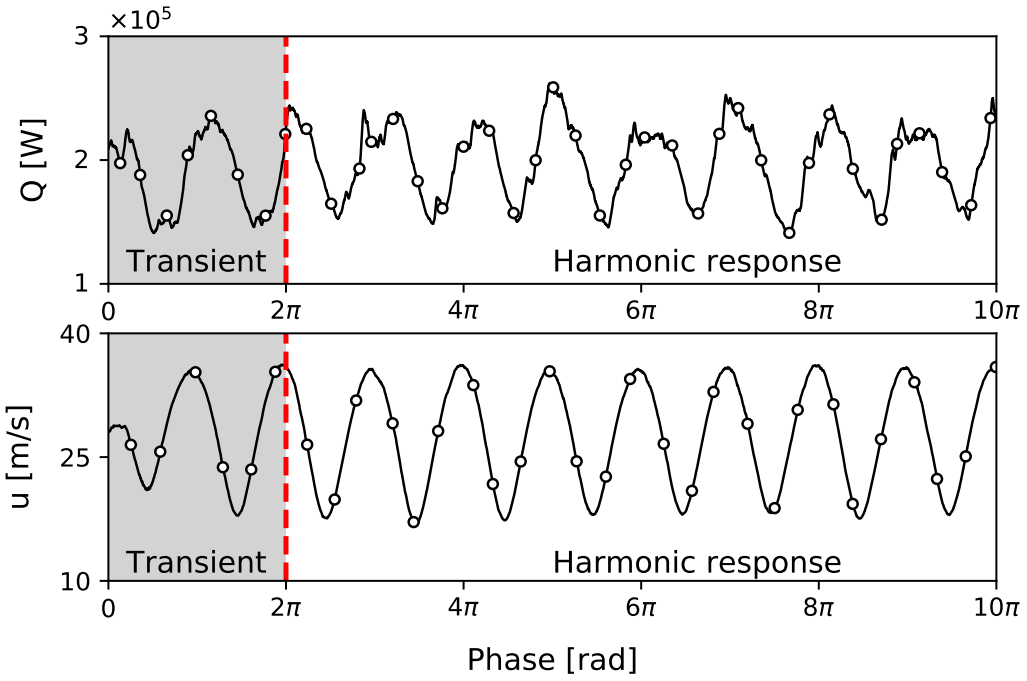

Figure 9.1: Sample of the velocity response taken at a probe location and heat release variation due to downstream forcing.

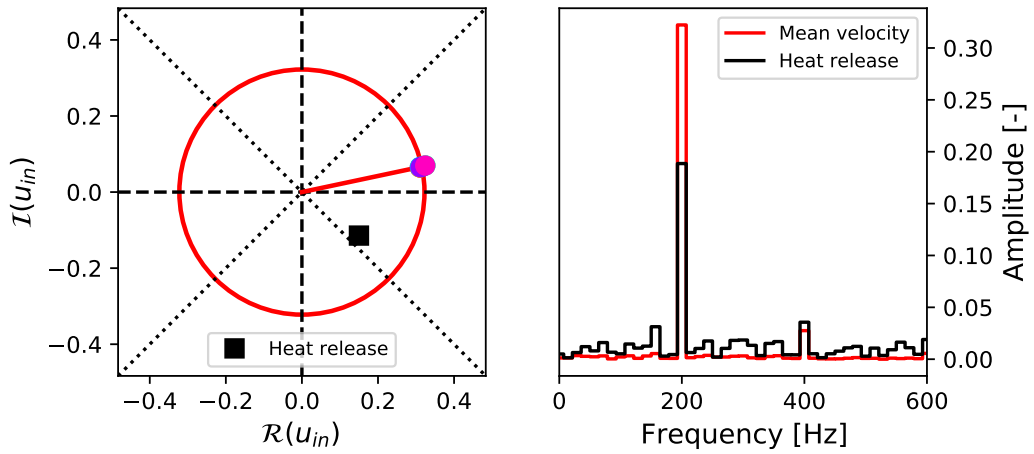

Figure 9.2: FFT of the mean velocity and heat release (left) and Fourier coefficients at probe locations (right), red circle and line indicate absolute value and phase of the mean velocity.

ϕ_{FTF} of the FTF are calculated as follows:

$$n_{FTF} = \text{abs}\left(\frac{\hat{Q}/\overline{Q}}{\hat{u}/\overline{u}}\right)$$
$$\phi_{FTF} = \arg\left(\frac{\hat{Q}/\overline{Q}}{\hat{u}/\overline{u}}\right) \tag{9.1}$$

The numerically obtained FTF for the LOTAR test-bench is finally compared with the experimental results in Figure 9.3. Good agreement with the measured values can be seen since the gain and phase are recovered. Note that the experimental gain shows a flat profile as a function of the frequency which indicates a saturation behaviour. Simulations, for all the discrete frequencies addressed show a gain 15% lower than the ones observed experimentally. The phase corresponds to a constant delay between the perturbations and the heat release response that is well captured by the simulations for all frequencies.

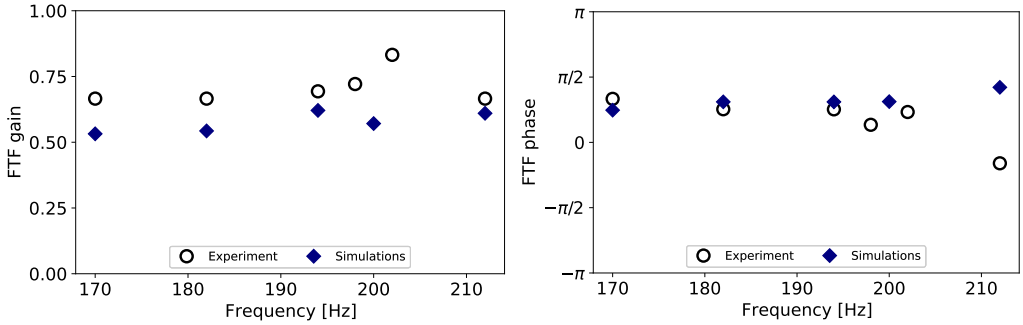

Figure 9.3: FTF of the the LOTAR setup.

9.3 Forced flame dynamics

To understand the flame dynamics, a representative frequency of 200 Hz is chosen for the analysis of the LES results. Considering an annular section at the exit of each of the individual sections of the swirling device, the velocity of the fluctuations due to the forcing is first shown in Figure 9.4. Of the three sub components, the exit velocity of the radial swirler marked as "swirler 1" shows the maximum response to the incoming acoustic fluctuations. This is in line with the flow rate split, with maximum incoming flow diverted through the radial swirler. The phase is with respect to the velocity signal obtained at the exit of swirler 1 (radial swirler) through which bulk of the flow variation takes place.

The time evolution of the averaged velocities, overall heat release, evaporation rate and are shown in Figure 9.5. Clearly lower pressure due to the acoustic forcing induces a higher inflow of fresh gases into the combustion chamber, peaking at $\Phi = \pi/2$. This leads to an increase in heat release with a slight delay due to the mixing and combustion process observable at $\Phi = \pi$. The evaporation rate inside in the combustor begins to increase after the heat release peak and is out of phase with the incoming mass flow of air. This is contrary to the expected behaviour under forced conditions where increasing

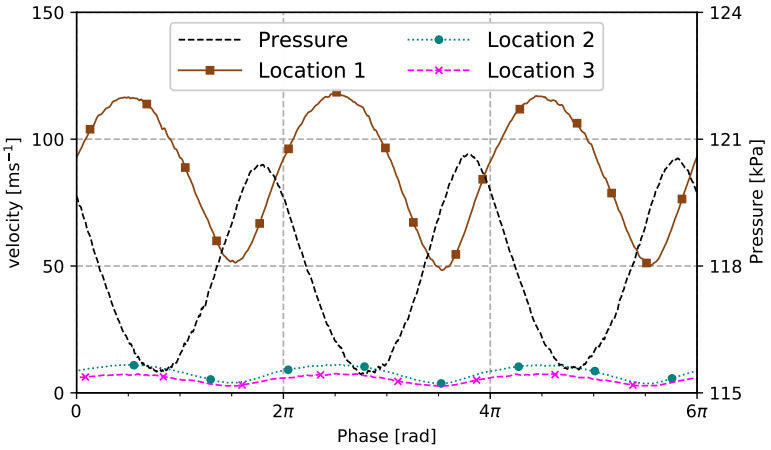

Figure 9.4: Response of the swirler to acoustic forcing at locations highlighted in Figure 7.12.

air mass flow of air leads to high relative velocities, droplet dispersion and hence increase in vaporisation followed by a peak in heat release as reported by [44].

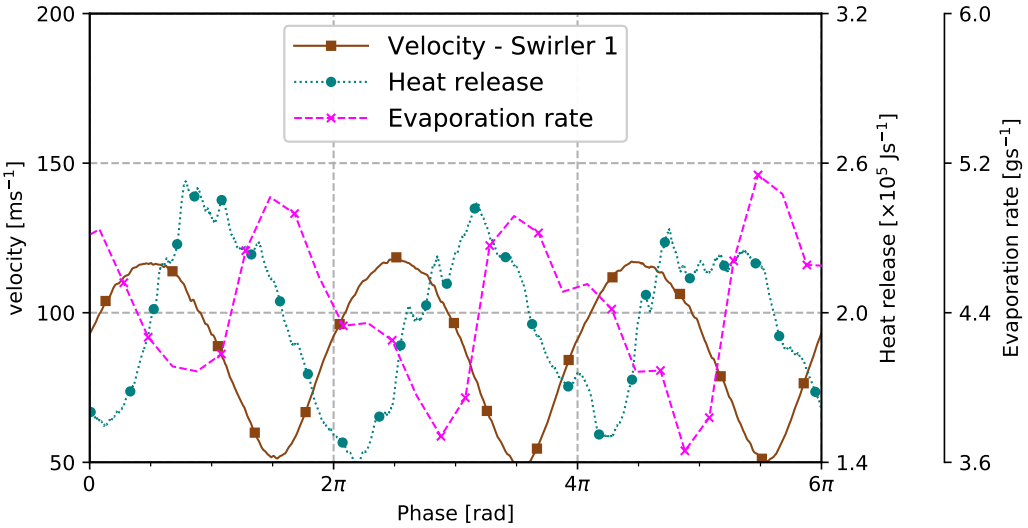

Figure 9.5: Reponse of global heat release and evaporation rate.

Using Dynamic mode decomposition (DMD), it is possible to extract coherent structures at the target frequency, which in the present case was done with 10 snapshots per cycle for 20 cycles. The variation in evaporation rate Γ inside the chamber is then reconstructed from DMD and shown in Figure 9.6. Two distinct zones are observed as playing a role: a primary evaporation zone being at the injector exit and a secondary zone further downstream and

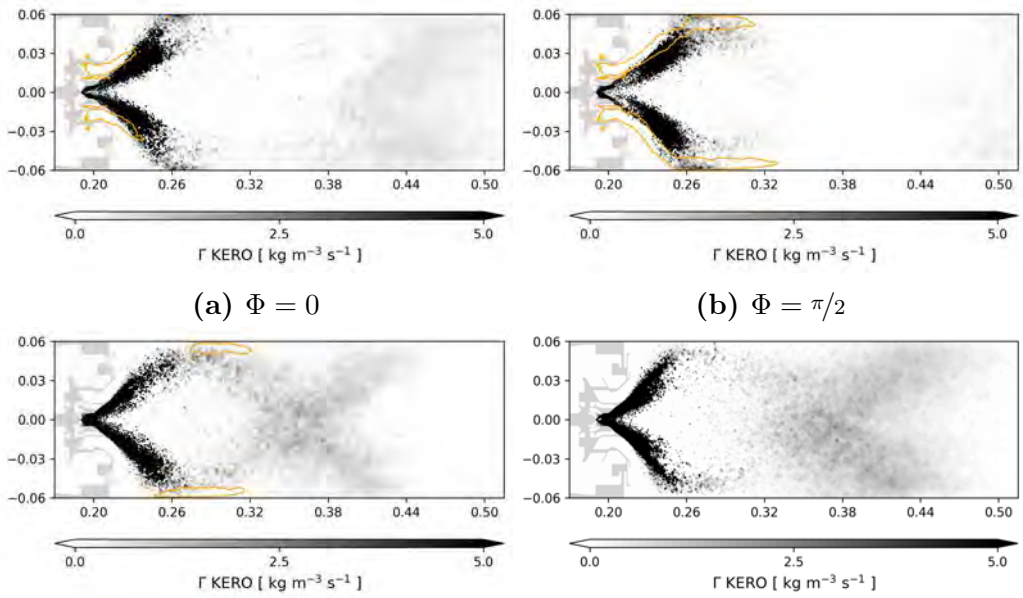

(a) $\Phi = 0$ **(b)** $\Phi = \pi/2$

(c) $\Phi = \pi$ **(d)** $\Phi = 3\pi/2$

Figure 9.6: Variation of the evaporation rate of injected liquid fuel over the combustion chamber during one forcing cycle. The orange lines are isocontours of axial gas velocity, $u_x = 50\,\mathrm{ms}^{-1}$. The phase Φ is with respect to the velocity signal at swirler exit.

covering a large volume. Note that the orange iso-contours of $u_x = 50\,\mathrm{ms}^{-1}$ indicate the high velocity regions over a forcing cycle.

At $\Phi = 0$, most of the droplets evaporate in the recirculation zone as seen in the stable case earlier. Since a large amount of vapour exists, the saturation causes a reduction of the evaporation rate in these regions. As the incoming velocity increases, droplets are carried by the incoming fresh gases and a large number of droplets are observed to impact the chamber walls as seen by the contours at $\Phi = \pi/2$. Note that there exists a slight delay during which the droplets are carried by the gaseous stream, impact the wall and rebound into the hot post combustion zone where quick evaporation occurs in the rich unsaturated regions, as shown at phases of $\Phi = \pi,\ 3\pi/2$. These specific effects caused by the transport, rebound and evaporation of the incoming droplets are the result of forcing, which leads to a phase difference of approximately π between the evaporation rates and velocity curves observed in Figure 9.5.

The variation of the heat release rates inside the combustion chamber at 200 Hz are shown in Figure 9.7 along with isocontours identifying the regions of high fuel concentration. The heat release shows mainly a "flapping" response and the main flame brush thickness and length vary, with the reaction zone reaching locations in the combustion chamber upto $x = 0.3\,\mathrm{m}$. Throughout

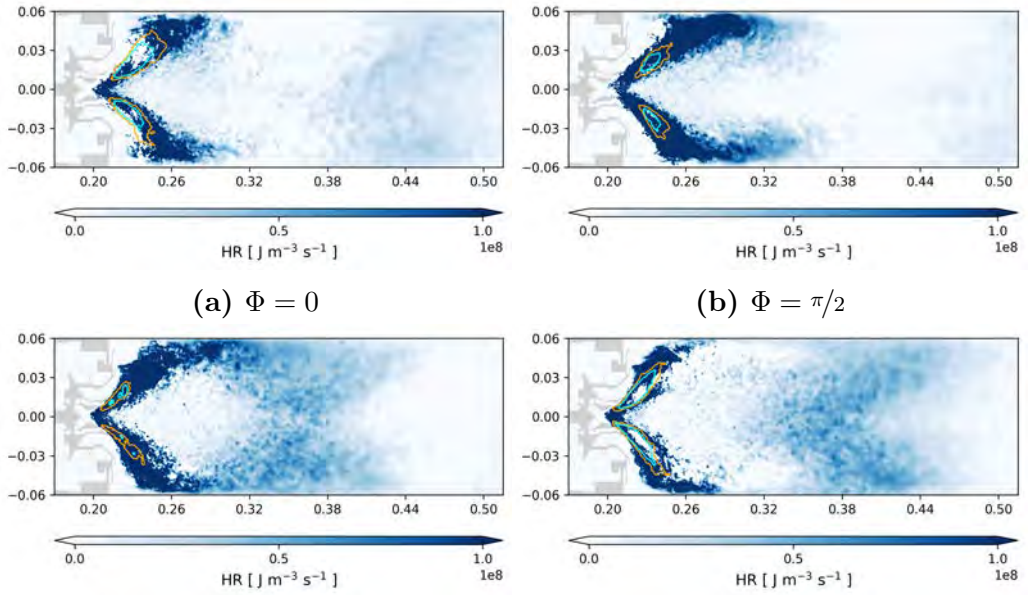

(a) $\Phi = 0$ **(b)** $\Phi = \pi/2$

(c) $\Phi = \pi$ **(d)** $\Phi = 3\pi/2$

Figure 9.7: Variation of the heat release rate inside the combustion chamber during one forcing cycle. The orange lines are isocontours of fuel mass fraction, $Y_{KERO} = 0.02$ indicating regions of high fuel concentration. The phase Φ is with respect to the velocity signal at swirler exit.

the forcing cycle, it is also evident that a large zone of fuel accumulation exits due to the single pilot injector used.

As the incoming air mass flow increases at $\Phi = \pi/2$, the accumulated fuel vapour mixes with the incoming fresh gases and ignites, resulting in a peak heat release at $\Phi = \pi$. Significant reactions occur in the downstream regions where droplets are carried by the fast incoming stream of gases. As the gas velocities reduce to a minimum, reached at $\Phi = 3\pi/2$, the liquid impact on the wall reduces and the droplets are directly in the flame zone. At this point, maximum fuel vaporisation and vapour accumulation occurs, indicated by the orange isocontours which are the largest at $\Phi = 3\pi/2$. This accumulated fuel is then consumed by the new cycles of incoming gases.

In continuation with the discussion of section 7.4, regions where the inter droplet spacing S is larger than the radius of the flame around a single burning droplet d_f can be used for predicting isolated liquid particle combustion events. The Proximity criteria is plotted in Figure 9.8 for the phase averaged data over one forcing cycle, with the main flame region being identified by the black heat release isocontour of $HR = 1 \times 10^8\,\mathrm{Jm^3 s^{-1}}$.

Possibility of regions with large inter droplet spacing is evident towards the combustor exit. In addition, the averaged heat release contribution from

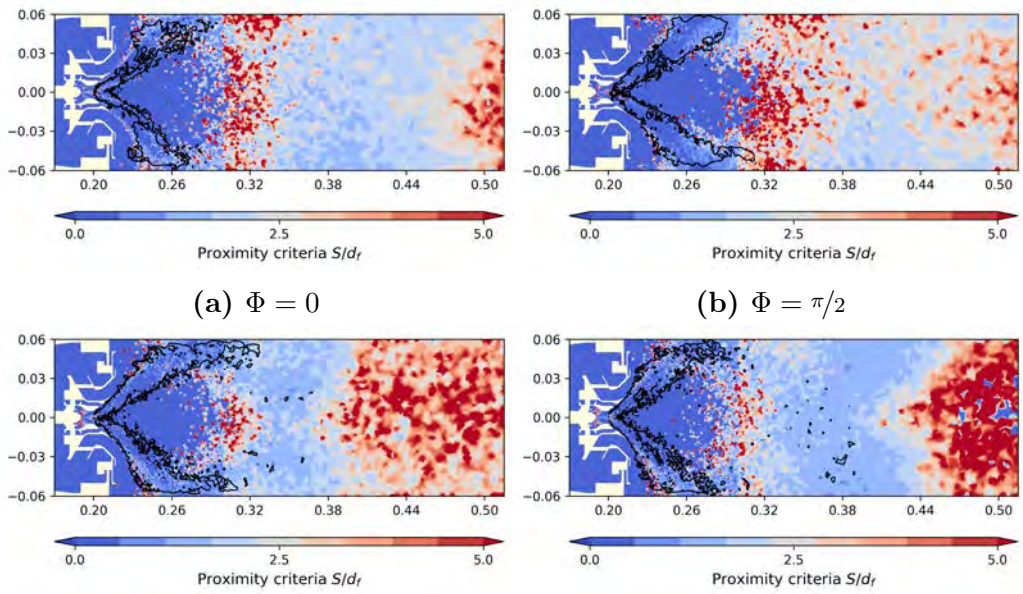

(a) $\Phi = 0$ **(b)** $\Phi = \pi/2$

(c) $\Phi = \pi$ **(d)** $\Phi = 3\pi/2$

Figure 9.8: Variation of the heat release rate inside the combustion chamber during one forcing cycle. The black lines are isocontours of $HR = 1 \times 10^8\,\mathrm{Jm^3s^{-1}}$ showing main flame zone. The phase Φ is with respect to the velocity signal at swirler exit.

these two separate zones: main flame region $x < 0.3\,\mathrm{m}$ and the downstream regions $x > 0.3\,\mathrm{m}$ is shown in Figure 9.9. On average contributions of the downstream regions is 30% towards the overall heat release rate. Further, it can be observed that the heat release fluctuations in the downstream regions are associated with a delay due compared to the main heat release zone. This delay is due to the transport, evaporation and combustion of droplets. When these fluctuations are studied in association with the evaporation rates of Figure 9.5, it can be concluded that strong two-phase effects and impact of the liquid phase is present on the heat release response in the downstream regions of the chamber.

9.4 A case for varying droplet distributions

For the LOTAR case the velocity and pressure signals at the injection location are shown in Figure 9.10. Considering a simple pressure swirl atomizer the liquid mass flow rate is given by [250]:

$$\dot{m}_{liq} = C_d A_o \sqrt{2\rho_l \Delta P}, \tag{9.2}$$

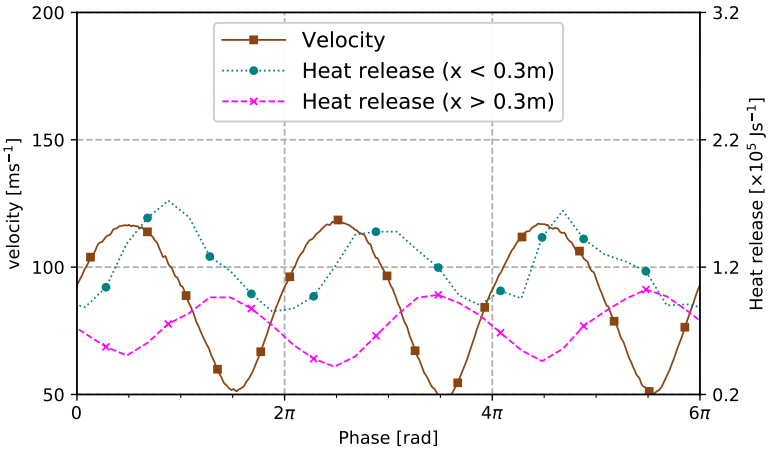

Figure 9.9: Heat release contributions from the main flame region and downstream regions.

where $\dot{m}_{liq}$ is the liquid flowrate out of the atomizer, C_d is the discharge coefficient, A_o is the exit area of the atomizer, ρ_l the liquid density and the injection pressure difference applied is ΔP. Considering a maximum amplitude of variation p' in the chamber which produces $\dot{m}'$ change in liquid massflow rate, by linearising Eq. (9.2) we get:

$$\dot{m}' \propto -\frac{p'}{\Delta P}, \tag{9.3}$$

with the negative sign indicating an inverse correlation between pressure and mass flow rate fluctuations. Considering the present case with injection $\Delta P = 11.5\,\text{bar}$ and an observed $p' \approx 10\,\text{kPa}$, the liquid mass flow rate variation can be considered negligible.

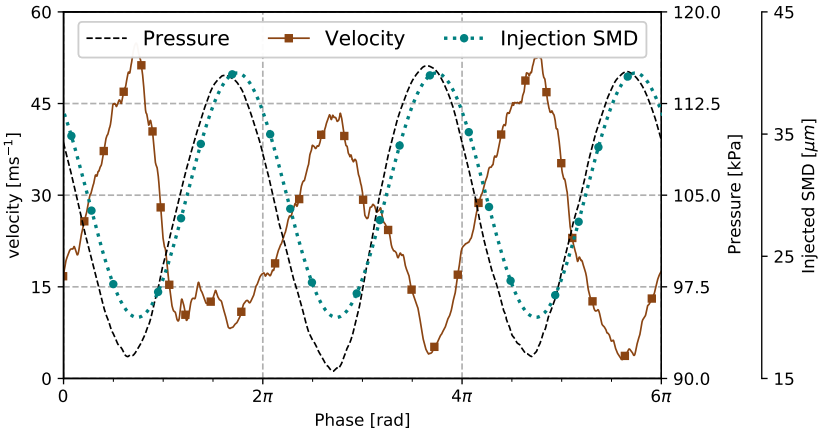

Figure 9.10: Axial velocity and pressure at probe position placed at the exit of liquid atomizer.

Instabilities induce pressure and velocity fluctuations at the atomizer exit which can also alter the complete distribution of particles exiting the atomizer. Zhu et al. [251] reported that the decreasing pressure results in increasing velocity across the fuel injector leading to better atomisation and increased heat release which appear as "hot-spots" being convected. Other experimental studies also highlight the changing atomisation characteristics due to fuel and airflow changes on account of instabilities [252, 253]. The inverse impact of velocity fluctuations on the SMD of the droplets measured downstream of simple model atomizers involving sheet breakup have been reported by Chaussonnet et al. [254], Christou et al. [255]. Using analytical expressions for jet in cross flow, Pillai et al. [241] integrated a dynamic injection model to analyse the effects of varying SMD on the instabilities in a backward facing step combustor.

In the present LOTAR case, to understand the impact of a varying injection distribution, for the forcing frequency of 200 Hz, a continuously varying Rosin Rammler distribution is injeted. A variation of 10 μm is considered with the minimum SMD corresponding to the maximum velocity at injector exit as shown in Figure 9.10. The limiting cases and the mean injection pattern is shown in Figure 9.11. The narrower PDF at $\Phi = \pi/2$ corresponds to the increased atomisation and conversely at $\Phi = 3\pi/2$ due to the low velocity at the injection location, the PDF is wide and shifts towards larger droplet diameters.

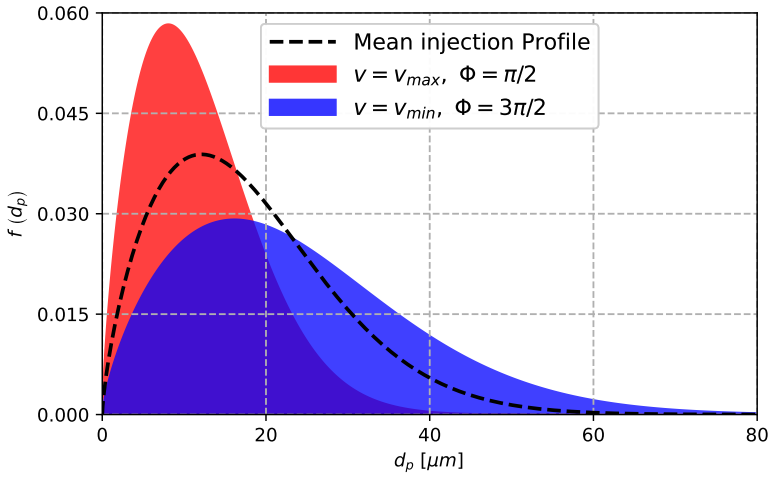

Figure 9.11: Plot showing the injected particle size distribution. $v_{max,\ min}$ correspond to the velocity just outside of the injection point.

The comparison between the two cases where a constant and a varying injection PDF is used is shown in Figure 9.12. Changing the droplet injection

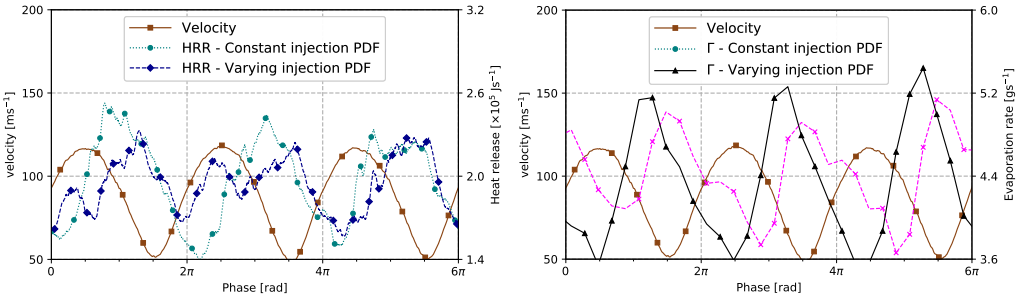

Figure 9.12: Variation of HRR and Evaporation rate over forcing cycles - comparision between constant and varying injection PDF cases.

pattern to account for the varying degrees of atomisation changes the response of the system. An increased delayed in the heat release peak of the system is observed, while an opposing pattern is noticeable for the evaporation rates in the system. The evaporation rate variation is also much higher than the previous case with constant injection PDF (see Figure 9.5). When comparing both HRR and evaporation rate together, in the former case with constant injection PDF, it was observed that the evaporation rate curves lagged the heat release peaks. However, upon changing the injection the injected PDF we observe an overlapping behaviour of the heat release and evaporation rates.

Over a forcing cycle the phase averaged particle statistics are visualised by the plotting the number of particles coloured by the particle diameters for the cases with constant and varying injection PDFs in Figure 9.13 and Figure 9.14 respectively. For the case with constant injection profiles the particle concentration shown in Figure 9.13 are in-line with the observations made in the earlier section. At the points $\Phi = \pi/2$ and $\Phi = \pi$, an increasing particle concentration increases the interaction of liquid spray and the chamber walls. Upto 50% of the incoming particles can be observed in the near wall regions leading to the post impact heat release zone shown in Figure 9.7.

In the latter case shown in Figure 9.14 where the injection profile varies across the forcing cycle, a completely different phenomenon is observed. When the velocity and flowrate is minimum at $\Phi = 3\pi/2$, the injection PDF mainly consists of large diameters reducing the total number injected, this effect is seen later at $\Phi = 0$ when significantly lesser particles of larger diameters are entering the chamber at $x = 210\,\text{mm}$. As the incoming velocity begins to rise, much of these larger droplets retain their ballistic trajectories and are seen in the recirculation zone (low particle number region between $x = 250\,\text{mm}$ and $x = 300\,\text{mm}$) at $\Phi = \pi/2$ and significantly lesser effects of particle wall interaction are noticed.

As the velocity increases at $\Phi = \pi/2$, the injection PDF begins to shift

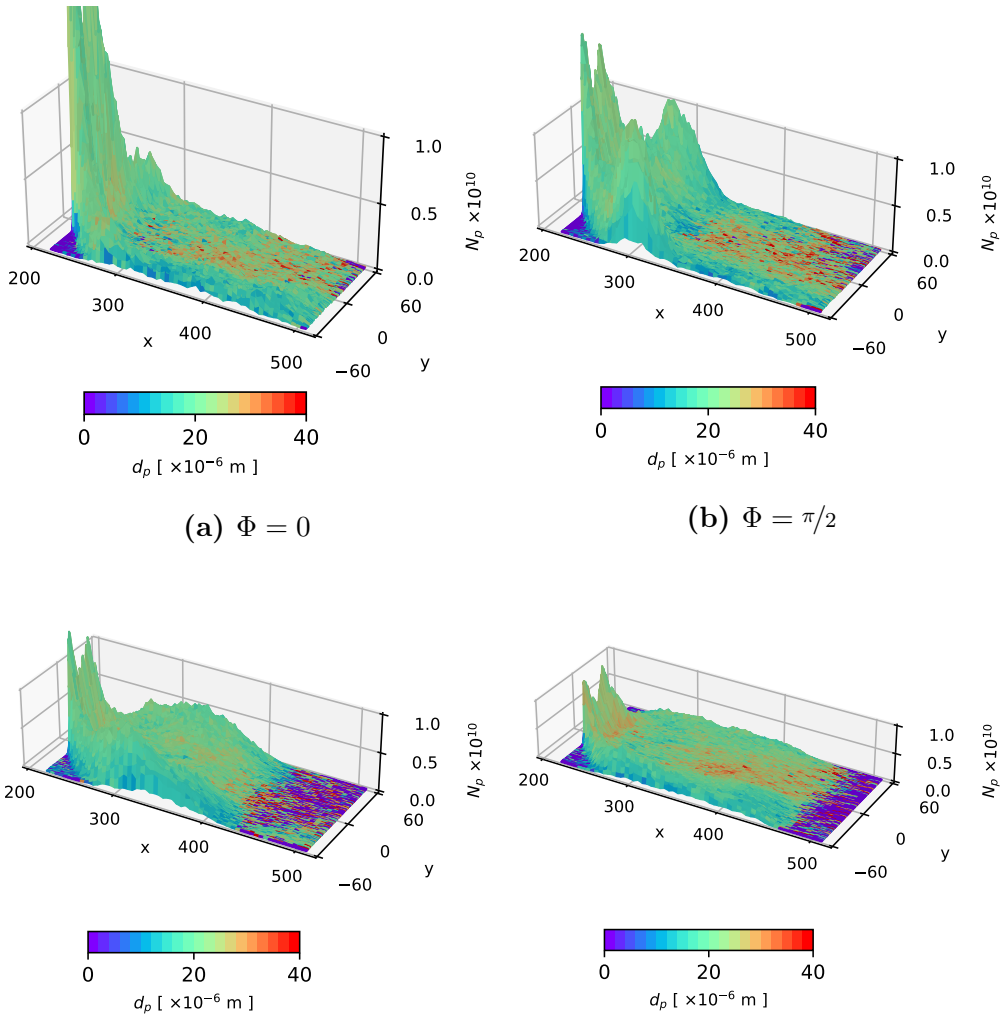

(a) $\Phi = 0$ **(b)** $\Phi = \pi/2$

(c) $\Phi = \pi$ **(d)** $\Phi = 3\pi/2$

Figure 9.13: The phase averaged variation of particle numbers coloured by particle diameter over a complete forcing cycle across the combustion chamber for the case with constant injection PDF.

towards smaller diameters and this results in the number of particles entering the chamber to suddenly increase at $\Phi = \pi$. The smaller droplets vapourise quickly explaining the peak in evaporation rate observed just after $|phi = \pi/2$ in Figure 9.12. This increase in fuel vapour leads to an increased heat release overlapping the evaporation rate. Due to saturation effects, a significant portion of the droplets impact the wall and concentrate in the post flame zone between $x = 350\,\text{mm}$ and $x = 400\,\text{mm}$.

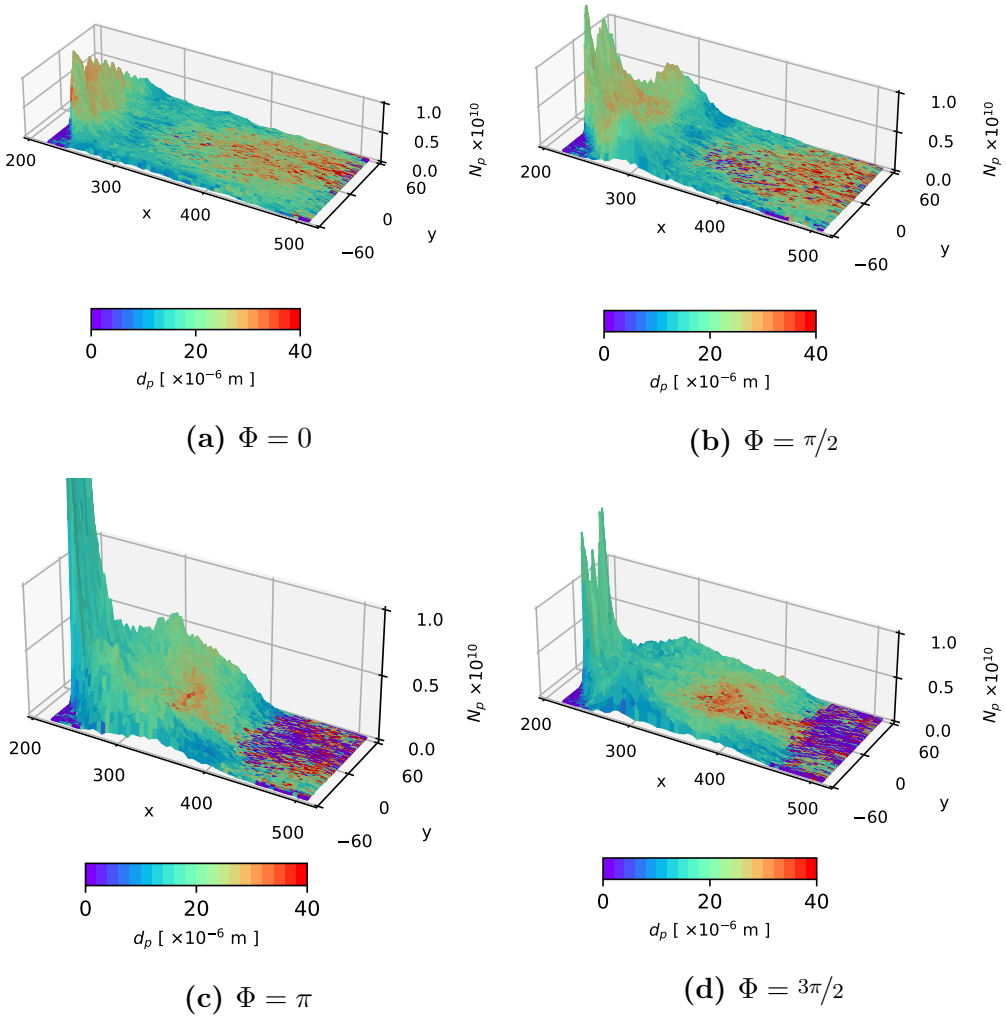

(a) $\Phi = 0$ **(b)** $\Phi = \pi/2$

(c) $\Phi = \pi$ **(d)** $\Phi = 3\pi/2$

Figure 9.14: The phase averaged variation of particle numbers coloured by particle diameter over a complete forcing cycle across the combustion chamber for the case with constant injection PDF.

9.5 Conclusions

Forced simulations of the LOTAR setup introduced earlier were carried out. The experimental results over the narrow range of 170 Hz- 212 Hz were reproduced in the simulations. A constant gain and time delay is observed for the present configuration. The flame and particle dynamics for 200 Hz were analysed in detail. The particle impact on the wall and combustion further downstream after a delay was shown to contribute significant portion of the heat release.

Since thermoacoustic instabilities result in varying pressure and velocity fluctuations at the injection locations, these can impact the atomisation effects. This was tested by injecting a varying PDF across the forcing cycle, which changed the interaction between heat release and evaporation. Phase average particle tracking show alternating periods of increasing and decreasing number of particles in the domain which alter the response. Further experimental data is needed to accurately model and validate such injection strategies for use in spray flame instability studies.

Chapter 10

Forced simulations of LOTAR - multicomponent flames

Contents

10.1 Introduction

Studies on combustion systems operating with real fuels are not numerous at present by [256, 257, 221] and out of those only Apeloig et al. [221] specifically looked at self sustained instabilities. While detailed experimental studies are required to understand the mechanisms, it is often very complex to characterise spray properties, spray-flame interactions under happening such instabilities. Models discussed so far are an attractive proposition to study the unsteady dynamics of real spray flames.

Combining the multicomponent flames of Chapter 8 and the forced simulations of Chapter 9, the goal of this chapter is to push the limits of state of the art by discussing the initial results of forced multicomponent spray flames. This is an important step in improving the predictive capabilities using LES for the design of future engines that are designed to be fuel flexible and also look at limitations that exist with current modelling capabilities. At present, no literature exist on forced multicomponent spray flames in a gas turbine chamber. This initial work is intended as a starting point to discuss limitations and improve existing modelling towards realistic forced spray flame simulations.

10.2 Global Response

Due to computational constrains, extracting the full FTF for the entire range as done using the global chemistry is out of reach presently. Hence a frequency of 500 Hz is chosen for the comparison between JetA-1 and At-J. The target of these simulations was to capture 5 full cycles for each of the cases to obtain a balance between the total time and number of cycles needed to establish a stable limit cycle. The global heat release response between the cases is shown in Figure 10.1.

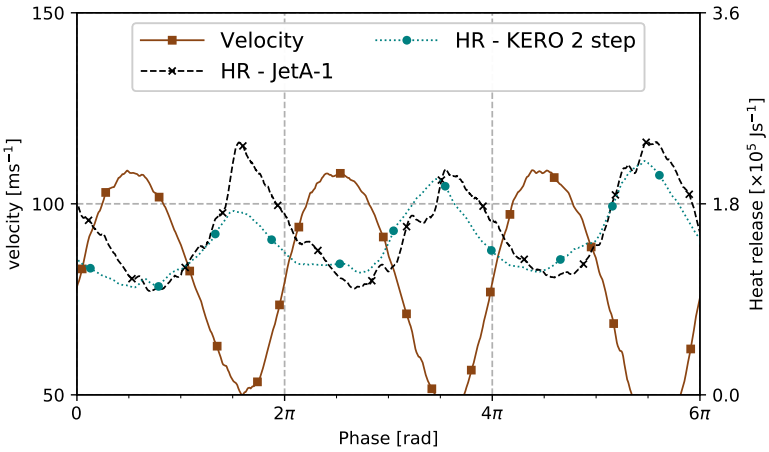

(a) JetA-1 reponse

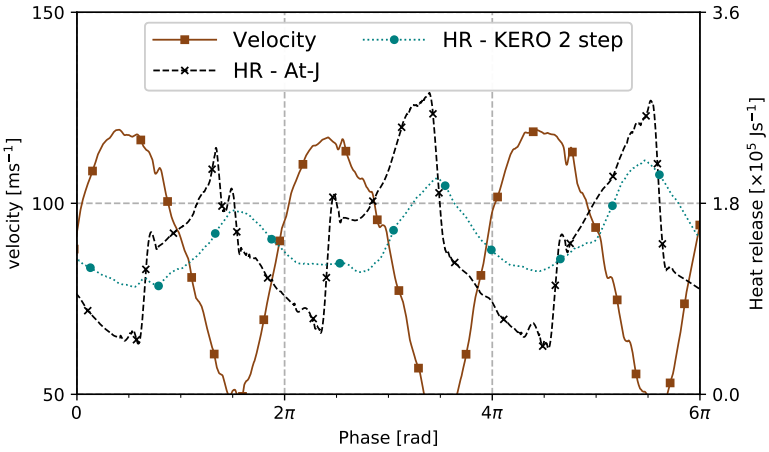

(b) At-J response

Figure 10.1: The heat release and velocity response (swirler 1) for the multicomponent cases at 500 Hz.

For the case with At-J fuel, we obtain a harmonic response similar to the case with global chemistry slightly out of phase with the incoming velocity.

However, a more complex pattern is observed for the At-J case with the dominant response still at forcing frequency. As the heat release increases, we see a double peak behaviour, with a rapid increase post the first heat release peak.

The response of the system for the two-step global chemistry has also been plotted in Figure 10.1. The response of multicomponent flames show a larger amplitude variation compared to the global chemistry. For the JetA-1 case, the heat release variations are comparable with a max variation $< 5\%$, and the last few cycles showing a similar pattern. For the case of At-J, the variations are much more pronounced along with the non linearities and a 10% difference in the peak variation is observed.

	Gain	Phase
KERO (1 component)	0.93	0.35 ms
JetA-1 (3 component)	1.2	0.46 ms
At-J (3 component)	2.12	0.15 ms

Table 10.1: Global gain-phase for the 3 different fuels representations at 500 Hz.

These variations have a significant change on the global response of the system in terms of the gain/phase, seen in Table 10.1. The multicomponent fuels show an increased gain at the tested frequency, specially the At-J fuel which is almost twice the gain obtained with the global mechanism. In addition, the stability of a system is sensitive to the time delay between the velocity and heat release fluctuations. Here we see that the two compositions of the fuel show deviations on either side of the reference two-step kerosene flame. The 3 component JetA-1 surrogate increases the time delay whereas the alternative At-J has much smaller time delay compared to the reference case. To obtain a clear conclusions and the effects, a complete FTFs must be extracted over a wide range of frequencies and compared to analyse the overall trends. The differences obtained in this case indicate a significant effect of fuel representation and chemistry on the repose of spray flames.

10.3 Dynamics of forced multicomponent spray flames

Firstly, the heat release dynamics of the main flame zone at 500 Hz is shown for case with global 2 step chemistry in Figure 10.2. The overall response is similar to the one discussed earlier in Chapter 9. However, at this higher forcing frequency, one obverses a separation and break off event at $\Phi = 0$ which

is due the low velocity and mass flow through the swirlers at the preceding point $\Phi = {}^{3\pi}/_{2}$. Subsequently, the flame extents upto $x = 0.3\,\mathrm{m}$ during the point of peak heat release.

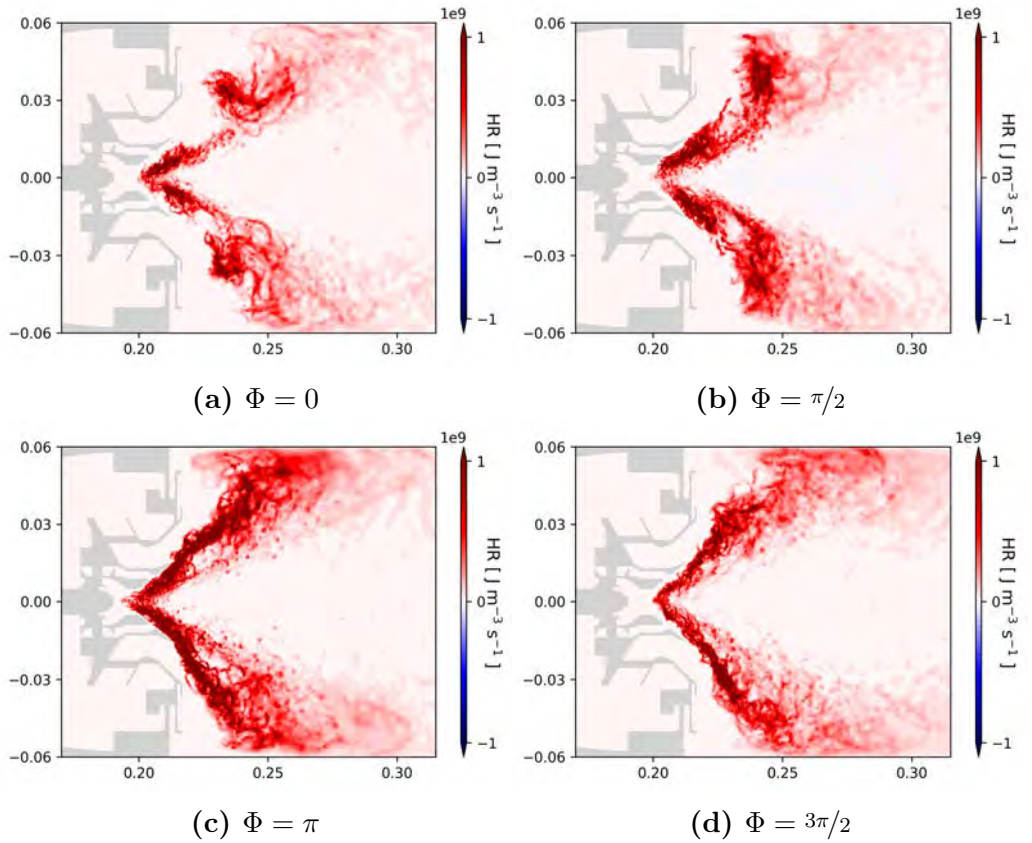

(a) $\Phi = 0$ **(b)** $\Phi = {}^{\pi}/_{2}$

(c) $\Phi = \pi$ **(d)** $\Phi = {}^{3\pi}/_{2}$

Figure 10.2: The variation of heat release for the KERO_2S (global chemistry) flame at 500 Hz over one cycle extracted from phase averaging.

For the multicomponent JetA-1 flame, the heat release patterns over a complete forcing cycle is shown in Figure 10.3. At $\Phi = 0$, we see the evaporation and pyrolysis regions close to the flame base (negative heat release) associated with the earlier observed separation and blow-off just above the exit of the radial swirler exit. The events leading to this point at $\Phi = {}^{3\pi}/_{2}$, when the velocity and flow through the swirlers is at a minimum, the recirculation zone becomes weaker and the trapped spray particles begin to evaporate. Next at $\Phi = {}^{\pi}/_{2}$, the increasing velocity brings in fresh gases and re-establishes a continuous reaction zone. The increasing velocity also increases the spray penetration resulting in significant increase in heat release. This is primarily in earlier observed **Region II** marked in Figure 8.9, eventually leading upto the peak heat release around the point.

At-J being a more volatile fuel in comparison to JetA-1 results in a different

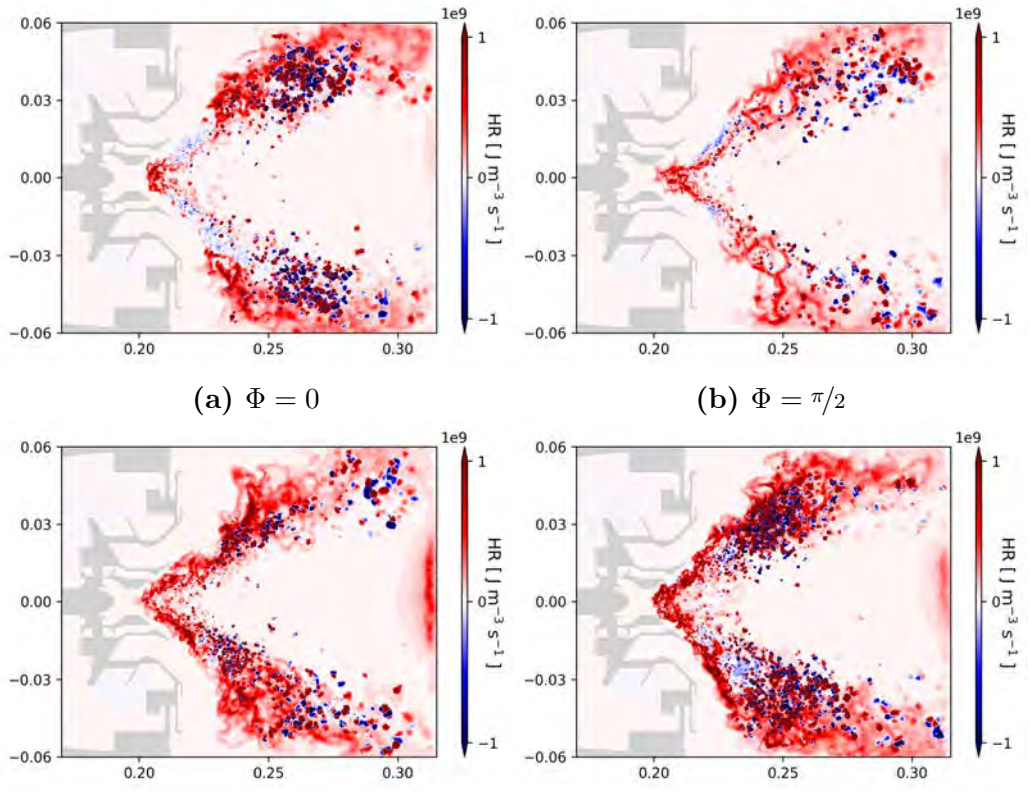

(a) $\Phi = 0$ **(b)** $\Phi = \pi/2$

(c) $\Phi = \pi$ **(d)** $\Phi = 3\pi/2$

Figure 10.3: The variation of heat release for the JetA-1 flame at 500 Hz over one cycle extracted from phase averaging.

response to harmonic forcing shown in Figure 10.4. The overall heat release regions do not show much variations across the cycle, except in their intensity. It was shown earlier that the downstream **Region III** (Figure 8.15) of the At-J flame is due to the premixing of fresh gases and smaller fuel products. When the flow through the swirlers at $\Phi = 3\pi/2$ is minimum, a weak reaction zone in the downstream regions is seen as a result at $\Phi = 0$. As flow again peaks through the swirlers, the heat release begins to increase where we observe the initial peak at $\Phi = \pi/2$. The increasing velocities result in increased evaporation and mixing resulting in the main secondary peak at $\Phi = \pi$, explaining the observed double peak behaviour of the heat release response.

Effects of the reactions and forcing on the spray evolution is shown in Figure 10.5. The plane at $x = 220$ mm is just at the exit of the swirler system into the chamber and $x = 250$ mm is further downstream. It is evident that spray reacts to the forcing and a slight variation of $4\mu m$ is observed as the spray enters the chamber however due to effects of evaporation, further downstream the spray diameter doesn't show any harmonic variation. The

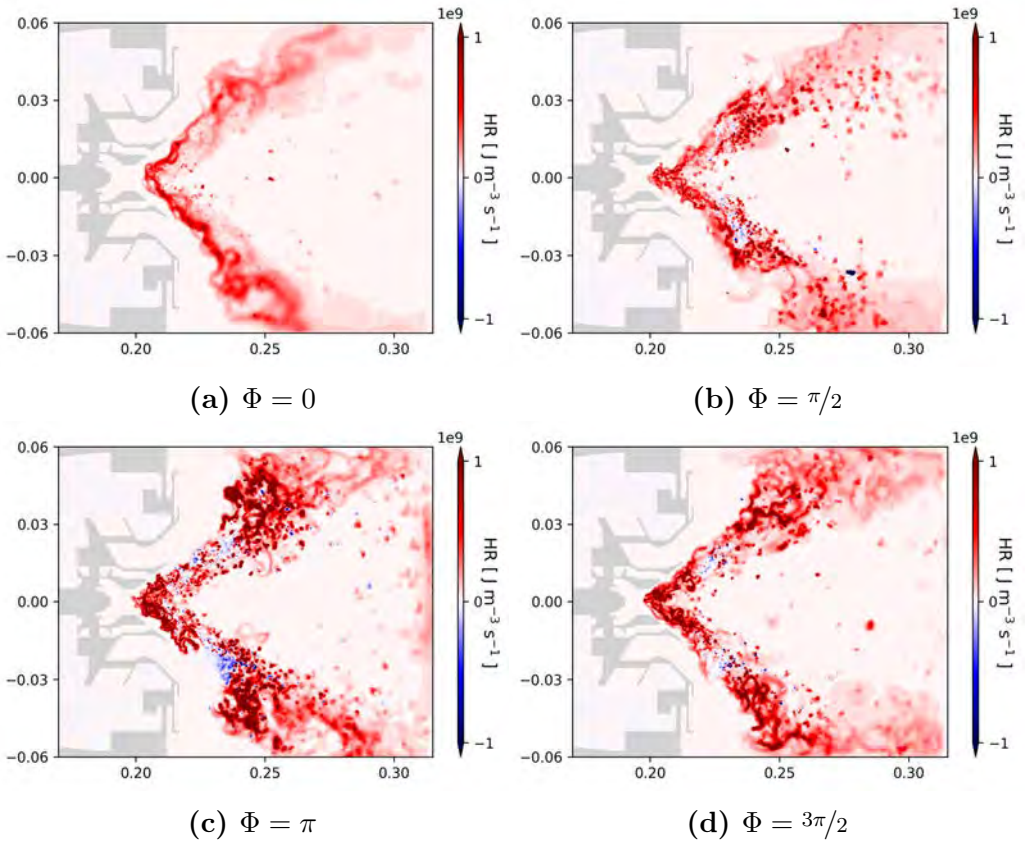

(a) $\Phi = 0$ **(b)** $\Phi = \pi/2$

(c) $\Phi = \pi$ **(d)** $\Phi = 3\pi/2$

Figure 10.4: The variation of heat release for the At-J flame at 500 Hz over one cycle extracted from phase averaging.

liquid flowrate however shows a periodic behaviour in both the planes analysed. Spray and the two phase behaviour downstream is governed mainly by number density variations while upstream, some segregation behaviours can also contribute especially if the variation is significant over a forcing cycle. Another observation is the reduced flowrate of At-J in the downstream region when the SMD is comparable indicating a lesser particle density as a result of its fast vapourisation behaviour.

10.4 Correlation Indices

The Rayleigh Index (RI) can be used to identify the regions which enhance and dampen the instability. The real part of the RI is commonly ustilised and is given by:

$$\mathfrak{Re}\left(\widehat{RI}\right) = \mid \widehat{p} \mid\mid \widehat{q} \mid \cos\left(\phi_p - \phi_q\right), \tag{10.1}$$

where $\widehat{p}$ and $\widehat{q}$ are the pressure and heat release rate fluctuations respectively.

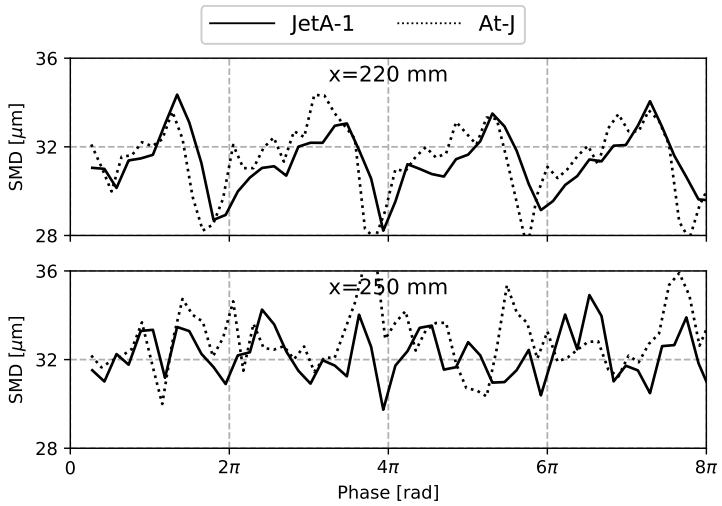

(a) SMD vatiation across two planes

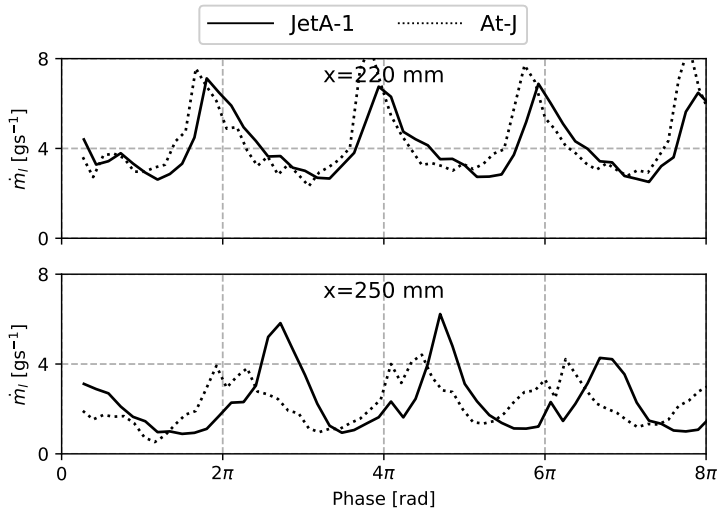

(b) $\dot{m}_l$ variation across two planes

Figure 10.5: The response (SMD, liquid mass flow rate $\dot{m}_l$) of the multicomponent spray across two different locations, $x = 220\,\text{mm}$ and $x = 250\,\text{mm}$.

The real part of the RI, normalised for ease of analysis is shown in Figure 10.6. For the flame with the two step chemistry, a strong correlations between the pressure and heat release variations exists in the outer branch of the main flame. Comparatively, a similar behaviour is observed for the multicomponent JetA-1 flame also, where one observes a region of coherent positive contribution corresponding to the main reactive zone identified in Figure 8.9. In case of the At-J however, strong positive contribution are seen from the flame base and downstream regions where maximum heat release occurs.

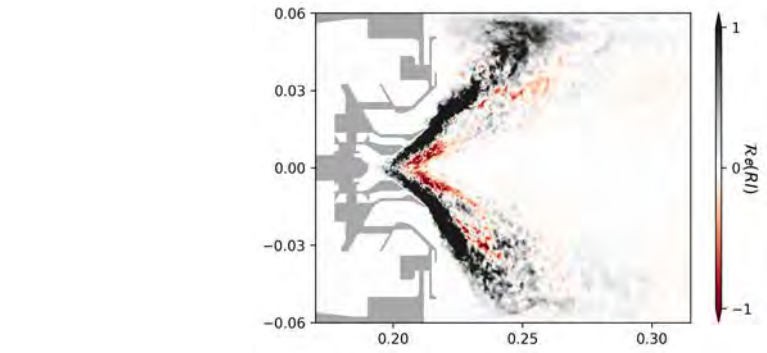

(a) KERO 2 step

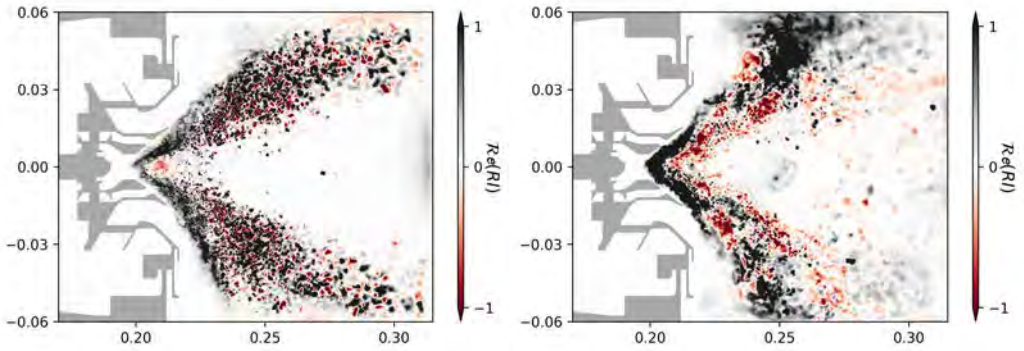

(b) JetA-1 **(c)** At-J

Figure 10.6: Real component of the Rayleigh Index.

Similar to the RI Schiavo et al. [243] introduced an Evaporation Index (EI) to indicate a correlation between the unsteady pressure and evaporation. The real part is calculated as:

$$\mathfrak{Re}\left(\widehat{EI}\right) = \mid \widehat{p} \mid\mid \widehat{\Gamma} \mid \cos\left(\phi_p - \phi_\Gamma\right), \tag{10.2}$$

where Γ is the evaporation rates, and plotted in Figure 10.7. In both cases, the inner regions of the spray indicates a region where there is a negative correlation. In all the cases, there exists a region where negative correlations are seen in the recirculation zone where droplets enter directly. This outer edge of the evaporation zone overlaps with the regions of positive $\mathfrak{Re}\left(\widehat{RI}\right)$ indicating little delay between the evaporation and flame response.

10.5 Conclusions

A first study of forced multicomponent spray flame in a realistic combustion chamber have been performed. The used of a multicomponent spray

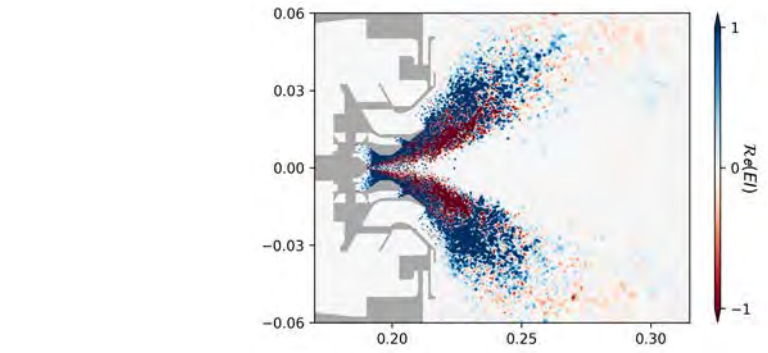

(a) KERO 2 step

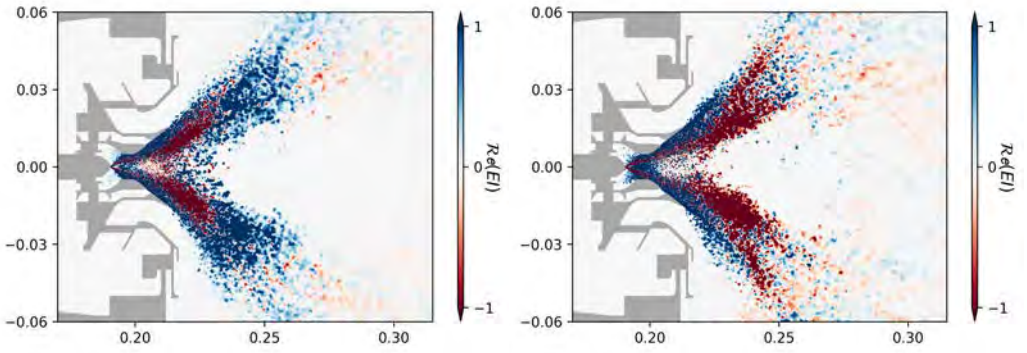

(b) JetA-1

(c) At-J

Figure 10.7: Real component of the Evaporation Index.

representation altered the observed gain and the delay of the FTF calcualted at 500 Hz. The forced cases for the At-J showed an increased gain that is almost twice of that observed for the case with a simple tw step chemistry. In addition, the time delay between the incoming flow perturbations and heat release fluctuations vary for both the fuel compositions considered. The flame dynamics for the JetA-1 flame showed the possibility of a separation even associated with the regions of high fuel concentration above the inlet swirlers. On the other hand, the At-J flame showed a two stages of heat release with the main peak being associated with the increased flow to the downstream regions of the flame. Spray dynamics suggest a dominant role of number density variation over droplet size segregation. Finally, the effect of fuel composition on the flame response in a realistic configuration has been demonstrated, however further simulations are needed for a deeper analysis.

Part IV

Conclusion and Perspective

Chapter 11

Conclusions and Perspectives

The major objectives of the PhD was to develop a framework for the simulation of complex spray flames. With these broad scopes of the work and integration of various ideas, the general conclusions and possibilities for future work based on this thesis is discussed:

— **Multicomponent evaporation modelling**
A discrete multicomponent evaporation model, capable of handling individual fuel components was shown to reproduce the vaporisation behaviour of a mixture hydrocarbons. Though complex models exist in literature to handle phase change, with the goal of performing combustion studies, the chosen model provides a good compromise between accuracy, computational effort and integration with Analytically Reduced Chemistry. Future studies on Sustainable Alternative Fuel sprays and combustion modelling will need the inclusion of complex interspecies interaction specially in presence of alcohols, esters groups. Additional activity coefficients, vapour liquid equilibrium equation would be needed to reproduce appropriate vapourisation behaviour. These models have to be extended such that high pressure conditions can also be targeted in spray flame simulations.

— **One-Dimensional Laminar Spray flames**
A fundamental understanding of spray flames was explored with the one-dimensional laminar spray flame cases. Various possibilities of regimes encountered in realistic combustion chambers were used to understand the effects of multicomponent liquid phase on flame propagation and structure. The preferential evaporation and relative velocity impact the flame propagation speed. The parameters were incorporated into an expression which predicts the general trend of the effective equivalence ratio and the laminar spray flame speed observed numerically. A further extension of these canonical cases is possible by using a polydisperse droplets to understand the instantaneous and averaged flame structures and there by extending the appropriate correlations. Use of these analytical expressions in turbulent spray combustion models would be an immediate and interesting applications. The canonical

cases are also a motivation to be used in a detailed solver to develop reductions tailored to spray flames.

— **Swirled multicomponent spray flames**
The LOTAR configuration chosen provided the necessary complexity to understand and study realistic spray flames. The objective of integrating multicomponent spray and chemistry description is successfully achieved. The standard control case of JetA-1 used a composition from three different hydrocarbon groups which was an adequate surrogate for both physical and chemical properties. The At-J fuel composed of branched chain alkanes is computationally lighter due to its chemical composition. The preferential evaporation effects in terms of flame stabilisation, regimes give an understanding not possible with the standard approach of a single component representation. However, multiple gaps in modelling and understanding have also been recognised. Interactions of the generic sensor with complex chemistry and in presence of liquid vaporisation needs to be rigorously tested and compared with other combustion models to establish the use case. Integration of these models with soot and pollutant chemistries are also needed which will definitely need attention towards even smaller ARC mechanisms to make it feasible on such a large scale. The present work provides a base to move towards extremely detailed complex spray flame computations.

— **Forced response of spray flames**
Thermoacoustic instabilities in spray flames is a topic that is gaining traction. Most computational studies rely on accurate modelling to reproduce the self sustained modes observed in the experiments. Flame transfer functions reproduced in this work match the experimental trends. To reproduce the effects of forcing on the spray, a varying PDF was injected, which showed a major change in the flame response. This application could be extended to automatic models which change the input droplet parameters as a function of the detected instability. Effects of spray wall interaction, secondary breakup and including single droplet combustion need to be further modelled and studied. State-of-the art was pushed by including forced simulations of multicomponent spray flames. These are critical for future studies on instabilities in gas turbine engines running on alternative fuels.

Bibliography

[1] Donella H Meadows, Jorgen Randers, and Dennis L Meadows. *The Limits to Growth (1972)*. Yale University Press, 2013. (Cited on page 3.)

[2] Graham M Turner. A comparison of the limits to growth with 30 years of reality. *Global environmental change*, 18(3):397–411, 2008. (Cited on pages 3 and 4.)

[3] Dennis Meadows and Jorgan Randers. *The limits to growth: the 30-year update*. Routledge, 2012. (Cited on page 3.)

[4] Gordon McBean. Climate Change and Extreme Weather: A Basis for Action. *Natural Hazards*, 31(1):177–190, jan 2004. doi: https://doi.org/10.1023/B:NHAZ.0000020259.58716.0d. (Cited on page 4.)

[5] M. Monirul Qader Mirza. Climate change and extreme weather events: can developing countries adapt? *Climate Policy*, 3(3):233–248, 2003. doi: 10.3763/cpol.2003.0330. URL https://www.tandfonline.com/doi/abs/10.3763/cpol.2003.0330. (Cited on page 4.)

[6] James Hansen, Makiko Sato, Paul Hearty, Reto Ruedy, Maxwell Kelley, Valerie Masson-Delmotte, Gary Russell, George Tselioudis, Junji Cao, Eric Rignot, et al. Ice melt, sea level rise and superstorms: evidence from paleoclimate data, climate modeling, and modern observations that 2° c global warming is highly dangerous. *Atmospheric Chemistry & Physics Discussions*, 15(14), 2015. (Cited on page 4.)

[7] Sarah CB Raper and Roger J Braithwaite. Low sea level rise projections from mountain glaciers and icecaps under global warming. *Nature*, 439 (7074):311–313, 2006. (Cited on page 4.)

[8] Thomas Wernberg, Dan A Smale, Fernando Tuya, Mads S Thomsen, Timothy J Langlois, Thibaut De Bettignies, Scott Bennett, and Cecile S Rousseaux. An extreme climatic event alters marine ecosystem structure in a global biodiversity hotspot. *Nature Climate Change*, 3(1):78–82, 2013. (Cited on page 4.)

[9] Daniel B Botkin, Henrik Saxe, Miguel B Araujo, Richard Betts, Richard HW Bradshaw, Tomas Cedhagen, Peter Chesson, Terry P Dawson, Julie R Etterson, Daniel P Faith, et al. Forecasting the effects of global warming on biodiversity. *Bioscience*, 57(3):227–236, 2007. (Cited on page 4.)

[10] Zekai Şen. Global warming threat on water resources and environment: a review. *Environmental geology*, 57(2):321–329, 2009. (Cited on page 4.)

[11] Alex C Ruane, John Antle, Joshua Elliott, Christian Folberth, Gerrit Hoogenboom, Daniel Mason-D Croz, Christoph Müller, Cheryl Porter, Meridel M Phillips, Rubi M Raymundo, et al. Biophysical and economic implications for agriculture of+ 1.5 and+ 2.0 c global warming using agmip coordinated global and regional assessments. *Climate research*, 76(1):17–39, 2018. (Cited on page 4.)

[12] Valérie Masson-Delmotte, Panmao Zhai, Hans-Otto Pörtner, Debra Roberts, Jim Skea, Priyadarshi R Shukla, Anna Pirani, W Moufouma-Okia, C Péan, R Pidcock, et al. Global warming of 1.5°C. Technical Report 5, IPCC, UN, 2018. URL https://www.ipcc.ch/sr15/. (Cited on page 4.)

[13] International Energy Agency. *World energy outlook 2020*. OECD Publishing, 2020. URL https://www.iea.org/reports/world-energy-outlook-2020. (Cited on page 5.)

[14] International Energy Agency. *World energy outlook 2019*. OECD Publishing, 2019. URL https://www.iea.org/reports/world-energy-outlook-2019. (Cited on page 5.)

[15] OPEC. *2021 World Oil Outlook*. Organization of the Petroleum Exporting Countries, 2021. URL https://woo.opec.org/. (Cited on page 5.)

[16] Nayan Patel and Suresh Menon. Simulation of spray–turbulence–flame interactions in a lean direct injection combustor. *Combustion and Flame*, 153(1-2):228–257, 2008. (Cited on page 7.)

[17] D Dewanji and AG Rao. Spray combustion modeling in lean direct injection combustors, part i: Single-element ldi. *Combustion Science and Technology*, 187(4):537–557, 2015. (Cited on page 7.)

[18] P Gokulakrishnan, MJ Ramotowski, G Gaines, C Fuller, R Joklik, LD Eskin, MS Klassen, and RJ Roby. A novel low nox lean, premixed, and prevaporized combustion system for liquid fuels. *Journal of engineering for gas turbines and power*, 130(5), 2008. (Cited on page 8.)

[19] Ao Ho Lefebvre. Lean premixed/prevaporized combustion. *NASA CP-2016*, 1977. (Cited on page 8.)

[20] A. S. Feitelberg and M. A. Lacey. The GE Rich-Quench-Lean Gas Turbine Combustor. *Journal of Engineering for Gas Turbines and Power*, 120(3):502–508, 07 1998. ISSN 0742-4795. doi: 10.1115/1.2818173. URL https://doi.org/10.1115/1.2818173. (Cited on page 8.)

[21] N Rizk and H Mongia. Low nox rich-lean combustion concept application. In *27th Joint Propulsion Conference*, page 1962, 1991. (Cited on page 8.)

[22] D Dewanji and A Gangoli Rao. Spray combustion modeling in lean direct injection combustors, part ii: Multi-point ldi. *Combustion Science and Technology*, 187(4):558–576, 2015. (Cited on page 8.)

[23] Robert Tacina, Changlie Wey, Peter Laing, and Adel Mansour. Sector tests of a low nox, lean-direct-injection, multipoint integrated module combustor concept. In *Turbo Expo: Power for Land, Sea, and Air*, volume 36061, pages 533–544, 2002. (Cited on page 8.)

[24] Sanjay M Correa. Power generation and aeropropulsion gas turbines: From combustion science to combustion technology. *Proceedings of the Combstion Institute*, 27(2):1793–1807, 1998. (Cited on page 8.)

[25] Yize Liu, Xiaoxiao Sun, Vishal Sethi, Devaiah Nalianda, Yi-Guang Li, and Lu Wang. Review of modern low emissions combustion technologies for aero gas turbine engines. *Progress in Aerospace Sciences*, 94:12–45, 2017. (Cited on page 8.)

[26] Medhat A Nemitallah, Sherif S Rashwan, Ibrahim B Mansir, Ahmed A Abdelhafez, and Mohamed A Habib. Review of novel combustion techniques for clean power production in gas turbines. *Energy & Fuels*, 32 (2):979–1004, 2018. (Cited on page 8.)

[27] Thierry Poinsot. Prediction and control of combustion instabilities in real engines. *Proceedings of the Combustion Institute*, 36(1):1–28, 2017. (Cited on page 8.)

[28] JG Lee and DA Santavicca. Experimental diagnostics for the study of combustion instabilities in lean premixed combustors. *Journal of propulsion and power*, 19(5):735–750, 2003. (Cited on page 8.)

[29] Lord Rayleigh. The explanation of certain acoustical phenomena. *Roy. Inst. Proc.*, 8:536–542, 1878. (Cited on page 8.)

[30] Pieter L Rijke. Lxxi. notice of a new method of causing a vibration of the air contained in a tube open at both ends. *The London, Edinburgh, and Dublin Philosophical Magazine and Journal of Science*, 17(116): 419–422, 1859. (Cited on page 8.)

[31] Sebastien Ducruix, Thierry Schuller, Daniel Durox, and Sebastien Candel. Combustion dynamics and instabilities: Elementary coupling and driving mechanisms. *Journal of propulsion and power*, 19(5):722–734, 2003. (Cited on page 8.)

[32] RAYLEIGH. THE EXPLANATION OF CERTAIN ACOUSTICAL PHENOMENA 1. *Nature*, 18(455):319–321, jul 1878. doi: https://doi.org/10.1038/018319a0. (Cited on page 9.)

[33] Thierry Poinsot and Dennis Veynante. *Theoretical and Numerical Combustion, Third Edition*. 3 edition, 2011. ISBN 978-2-7466-3990-4. URL https://www.cerfacs.fr/elearning/. (Cited on pages 9, 11, 18, 29 and 32.)

[34] Franck Nicoud and Thierry Poinsot. Thermoacoustic instabilities: Should the rayleigh criterion be extended to include entropy changes? *Combustion and flame*, 142(1-2):153–159, 2005. (Cited on page 9.)

[35] T Sattelmayer and W Polifke. Assessment of methods for the computation of the linear stability of combustors. *Combustion Science and Technology*, 175(3):453–476, 2003. (Cited on page 9.)

[36] Franck Nicoud and Kerstin Wieczorek. About the zero mach number assumption in the calculation of thermoacoustic instabilities. *International journal of spray and combustion dynamics*, 1(1):67–111, 2009. (Cited on page 9.)

[37] Franck Nicoud, Laurent Benoit, Claude Sensiau, and Thierry Poinsot. Acoustic modes in combustors with complex impedances and multidimensional active flames. *AIAA journal*, 45(2):426–441, 2007. (Cited on page 9.)

[38] Michaël Bauerheim, Franck Nicoud, and Thierry Poinsot. Progress in analytical methods to predict and control azimuthal combustion instability modes in annular chambers. *Physics of Fluids*, 28(2):021303, 2016. doi: https://doi.org/10.1063/1.4940039. URL https://doi.org/10.1063/1.4940039. (Cited on pages 9 and 132.)

[39] Jingxuan Li, Dong Yang, Charles Luzzato, and Aimee S Morgans. Open sounce combustion instability low order simulator (oscilos–long) technical report. Technical report, 2015. (Cited on page 9.)

[40] Charlélie Laurent, Michaël Bauerheim, Thierry Poinsot, and Franck Nicoud. A novel modal expansion method for low-order modeling of thermoacoustic instabilities in complex geometries. *Combustion and Flame*, 206:334–348, 2019. (Cited on page 9.)

[41] Pierre Wolf, Gabriel Staffelbach, Anthony Roux, L Gicquel, Thierry Poinsot, and Vincent Moureau. Massively parallel les of azimuthal thermo-acoustic instabilities in annular gas turbines. *Comptes Rendus Mecanique*, 337(6-7):385–394, 2009. (Cited on page 9.)

[42] G. Staffelbach, L.Y.M. Gicquel, G. Boudier, and T. Poinsot. Large eddy simulation of self excited azimuthal modes in annular combustors. 32 (2):2909–2916, 2009. doi: https://doi.org/10.1016/j.proci.2008.05.033. URL https://doi.org/10.1016/j.proci.2008.05.033. (Cited on page 9.)

[43] Pierre Wolf, Gabriel Staffelbach, Laurent Y.M. Gicquel, Jens-Dominik Müller, and Thierry Poinsot. Acoustic and large eddy simulation studies of azimuthal modes in annular combustion chambers. 159(11):3398–3413, nov 2012. doi: https://doi.org/10.1016/j.combustflame.2012.06.016. (Cited on page 9.)

[44] Shigeru Tachibana, Kinya Saito, Takeshi Yamamoto, Mitsumasa Makida, Tomoaki Kitano, and Ryoichi Kurose. Experimental and numerical investigation of thermo-acoustic instability in a liquid-fuel aero-engine combustor at elevated pressure: Validity of large-eddy simulation of spray combustion. *Combustion and Flame*, 162(6):2621–2637, 2015. (Cited on pages 9, 132 and 136.)

[45] Luigi Crocco and Sig-I Cheng. Theory of combustion instability in liquid propellant rocket motors. Technical report, Princeton Univ Nj, 1956. (Cited on page 10.)

[46] N. NOIRAY, D. DUROX, T. SCHULLER, and S. CANDEL. A unified framework for nonlinear combustion instability analysis based on the flame describing function. *Journal of Fluid Mechanics*, 615:139–167, nov 2008. doi: https://doi.org/10.1017/S0022112008003613. (Cited on page 10.)

[47] Wolfgang Polifke. Black-box system identification for reduced order model construction. *Annals of Nuclear Energy*, 67:109–128, 2014. (Cited on page 10.)

[48] Thomas Steinbacher, Alp Albayrak, Abdulla Ghani, and Wolfgang Polifke. Consequences of flame geometry for the acoustic response of premixed flames. *Combustion and Flame*, 199:411–428, 2019. (Cited on page 10.)

[49] Luis Tay Wo Chong, Thomas Komarek, Roland Kaess, Stephan Fo¨ ller, and Wolfgang Polifke. Identification of flame transfer functions from les of a premixed swirl burner. In *Turbo Expo: Power for Land, Sea, and Air*, volume 43970, pages 623–635, 2010. (Cited on page 10.)

[50] Adrien Chatelier, Thibault Guiberti, Renaud Mercier, Nicolas Bertier, Benoît Fiorina, and Thierry Schuller. Experimental and numerical investigation of the response of a swirled flame to flow modulations in a non-adiabatic combustor. *Flow, Turbulence and Combustion*, 102(4): 995–1023, 2019. (Cited on page 10.)

[51] Daniele Pampaloni, Antonio Andreini, Bruno Facchini, and Christian Oliver Paschereit. Large-eddy-simulation modeling of the flame describing function of a lean-premixed swirl-stabilized flame. *Journal of Propulsion and Power*, 35(5):994–1004, 2019. (Cited on page 10.)

[52] Fabien Dupuy, Marco Gatti, Clément Mirat, Laurent Gicquel, Franck Nicoud, and Thierry Schuller. Combining analytical models and LES data to determine the transfer function from swirled premixed flames. 217:222–236, jul 2020. doi: https://doi.org/10.1016/j.combustflame.2020.03.026. (Cited on page 10.)

[53] Kevin Prieur. *Dynamique de la combustion dans un foyer annulaire multi-injecteurs diphasique*. Theses, Université Paris-Saclay, December 2017. URL https://tel.archives-ouvertes.fr/tel-01688256. (Cited on page 10.)

[54] S Balachandar and John K Eaton. Turbulent dispersed multiphase flow. *Annual review of fluid mechanics*, 42:111–133, 2010. (Cited on page 11.)

[55] Kyle D Squires and John K Eaton. Preferential concentration of particles by turbulence. *Physics of Fluids A: Fluid Dynamics*, 3(5):1169–1178, 1991. (Cited on page 11.)

[56] Patrick Jenny, Dirk Roekaerts, and Nijso Beishuizen. Modeling of turbulent dilute spray combustion. *Progress in Energy and Combustion Science*, 38(6):846–887, 2012. (Cited on pages 11, 12 and 95.)

[57] Bastien Rochette. *Modélisation et simulation de la combustion turbulente diphasique dans les moteurs aéronautiques*. PhD thesis, INP Toulouse, 2019. (Cited on pages 12, 31, 43 and 46.)

[58] HH Chiu, HY Kim, and EJ Croke. Internal group combustion of liquid droplets. In *Symposium (international) on combustion*, volume 19, pages 971–980. Elsevier, 1982. (Cited on pages 12 and 13.)

[59] HH Chiu and TM Liu. Group combustion of liquid droplets. *Combustion Science and Technology*, 17(3-4):127–142, 1977. (Cited on page 12.)

[60] Julien Reveillon and Luc Vervisch. Analysis of weakly turbulent dilute-spray flames and spray combustion regimes. *Journal of Fluid Mechanics*, 537:317–347, 2005. (Cited on pages 13 and 14.)

[61] Akira Umemura and Shoichi Takamori. Percolation theory for flame propagation in non-or less-volatile fuel spray: A conceptual analysis to group combustion excitation mechanism. *Combustion and flame*, 141 (4):336–349, 2005. (Cited on page 13.)

[62] William A Sirignano. Advances in droplet array combustion theory and modeling. *Progress in Energy and Combustion Science*, 42:54–86, 2014. (Cited on page 13.)

[63] JH Burgoyne and L Cohen. The effect of drop size on flame propagation in liquid aerosols. *Proceedings of the Royal Society of London. Series A. Mathematical and Physical Sciences*, 225(1162):375–392, 1954. (Cited on page 13.)

[64] CE Polymeropoulos. Flame propagation in a one-dimensional liquid fuel spray. *Combustion Science and Technology*, 9(5-6):197–207, 1974. (Cited on page 13.)

[65] DR Ballal and AH Lefebvre. Flame propagation in heterogeneous mixtures of fuel droplets, fuel vapor and air. In *Symposium (International) on combustion*, volume 18, pages 321–328. Elsevier, 1981. (Cited on pages 13, 14 and 77.)

[66] GD Myers and Arthur Henry Lefebvre. Flame propagation in heterogeneous mixtures of fuel drops and air. *Combustion and Flame*, 66(2): 193–210, 1986. (Cited on page 13.)

[67] S Hayashi, S Kumagai, and T Sakai. Propagation velocity and structure of flames in droplet-vapor-air mixtures. *Combustion Science and Technology*, 15(5-6):169–177, 1977. (Cited on pages 14 and 77.)

[68] JB Greenberg, I Silverman, and Y Tambour. On the origins of spray sectional conservation equations. *Combustion and flame*, 93(1-2):90–96, 1993. (Cited on page 14.)

[69] I Silverman, JB Greenberg, and Y Tambour. Stoichiometry and polydisperse effects in premixed spray flames. *Combustion and Flame*, 93 (1-2):97–118, 1993. (Cited on page 14.)

[70] JB Greenberg, I Silverman, and Y Tambour. On droplet enhancement of the burning velocity of laminar premixed spray flames. *Combustion and flame*, 113(1-2):271–273, 1998. (Cited on page 14.)

[71] A Neophytou and E Mastorakos. Simulations of laminar flame propagation in droplet mists. *Combustion and Flame*, 156(8):1627–1640, 2009. (Cited on page 14.)

[72] M Zhu and B Rogg. Modelling and simulation of sprays in laminar flames. *Meccanica*, 31(2):177–193, 1996. (Cited on page 14.)

[73] A.N. Lipatnikov and J. Chomiak. Turbulent flame speed and thickness: phenomenology, evaluation, and application in multi-dimensional simulations. 28(1):1–74, jan 2002. doi: https://doi.org/10.1016/S0360-1285(01)00007-7. (Cited on page 14.)

[74] K Luo, H Pitsch, MG Pai, and O Desjardins. Direct numerical simulations and analysis of three-dimensional n-heptane spray flames in a model swirl combustor. *Proceedings of the Combustion Institute*, 33(2): 2143–2152, 2011. (Cited on pages 14 and 95.)

[75] F. A. Williams. *Combustion theory : the fundamental theory of chemically reacting flow systems*. Addison/Wesley Pub. Co, Redwood City, Calif, 1985. ISBN 9780201407778. (Cited on pages 18 and 29.)

[76] Kenneth K Kuo. *Principles of combustion*. John Wiley, Hoboken, NJ, 2005. ISBN 978-0-471-04689-9. (Cited on page 18.)

[77] Osborne Reynolds. Xxix. an experimental investigation of the circumstances which determine whether the motion of water shall be direct or sinuous, and of the law of resistance in parallel channels. *Philosophical Transactions of the Royal society of London*, (174):935–982, 1883. (Cited on page 22.)

[78] Lewis Fry Richardson. *Weather prediction by numerical process*. Cambridge university press, 2007. (Cited on page 22.)

[79] Andrei Nikolaevich Kolmogorov. The local structure of turbulence in incompressible viscous fluid for very large reynolds numbers. *Proceedings of the Royal Society of London. Series A: Mathematical and Physical Sciences*, 434(1890):9–13, 1991. (Cited on page 22.)

[80] Stephen B. Pope. *Turbulent Flows*. Cambridge University Press, aug 2000. doi: https://doi.org/10.1017/CBO9780511840531. URL https://doi.org/10.1017/CBO9780511840531. (Cited on page 22.)

[81] Joseph Oakland Hirschfelder, Charles F Curtiss, and R Byron Bird. Molecular theory of gases and liquids. *Molecular theory of gases and liquids*, 1964. (Cited on page 24.)

[82] Alan R Kerstein, William T Ashurst, and Forman A Williams. Field equation for interface propagation in an unsteady homogeneous flow field. *Physical Review A*, 37(7):2728, 1988. (Cited on page 29.)

[83] Olivier Gicquel, Nasser Darabiha, and Dominique Thévenin. Liminar premixed hydrogen/air counterflow flame simulations using flame prolongation of ildm with differential diffusion. *Proceedings of the Combustion Institute*, 28(2):1901–1908, 2000. (Cited on page 29.)

[84] JA Van Oijen and LPH De Goey. Modelling of premixed laminar flames using flamelet-generated manifolds. *Combustion Science and Technology*, 161(1):113–137, 2000. (Cited on page 29.)

[85] Benoit Fiorina, Ronan Vicquelin, Pierre Auzillon, Nasser Darabiha, Olivier Gicquel, and Denis Veynante. A filtered tabulated chemistry model for les of premixed combustion. *Combustion and Flame*, 157(3): 465–475, 2010. (Cited on pages 29 and 35.)

[86] TD Butler and PJ O'rourke. A numerical method for two dimensional unsteady reacting flows. In *Symposium (international) on combustion*, volume 16, pages 1503–1515. Elsevier, 1977. (Cited on page 29.)

[87] PJ O'Rourke and FV Bracco. Two scaling transformations for the numerical computation of multidimensional unsteady laminar flames. *Journal of Computational Physics*, 33(2):185–203, 1979. (Cited on page 29.)

[88] Jean-Philippe Legier, Thierry Poinsot, and Denis Veynante. Dynamically thickened flame les model for premixed and non-premixed turbulent combustion. In *Proceedings of the summer program*, volume 12. Citeseer, 2000. (Cited on pages 30 and 32.)

[89] B Franzelli. *Impact of the chemical description on DNS and LES of turbulent combustion in industrial aero-engines*. PhD thesis, INPT, 2011. (Cited on page 30.)

[90] Thomas Jaravel. *Prediction of pollutants in gas turbines using large eddy simulation*. PhD thesis, INPT, 2016. (Cited on pages 30, 33 and 54.)

[91] Bastien Rochette, Eleonore Riber, Bénédicte Cuenot, and Olivier Vermorel. A generic and self-adapting method for flame detection and thickening in the thickened flame model. *Combustion and Flame*, 212: 448–458, 2020. (Cited on pages 30 and 31.)

[92] O. Colin, F. Ducros, D. Veynante, and T. Poinsot. A thickened flame model for large eddy simulations of turbulent premixed combustion. *Physics of Fluids*, 12(7):1843–1863, jul 2000. doi: https://doi.org/10.1063/1.870436. URL https://doi.org/10.1063/1.870436. (Cited on pages 32 and 100.)

[93] Fabrice Charlette, Charles Meneveau, and Denis Veynante. A power-law flame wrinkling model for LES of premixed turbulent combustion part i: non-dynamic formulation and initial tests. *Combustion and Flame*, 131 (1-2):159–180, oct 2002. doi: https://doi.org/10.1016/S0010-2180(02)00400-5. URL https://doi.org/10.1016/S0010-2180(02)00400-5. (Cited on pages 32 and 100.)

[94] Fabrice Charlette, Charles Meneveau, and Denis Veynante. A power-law flame wrinkling model for LES of premixed turbulent combustion part II: dynamic formulation. *Combustion and Flame*, 131(1-2):181–197, oct 2002. (Cited on pages 32 and 100.)

[95] H. Yamashita, M. Shimada, and T. Takeno. A numerical study on flame stability at the transition point of jet diffusion flames. *Symposium (International) on Combustion*, 26(1):27–34, jan 1996. doi: 10.1016/s0082-0784(96)80196-2. (Cited on page 33.)

[96] K BRAY, P DOMINGO, and L VERVISCH. Role of the progress variable in models for partially premixed turbulent combustion. *Combustion and Flame*, 141(4):431–437, jun 2005. doi: https://doi.org/10.

1016/j.combustflame.2005.01.017. URL https://doi.org/10.1016/j.combustflame.2005.01.017. (Cited on page 33.)

[97] Anne Felden, Lucas Esclapez, Eleonore Riber, Benedicte Cuenot, and Hai Wang. Including real fuel chemistry in les of turbulent spray combustion. *Combustion and Flame*, 193:397–416, 2018. doi: 10.1016/j.combustflame.2018.03.027. (Cited on pages 33 and 123.)

[98] Quentin Cazeres. *Analysis and reduction of chemical kinetics for combustionapplications*. PhD thesis, INP Toulouse, 2021. (Cited on pages 33, 39 and 57.)

[99] Anne Felden. *Development of Analytically Reduced Chemistries (ARC) and applicationsin Large Eddy Simulations (LES) of turbulent combustion*. PhD thesis, INP Toulouse, 2017. (Cited on page 33.)

[100] Charles K Westbrook and Frederick L Dryer. Simplified reaction mechanisms for the oxidation of hydrocarbon fuels in flames. *Combustion science and technology*, 27(1-2):31–43, 1981. (Cited on page 34.)

[101] Benedetta Franzelli, Eleonore Riber, Laurent YM Gicquel, and Thierry Poinsot. Large eddy simulation of combustion instabilities in a lean partially premixed swirled flame. *Combustion and flame*, 159(2):621–637, 2012. (Cited on page 34.)

[102] B Franzelli, E Riber, M Sanjosé, and Thierry Poinsot. A two-step chemical scheme for kerosene–air premixed flames. *Combustion and Flame*, 157(7):1364–1373, jul 2010. doi: https://doi.org/10.1016/j.combustflame.2010.03.014. URL https://doi.org/10.1016/j.combustflame.2010.03.014. (Cited on pages 34, 55, 56, 101, 102 and 103.)

[103] Damien Paulhiac, Bénédicte Cuenot, Eleonore Riber, Lucas Esclapez, and Stéphane Richard. Analysis of the spray flame structure in a lab-scale burner using large eddy simulation and discrete particle simulation. *Combustion and Flame*, 212:25–38, 2020. (Cited on pages 34, 95, 110 and 122.)

[104] Norbert Peters. Laminar diffusion flamelet models in non-premixed turbulent combustion. *Progress in energy and combustion science*, 10(3):319–339, 1984. (Cited on page 35.)

[105] Ulrich Maas and Stephen B Pope. Simplifying chemical kinetics: intrinsic low-dimensional manifolds in composition space. *Combustion and flame*, 88(3-4):239–264, 1992. (Cited on page 35.)

[106] Olivier Gicquel, Nasser Darabiha, and Dominique Thévenin. Laminar premixed hydrogen/air counterflow flame simulations using flame prolongation of ILDM with differential diffusion. *Proceedings of the Combustion Institute*, 28(2):1901–1908, 2000. (Cited on page 35.)

[107] Charles D Pierce and Parviz Moin. Progress-variable approach for large-eddy simulation of non-premixed turbulent combustion. *Journal of fluid Mechanics*, 504:73–97, 2004. (Cited on page 35.)

[108] JA Van Oijen, FA Lammers, and LPH De Goey. Modeling of complex premixed burner systems by using flamelet-generated manifolds. *Combustion and Flame*, 127(3):2124–2134, 2001. (Cited on page 35.)

[109] Amer Avdić, Guido Kuenne, Francesca di Mare, and Johannes Janicka. Les combustion modeling using the eulerian stochastic field method coupled with tabulated chemistry. *Combustion and Flame*, 175:201–219, 2017. (Cited on page 35.)

[110] Benoit Fiorina, R Mercier, G Kuenne, A Ketelheun, A Avdić, J Janicka, D Geyer, A Dreizler, Emma Alenius, Christophe Duwig, et al. Challenging modeling strategies for les of non-adiabatic turbulent stratified combustion. *Combustion and Flame*, 162(11):4264–4282, 2015. (Cited on page 35.)

[111] Edward Knudsen, Heinz Pitsch, et al. Modeling partially premixed combustion behavior in multiphase les. *Combustion and Flame*, 162(1): 159–180, 2015. (Cited on page 35.)

[112] Michael. E. Mueller and Heinz. Pitsch. LES model for sooting turbulent nonpremixed flames. *Combustion and Flame*, 159(6):2166–2180, 2012. (Cited on page 35.)

[113] B Franzelli, B Fiorina, and N Darabiha. A tabulated chemistry method for spray combustion. *Proceedings of the Combustion Institute*, 34(1): 1659–1666, 2013. (Cited on page 35.)

[114] B Yang and SB Pope. Treating chemistry in combustion with detailed mechanisms—in situ adaptive tabulation in principal directions—premixed combustion. *Combustion and Flame*, 112(1-2):85–112, 1998. (Cited on page 35.)

[115] Quentin Cazères, Perrine Pepiot, Eleonore Riber, and Bénédicte Cuenot. A fully automatic procedure for the analytical reduction of chemical kinetics mechanisms for computational fluid dynamics applications. *Fuel*, 303:121247, 2021. (Cited on pages 35 and 57.)

[116] Tamás Turányi. Sensitivity analysis of complex kinetic systems. tools and applications. *Journal of mathematical chemistry*, 5(3):203–248, 1990. (Cited on page 36.)

[117] Christos E Frouzakis and Konstantinos Boulouchos. Analysis and reduction of the ch4-air mechanism at lean conditions. *Combustion science and technology*, 159(1):281–303, 2000. (Cited on page 36.)

[118] Tianfeng Lu and Chung K Law. A directed relation graph method for mechanism reduction. *Proceedings of the Combustion Institute*, 30(1): 1333–1341, 2005. (Cited on page 36.)

[119] Perrine Pepiot-Desjardins and Heinz Pitsch. An efficient error-propagation-based reduction method for large chemical kinetic mechanisms. *Combustion and Flame*, 154(1-2):67–81, 2008. (Cited on pages 36, 37 and 38.)

[120] Tianfeng Lu and Chung K Law. Systematic approach to obtain analytic solutions of quasi steady state species in reduced mechanisms. *The Journal of Physical Chemistry A*, 110(49):13202–13208, 2006. (Cited on page 37.)

[121] T Løvs, D Nilsson, and F Mauss. Automatic reduction procedure for chemical mechanisms applied to premixed methane/air flames. *Proceedings of the Combustion Institute*, 28(2):1809–1815, 2000. (Cited on page 37.)

[122] Alessandro Stagni, Alberto Cuoci, Alessio Frassoldati, Tiziano Faravelli, and Eliseo Ranzi. Lumping and reduction of detailed kinetic schemes: an effective coupling. *Industrial & Engineering Chemistry Research*, 53 (22):9004–9016, 2014. (Cited on page 38.)

[123] Simon Blanchard, Quentin Cazères, and Bénédicte Cuenot. Chemical modeling for methane oxy-combustion in liquid rocket engines. *Acta Astronautica*, 190:98–111, jan 2022. doi: https://doi.org/10.1016/j.actaastro.2021.09.039. (Cited on pages 38 and 39.)

[124] PIERRE FÉVRIER, OLIVIER SIMONIN, and KYLE D. SQUIRES. Partitioning of particle velocities in gas–solid turbulent flows into a continuous field and a spatially uncorrelated random distribution: theoretical formalism and numerical study. *Journal of Fluid Mechanics*, 533: 1–46, 2005. doi: 10.1017/S0022112005004088. (Cited on page 41.)

[125] Eleonore Riber. *Développement de la méthode de simulation aux grandes échelles pour les écoulementsdiphasiques turbulents*. PhD thesis, Institut National Polytechnique de Toulouse, 2007. URL http://www.theses.fr/2007INPT047H. (Cited on page 41.)

[126] Jean-Mathieu Senoner. *Simulation aux Grandes Échelles de l'écoulement diphasique dans un brûleur aéronautique par une approche Euler-Lagrange*. PhD thesis, Institut National Polytechnique de Toulouse, 2009. URL https://www.theses.fr/2010INPT0024. (Cited on page 41.)

[127] Maelene Sanjosé. *Evaluation de la méthode Euler-Euler pour la simulation aux grandes échelles des chambres à carburant liquide*. PhD thesis, Institut National Polytechnique de Toulouse, 2009. URL http://www.theses.fr/2009INPT066H. (Cited on page 41.)

[128] Alfred Barnard Basset. *A treatise on hydrodynamics: with numerous examples*, volume 2. Deighton, Bell and Company, 1888. (Cited on page 42.)

[129] J Boussinesq. *Théorie analytique de la chaleur, volume 2 of Lecture Notes in Mathematics*. 1903. (Cited on page 42.)

[130] Carl Wilhelm Oseen. *Hydrodynamik*. Akademische Verlagsgesellschaft, 1927. (Cited on page 42.)

[131] Clayton T. Crowe, John D. Schwarzkopf, Martin Sommerfeld, and Yutaka Tsuji. *Multiphase Flows with Droplets and Particles (2nd ed.)*. CRC Press., 2011. doi: https://doi.org/10.1201/b11103. URL https://doi.org/10.1201/b11103. (Cited on pages 42, 44 and 109.)

[132] L Schiller and A. Z. Nauman. Über die grundlegenden berechnungen bei der schwerkraftaufbereitung. *Z. Vereines Deutscher Inge.*, 77:318–321, 1933. (Cited on page 44.)

[133] B. Abramzon and W.A. Sirignano. Droplet vaporization model for spray combustion calculations. *International Journal of Heat and Mass Transfer*, 32(9):1605–1618, sep 1989. doi: 10.1016/0017-9310(89)90043-4. (Cited on page 48.)

[134] William E Ranz and W. R. Marshall. Evaporation from drops, parts I & II. *Chem Eng Prog.*, 48:141–146, 174–180, 1952. (Cited on page 48.)

[135] Joshua Heyne, Bastian Rauch, Patrick Le Clercq, and Meredith Colket. Sustainable aviation fuel prescreening tools and procedures. *Fuel*, 290: 120004, 2021. (Cited on page 52.)

[136] Martha. Hajiw-Riberaud and Maria. Alves-Fortunato. Jetscreen deliverable D2.1 - Report about the detailed chemical composition of the fuels and pseudo-components formula. Technical report, IFPEN, 2020. (Cited on pages 53, 54 and 56.)

[137] Tim Edwards and Lourdes Q. Maurice. Surrogate mixtures to represent complex aviation and rocket fuels. 17(2):461–466, mar 2001. doi: https://doi.org/10.2514/2.5765. (Cited on page 54.)

[138] J. LUCHE, M. REUILLON, J.-C. BOETTNER, and M. CATHONNET. REDUCTION OF LARGE DETAILED KINETIC MECHANISMS: APPLICATION TO KEROSENE/AIR COMBUSTION. 176(11):1935–1963, nov 2004. doi: https://doi.org/10.1080/00102200490504571. (Cited on page 55.)

[139] Marco. Mehl and Matteo. Pelucchi. Jetscreen d2.5 – report about the high temperature regime regarding auto-ignition, combustion and soot. Technical report, POLIMI, 2020. (Cited on page 56.)

[140] Stefan Humer, Reinhard Seiser, and Kalyanasundaram Seshadri. Experimental investigation of combustion of jet fuels and surrogates in nonpremixed flows. *Journal of Propulsion and Power*, 27(4):847–855, 2011. (Cited on page 55.)

[141] Krithika Narayanaswamy and Perrine Pepiot. Simulation-driven formulation of transportation fuel surrogates. 22(5):883–897, may 2018. doi: https://doi.org/10.1080/13647830.2018.1464210. (Cited on page 55.)

[142] Krithika Narayanaswamy, Heinz Pitsch, and Perrine Pepiot. A component library framework for deriving kinetic mechanisms for multi-component fuel surrogates: Application for jet fuel surrogates. *Combustion and Flame*, 165:288–309, 2016. doi: 10.1016/j.combustflame.2015.12.013. (Cited on pages 55 and 77.)

[143] Sandra Richter, Clemens Naumann, and Uwe Riedel. Experimental study on the combustion properties of an alcohol-to-jet fuel. In *Proceedings of the 2nd World Congress on Momentum, Heat and Mass Transfer (MHMT 17)*, 2017. (Cited on page 56.)

[144] RB Landis and Anthony F Mills. Effect of internal diffusional resistance on the evaporation of binary droplets. In *International Heat Transfer Conference Digital Library*. Begel House Inc., 1974. (Cited on page 61.)

[145] Chung King Law. Multicomponent droplet combustion with rapid internal mixing. *Combustion and Flame*, 26:219–233, 1976. (Cited on page 61.)

[146] Chung King Law. Recent advances in droplet vaporization and combustion. *Progress in energy and combustion science*, 8(3):171–201, 1982. (Cited on pages 61, 62 and 71.)

[147] CK Law. Internal boiling and superheating in vaporizing multicomponent droplets. *AIChE Journal*, 24(4):626–632, 1978. (Cited on page 61.)

[148] Chung King Law and HK Law. A d2-law for multicomponent droplet vaporization and combustion. *AIAA journal*, 20(4):522–527, 1982. (Cited on pages 61 and 64.)

[149] Chung King Law, S Prakash, and WA Sirignano. Theory of convective, transient, multicomponent droplet vaporization. *Symposium (International) on Combustion*, 16(1):605–617, 1977. (Cited on page 62.)

[150] Pedro Lara-Urbaneja and WA Sirignano. Theory of transient multicomponent droplet vaporization in a convective field. *Symposium (International) on Combustion*, 18(1):1365–1374, 1981. (Cited on page 62.)

[151] AY Tong and WA Sirignano. Multicomponent droplet vaporization in a high temperature gas. *Combustion and Flame*, 66(3):221–235, 1986. (Cited on page 62.)

[152] Suresh K Aggarwal, Albert Y Tong, and William A Sirignano. A comparison of vaporization models in spray calculations. *AIAA journal*, 22 (10):1448–1457, 1984. (Cited on page 62.)

[153] Suresh K Aggarwal. Modeling of a dilute vaporizing multicomponent fuel spray. *International journal of heat and mass transfer*, 30(9):1949–1961, 1987. (Cited on page 62.)

[154] SK Aggarwal and HC Mongia. Multicomponent and high-pressure effects on droplet vaporization. *J. Eng. Gas Turbines Power*, 124(2): 248–255, 2002. (Cited on page 62.)

[155] JED Gauthier, Michael F Bardon, and VK Rao. Combustion characteristics of multicomponent fuels under cold starting conditions in a gas turbine. In *ASME 1991 International Gas Turbine and Aeroengine Congress and Exposition*. American Society of Mechanical Engineers Digital Collection, 1991. (Cited on page 62.)

[156] CK Law, CH Lee, and N Srinivasan. Combustion characteristics of water-in-oil emulsion droplets. *Combustion and flame*, 37:125–143, 1980. (Cited on page 62.)

[157] Mohamed Mohamed El Wakil, RJ Priem, HJ Brikowski, PS Myers, and OA Uyehara. Experimental and calculated temperature and mass histories of vaporizing fuel drops. Technical report, NASA, 1956. (Cited on page 62.)

[158] Bernard J Wood, Henry Wise, and SH Inami. Heterogeneous combustion of multicomponent fuels. *Combustion and Flame*, 4:235–242, 1960. (Cited on page 62.)

[159] Jochen Wilms. *Evaporation of multicomponent droplets*. PhD thesis, Institut für Thermodynamik der Luft und Raumfahrt, Universität Stuttgart, 2005. (Cited on pages 62, 68 and 70.)

[160] Günter Brenn, LJ Deviprasath, Franz Durst, and Clemens Fink. Evaporation of acoustically levitated multi-component liquid droplets. *International journal of heat and mass transfer*, 50(25-26):5073–5086, 2007. (Cited on page 62.)

[161] Bastian Rauch, Raffaela Calabria, Fabio Chiariello, Patrick Le Clercq, Patrizio Massoli, and Michael Rachner. Accurate analysis of multicomponent fuel spray evaporation in turbulent flow. *Experiments in fluids*, 52(4):935–948, 2012. (Cited on page 62.)

[162] Longfei Chen, Zhixin Liu, Yuzhen Lin, and Chi Zhang. Different spray droplet evaporation models for non-ideal multi-component fuels with experimental validation. *International Journal of Heat and Mass Transfer*, 94:292–300, 2016. (Cited on page 62.)

[163] Longfei Chen, Guangze Li, and Bin Fang. Droplet evaporation characteristics of aviation kerosene surrogate fuel and butanol blends under forced convection. *International Journal of Multiphase Flow*, 114:229–239, 2019. (Cited on page 62.)

[164] Benjamin Gal-Or, Harry T Cullinan Jr, and Ran Galli. New thermodynamic-transport theory for systems with continuous component density distributions. *Chemical Engineering Science*, 30(9):1085–1092, 1975. (Cited on page 63.)

[165] JG Briano and ED Glandt. Molecular thermodynamics of continuous mixtures. *Fluid Phase Equilibria*, 14:91–102, 1983. (Cited on page 63.)

[166] MT Rätzsch and H Kehlen. Continuous thermodynamics of complex mixtures. *Fluid Phase Equilibria*, 14:225–234, 1983. (Cited on page 63.)

[167] Ronald L Cotterman, Rainer Bender, and John M Prausnitz. Phase equilibria for mixtures containing very many components. development and application of continuous thermodynamics for chemical process design. *Industrial & Engineering Chemistry Process Design and Development*, 24(1):194–203, 1985. (Cited on page 63.)

[168] Grace F Chou and John M Prausnitz. Adiabatic flash calculations for continuous or semicontinuous mixtures using an equation of state. *Fluid Phase Equilibria*, 30:75–82, 1986. (Cited on page 63.)

[169] Bert Willman and Amyn S Teja. Prediction of dew points of semicontinuous natural gas and petroleum mixtures. 1. characterization by use of an effective carbon number and ideal solution predictions. *Industrial & engineering chemistry research*, 26(5):948–952, 1987. (Cited on page 63.)

[170] Jihane Tamim and William LH Hallett. A continuous thermodynamics model for multicomponent droplet vaporization. *Chemical Engineering Science*, 50(18):2933–2942, 1995. (Cited on pages 63 and 64.)

[171] Andreas M. Lippert and Rolf D. Reitz. Modeling of multicomponent fuels using continuous distributions with application to droplet evaporation and sprays. In *International Fuels & Lubricants Meeting & Exposition*. SAE International, oct 1997. URL https://doi.org/10.4271/972882. (Cited on page 64.)

[172] William LH Hallett. A simple model for the vaporization of droplets with large numbers of components. *Combustion and Flame*, 121(1-2):334–344, 2000. (Cited on page 64.)

[173] Kenneth G Harstad, Patrick C Le Clercq, and Josette Bellan. Statistical model of multicomponent-fuel drop evaporation for many-drop flow simulations. *AIAA journal*, 41(10):1858–1874, 2003. (Cited on page 64.)

[174] Kenneth Harstad and Josette Bellan. Modeling evaporation of jet a, jp-7, and rp-1 drops at 1 to 15 bars. *Combustion and flame*, 137(1-2): 163–177, 2004. (Cited on page 64.)

[175] Kenneth Harstad and Josette Bellan. Modeling of multicomponent homogeneous nucleation using continuous thermodynamics. *Combustion and flame*, 139(3):252–262, 2004. (Cited on page 64.)

[176] PC Le Clercq and J Bellan. Direct numerical simulation of a transitional temporal mixing layer laden with multicomponent-fuel evaporating drops using continuous thermodynamics. *Physics of Fluids*, 16(6): 1884–1907, 2004. URL https://doi.org/10.1063/1.1688327. (Cited on page 64.)

[177] Patrick C Le Clercq and Josette Bellan. Direct numerical simulation of gaseous mixing layers laden with multicomponent-liquid drops: liquid-specific effects. *Journal of Fluid Mechanics*, 533:57–94, 2005. URL https://doi.org/10.1017/S0022112005003940. (Cited on page 64.)

[178] PC Le Clercq and J Bellan. Modeling of multicomponent-fuel drop-laden mixing layers having a multitude of species. *Proceedings of the Combustion Institute*, 30(2):2011–2019, 2005. URL https://doi.org/10.1016/j.proci.2004.07.023. (Cited on page 64.)

[179] LC Selle and Josette Bellan. Scalar-dissipation modeling for passive and active scalars: a priori study using direct numerical simulation. *Proceedings of the Combustion Institute*, 31(1):1665–1673, 2007. URL https://doi.org/10.1016/j.proci.2006.07.003. (Cited on page 64.)

[180] LC Selle and Josette Bellan. Evaluation of assumed-pdf methods in two-phase flows using direct numerical simulation. *Proceedings of the Combustion Institute*, 31(2):2273–2281, 2007. URL https://doi.org/10.1016/j.proci.2006.07.004. (Cited on page 64.)

[181] LC Selle and Josette Bellan. Characteristics of transitional multicomponent gaseous and drop-laden mixing layers from direct numerical simulation: Composition effects. *Physics of Fluids*, 19(6):063301, 2007. URL https://doi.org/10.1063/1.2734997. (Cited on page 64.)

[182] LC Selle and Josette Bellan. Large eddy simulation composition equations for single-phase and two-phase fully multicomponent flows. *Proceedings of the Combustion Institute*, 32(2):2239–2246, 2009. URL https://doi.org/10.1016/j.proci.2008.06.005. (Cited on page 64.)

[183] Shiyou Yang, Youngchul Ra, Rolf D Reitz, Brad VanDerWege, and Jianwen Yi. Development of a realistic multicomponent fuel evaporation model. *Atomization and Sprays*, 20(11), 2010. URL https://doi.org/10.1615/AtomizSpr.v20.i11.40. (Cited on pages 64 and 65.)

[184] Shiyou Yang, Youngchul Ra, and Rolf D Reitz. A vaporization model for realistic multi-component fuels. In *Proceedings of the 22nd Annual Conference on Liquid Atomization and Spray Systems-USA*, pages 16–19, 2010. URL http://ilass.org/2/ConferencePapers/ILASS2010-123.PDF. (Cited on page 64.)

[185] Patrick Le Clercq, Nicolas Doué, Michael Rachner, and Manfred Aigner. Validation of a multicomponent-fuel model for spray computations. In *47th AIAA Aerospace Sciences Meeting including The New Horizons Forum and Aerospace Exposition*, page 1188, 2009. URL https://doi.org/10.2514/6.2009-1188. (Cited on pages 64 and 65.)

[186] Jörn Hinrichs, Varun Shastry, Malte Junk, Yasmin Hemberger, and Heinz Pitsch. An experimental and computational study on multicomponent evaporation of diesel fuel droplets. *Fuel*, 275:117727, 2020. doi: 10.1016/j.fuel.2020.117727. (Cited on page 64.)

[187] Lei Zhang and Song-Charng Kong. Vaporization modeling of petroleum–biofuel drops using a hybrid multi-component approach. *Combustion and Flame*, 157(11):2165–2174, 2010. URL https://doi.org/10.1016/j.combustflame.2010.05.011. (Cited on page 65.)

[188] Lei Zhang and Song-Charng Kong. High-pressure vaporization modeling of multi-component petroleum–biofuel mixtures under engine conditions. *Combustion and flame*, 158(9):1705–1717, 2011. URL https://doi.org/10.1016/j.combustflame.2011.01.002. (Cited on page 65.)

[189] Ping Yi, Wuqiang Long, Ming Jia, Liyan Feng, and Jiangping Tian. Development of an improved hybrid multi-component vaporization model for realistic multi-component fuels. *International Journal of Heat and Mass Transfer*, 77:173–184, 2014. URL https://doi.org/10.1016/j.ijheatmasstransfer.2014.05.008. (Cited on page 65.)

[190] Zeyu Ren, Lei Zhang, and Xiaohua Ren. A hybrid multicomponent model for the vaporisation simulation of gasoline drop. *Combustion Theory and Modelling*, 23(2):210–225, 2019. URL https://doi.org/10.1080/13647830.2018.1508750. (Cited on page 65.)

[191] Georg Eckel, Jasper Grohmann, Luca Cantu, Nadja Slavinskaya, Trupti Kathrotia, Michael Rachner, Patrick Le Clercq, Wolfgang Meier, and Manfred Aigner. Les of a swirl-stabilized kerosene spray flame with a multi-component vaporization model and detailed chemistry. *Combustion and Flame*, 207:134–152, 2019. (Cited on pages 65, 66, 113 and 125.)

[192] B Abramzon and WA Sirignano. Droplet vaporization model for spray combustion calculations. *International journal of heat and mass transfer*, 32(9):1605–1618, 1989. (Cited on page 66.)

[193] Carl L Yaws. *Transport properties of chemicals and hydrocarbons*. William Andrew, 2014. (Cited on page 67.)

[194] Carl L Yaws. *The yaws handbook of physical properties for hydrocarbons and chemicals: physical properties for more than 54,000 organic and inorganic chemical compounds, Coverage for C1 to C100 Organics and Ac to Zr Inorganics*. Gulf Professional Publishing, 2015. (Cited on page 67.)

[195] Robert C Reid, John M Prausnitz, and Bruce E Poling. *The properties of gases and liquids*. McGraw Hill Book Co., New York, NY, 1987. (Cited on page 67.)

[196] Kai Han, Guoqian Song, Xiaokang Ma, and Bo Yang. An experimental and theoretical study of the effect of suspended thermocouple on the single droplet evaporation. *Applied Thermal Engineering*, 101:568–575, may 2016. doi: https://doi.org/10.1016/j.applthermaleng.2015.12.022. URL https://doi.org/10.1016/j.applthermaleng.2015.12.022. (Cited on page 68.)

[197] S. Radhakrishnan, N. Srivathsan, T.N.C. Anand, and Shamit Bakshi. Influence of the suspender in evaporating pendant droplets. *International Journal of Thermal Sciences*, 140:368–376, jun 2019. doi: https://doi.org/10.1016/j.ijthermalsci.2019.03.004. URL https://doi.org/10.1016/j.ijthermalsci.2019.03.004. (Cited on page 68.)

[198] HA Duguid and J. F Stampfer Jr. The evaporation rates of small, freely falling water drops. *Journal of Atmospheric Sciences*, 28 (7):1233–1243, 1971. doi: https://doi.org/10.1175/1520-0469(1971)028<1233:TEROSF>2.0.CO;2. URL https://doi.org/10.1175/1520-0469(1971)028<1233:TEROSF>2.0.CO;2. (Cited on page 68.)

[199] Michael Stöhr, Stephan Ruoff, Bastian Rauch, Wolfgang Meier, and Patrick Le Clercq. Droplet vaporization for conventional and alternative jet fuels at realistic temperature conditions: Systematic measurements and numerical modeling. *Proceedings of the Combustion Institute*, 38 (2):3269–3276, 2021. (Cited on pages 68 and 114.)

[200] A. L. YARIN, G. BRENN, O. KASTNER, D. RENSINK, and C. TROPEA. Evaporation of acoustically levitated droplets. *Journal of Fluid Mechanics*, 399:151–204, 1999. doi: 10.1017/S0022112099006266. (Cited on page 68.)

[201] Malte Junk, Jörn Hinrichs, Fritz Polt, Jonas Fechner, and Werner Pauer. Quantitative experimental determination of evaporation influencing factors in single droplet levitation. *International Journal of Heat and Mass Transfer*, 149:119057, mar 2020. URL https://doi.org/10.1016/j.ijheatmasstransfer.2019.119057. (Cited on page 68.)

[202] Madjid Birouk. *Influence de la turbulence homogene et isotrope sur la vaporisation et la combustion de gouttes de combustibles liquides*. PhD thesis, Université d'Orléans, 1996. (Cited on pages 68 and 69.)

[203] Seyed Vahid Ebrahimian Shiadeh. *Développement de modèles d'évaporation multi-composants et modélisation 3D des systèmes de réduction de NOx (SCR)*. PhD thesis, Toulouse, INPT, 2011. (Cited on page 68.)

[204] Youngchul Ra and Rolf D Reitz. A vaporization model for discrete multi-component fuel sprays. *International Journal of Multiphase Flow*, 35(2):101–117, feb 2009. URL https://doi.org/10.1016/j.ijmultiphaseflow.2008.10.006. (Cited on pages 68, 71 and 72.)

[205] William A Sirignano. *Fluid dynamics and transport of droplets and sprays*. Cambridge University press, 2010. (Cited on pages 76, 79, 81 and 87.)

[206] Antonio L Sánchez, Javier Urzay, and Amable Liñán. The role of separation of scales in the description of spray combustion. *Proceedings of the Combustion Institute*, 35(2):1549–1577, 2015. (Cited on page 76.)

[207] Anne Felden, Lucas Esclapez, Eleonore Riber, Bénédicte Cuenot, and Hai Wang. Including real fuel chemistry in LES of turbulent spray combustion. *Combustion and Flame*, 193:397–416, jul 2018. doi: 10.1016/j.combustflame.2018.03.027. (Cited on pages 76 and 78.)

[208] A. Giusti and E. Mastorakos. Detailed chemistry LES/CMC simulation of a swirling ethanol spray flame approaching blow-off. *Proceedings of the Combustion Institute*, 36(2):2625–2632, 2017. doi: 10.1016/j.proci.2016.06.035. (Cited on page 76.)

[209] Dongwon Noh, Simon Gallot-Lavallée, William P Jones, and Salvador Navarro-Martinez. Comparison of droplet evaporation models for a turbulent, non-swirling jet flame with a polydisperse droplet distribution. *Combustion and Flame*, 194:135–151, 2018. (Cited on page 76.)

[210] A. Stagni, L. Esclapez, P. Govindaraju, A. Cuoci, T. Faravelli, and M. Ihme. The role of preferential evaporation on the ignition of multicomponent fuels in a homogeneous spray/air mixture. *Proceedings of the Combustion Institute*, 36(2):2483–2491, 2017. doi: 10.1016/j.proci.2016.06.052. (Cited on page 76.)

[211] Pavan B. Govindaraju, Thomas Jaravel, and Matthias Ihme. Coupling of turbulence on the ignition of multicomponent sprays. *Proceedings of the Combustion Institute*, 37(3):3295–3302, 2019. doi: 10.1016/j.proci.2018.05.166. (Cited on page 76.)

[212] Georg Eckel, Jasper Grohmann, Luca Cantu, Nadja Slavinskaya, Trupti Kathrotia, Michael Rachner, Patrick Le Clercq, Wolfgang Meier, and Manfred Aigner. LES of a swirl-stabilized kerosene spray flame with a multi-component vaporization model and detailed chemistry. *Combustion and Flame*, 207:134–152, sep 2019. doi: 10.1016/j.combustflame.2019.05.011. (Cited on page 76.)

[213] A Neophytou and E Mastorakos. Simulations of laminar flame propagation in droplet mists. *Combustion and Flame*, 156(8):1627–1640, 2009. (Cited on page 77.)

[214] B Rochette, E Riber, and B Cuenot. Effect of non-zero relative velocity on the flame speed of two-phase laminar flames. *Proceedings of the Combustion Institute*, 37(3):3393–3400, 2019. (Cited on pages 77, 78, 81, 85 and 88.)

[215] ELISEO Ranzi, Alessio Frassoldati, Roberto Grana, Alberto Cuoci, Tiziano Faravelli, AP Kelley, and Chung King Law. Hierarchical and comparative kinetic modeling of laminar flame speeds of hydrocarbon and oxygenated fuels. *Progress in Energy and Combustion Science*, 38 (4):468–501, 2012. (Cited on page 78.)

[216] Perrine Pepiot. *Automatic strategies to model transportation fuel surrogates*. PhD thesis, Stanford University, Department of Mechanical Engineering, 2008. (Cited on page 78.)

[217] Bastian Rauch, Raffaela Calabria, Fabio Chiariello, Patrick Le Clercq, Patrizio Massoli, and Michael Rachner. Accurate analysis of multicomponent fuel spray evaporation in turbulent flow. *Experiments in fluids*, 52(4):935–948, 2012. (Cited on page 78.)

[218] Irfan Javed, Seung Wook Baek, Khalid Waheed, Ghafar Ali, and Sung Oh Cho. Evaporation characteristics of kerosene droplets with dilute concentrations of ligand-protected aluminum nanoparticles at elevated temperatures. *Combustion and flame*, 160(12):2955–2963, 2013. (Cited on page 79.)

[219] Likun Ma and Dirk Roekaerts. Numerical study of the multi-flame structure in spray combustion. *Proceedings of the Combustion Institute*, 36(2):2603–2613, 2017. (Cited on page 95.)

[220] F Shum-Kivan, J Marrero Santiago, A Verdier, E Riber, B Renou, G Cabot, and B Cuenot. Experimental and numerical analysis of a turbulent spray flame structure. *Proceedings of the Combustion Institute*, 36(2):2567–2575, 2017. (Cited on page 95.)

[221] Julien M Apeloig, François-Xavier d'Herbigny, Frank Simon, Pierre Gajan, Mikael Orain, and Sébastien Roux. Liquid-fuel behavior in an aeronautical injector submitted to thermoacoustic instabilities. *Journal of Propulsion and Power*, 31(1):309–319, 2015. (Cited on pages 96, 133 and 147.)

[222] Pierre Gajan; Anthony Desclaux; Julien Garraud and Mikael Orain. Jetscreen-Deliverable 6.6_Onera_R1.3. Technical report, Office national d'études et de recherches aérospatiales, 2019. (Cited on pages 96, 98 and 133.)

[223] Léa Voivenel; Jean-Baptiste May-Carle; Stefano Puggelli; Virginel Bodoc; Julien Garraud; Pierre Gajan; Varun Shastry; Eleonore Riber and Bénédicte Cuenot. Jetscreen-Deliverable 6.3_Onera_R2. Technical report, SAFRAN Tech, 2020. (Cited on pages 96 and 133.)

[224] Anthony Desclaux. *Etude expérimentale du comportement linéaire et non linéaire d'une flamme diphasique soumise à une excitation acoustique. Mise en œuvre d'une méthode de contrôle adaptative*. PhD thesis,

ISAE, Toulouse, 2020. URL http://www.theses.fr/2020ESAE0003. (Cited on page 98.)

[225] Parviz Moin and Sourabh V Apte. Large-eddy simulation of realistic gas turbine combustors. *AIAA journal*, 44(4):698–708, 2006. (Cited on page 99.)

[226] Guillaume Daviller, Maxence Brebion, Pradip Xavier, Gabriel Staffelbach, Jens-Dominik Müller, and Thierry Poinsot. A mesh adaptation strategy to predict pressure losses in LES of swirled flows. *Flow, Turbulence and Combustion*, 99(1):93–118, mar 2017. doi: 10.1007/s10494-017-9808-z. URL https://doi.org/10.1007/s10494-017-9808-z. (Cited on page 99.)

[227] Peter D Lax and Burton Wendroff. Difference schemes for hyperbolic equations with high order of accuracy. *Communications on pure and applied mathematics*, 17(3):381–398, 1964. (Cited on page 100.)

[228] Franck Nicoud, Hubert Baya Toda, Olivier Cabrit, Sanjeeb Bose, and Jungil Lee. Using singular values to build a subgrid-scale model for large eddy simulations. *Physics of fluids*, 23(8):085106, 2011. (Cited on page 100.)

[229] S. Mendez and F. Nicoud. Adiabatic homogeneous model for flow around a multiperforated plate. *AIAA Journal*, 46(10):2623–2633, oct 2008. (Cited on page 101.)

[230] S. MENDEZ and F. NICOUD. Large-eddy simulation of a bi-periodic turbulent flow with effusion. *Journal of Fluid Mechanics*, 598:27–65, feb 2008. (Cited on page 101.)

[231] S. Mendez and J.D. Eldredge. Acoustic modeling of perforated plates with bias flow for large-eddy simulations. *Journal of Computational Physics*, 228(13):4757–4772, jul 2009. (Cited on page 101.)

[232] J. LUCHE, M. REUILLON, J.-C. BOETTNER, and M. CATHONNET. REDUCTION OF LARGE DETAILED KINETIC MECHANISMS: APPLICATION TO KEROSENE/AIR COMBUSTION. *Combustion Science and Technology*, 176(11):1935–1963, nov 2004. doi: https://doi.org/10.1080/00102200490504571. URL https://doi.org/10.1080/00102200490504571. (Cited on pages 102 and 103.)

[233] M Sanjosé, JM Senoner, F Jaegle, B Cuenot, S Moreau, and Thierry Poinsot. Fuel injection model for euler–euler and euler–lagrange large-eddy simulations of an evaporating spray inside an aeronautical combustor. *International Journal of Multiphase Flow*, 37(5):514–529, 2011. (Cited on page 102.)

[234] N Syred and JM Beer. Combustion in swirling flows: a review. *Combustion and flame*, 23(2):143–201, oct 1974. doi: https://doi.org/10.1016/0010-2180(74)90057-1. URL https://doi.org/10.1016/0010-2180(74)90057-1. (Cited on page 104.)

[235] T. Ivanic, E. Foucault, and J. Pecheux. Dynamics of swirling jet flows. *Experiments in Fluids*, 35(4):317–324, oct 2003. doi: https://doi.org/10.1007/s00348-003-0646-5. URL https://doi.org/10.1007/s00348-003-0646-5. (Cited on page 104.)

[236] William A Sirignano. *Fluid dynamics and transport of droplets and sprays*. Cambridge university press, 2010. (Cited on page 109.)

[237] Damien Paulhiac. *Modélisation de la combustion d'un spray dans un brûleur aéronautique*. PhD thesis, Institut National Polytechnique de Toulouse, 2015. URL http://www.theses.fr/2015INPT0051. (Cited on page 110.)

[238] Mastorakos de la Cruz García, E Mastorakos, and AP Dowling. Investigations on the self-excited oscillations in a kerosene spray flame. *Combustion and Flame*, 156(2):374–384, feb 2009. doi: https://doi.org/10.1016/j.combustflame.2008.11.018. (Cited on page 131.)

[239] E Bärow, R Koch, and HJ Bauer. Comparison of oscillation modes of spray and gaseous flames. In *Proceedings of the Eighth Mediterranean Combustion Symposium: EGTSC-26*, 2013. (Cited on page 131.)

[240] Tomoaki Kitano, Keisuke Kaneko, Ryoichi Kurose, and Satoru Komori. Large-eddy simulations of gas-and liquid-fueled combustion instabilities in back-step flows. *Combustion and Flame*, 170:63–78, 2016. (Cited on page 131.)

[241] Abhishek L Pillai, Jun Nagao, Ryo Awane, and Ryoichi Kurose. Influences of liquid fuel atomization and flow rate fluctuations on spray combustion instabilities in a backward-facing step combustor. *Combustion and Flame*, 220:337–356, 2020. (Cited on pages 131 and 141.)

[242] E Lo Schiavo, Davide Laera, Eleonore Riber, L Gicquel, and Thierry Poinsot. Effects of liquid fuel/wall interaction on thermoacoustic instabilities in swirling spray flames. *Combustion and Flame*, 219:86–101, 2020. (Cited on page 132.)

[243] E Lo Schiavo, Davide Laera, Eleonore Riber, L Gicquel, and Thierry Poinsot. On the impact of fuel injection angle in euler–lagrange large eddy simulations of swirling spray flames exhibiting thermoacoustic instabilities. *Combustion and Flame*, 227:359–370, 2021. (Cited on pages 132 and 154.)

[244] Guillaume Vignat, Ermanno Lo Schiavo, Davide Laera, Antoine Renaud, Laurent Gicquel, Daniel Durox, and Sébastien Candel. Dynamics of spray and swirling flame under acoustic oscillations: A joint experimental and les investigation. *Proceedings of the Combustion Institute*, 38(4):6015–6024, 2021. (Cited on page 132.)

[245] F. Nicoud, L. Benoit, C. Sensiau, and T. Poinsot. Acoustic modes in combustors with complex impedances and multidimensional active flames. *AIAA Journal*, 45(2):426–441, feb 2007. doi: https://doi.org/10.2514/1.24933. (Cited on page 132.)

[246] Laurent Selle, Franck Nicoud, and Thierry Poinsot. Actual impedance of nonreflecting boundary conditions: Implications for computation of resonators. *AIAA journal*, 42(5):958–964, 2004. (Cited on page 133.)

[247] Guillaume Daviller, Gorkem Oztarlik, and Thierry Poinsot. A generalized non-reflecting inlet boundary condition for steady and forced compressible flows with injection of vortical and acoustic waves. *Computers & Fluids*, 190:503–513, 2019. (Cited on page 133.)

[248] Renaud Gaudron, Marco Gatti, Clément Mirat, and Thierry Schuller. Flame describing functions of a confined premixed swirled combustor with upstream and downstream forcing. *Journal of Engineering for Gas Turbines and Power*, 141(5):051016, 2019. (Cited on page 133.)

[249] Dupuy Fabien. *Reduced Order Models and Large Eddy Simulation for-Combustion Instabilities in aeronautical Gas Turbines*. PhD thesis, INPT, 2020. (Cited on page 133.)

[250] Arthur H Lefebvre and Vincent G McDonell. *Atomization and sprays*. CRC press, mar 2017. URL https://doi.org/10.1201/9781315120911. (Cited on page 139.)

[251] M Zhu, AP Dowling, and KNC Bray. Self-excited oscillations in combustors with spray atomizers. *J. Eng. Gas Turbines Power*, 123(4): 779–786, oct 2001. doi: https://doi.org/10.1115/1.1376717. URL https://doi.org/10.1115/1.1376717. (Cited on page 141.)

[252] J Eckstein, E Freitag, C Hirsch, T Sattelmayer, R Von der Bank, and T Schilling. Forced low-frequency spray characteristics of a generic airblast swirl diffusion burner. *J. Eng. Gas Turbines Power*, 127(2): 301–306, apr 2005. doi: https://doi.org/10.1115/1.1789515. URL https://doi.org/10.1115/1.1789515. (Cited on page 141.)

[253] Fabrice Giuliani, Pierre Gajan, Olaf Diers, and Michel Ledoux. Influence of pulsed entries on a spray generated by an air-blast injection device: An experimental analysis on combustion instability processes in aeroengines. *Proceedings of the combustion institute*, 29 (1):91–98, 2002. doi: https://doi.org/10.1016/S1540-7489(02)80016-5. URL https://doi.org/10.1016/S1540-7489(02)80016-5. (Cited on page 141.)

[254] Geoffroy Chaussonnet, Armin Müller, Simon Holz, Rainer Koch, and H-J Bauer. Time-response of recent prefilming airblast atomization models in an oscillating air flow field. *Journal of Engineering for Gas Turbines and Power*, 139(12), 2017. (Cited on page 141.)

[255] Thomas Christou, Björn Stelzner, and Nikolaos Zarzalis. Influence of acoustically excited airflows on a planar airblast prefilmer. jun 2021. doi: https://doi.org/10.1115/GT2021-58862. URL https://doi.org/10.1115/GT2021-58862. (Cited on page 141.)

[256] Jun Cai, San-Mou Jeng, and Robert Tacina. The structure of a swirl-stabilized reacting spray issued from an axial swirler. jan 2005. doi: https://doi.org/10.2514/6.2005-1424. URL https://doi.org/10.2514/6.2005-1424. (Cited on page 147.)

[257] Renaud Lecourt, Guillaume Linassier, and Ge´rard Lavergne. Detailed characterisation of a swirled air/kerosene spray in reactive and non-reactive conditions downstream from an actual turbojet injection system. jan 2011. doi: https://doi.org/10.1115/GT2011-45173. (Cited on page 147.)